



University of  
**Strathclyde**  
Engineering

**Numerical Modelling of Blood Fluid Dynamics in  
Patient-Specific Paediatric and Adult Aortae**

**Lauren Johnston**

Department of Biomedical Engineering

University of Strathclyde

This thesis is submitted for the degree of

**Doctor of Philosophy**

2024

## Declaration

This thesis is the result of the author's original research. It has been composed by the author and has not been previously submitted for examination which has led to the award of a degree.

The copyright of this thesis belongs to the author under the terms of the United Kingdom Copyright Acts as qualified by University of Strathclyde Regulation 3.50. Due acknowledgement must always be made of the use of any material contained in, or derived from, this thesis.

Signed: 

Date: 01/07/2024

# Acknowledgements

I would like to thank the following people, both academically and personally, for being on this journey with me.

I would first like to acknowledge and give my warmest thanks to my supervisor Dr Asimina Kazakidi who made this work possible. Her enthusiasm for research and dedication to both her work and students is what first drew me to do a PhD. Without her experience, knowledge, and guidance my journey would not have been nearly as fulfilling. I would also like to thank the staff from the Biomedical Engineering Department at the University of Strathclyde. I enjoyed the community so much during my undergraduate degree that I chose to stay for the PhD too! Finally, it would be impossible to forget the rest of the Biofluids group Maria Boumpouli, Marianna Syntouka, George Linaker, and Scott Black. They were not only great co-workers and collaborators but also friends that made this journey unforgettable.

I would also like to thank our collaborators from the Queen Elizabeth University Hospital, Dr Avril Mason, Dr Ruth Allen, and Dr Pauline Hall-Barrientos. For sharing with us clinical data which was fundamental for the outcome of the thesis and for providing us with insights as both clinicians and researchers. In addition, they steered this research with their guidance and advice, and facilitated discussions at journal clubs with the wider hospital community.

In addition, I would like to thank Dr Cristina Amon, Dr David Romero, and the rest of the team from the Advanced Thermofluids Optimization, Modelling, and Simulation (ATOMS) Laboratory at the University of Toronto. Their dedication to myself as a researcher was apparent as we spent two years organising my visit due to the COVID-19 pandemic. When I finally arrived in March 2022, they welcomed me with open arms and continued to do so for my three-month visit.

I am grateful to the UK Research and Innovation (UKRI) Engineering and Physical Sciences Research Council (EPSRC) who funded my PhD and to the University of Strathclyde Research Studentship Scheme (SRSS) Student Excellence Awards, Project No 1619, who selected my

PhD application back in 2018. Also, to the UKRI UK-Canada Globalink Doctoral Exchange Scheme and Mitacs who joint funded my 12-week research placement in Canada.

To my friends, old and new, you have been the best support network over the past few years and the greatest distraction when I need it. Caitlin, I still remember meeting you on day 1 of university in 2014, and instantly feeling like long lost sisters (even stranger as we share the same birthday!). We accidently ended up on this journey together, and now we'll (hopefully) be graduating with doctorates in the same year! Fiona, the other musketeer in our trio, you've always been my gym buddy in between studying and my welcome escape from PhD work. I don't think I would have enjoyed my degree nearly as much without my two best friends.

To Ross, thank you for always encouraging me to reach for the stars and cheering me on at every milestone. I admire your *cool as a cucumber* attitude to life, which kept me sane during the unpredictable combination of covid and a PhD. You really are the best partner (and dog dad) I could have asked for.

And to my parents, who always told me I could be anything I wanted... mum, I'm sorry that ended up being an engineer like dad!

# Abstract

In the human body, the aorta is the largest artery and is responsible for distributing oxygenated blood from the heart to the surrounding organs and tissues. However, the aorta is vulnerable to a number of disorders, many of which are life-threatening. The root cause of aortic disease is unknown, but we do know that some individuals are more prone than others. In some cases, individuals with a genetic abnormality are predisposed to an increased risk of aortic disease. This is true for females with Turner syndrome (TS), a rare genetic disorder, who have a higher prevalence of cardiovascular disease than the general population. While there are established clinical practice guidelines for cardiovascular risk assessment in TS, evaluation using the current guidelines have seen life-threatening aortic events occurring out with measurements classified within the normal threshold. This is largely due to a lack of clinical data and understanding of the developmental origins of the cardiovascular manifestations seen specifically in TS. Thoracic Endovascular Aortic Repair (TEVAR) is an established treatment for a range of aortic diseases, including aortic aneurysm and dissection, and is favored in acutely unstable patients or individuals with a high operative risk (inclusive of Turner syndrome).

In this work, three-dimensional geometries of the diseased aorta from two patient groups were studied: the first being children with a genetic abnormality (Turner syndrome) and the second being adult patients without a genetic abnormality who underwent TEVAR for aortic aneurysm repair. Our aims were to: (1) characterise the aortic geometries and evaluate various morphological parameters, such as diameter, curvature, and torsion; (2) compute the flow field in these geometries using computational fluid dynamics (CFD); and (3) compare the morphological and haemodynamic results between TS children and their age-matched healthy counterparts, and Post- and Pre-TEVAR adults.

CFD was chosen as it enables detailed, non-invasive characterisation of complex physiological pressure and flow fields, thus improving our understanding of haemodynamics in specific groups of patients. In recent years, CFD models have driven clinical decision-making, surgical planning, and the evaluation of innovative surgical techniques.

In the child aorta, healthy-to-Turner syndrome differences were observed, with Turner syndrome children presenting a greater variance in aortic arch morphology than their healthy counterparts. The visualisation of multidirectional blood flow revealed an increase in vortical

flow in the arch, supra-aortic vessels, and descending aorta, and a correlation between the presence of aortic abnormalities and disturbed flow. Additionally, markers of abnormal aortic morphology were significantly associated with markers of obesity, which is believed to accelerate the initiation and progression of endothelial dysfunction. Given the young age of our study group, these findings may be an indication of atherosclerotic disease manifesting earlier in life in these patients. Clinically, age, obesity and aortic morphology may, therefore, play a key role in assessing cardiovascular risk in TS children.

In the adult aorta, pre- and post-TEVAR differences were observed, with significant remodeling of the aortic vessel wall post-TEVAR. The radius at the aneurysm site, aortic curvature, torsion, and the combined curvature-torsion score were all reduced in the post-TEVAR geometries. A favourable return to more physiological flow structures and a decrease in overall aortic time-averaged wall shear stress was observed post-TEVAR. For these patients who underwent elective TEVAR for thoracic aortic aneurysm repair, the numerical simulations revealed a positive return to a more physiologically normal aorta within two years.

Future work in this field would be to assess the aorta of Turner syndrome patients pre- and post-TEVAR and compare these results to those presented in this thesis.

# Impact Statement

Congenital heart disease is diagnosed in more than one million newborns globally each year. Defined as structural abnormalities of the heart, and/or great vessels, congenital heart disease can range from minor abnormalities, such as bicuspid aortic valve, to severe such as coarctation of the aorta. Congenital abnormalities of the aorta contribute to an increased risk of cardiovascular disease and ultimately reduced life expectancy.

In girls and women with Turner syndrome, the risk of both congenital heart disease and cardiovascular disease is heightened. From birth, Turner syndrome individuals face a lifelong battle with their cardiovascular health. Up to 50% of individuals are born with a congenital defect, and cardiovascular disease accounts for half of all deaths. Across all ages, aortic aneurysm is the highest cause of mortality in Turner syndrome when comparing standardised mortality ratios. The current management of cardiovascular conditions in TS is the same as in the general population, despite the increased risk. This tends to be either open surgical repair, or thoracic endovascular aortic repair. The American Heart Association [1] have acknowledged our limited understanding of the developmental origins of the cardiovascular manifestations seen specifically in TS. As such they have declared this area a research priority.

Computational fluid dynamic modelling is the use of computer-based simulation to analyse fluid flow in a system and was first applied to patient-specific aortic geometries by bioengineers in the late 1990s. Unlike any other modality, computational models can be personalised to predict the disease progression or intervention outcome for any given patient, enhancing diagnostic assessment and facilitating product design and clinical trials. In the present research, CFD methods are used to solve the complex haemodynamic environment in patient-specific geometries of (1) Turner syndrome children, and (2) adult patients who underwent TEVAR. Using this methodology, important biomarkers of cardiovascular disease are calculated which would not be possible with current imaging methods. In both patient groups, our clinical understanding of the complex flows in diseased aorta (albeit due to Turner syndrome or not) was enhanced, and these results were relayed to the relevant clinicians.

# List of Publications

The research undertaken in the present thesis was disseminated internationally through journal publications, and both oral and poster presentations.

## Journal publications

- Johnston L, Allen R, Hall Barrientos P, Mason A and Kazakidi A. (2021) Haemodynamic Abnormalities in the Aorta of Turner Syndrome Girls. *Frontiers in Cardiovascular Medicine* 8:670841. doi: 10.3389/fcvm.2021.670841
- Johnston L, Boumpouli M and Kazakidi A. (2021) Hemodynamics in the aorta and pulmonary arteries of congenital heart disease patients: a mini review. *Journal of Cardiology and Cardiovascular Sciences* 5(2):1-5. doi: 10.29245/2578-3025/2021/2.1213
- Johnston L, Allen R, Mason A and Kazakidi A. (2023) Morphological characterisation of pediatric turner syndrome aortae: insights from a small cohort study. *Medical Engineering and Physics* 120:104045. Doi: 10.1016/j.medengphy.2023.104045
- Johnston L, Shahbazian N, Romero D, Boumpouli M, Amon C and Kazakidi A. (2024) Computational Fluid Dynamics Study of Pre- and Post-Thoracic Endovascular Repair (TEVAR) in Patients with Thoracic Aortic Aneurysm. *Under review by the Journal of Vascular Surgery-Vascular Science*.

## Oral presentations

- Johnston L and Kazakidi A. (2018) A computational model of blood flow in normal and diseased arteries. International Multilateral Symposium of Biomedical Engineering, 30 November – 1 December 2018, Beijing, China.
- Johnston L, Allen R, Hall Barrientos P, Mason A and Kazakidi A. (2019) A numerical investigation of blood flow through patient-specific aortae of children with Turner syndrome. 4D Flow conference, 22 October 2019, Glasgow, UK.
- Johnston L, Allen R, Hall Barrientos P, Mason A and Kazakidi A. (2020) A computational investigation of cardiovascular abnormalities on blood flow in Turner

syndrome children. Endocrinology meeting, Queen Elizabeth University Hospital, 27 February 2020, Glasgow, UK.

- Johnston L, Allen R, Hall Barrientos P, Mason A and Kazakidi A. (2020) A numerical investigation of cardiovascular abnormalities in Turner syndrome aortae. Cardiology meeting, Queen Elizabeth University Hospital, 21 August 2020, Glasgow, UK (virtual).
- Johnston L, Allen R, Hall Barrientos P, Mason A and Kazakidi A. (2021) A Computational Investigation of Cardiovascular Haemodynamic Abnormalities in Turner Syndrome Patients. World Congress in Computational Mechanics, 11–15 January 2021, Paris, France (virtual).
- Johnston L, Allen R, Hall Barrientos P, Mason A and Kazakidi A. (2021) Haemodynamics in patient-specific aortae of Turner syndrome children with MRI-obtained aortic inflow. European Society of Biomechanics, 11–14 July 2021, Milan, Italy (virtual).
- Johnston L, Allen R, Hall Barrientos P, Mason A and Kazakidi A. (2021) Abnormal Wall Shear Stress Patterns in Turner Syndrome Aortae. BioMedEng21, 6–7 September 2021, Sheffield, UK (virtual).
- Johnston L, Allen R, Hall Barrientos P, Mason A and Kazakidi A. (2022) A Numerical Investigation of Haemodynamic Abnormalities in Turner Syndrome Aortae. European Community on Computational Methods in Applied Sciences, 5–9<sup>th</sup> June 2022, Oslo, Norway.

### **Poster presentations**

- Johnston L and Kazakidi A. (2019) Blood Flow Simulations in the Human Aortic Arch in Relation to Obesity. Scottish Fluid Mechanics Meeting, 30 May 2019, Dundee, UK.
- Johnston L and Kazakidi A. (2019) Blood Flow Simulations in the Aortic Arch in relation to Haemodynamic Wall Shear Stress and Obesity-induced Vascular Changes. BioMedEng19, 5–6 September 2019, London, UK.
- Johnston L, Allen R, Hall Barrientos P, Mason A and Kazakidi A. (2019) Computational investigation in the aorta of children with Turner syndrome. CMALS One Health Workshop, 12 December 2019, Glasgow, UK

- Johnston L, Allen R, Hall Barrientos P, Mason A and Kazakidi A. (2020) Computational haemodynamics in Turner syndrome patient-specific aortae with PC-MRI obtained boundary conditions. Scottish Cardiovascular Forum, 1 February 2020, Glasgow, UK
- Johnston L, Allen R, Hall Barrientos P, Mason A and Kazakidi A. (2022) Morphological and Haemodynamic Characterisation of Turner Syndrome Aortae. European Society of Biomechanics, 25–28<sup>th</sup> June 2022, Porto, Portugal.

# Contents

<b>List of Figures .....</b>	<b>xv</b>
<b>List of Tables.....</b>	<b>xviii</b>
<b>Abbreviations.....</b>	<b>xx</b>
<b>Chapter 1 Thesis Overview.....</b>	<b>1</b>
1.1 Research Motivation	1
1.2 Hypothesis and Research Questions	1
1.3 Methodological Approach	2
1.4 Objectives	2
1.5 Thesis Outline	3
<b>Chapter 2 Literature Review &amp; Theoretical Background.....</b>	<b>4</b>
2.1 Turner Syndrome	4
2.1.1 Aetiology and Pathophysiology	4
2.1.2 Clinical Presentation and Diagnosis	5
2.1.3 Cardiovascular Risk	6
2.1.3.1 Congenital Heart Disease .....	6
2.1.3.2 Acquired Cardiovascular Conditions .....	9
2.1.3.3 Hypertension.....	10
2.1.4 Obesity	11
2.1.5 Morbidity, Mortality, and Clinical Management	11
2.1.5.1 Treatment of Aortic Aneurysm .....	14
2.2 The Aorta	14
2.2.1 Anatomy	14
2.2.2 Physiological Environment	17
2.2.2.1 Physical Properties of the Arterial Wall	17
2.2.2.2 Physical Properties of Blood .....	19
2.3 Fluid Dynamic Principles of Blood	20
2.3.1 Governing Equations of Fluid Flow	20
2.3.2 Blood Rheology	21
2.3.3 Characterisation of Different Flows	22
2.3.3.1 Steady Laminar Flow .....	22
2.3.3.2 Steady Turbulent Flow .....	23
2.3.3.3 Unsteady Flow.....	23
2.4 Haemodynamics in the Aorta of Congenital Heart Disease Patients	25
2.4.1 Congenital Abnormalities of the Aorta	26
2.4.2 CFD Studies on CHD Haemodynamics	26
2.4.3 Clinical Relevance and Future Direction	27

2.5	Computational Fluid Dynamic Modelling of Blood flow	28
2.5.1	Flow Model	29
2.5.1.1	Steady-state vs Transient Simulations.....	29
2.5.1.2	Laminar vs Turbulent .....	30
2.5.2	Boundary Conditions	31
2.5.2.1	Inlet Boundary Conditions .....	31
2.5.2.2	Outlet Boundary Conditions.....	31
2.5.3	Haemodynamic Parameters	33
2.5.4	Fluid Dynamics in Turner Syndrome Aortae	35
2.5.5	Clinical Translation and Challenges	36
2.6	Reminder of Thesis Outline	37
<b>Chapter 3</b>	<b>General Background on Methods .....</b>	<b>38</b>
3.1	Computational Fluid Dynamic Methodologies	38
3.1.1	Geometrical Domain and Mesh Generation	41
3.1.1.1	Polyhedral Mesh.....	43
3.1.1.2	Boundary Layer.....	43
3.1.2	Numerical Methods	45
3.1.2.1	Boundary Conditions in Numerical Methods	45
3.1.2.2	Finite Element Method	45
3.1.2.3	Finite Volume Method	46
3.1.2.4	Properties of Numerical Methods	48
3.1.3	Implicit and Explicit Methods	49
3.2	Cardiovascular Computational Fluid Dynamics Methodologies	49
3.2.1	Zero-, One-, Two-, and Three-Dimensional Models	49
3.2.2	Image-based Models	51
3.2.3	Coupled Models	52
3.2.3.1	Fluid Structure Interaction.....	52
3.3	Reminder of Thesis Outline	53
<b>Chapter 4</b>	<b>Morphological Characterisation of Turner Syndrome Aorta.....</b>	<b>54</b>
4.1	Abstract	54
4.2	Introduction	55
4.3	Materials and methods	57
4.3.1	Patient Cohorts	57
4.3.2	Image Acquisition and Geometry Segmentation	58
4.4	Morphometric Analysis	59
4.4.1	Geometric Centreline	59
4.4.2	Morphological Parameters	60
4.4.3	Statistical Analysis	62

4.5	Results	63
4.6	Discussion	72
4.6.1	Findings and Clinical Significance	73
4.6.2	Comparison With Other Studies	74
4.6.3	Limitations	75
4.7	Conclusions	75
<b>Chapter 5</b>	<b>Personalised Haemodynamic Simulations of Paediatric Aorta.....</b>	<b>77</b>
5.1	Abstract	77
5.2	Introduction	78
5.3	Materials and Methods	80
5.3.1	Magnetic Resonance Imaging (MRI) and Patient Cohort	80
5.3.2	Anatomical Reconstruction and Mesh Generation	82
5.3.3	Boundary Conditions	85
5.3.4	Numerical Methods	87
5.3.5	Shear Stress Parameters	88
5.4	Results	88
5.4.1	Blood Flow in the Aorta	88
5.4.1.1	Velocity Streamlines .....	89
5.4.1.2	Through-plane and In-plane Velocities .....	91
5.4.2	Other Haemodynamic Metrics	93
5.5	Discussion	98
5.5.1	Comparison With Other Studies	100
5.5.2	Study Limitations	102
5.6	Clinical Significance	103
5.7	Conclusions	103
<b>Chapter 6</b>	<b>Personalised Haemodynamic Simulations of Adults.....</b>	<b>105</b>
6.1	Abstract	105
6.2	Introduction	106
6.3	Materials and methods	109
6.3.1	Clinical cases and medical image acquisition	109
6.3.2	Reconstruction of patient-specific geometries	110
6.3.2.1	Aortic Morphological Parameters .....	111
6.3.2.2	Aneurysm Morphological Parameters (Pre-operative geometries only)...	112
6.3.3	Mesh Generation	112
6.3.4	Boundary Conditions	114
6.3.5	Numerical Method	115
6.3.6	Haemodynamic Parameters	115
6.4	Results	115
6.4.1	Morphological Characterisation	115

6.4.2	Haemodynamic Parameters	117
6.4.2.1	Flow patterns .....	117
6.4.2.2	Time-averaged wall shear stress.....	119
6.5	Discussion	121
6.6	Conclusions	122
<b>Chapter 7</b>	<b>Conclusions &amp; Future Work .....</b>	<b>124</b>
7.1	Conclusions	124
7.2	Future Work	126
<b>List of References</b>	<b>.....</b>	<b>127</b>
<b>Appendices</b>	<b>.....</b>	<b>152</b>
	Appendix 1	152
	Appendix 2	153
	Appendix 3	154
	Appendix 4	156
	Appendix 5	158
	Appendix 6	159
	Appendix 7	160
	Appendix 8	161
	Appendix 9	162
	Appendix 10	163

# List of Figures

Figure 2.1. (a) congenital anomalies associated with Turner syndrome, and (b) acquired heart diseases in adult Turner syndrome. Figure reprinted from Gravholt et al., (2019) [21].	6
Figure 2.2. Graph of standardised mortality ratio (SMR) values for 3439 females diagnosed with Turner syndrome between 1959-2002 in Great Britain [70]. See Table 2.2 for values.	13
Figure 2.3. Percentage of absolute excess mortality attributed to disorders seen in a British population of 3439 Turner syndrome females. Values obtained from Schoemaker et al. (2008) [70], and figure adapted from Mortensen et al. (2012) [12]. Greatest excess mortality due to cardiovascular disease for all ages and at 45-94 years, and congenital heart disease <15 years.	13
Figure 2.4. Anatomy of the human aortic arch. Reprinted with permission from G. Oomen [83].	15
Figure 2.5. Cross-section of the aorta detailing the layers of the aortic wall. Reprinted with permission from Glen Oomen [88] (appendix 5).	17
Figure 2.6. Relationship between aortic stiffness and structural changes in the aorta which lead to increased atherosclerosis. Figure adapted from Cavalcante et al. (2011) [89] based on Turner Syndrome literature.	18
Figure 2.7 Rheological classification of fluids.	22
Figure 2.8 Development of laminar (Poiseuille) flow in a pipe where $\delta$ is the boundary layer thickness.	23
Figure 2.9 Development of turbulent flow in a pipe [108].	23
Figure 2.10 Velocity profiles for flow between two flat plates at different Womersley numbers for a sinusoidally oscillating pressure gradient [110].	25
Figure 2.11. Pipeline for patient-specific computational fluid dynamic modelling.	29
Figure 2.12. Force exerted on the vessel wall due to the flow of blood. Figure adapted from Glen Oomen [88].	34
Figure 3.1. List of the main OpenFOAM classes and their functions. Figure adapted from Moukalled, 2016 [179].	40
Figure 3.2 Components of computational meshes. (A) Two- and three-dimensional element types, and (B) mesh structure including the vertices, edges, and faces that collectively create the surface mesh. Figure adapted from COMSOL® and Autodesk® user manuals [190].	42
Figure 3.3 STAR-CCM+ polyhedral mesh generated on a patient-specific aortic model (left) with zoomed views of the polyhedral surface mesh and the boundary layer mesh (right).	45
Figure 3.4 Lagrangian coordinate system illustrated on a single element in a finite element mesh. (A) Approximation of the dependent function, $g$ , using $\tilde{g}$ . (B) Definition of the Lagrangian coordinates using the area of the sub triangles created by the point S [201].	46

Figure 3.5 (a) cell-centered and (b) vertex-centered arrangements where the unknown variables are associated to the black nodes [202]. ..... 47

Figure 4.1 Morphometric parameters exemplified (A, B) and listed (C) for the three-dimensional aorta of TS1. (A) Model centreline shown with regional points *Dasc*, *Dbca*, *Dtrans*, *Dsth*, and *Ddesc* as described in the text. (B) MRI slice showing the location of the arch width ( $W_{arch}$ ) and height ( $H_{arch}$ ) measurements, taken relative to the cranial edge of the pulmonary artery. (C) List of full morphological parameters. .... 62

Figure 4.2 (A) Colourmap distributions of the aortic radius and (B-C) line plots of the aortic diameter for the (H1-H4) healthy and (TS1-TS8) Turner syndrome (TS) girls. Geometries in (A) are shown in scale. All values are in millimetres..... 64

Figure 4.3. Anterior view of the (A) curvature and (B) torsion for the (H1-H4) healthy and (TS1-TS8) Turner syndrome girls. Geometries are in scale. All values are in millimetres<sup>-1</sup>. 65

Figure 4.4. Plots of the curvature (black line, primary y-axis) and torsion (red line, secondary y-axis) along the centreline length for each healthy (H1-H4) and Turner syndrome (TS1-TS8) girl. Note the difference in the torsion scale between the healthy (-5 to 5 mm<sup>-1</sup>) and TS (-2 to 2 mm<sup>-1</sup>) groups. .... 66

Figure 4.5. Non-dimensional, normalised, data for (A) diameter, (B) curvature, and (C) torsion, plotted against the non-dimensional normalised centreline length for the healthy and Turner syndrome groups. Group average and standard deviation represented by the solid line and shaded region respectively. Diameter normalised with respect to the model inlet diameter, and centreline length, curvature, and torsion normalised with respect to the maximum values for each parameter..... 67

Figure 4.6. Boxplots of average and maximum values for diameter (A, E), curvature (B, F), torsion (C, G), and the combined curvature torsion score (D, H) at four locations: ascending aorta, aortic arch, descending aorta, and the entire model. Results presented as the mean of the healthy (H1-H4) and Turner syndrome (TS1-TS8) groups, with the median value (horizontal line), interquartile range (box), and values for 95% coverage of the data (whiskers)..... 69

Figure 5.1. Anterior view of the reconstructed aortic models from the (H1-H3) healthy and (TS1-TS4) Turner syndrome (TS) girls. RSA: Right subclavian artery; RCCA: right common carotid artery; LCCA: left common carotid artery; LSA: left subclavian artery. Inset: Superior view of TS3 to highlight the origin of the aberrant RSA. Geometries are in scale. .... 82

Figure 5.2. STAR-CCM+ polyhedral mesh shown on a healthy (H1) model with zoomed views of the inlet mesh with a prism boundary layer (left) and the arch surface mesh (right)..... 84

Figure 5.3. PC-MRI derived (a) volumetric flow rate and (b) normalised waveforms at the aortic root during one cardiac cycle for healthy (H) and Turner syndrome (TS) girls. Insets: average data calculated from H1-H3 (black line) and TS1-TS4 (red line). Flow rate and time normalised by the mean flow rate and cardiac cycle period (see Table 5.2 for values)..... 85

Figure 5.4. Velocity streamlines in the aortic arch of the healthy (H1-H3) and Turner syndrome (TS1-TS4) girls at (a) peak velocity ( $t_1$ ), (b) maximum deceleration ( $t_2$ ), and (c) mid-diastole ( $t_3$ ), colored by non-dimensional velocity magnitude that is normalised according to the average inlet velocity ( $U_{mean}$ ), derived from patient PC-MRI data (anterior view). Note that the colour legends in (b) and (c) were shifted compared to (a) to enhance visualisation. For interpretation of the coloured legends, please refer to the online version of the paper. .... 90

Figure 5.5. (left) Through-plane velocity profiles and (right) contours of through-plane velocity overlaid by vectors of in-plane velocity (components calculated normal to the vessel centreline in Paraview) on seven cross-sections  $\alpha\text{-}\alpha'$  to  $\eta\text{-}\eta'$  along the aorta (locations shown on the 3D healthy (H1) model). Contours coloured by non-dimensional axial velocity at peak velocity for the healthy (H1-H3) and Turner syndrome (TS1-TS4) girls. Cross-sections are oriented looking downstream, with the top and bottom edges corresponding to the anterior and posterior sides of the aorta, respectively, and the left and right points as shown on the left. Cross-sections are not to scale..... 93

Figure 5.6. (a-b) Instantaneous normalised wall shear stress ( $WSS_n$ ), and (c) normalised time-averaged wall shear stress ( $TAWSS_n$ ) distributions shown (anterior view) for the (H1-H3) healthy, and (TS1-T4) Turner syndrome cases. (a) Peak systole and (b) maximum deceleration. WSS and TAWSS were normalised with respect to the mean WSS at the inlet for each individual case. .... 95

Figure 5.7 (a) Oscillatory shear index (OSI), (b) relative residence time (RRT), and (c) transverse wall shear stress (transWSS) distributions shown (anterior view) for the (H1-H3) healthy and (TS1-T4) Turner syndrome cases. .... 97

Figure 5.8. Normalised time-averaged wall shear stress ( $TAWSS_n$ ) values at seven cross-sections along the aorta of the healthy (black, dotted lines, as average of H1-H3) and Turner syndrome girls (red, solid lines, as average of TS1-TS4). Cross-sections are located as shown on the 3D model of a healthy (H1) case. Standard deviation shown as error bars at each point. .... 98

Figure 6.1. Deployment of an endovascular stent graft introduced via trans-femoral approach to repair a thoracic aneurysm. Figure reprinted from [341]. .... 107

Figure 6.2 (A) Pre-operative and (B) post-operative geometries of the thoracic aorta for patients 001 – 005 coloured by the Euclidean distance (the distance between the centreline and the lumen) in millimetres. All geometries are in scale. .... 111

Figure 6.3. Mesh generation displayed on the pre-operative geometry of patient 001. Boundary layer and branch junction meshes shown in insets. .... 113

Figure 6.4. Pulsatile waveform applied as the inlet boundary condition to the aortic geometries. (A) Patient-specific flow rate waveform from a 51-year-old with a thoracic aortic aneurysm post TEVAR [356], and (B) corresponding velocity waveforms for each pre-operative patient. .... 114

Figure 6.5. Non-dimensional vessel radius along the length of the aortic centreline for patients 001 – 005 both pre- (A) and post-operatively (B). Values normalised with respect to the maximum centreline length and radius. Pre-operative (C) and post-operative (D) radius plotted as patient average (solid line) and standard deviation (shaded area) ( $n=5$ ). .... 117

Figure 6.6. (A) Pre- operative and (B) post-operative instantaneous velocity streamlines at peak systole (0.18 s) in the cardiac cycle. Velocity streamlines coloured according to magnitude (0 – 1 m/s). Geometries not to scale. .... 118

Figure 6.7. Pre- and post-operative in-plane velocity streamlines (B) at a cross-sectional slice of maximum diameter in the aneurysm (exemplified on patient 1) at peak systole (A). Velocity streamlines coloured according to magnitude (0 – 0.15 m/s). Cross-sections not to scale. .. 119

Figure 6.8. Anterior view of the (A) pre-operative and (B) post-operative time-averaged wall shear stress (0 – 2 Pa). Geometries not to scale. .... 120

# List of Tables

Table 2.1 Literature review findings on the prevalence of congenital and acquired cardiovascular conditions in Turner syndrome. See Appendix 1 for further details. Prevalence is the number of recorded individuals (across the collected literature) with the characteristic of interest, divided by the total number of people. ....	7
Table 2.2. Total and cause-specific standardised mortality ratio (SMR) values for a population of 3439 females diagnosed with Turner syndrome between 1959-2002 in Great Britain. Table adapted from Schoemaker et al. [73]. Standardized mortality ratios (SMRs) computed as the ratio of observed to expected deaths. ....	12
Table 4.1. Healthy and Turner syndrome baseline characteristics. Data shown as mean $\pm$ standard deviation. Hypertension was defined as systolic blood pressure $\geq$ 95th% for patient age and height. BMI category defined as normal weight (0 – 85 <sup>th</sup> percentile), overweight (86 <sup>th</sup> – 95 <sup>th</sup> percentile), and obese ( $>$ 95 <sup>th</sup> percentile). *Information available for one healthy patient only from the Vascular Model Repository ( <a href="http://www.vascularmodel.com">www.vascularmodel.com</a> ).....	58
Table 4.2. Comparison of clinical and morphometric parameters averaged over the healthy (n=4) and Turner syndrome groups (n=8). Data presented as mean $\pm$ standard deviation. The Mann-Whitney U test was performed to determine if the values for each parameter were significantly different ( $p \leq 0.05$ ) between the healthy and Turner syndrome groups. Note, there was not enough data available to perform this analysis for height or weight. ....	71
Table 4.3. Univariate regression of Turner syndrome parameters and body mass index (BMI), body surface area (BSA), weight, and systolic blood pressure (SBP). Significance level of $P \leq 0.05$ . ....	72
Table 5.1 Biometric and anatomical data for the Turner syndrome (TS) girls (n=4). Age, height, weight, and blood pressure (BP) obtained from the patient electronic clinical records, as well as body surface area (BSA) and body mass index (BMI). The cardiac output (CO) and heart rate (HR) was obtained from within Medviso Segment software ( <a href="http://medviso.com/segment">http://medviso.com/segment</a> ). ....	81
Table 5.2. Hemodynamic information for healthy (H1-H3) and Turner syndrome (TS1-TS4) patients. T: cardiac cycle period; $Q_{\text{mean}}$ , $Q_{\text{peak}}$ : mean and peak flow rates, respectively, and $Re_{\text{mean}}$ , $Re_{\text{peak}}$ the corresponding Reynolds numbers; $Wo$ : Womersley number; $\Delta y_1$ : first boundary layer height; $\Delta y_n = 5$ : total boundary layer height (Eq. 1 – 4). ....	83
Table 5.3. Outlet flow percentages for each individual case calculated using Murray’s Law (exponential power of 2, equation 5.1).....	87
Table 5.4. Time-averaged wall shear stress (TAWSS), expressed in Pascals (Pa), and normalised time-averaged wall shear stress (TAWSS <sub>n</sub> ) averaged over each analysis plane ( $\alpha$ - $\alpha'$ to $\eta$ - $\eta'$ ) for the healthy (n=3) and the turner syndrome groups (n=4). ....	99
Table 6.1. Summary of the patient details including sex and age (years) at the time of surgical intervention and post-operative follow-up imaging, as well as the implanted stent details..	110
Table 6.2. Minimum, average, and maximum aneurysmal diameters for the pre-operative geometries of patients 001 – 005.....	112

Table 6.3. Morphological analysis of the pre- and post-operative aorta of patients 001 – 005. The mean  $\pm$  standard deviation of the aortic surface area, curvature, torsion, and combined curvature-torsion score are provided. .... 116

# Abbreviations

AHA	American Heart Association
ALE	Arbitrary Lagrangian Eulerian
ARSA	Aberrant right subclavian artery
ASI	Aortic size index
BAV	Bicuspid aortic valve
BC	Boundary condition
BCA	Brachiocephalic artery
BMI	Body mass index
BP	Blood pressure
BSA	Body surface area
CAD	Computer aided design
CAE	Computer aided engineering
CAVI	Cardio-ankle vascular index
CC	Combined curvature score
CFD	Computational fluid dynamics
CHD	Congenital heart disease
CMR	Cardiovascular magnetic resonance
CO	Cardiac output
COA	Coarctation of the aorta
CT	Computed tomography
CTA	Computed tomography angiography
CVD	Cardiovascular disease
DBP	Diastolic blood pressure
DICOM	Digital imaging and communications in medicine
DNS	Direct numerical simulation
ECG	Electrocardiogram
ETA	Elongated transverse arch
FDM	Finite difference method
FEM	Finite element method
FSI	Fluid structure interaction
FVM	Finite volume method

HR	Heart rate
IBM	Immersed Boundary Method
LCCA	Left common carotid artery
LDL	Low density lipoprotein
LES	Large eddy simulation
LPA	Left pulmonary artery
LSA	Left subclavian artery
MRI	Magnetic resonance imaging
MS	Marfan syndrome
NO	Nitric oxide
OSI	Oscillatory shear index
PCMRI	Phase contrast magnetic resonance imaging
PWV	Pulse wave velocity
RANS	Reynolds averaged Navier Stokes
RBC	Red blood cell
RCCA	Right common carotid artery
RRT	Relative residence time
RSA	Right subclavian artery
SBP	Systolic blood pressure
SD	Standard deviation
SMR	Standardised mortality ratio
TAWSS	Time averaged wall shear stress
TEVAR	Thoracic endovascular repair
TS	Turner syndrome
TTE	Transthoracic echocardiography
UAV	Unicuspid aortic valve
WKM	Windkessel model
WSS	Wall shear stress

# Chapter 1

## Thesis Overview

### 1.1 Research Motivation

Premature morbidity and mortality are greater in Turner syndrome than the general population [2], with cardiovascular disease being the most common cause of death. Congenital heart abnormalities affect up to 50% of TS individuals, and these congenital abnormalities, alongside an underlying predisposition to obesity and hypertension, contribute to a greater risk of cardiovascular disease and ultimately reduced life expectancy. Despite its prevalence [3], [4], Turner-specific medical evidence is very limited, as identified by [2-3]. Further clinical research is crucial to improve the cardiovascular health of patients living with TS. In fact, the American Heart Association has declared understanding “the pathogenesis of increased cardiovascular morbidity and mortality in women with TS compared with the general population and determining the contributions of atherosclerotic disease, dyslipidemia, hypertension, and obesity” a key research priority [1].

Thoracic Endovascular Aortic Repair is an established treatment for a range of thoracic aortic diseases, including aortic aneurysm and dissection, and is favoured in acutely unstable patients or individuals with a high operative risk e.g. those with Turner syndrome. For treatment planning and long-term outcomes of TEVAR, both the vascular morphology and the consequent haemodynamic environment are crucial.

### 1.2 Hypothesis and Research Questions

The hypothesis proposed in this thesis is that patients with Turner syndrome present a greater variance in both aortic arch morphology and haemodynamic environment than their healthy counterparts, and that these differences may explain the increased cardiovascular risk in TS. To that end, the following research questions are proposed:

- Does the morphology of the aortic arch vary among Turner syndrome individuals, and is this related to the individuals body mass index or body surface area?
- Does the morphology of the aortic arch vary between Turner syndrome individuals and individuals with no known health conditions?

- Is there a correlation between aortic arch morphology and aortic arch haemodynamics?
- Does aortic arch haemodynamics vary between Turner syndrome individuals and individuals with no known health conditions?

In adult patients who underwent TEVAR, the key research questions explored are:

- Do haemodynamic parameters correlate to the geometric changes pre- and post-operatively in patients with thoracic aortic aneurysms?
- Does the morphology and haemodynamic environment of the aortic arch improve following TEVAR for thoracic aortic aneurysm repair?

### **1.3 Methodological Approach**

Computational fluid dynamic (CFD) modelling is the use of computer-based simulation to analyse fluid flow, heat transfer, and associated phenomena, and was traditionally applied to complex mechanical engineering problems. In situations where experimental methods are expensive, time-consuming, or simply not feasible, computational fluid dynamic methods can be used instead. In fact, CFD methods are capable of resolving the fluid environment with greater detail and accuracy than several experimental and in vivo methods. CFD is non-invasive and reasonably accessible with several software offering free licenses and training material. In the context of this research, CFD methods were utilised to provide detailed information on the flow environment in two patient groups at higher risk of cardiovascular complications.

### **1.4 Objectives**

The research carried out in this thesis aims to provide a better understanding of cardiovascular health in the aortae of paediatric Turner syndrome patients and adult non-Turner syndrome patients who underwent TEVAR through the following objectives:

- To use retrospective cardiac imaging data at the location of the aorta for all patients, and to extract the three-dimensional geometric and flow information from this data to create patient-specific geometries and boundary conditions.
- To solve the complex haemodynamic environment in three-dimensional patient-specific geometries of the aorta through computational fluid dynamic simulations, and to analyse the flow patterns and wall shear stresses.

- To evaluate various morphological parameters of the aortic arch geometries, such as diameter, curvature, and torsion, and perform statistical analysis between (1) healthy and Turner Syndrome females, and (2) Pre- and Post- TEVAR.

To the best of the authors knowledge, this thesis presents the first in-depth computational fluid dynamic investigation of haemodynamics in the aorta of children with Turner syndrome, and with reference to healthy age-matched females. It also highlights both the morphological and haemodynamic changes induced in the thoracic aorta of TEVAR patients with the placement of a stent graft, and the statistical differences between the pre- and post-environments.

## **1.5 Thesis Outline**

The structure of this thesis is as follows. In Chapter 2 a review of the literature and description of the theoretical principles will give the reader a solid background to understand the methodologies and results presented in the subsequent chapters. In Chapter 3, the framework for computational fluid dynamic simulations will be presented. The proposed methodology will be explained in detail, beginning with the segmentation and reconstruction of the computational geometries, to the process of defining the computational environment. This purpose of this chapter is to provide the reader with the background theory to the methodologies used in this thesis, with the specific methods presented in chapters 4-6. These three chapters (4-6) are presented in the form of published papers, adapted for the purposes of this thesis. In Chapter 4 (published in the Journal of Medical Engineering and Physics [5]), the morphology of paediatric patient geometries is characterised and compared to healthy data. Chapter 5 (published in the Journal of Frontiers in Cardiovascular Medicine [6]) presents the results of computational fluid dynamic simulations for three-dimensional patient-specific models of Turner syndrome and healthy children. Chapter 6 (journal manuscript under review) continues with the theme of computational fluid dynamic simulations of patient-specific models in the diseased aorta. In this chapter, the patients were adults who had undergone cardiovascular intervention. The work in this chapter was the result of a UKRI awarded placement at the University of Toronto under supervision of Professor Cristina Amon. The thesis will conclude with Chapter 7 which will summarise the results of this research and discuss both the limitations and clinical implications of the key findings.

## Chapter 2

# Literature Review & Theoretical Background

This chapter presents the background, theory, and existing literature relating to the study of blood flow in the aortic arch of Turner syndrome children, and adults with thoracic aortic aneurysm who underwent TEVAR. This area of research is interdisciplinary, combining both clinical and engineering knowledge and expertise. Section 2.1 introduces Turner syndrome and presents a review of the current literature relating to cardiovascular health in Turner syndrome. In section 2.2, the physiology and haemodynamic properties of the aorta, the main vessel leaving the heart, are discussed in detail. Finally, the fluid principles of blood and the applications of computational fluid dynamic (CFD) modelling in the cardiovascular system are explored in sections 2.3 and 2.4, respectively.

### 2.1 Turner Syndrome

Turner syndrome, named after endocrinologist Dr Henry Turner, was first described in 1938 in a group of women with a triad of phenotypic findings - achondroplasia, amenorrhea and a lack of secondary sex characteristics [7]. It was not until 20 years later that Dr Charles Ford discovered the cytogenetic basis behind TS [8]. Although rare, TS is the most common chromosomal abnormality among females, and can present as an array of genetic, developmental, endocrine, cardiovascular, psychosocial, and reproductive issues [9]. The predisposition to cardiovascular disease (CVD), which may be both congenital and acquired, is thoroughly examined in this section. For context, the pathophysiology, clinical presentation, and treatment of the disease are also discussed.

#### 2.1.1 Aetiology and Pathophysiology

Turner syndrome affects approximately 1 in 2000 [3] to 2500 [4] live female births, making it the most common sex chromosomal disorder affecting girls and women. In fact, an estimated 3% of all females conceived are presumed to be affected, but only 10% survive to term [10]. The genetic advent of Turner syndrome is the result of a random chromosomal nondisjunction, specifically the deletion or the non-functioning of the X chromosome [11], [12].

Approximately half of those with TS have complete monosomy (45X or 45XO), while the other half have partial monosomy or mosaicism [11]. In TS, complete or partial loss of activity of the X-chromosome detrimentally impacts both prenatal and postnatal survival [12]. The exact nature in which TS develops is not clear, but it is known to occur sporadically (i.e., not inherited) and unlike other chromosomal abnormalities, not found to be related to advanced maternal age [13].

### 2.1.2 Clinical Presentation and Diagnosis

The clinical features of TS vary widely between individuals due to the variation in gene expression. As a result, the diagnosis of TS occurs at a variety of ages and in some cases leads to a diagnostic delay or even non-diagnosis. Short stature is the most common clinical phenotype, present in over 90% of TS individuals [14], and is visible as early as in the womb [15]. This delay in growth continues throughout childhood and results in progressive separation from the average population in terms of height [15]. Delayed puberty (60-90%) and primary amenorrhea (90%) are the other most common clinical features of Turner syndrome, putting this group at an extremely high risk for primary ovarian insufficiency and infertility [16]. Other physical characteristics of Turner syndrome include edema of the hands or feet, webbed neck, broad shield chest, cubitus valgus, low posterior hairline, rotated ears, a narrow palate with crowded teeth, nail hypoplasia, and hyperconvex nails [17]. However, it is the cardiovascular phenotype in Turner syndrome that is pertinent to this research. Congenital heart abnormalities occur in up to 50% of TS females, affecting mainly the left side of the heart, including bicuspid aortic valve (BAV), and coarctation of the aorta (CoA) [18], [19], [20]. The cardiovascular phenotype will be discussed in further detail in section 2.1.3.

If Turner syndrome is suspected prenatally, usually based on ultrasound findings of left-sided cardiovascular abnormalities in the foetus, then genetic testing is performed via amniocentesis or chorionic villous sampling. Postnatally, diagnosis of a left-sided cardiovascular abnormalities in a female (child or adult) should also be followed by genetic evaluation for the presence of TS [1]. The American Health Association also recommends that women with short stature (below the fifth percentile for height) along with at least one additional characteristic clinical feature be screened for TS [1].

### 2.1.3 Cardiovascular Risk

Turner syndrome has been proposed as an independent risk marker for cardiovascular disease, which manifests as both congenital and acquired cardiovascular conditions (Figure 2.1). These patients also have an increased predisposition for hypertension, atherosclerosis, and obesity. The following text provides an up-to-date review of the current literature on the cardiovascular phenotype in females with TS. The publications cited in this review are selected from a search of the PubMed database (in April 2021) using the keyword “Turner syndrome” in publication titles. Over 2000 articles were returned (dating from 1954) which was then refined based on cardiovascular relevance.

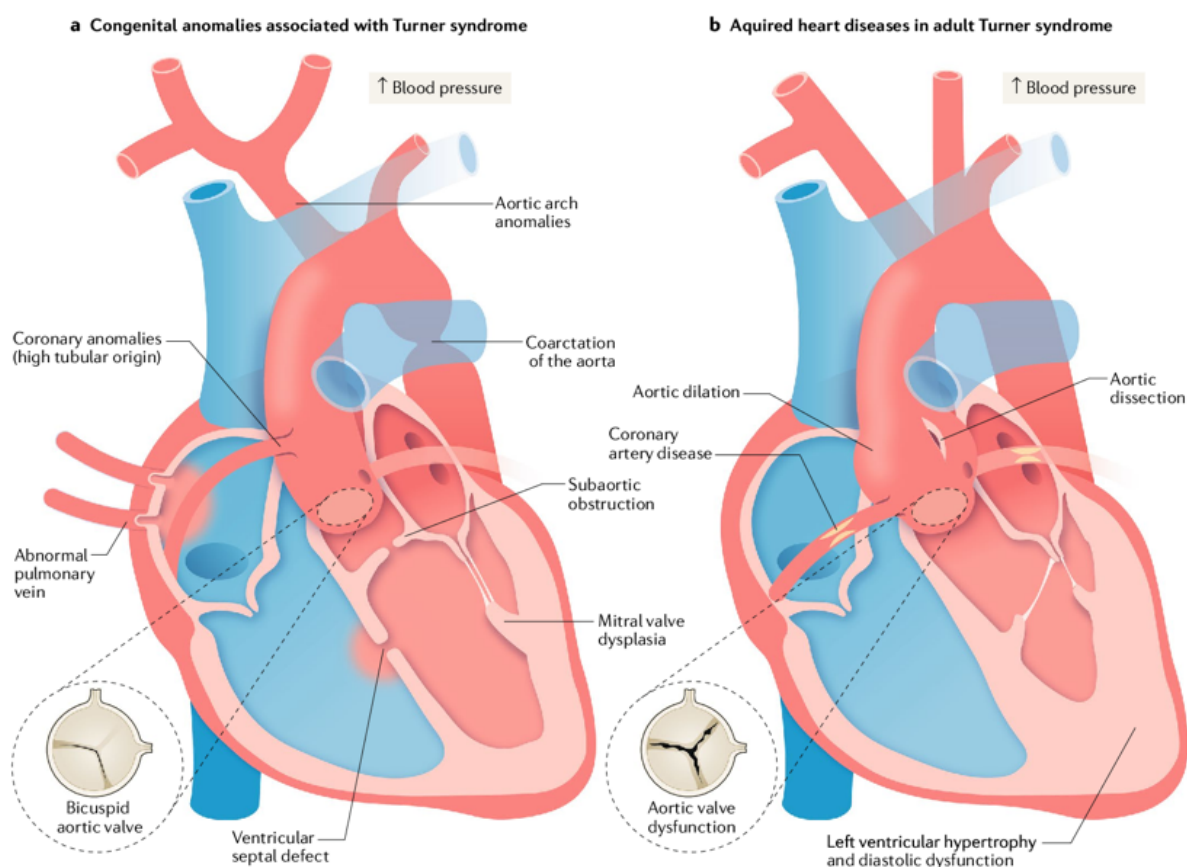


Figure 2.1. (a) congenital anomalies associated with Turner syndrome, and (b) acquired heart diseases in adult Turner syndrome. Figure reprinted from Gravholt et al., (2019) [21].

#### 2.1.3.1 Congenital Heart Disease

The spectrum of congenital heart disease (CHD) in individuals with Turner syndrome ranges from minor abnormalities to severe and highly complex disorders, predominantly involving the left side of the heart (Figure 2.1) [1]. Bicuspid aortic valve (BAV) is one of the most common,

with a reported prevalence of 15-30% [19], [22], [23], [24]. This is in agreement with the current literature (n=48 articles) which revealed a prevalence of 26.0% (Table 2.1). For perspective, the prevalence of BAV in the general population is less than 1% [25], [26]. TS is therefore a definite risk factor of BAV [27]. In the majority of cases (89%) BAV is determined by echocardiography [24], with cardiac MRI used in cases where the valve is not adequately visualized due to its higher sensitivity. In TS, BAV more often than not occurs in isolation or in conjunction with proximal aortic abnormalities including coarctation of the aorta [24]. The presence of BAV also increases the risk of developing complications such as aortic stenosis and/or valve insufficiency, aortic dilatation, and dissection [28].

Table 2.1 Literature review findings on the prevalence of congenital and acquired cardiovascular conditions in Turner syndrome. See Appendix 1 for further details. Prevalence is the number of recorded individuals (across the collected literature) with the characteristic of interest, divided by the total number of people.

<b>Congenital abnormality or acquired disease</b>	<b>Number of Articles</b>	<b>Prevalence</b>
Bicuspid aortic valve (BAV)	48	26.0%
Unicuspid aortic valve (UAV)	2	1.6%
Elongated transverse arch (ETA)	13	44.3%
Bovine arch	3	15.8%
Aberrant right subclavian artery (ARSA)	6	9.5%
Coarctation of the aorta (CoA)	47	13.1%
Aortic dilatation	29	27.4%
Aortic dissection	6	2.4%
Hypertension	23	29.8%

Unicuspid aortic valve (UAV) is a very rare cardiac malformation in the general population (0.02% prevalence) [29] and despite the high prevalence of aortic valve disease in TS, UAV is still rarely seen. Engelen et al. (2014), reported a 5% prevalence of UAV in a cohort of 37, and Olivieri et al. (2013), reported a prevalence of 1% in a cohort of 208 patients [30], [31]. Several case studies have also reported findings of UAV in TS women [32], [33], [34]. In all three case studies, the patients also presented with ascending aortic dilatation.

Aortic arch abnormalities including elongation of the transverse aortic arch (ETA), bovine arch, and aberrant right subclavian artery are more common in TS than in the general population. Elongation of the transverse aorta, defined as an increase in vertical distance from the top of the aortic arch to the origin of the innominate artery, is the most common abnormality in TS with a prevalence of 44.3% (Table 2.1), compared to just 1.1% in the general population [35]. ETA is also associated with BAV ( $p < 0.05$ ), CoA ( $p < 0.01$ ), and aortic sinus dilation ( $p < 0.05$ ) [36]. Bovine aortic arch, defined as common aortic origin of the brachiocephalic and left subclavian arteries, is reported in as many as 28.6% of TS women [37]. However, this estimate is significantly higher than the prevalence of 5.9-8.2% reported by Kim et al. (2011) and Ho et al. (2004) [23], [36]. Aberrant right subclavian artery (ARSA), where the right subclavian artery arises abnormally as a fourth branch of the aortic arch, has a prevalence of 9.5% in TS (Table 2.1) compared to just 0.11% in the normal population [38].

Coarctation of the aorta, defined as concentric narrowing of the aortic lumen (typically juxtaductal in location) [23], is statistically over-represented in TS women [37], with a prevalence of 13.1% (Table 2.1). This value is much lower ( $<3\%$ ) in assessments using echocardiography [39], [40], [41] (as opposed to cardiac MRI), as the coarctation site is not always visible due to the shape of the chest wall in women with TS [42]. In studies by Ho et al. (2004) and Kim et al. (2011), the presence of coarctation was significantly ( $p < 0.05$  and  $p < 0.01$  respectively) associated with elongation of the transverse aorta in women with TS [23], [36]. When detected by clinicians, coarctation is corrected through open surgery, balloon angioplasty, or stenting, making it the most commonly performed surgical procedure in TS, accounting for almost one third (28%) of all cardiovascular interventions [43]. Surgical repair of CoA is the standard method despite reports of aortic wall injuries (dissection and aneurysm formation) occurring in almost one third (30.4%) of operations, and mortality in 10.8% [44]. Operative mortality during surgical repair of COA is disproportionately higher in TS patients than those without TS (12.5% vs 0.29%) [45]. Endovascular repair of CoA (balloon angioplasty or stenting) carries lower risks of aortic wall injury (2% and 20% respectively) and mortality (0% and 6.6% respectively) than open surgery [44]. History of coarctation, even once repaired and without residual obstruction, is a significant risk factor for elevated blood pressure (hypertension) in Turner syndrome [46].

### 2.1.3.2 Acquired Cardiovascular Conditions

Aortic dissection is a severe cardiovascular complication that occurs more frequently and at a younger age in Turner syndrome females. In the general population, the incidence of aortic dissection is 6 per 100,000 per year, with dissection occurring on average between 50 and 80 years and at a median age of 77 years in females [47]. In a large epidemiological study by Danish team, Gravholt et al. (2006), the incidence of aortic dissection was 36 per 100,000 Turner's syndrome years, with a median age of 35 years at onset [48]. Specifically, aortic dissection occurred in 11 of 783 Turner syndrome females, equating to a prevalence of 1.4% [48]. A similar prevalence was recorded throughout the literature (Table 2.1, 2.4%), with five studies [20], [49], [50], [51], [52] recording incidences between 1 and 5%. Aortic dissection is predominantly a disease of the older generation [47], but has been seen in younger patients with connective tissue disorders such as Marfan and Ehlers-Danlos syndrome [48]. In the younger (20-39 years) TS population, an even greater incidence rate was found (73-78 per 100,000 TS years) [48], and several case studies even recorded aortic dissection in TS children as young as 8 or 9 years of age [20], [45], [53]. The prognosis for aortic dissection is dependent on both the location and degree of dissection: this is improved when the dissection is isolated to the descending aorta (Stanford B/DeBakey III), rather than the ascending aorta (Stanford A/DeBakey II) or both the ascending and descending aorta (Stanford A/DeBakey I) [54], [55]. Of the TS women reported on by Gravholt et al., 10 died from aortic dissection: 6 patients were type A (60%), 3 were type B (30%), and 1 was undetermined [48]. Widely acknowledged risk factors for aortic dissection in TS are hypertension, bicuspid aortic valve, and coarctation of the aorta [12]. In a review of the literature from 1961 to 2006, Carlson and Silberbach reported 87 instances of aortic dissection in TS individuals, 89% of which had at least one of three aforementioned risk factors [56]. In a more recent (2014) literature review by Wong et al, 122 cases of aortic dissection were reported in TS women [57], 87 of which were included in the previous review by Carlson and Silberbach [56]. In this more comprehensive review [57], the proportion of dissecting women with no known cardiovascular abnormalities was almost double (20.5% vs 11%) that of Carlson and Silberbach. Pregnancy, although rare in TS, presents an additional risk of aortic dissection with a mortality risk 100 times greater than the general population [57].

Aortic dilatation and aneurysm (localised dilatation) are common in TS, and the entire thoracic aorta is at risk regardless of patient age [51], [58]. The presence of hypertension, BAV, and

CoA are risk factors known to accelerate aortic growth and aortic dilation [51] - the primary risk factor for aortic events [9]. The reported prevalence of aortic dilation in TS women varies from 4% [39] to 57% [59], depending on the definition, mode and site of assessment. From 1986 to 2020, 801 instances were recorded across 29 studies equating to a prevalence of 27.4% (Table 2.1). Considering aortic diameter is influenced by both age and body size [60], evaluating aortic dilatation and aneurysm against absolute reference values in TS, where short stature is the single most common physical abnormality, is grossly inaccurate. One approach is to compute the ratio of ascending to descending aortic diameter (AD/DD), where a value greater than 1.5 [61] indicates ascending aortic dilatation/aneurysm. However, Bondy et al. [62] do not support the use of this method as it assumes the descending aorta is of normal diameter, and instead prefer the aortic size index (ASI) which normalises the aortic diameter using body surface area (BSA). According to Matura et al. (2007) [51], and Bondy et al. (2008) [62], TS individuals with an aortic size index exceeding 2 cm/m<sup>2</sup> should be monitored closely for cardiovascular events, and considered for surgical intervention if ASI exceeds 2.5 cm/m<sup>2</sup>. The management of aortic dilatation/aneurysms is discussed further on in section 2.1.5.1.

### 2.1.3.3 Hypertension

Hypertension is common in Turner syndrome females affecting up to 40% of girls and adolescents [63] and up to 58% of women [64]. In a review of 23 published articles, 573 females (29.8%) with TS were recorded as hypertensive (Table 2.1). Evidence shows that elevated blood pressure in children and adolescents manifests as end-organ alterations, and if left untreated increases the risk of early onset cardiovascular disease in adulthood [65]. Even a short period of systemic hypertension can promote chronic vascular changes that manifest as hypertension later in life [1]. The most commonly reported risk factors for hypertension in TS are coarctation of the aorta (repaired or unrepaired) and obesity [46], [63], [66]. Dilation of the ascending aorta and abnormal arch morphology are also significantly associated with hypertension [23], [67]. Impaired aortic wall function in the ascending and descending aorta, and lower aortic distensibility in patients with CoA, may also contribute to elevated blood pressure seen in TS patients [68]. Hypertension is an important risk factor for cardiovascular complications, especially aortic dissection, and is associated with substantial morbidity and mortality in TS [69], [70].

#### 2.1.4 Obesity

Overweight children are at risk of developing diabetes and cardiovascular diseases in adulthood, which may lead to premature death [71], [72]. In addition to the congenital heart abnormalities and acquired cardiovascular disease, girls with TS are also at an increased risk of obesity. In an assessment of risk factors for coronary heart disease in TS women, Elsheikh and Conway (1998) [73] found an independent contribution from obesity. Lebenthal et al. (2018), [74] conducted a longitudinal, cross-sectional study using retrospective data from 98 TS patients. The rate of overweight and obesity increased from childhood to young adulthood, and BMI percentile was consistently higher [74]. In a similar study, Hanew et al. (2016), [75] compared BMI in 492 TS patients with the general female population. BMI was greater in TS for all age groups, and the authors concluded that obesity occurs prematurely in those with TS but does not increase in prevalence with age [75]. Reinehr et al. (2016), [76] compared body mass index in a larger cohort of TS girls and found 24.9% were overweight, 6.4% obese, 67.0% normal weight and 1.7% underweight. However, obesity determined using the height-based BMI calculation might not be so accurate due to the short stature seen in TS, and it may be more representative to use other metrics such as body composition. Using this method, Gravholt et al. (2006), [77] reported a profoundly different body composition in Turner syndrome compared to the general female population, with lower total lean body mass and higher body mass index and total fat mass.

#### 2.1.5 Morbidity, Mortality, and Clinical Management

Turner syndrome is associated with a 3-fold (standardised mortality ratio, SMR = 3.0) higher mortality rate than the general population (Table 2.2, Figure 2.2) [2], [70]. Early morbidity and mortality in TS can be attributed to diseases of the endocrine, nervous, cardiovascular, respiratory, and digestive systems [2], [69], [70].

Cardiovascular disease accounts for approximately half of all deaths (Figure 2.3), occurring 6-13 years prematurely [69]. Specifically, cardiovascular morbidity and mortality are attributed to congenital heart disease (SMR = 20.7), aortic dilatation and dissection (SMR = 23.6), ischemic heart disease (SMR = 2.8), and cerebrovascular disease (SMR = 3.9) [2], [69], [70]. Congenital abnormalities account for 8% of excess deaths (Figure 2.3), and include coarctation of the aorta, bicuspid aortic valve and atrial septal defect [70]. Even when mortality from congenital heart disease is excluded, mortality rates remain excessive [70].

Table 2.2. Total and cause-specific standardised mortality ratio (SMR) values for a population of 3439 Turner syndrome females in Great Britain. Table adapted from Schoemaker et al. [70]. Standardized mortality ratios computed as the ratio of observed to expected deaths. For all ages, SMR greatest due to congenital heart disease (12.6) and aortic aneurysm (23.6).

Cause of mortality	standardised mortality ratio (95% CI)			
	All ages	< 15 years	15 – 44 years	45 – 84 years
All causes (total)	3.0	4.9	3.9	2.6
Respiratory system	3.9	6.5	2.5	3.9
Cerebrovascular	3.9	0	5.9	3.7
Circulatory system	4.0	7.0	8.2	3.5
Digestive system	4.5	12.3	7.6	3.3
Nervous system	5.5	9.1	6.2	4.1
Endocrine	7.6	7.3	6.9	8.1
Musculoskeletal	8.2	0	15.5	5.7
Urogenital	8.9	0	12.5	8.1
Congenital	12.6	11.4	17.2	5.5
Aortic Aneurysm	23.6	0	278	7.4

Management of girls and women with TS requires a multidisciplinary approach. In TS children, routine cardiovascular monitoring and treatment of congenital heart disease and hypertension is crucial. Growth hormone and oestrogen therapy are also necessary to increase adult height and sexual development [78]. TS management also includes but is not limited to audiometry testing to monitor hearing loss; annual blood testing to assess thyroid function; fasting lipid and glucose monitoring; ophthalmologist assessment of hyperopia and strabismus; and orthodontic evaluation for malocclusion. When transitioning to adult care, women should be offered reproductive counselling in addition to the aforementioned treatment.

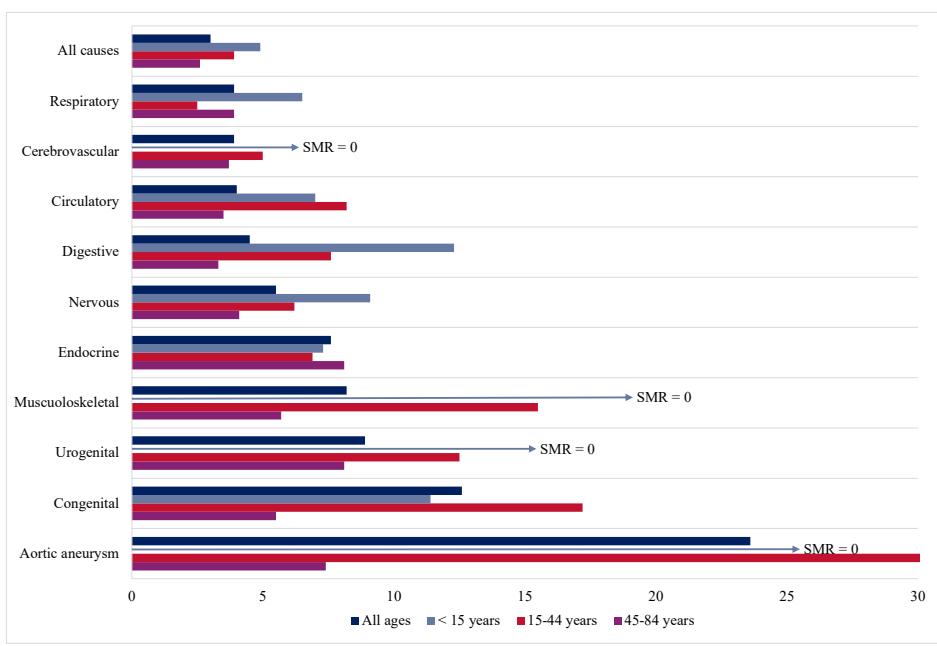


Figure 2.2. Graph of standardised mortality ratio (SMR) values for 3439 females diagnosed with Turner syndrome between 1959-2002 in Great Britain [70]. See Table 2.2 for values.

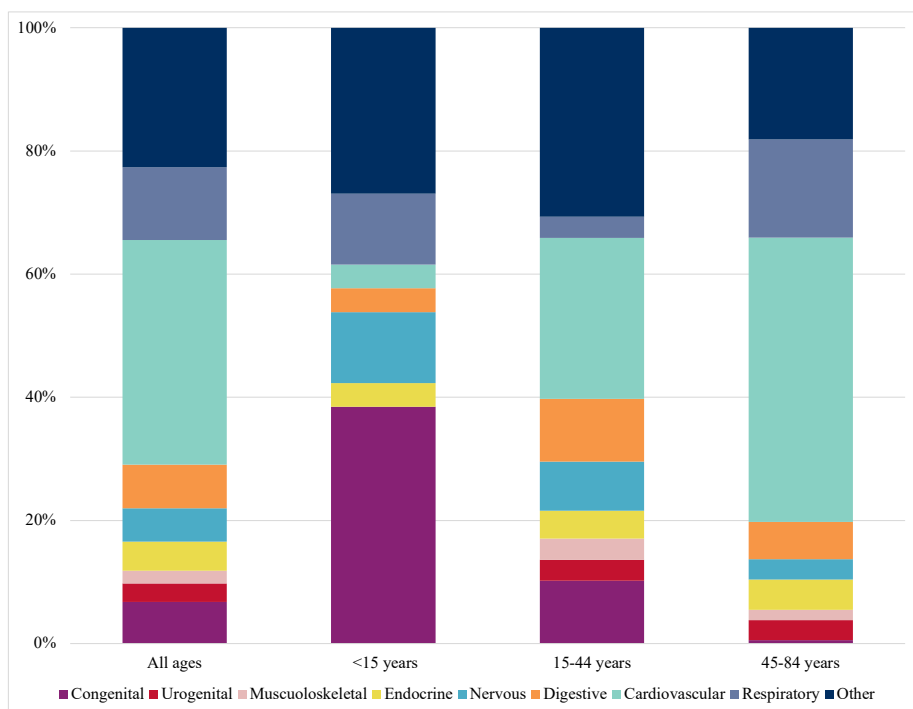


Figure 2.3. Percentage of absolute excess mortality attributed to disorders seen in a British population of 3439 Turner syndrome females. Values obtained from Schoemaker et al. (2008) [70], and figure adapted from Mortensen et al. (2012) [12]. Greatest excess mortality due to cardiovascular disease for all ages and at 45-94 years, and congenital heart disease <15 years.

### *2.1.5.1 Treatment of Aortic Aneurysm*

When an aneurysm is diagnosed, medical or operative interventions may be necessary. Thoracic endovascular aortic repair is an effective, less invasive treatment option for the repair of aortic aneurysm in both the general and TS population. The procedure involves making an incision, usually in the femoral artery, and using X-ray to guide a stent-graft to the aneurysm site. Once in position, the stent is deployed into place, providing a new route for the blood to flow. With the blood supply now cut off from the aneurysm, over time the aneurysm shrinks. For further information on the procedure itself, including complications and outcomes, see the publication by Nation and Wang [79].

There is limited, and somewhat contradictory, guidance on the treatment of aortic aneurysm in Turner syndrome. Traditionally, the presence of a genetic or heritable aortic condition has been considered a contraindication to endovascular intervention, and the current consensus is that thoracic aneurysms in these patients should be treated with conventional open surgery [80]. However, the clinical guidance by the American Heart Association states that general technical concepts and perioperative care are not different (in TS) from those for other patients (without TS) with thoracic aortic aneurysms and dissections [1]. A recent study by Le Huu et al. on endovascular outcomes in patients with heritable thoracic aortic disease (including TS) suggest that TEVAR might be suitable in emergency settings or for patients in this population who are not candidates for open surgery, or who are at high risk for reintervention [81].

## **2.2 The Aorta**

### *2.2.1 Anatomy*

The aorta is the largest vessel in the human body, with a primary function of delivering oxygenated blood directly from the heart to the limbs and major organs via the systemic circulation. The aorta is a highly complex component of the vascular network, originating from the left ventricle in the heart, through the aortic valve, and extending to its major thoracic and abdominal branches. Anatomically, the aorta can be segmented into three main regions: the ascending aorta, the arch, and the descending aorta, the latter of which is further divided into the thoracic and abdominal aorta (Figure 2.4) [82].

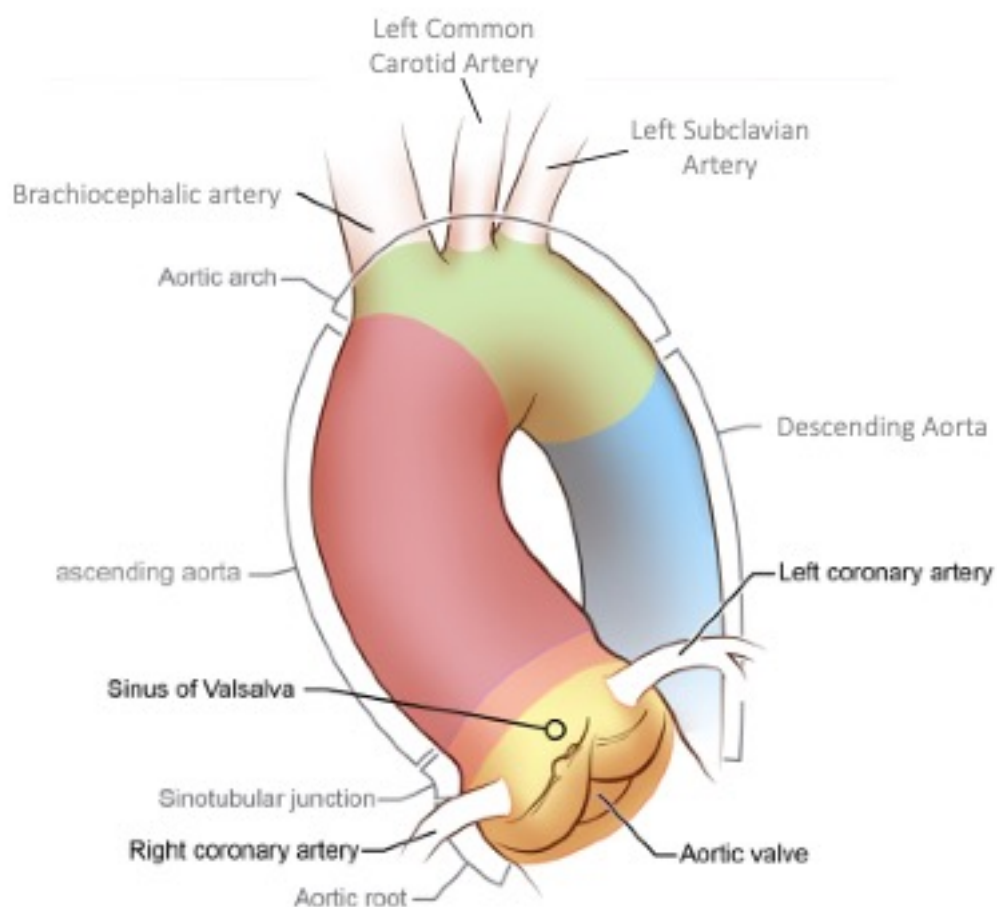


Figure 2.4. Anatomy of the human aortic arch. Reprinted with permission from G. Oomen [83].

At the base of the aorta is the aortic root, located between the left ventricular outflow tract and the ascending aorta. The aortic root is a collective term for the aortic valve, the sinuses of Valsalva, and the sinotubular junction. A healthy aortic valve has three leaflets, hence the name tricuspid, and ensures that blood leaving the heart maintains unidirectional, forward flow. The aortic root projects outwards to form the three sinuses of Valsalva, two of which give rise to the left and right coronary arteries. The sinotubular junction is the junction between the aortic root and the ascending aorta and is where the tubular morphology of the aorta begins. The ascending aorta is a direct continuation from the aortic root and follows a slight curve upwards and to the right. The ascending aorta of a healthy adult is 71 mm on average (range 47–114 mm) in length [84]. The aorta continues from the ascending aorta into the aortic arch, where the vessel curves upwards and then posteriorly over the right and left pulmonary artery [79]. It is here that three branches originate from the aortic arch: the most proximal being the brachiocephalic artery (BCA) or innominate artery, followed by the left common carotid artery

(LCCA), and then the left subclavian artery (LSA). The brachiocephalic artery then bifurcates into the right subclavian artery (RSA) and right common carotid artery (RCCA). The aortic arch then passes down the left side of the vertebral column and transitions to the descending aorta at the level of the fourth thoracic vertebrae. The descending thoracic aorta continues from the fourth to the twelfth thoracic vertebrae, and gives rise to the intercostal, subcostal, and left bronchial arteries. The twelfth thoracic vertebrae, also where the diaphragm is located, marks the transition from the thoracic aorta to the abdominal aorta. There are five arteries that branch from the abdominal aorta: the celiac artery, the superior mesenteric artery, the inferior mesenteric artery, the renal arteries, and the iliac arteries. The bifurcation of the iliac arteries marks the end of the abdominal aorta and therefore the aorta itself.

The aorta is a type of elastic artery, composed of three layers: the tunica intima, tunica media, and tunica adventitia (Figure 2.5). The innermost and thinnest layer, the tunica intima, is composed of a single row of smooth endothelial cells, supported by subendothelial connective tissue, and an internal elastic lamina [85]. Positioned at the interface between circulating blood and vascular tissue, the endothelium has a multifaceted role. Functions of the vascular endothelium include: regulation of thrombosis, thrombolysis and platelet adherence; transport of molecules and cells from the blood to the surrounding tissues; facilitation of host defence and inflammation; and modulation of vascular tone [86]. Injury or dysfunction of the endothelium, which we know plays a key role in many physiological functions, is associated with many disease processes such as atherosclerosis, hypertension, pulmonary hypertension, sepsis and inflammatory syndrome [86]. Bordering the tunica intima is the tunica media, which constitutes the greatest thickness of the aortic wall. The tunica media is composed of several layers of smooth muscle cells, elastin, and collagen, and provides the aorta with both structural support and elasticity. It is the smooth muscle in this layer which contracts and dilates to regulate blood flow and pressure in the aorta. The outermost layer, the tunica adventitia, is a connective tissue layer composed mainly of collagen. This layer also contains small blood vessels, known as vasa vasorum, which supply the vessel wall with oxygen and nutrition [87].

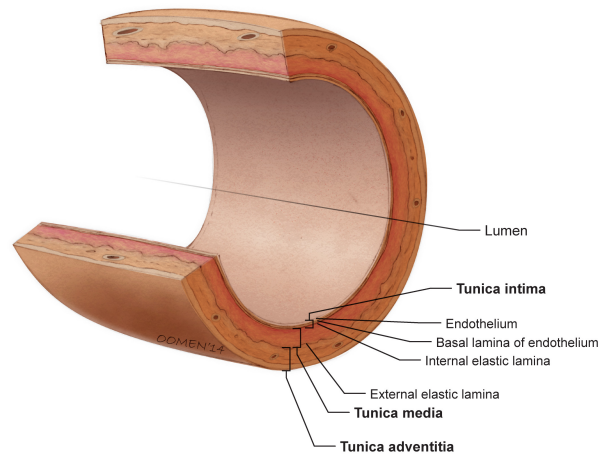


Figure 2.5. Cross-section of the aorta detailing the layers of the aortic wall. Reprinted with permission from Glen Oomen [88] (appendix 5).

## 2.2.2 Physiological Environment

### 2.2.2.1 Physical Properties of the Arterial Wall

Biophysical properties of the arterial wall play an important role in the pathogenesis of cardiovascular diseases. In fact, arterial stiffness and compliance are some of the earliest detectable manifestations of adverse structural and functional changes in the vessel wall [89].

Arterial stiffness is defined as the resistance of the vessel wall to deformation and can be measured non-invasively via pulse wave velocity (PWV). This method, which uses echocardiography to measure the speed at which the arterial pulse propagates along the arterial wall, is considered the gold standard in assessing arterial stiffness [89]. PWV can be expressed in terms of vessel properties using the Moens-Korteweg equation [90], [91]

$$PWV = \sqrt{\frac{E \cdot h}{2 \cdot r \cdot \rho}} \quad 2.1$$

where  $E$  is the elastic modulus of the vessel,  $h$  is the vessel wall thickness,  $r$  is the vessel radius, and  $\rho$  is the density of blood. Other less commonly used measures of aortic stiffness include the cardio-ankle vascular index (CAVI), arterial pressure-strain elastic modulus and arterial wall stiffness index. On the other hand, compliance and distensibility markers provide information on the elasticity of the artery. Arterial compliance is defined as the absolute change in area, diameter, or volume ( $\Delta A$ ,  $\Delta D$  or  $\Delta V$ ) of the artery per unit change in blood pressure ( $\Delta P$ ), while arterial distensibility is defined as the relative compliance [89]. Pulse wave velocity

is inversely related to vascular compliance hence a stiffer vessel will propagate the pulse wave faster than a more distensible and compliant vessel ( Figure 2.6).

Aortic stiffness naturally increases with age and is also shown to be increased in obese adults, and more recently in obese children [92] (

Figure 2.6). As well as aging, increased aortic stiffness has been associated with atherosclerosis, hypertension, and hyperlipidaemia, and an independent risk factor for cardiovascular events such as primary coronary events, stroke and mortality [93]. Multiple studies have also shown a direct association between aortic stiffness and Turner syndrome using both PWV [94], [95], [96] and CAVI [97], [98].

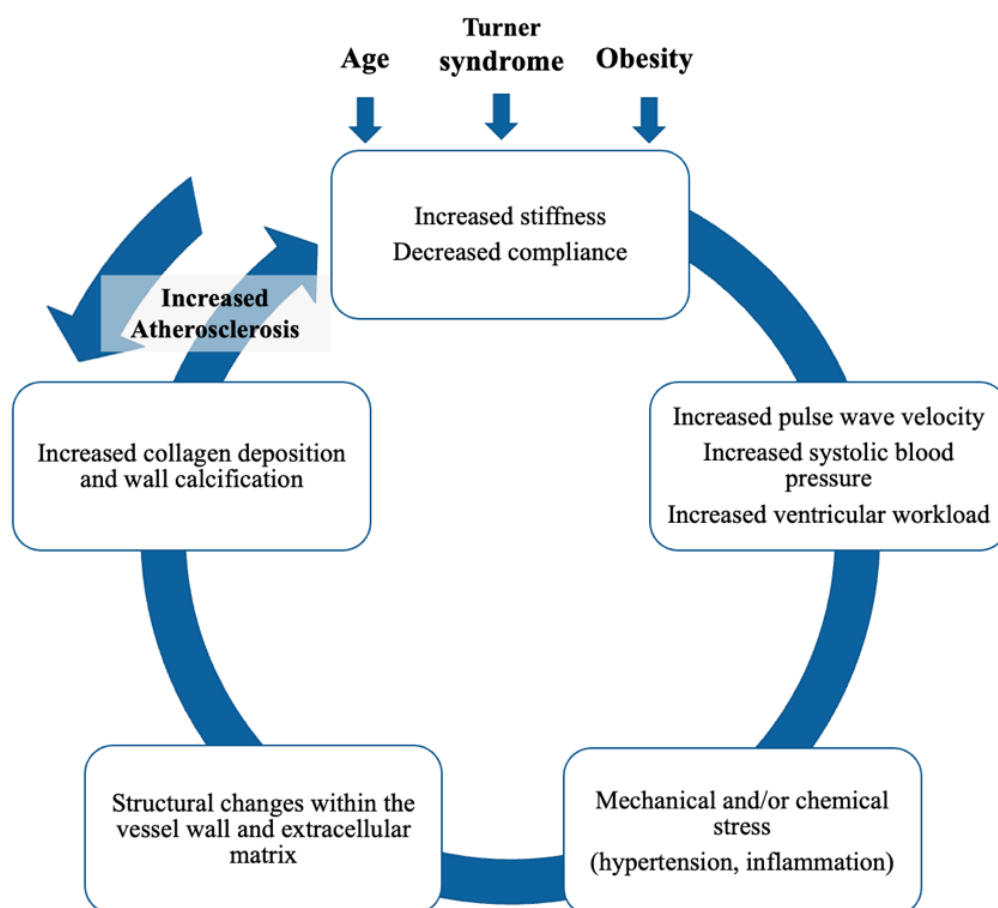


Figure 2.6. Relationship between aortic stiffness and structural changes in the aorta which lead to increased atherosclerosis. Figure adapted from Cavalcante et al. (2011) [89] based on Turner Syndrome literature.

### 2.2.2.2 Physical Properties of Blood

Blood is a viscous fluid consisting of formed elements suspended in a plasma solution. Specifically, whole blood is a suspension of formed elements, namely erythrocytes, leukocytes, and platelets, in a protein-rich aqueous solution (plasma). Erythrocytes, or red blood cells (RBCs), account for 99% of the cellular component of blood and function as oxygen transporters. These cells are unique in their shape (biconcave disc) and mechanical properties which vary when exposed to an increase or decrease in blood flow or shear rates. At high shear rates, RBCs deform and orient with laminar flow streamlines, therefore reducing the internal resistance of fluid to flow. At low shear rates, RBCs return to their original shape and stack together into structures called rouleaux, thus increasing the fluid viscosity [99]. The other components of blood are platelets, which function in blood coagulation and haemostasis, and leukocytes (white blood cells), which are crucial in the body's immune response. These cells are found in much smaller abundance and so, unlike RBCs, their influence on the flow characteristics of blood is negligible.

The flow of blood in arteries is determined by two parameters, pressure (P) and resistance to flow (R):

$$Q = \frac{\Delta P}{R} \quad 2.2$$

where Q is the flow rate and  $\Delta P$  is the pressure difference [100]. The values of flow rate and resistance are dependent on many factors, including vessel radius (r) and length (L), and blood viscosity ( $\eta$ ). In a cylindrical tube, flow rate can be calculated using the Poiseuille equation:

$$Q = \frac{\Delta P \pi r^4}{8 L \eta} \quad 2.3$$

It is this pressure difference  $\Delta P$  between any two points along a given length of the vessel which drives the flow of blood. If equations 2.2 and 2.3 are combined, then the resistance to flow can be approximated:

$$R = \frac{8 L \eta}{\pi r^4} \quad 2.4$$

From equation 2.4, three parameters determine the resistance to blood flow: viscosity ( $\eta$ ), vessel length (L), and vessel radius (r). Of these factors, vessel radius is the most important quantitatively and physiologically due to contraction and relaxation of the smooth muscle in

the vascular wall (introduced in section 2.2.2). Vessel length and blood viscosity have little impact on vascular resistance as vessel length does not change significantly, and blood viscosity remains within a physiological range of 3.5 and 5.5 centipoise [101].

## 2.3 Fluid Dynamic Principles of Blood

The application of fluid dynamics to the flow of blood in blood vessels is known as haemodynamics (haem comes from the Greek *haîma*, meaning “blood”). In the simplest sense, fluid dynamics in the cardiovascular system can be likened to a basic network of pipes (arteries and veins) driven by a pump (the heart). In simpler cases, the haemodynamic behaviour of blood flow is described through a set of governing equations for either Poiseuille flow (steady-state laminar flow, in a straight rigid pipe) or Womersley flow (pulsatile, laminar flow in a straight rigid pipe). In order to study the blood flow in more complex scenarios (i.e., patient-specific geometries and boundary conditions), approximate numerical solutions are needed which will be discussed in chapter three (see 3.2 Cardiovascular Computational Fluid Dynamics Methodologies).

Studying the blood flow in arteries can be computationally challenging, therefore several assumptions are usually made which are considered acceptable in larger arteries [102]. Some of the most common simplifications are the description of blood as a Newtonian fluid, the consideration of arteries as circular tubes with rigid walls, and the no-slip boundary, where the velocity adjacent to the vessel walls is assumed to be zero. These concepts will be discussed in the following sections, beginning with the governing equations of fluid flow, the rheology of blood, and the development of different types of flows seen in arteries.

### 2.3.1 Governing Equations of Fluid Flow

Fluid dynamic problems can be modelled across a range of scales from the macro scales, where the fluid is considered as a continuum, down to the micro scales at which the continuum approximation no longer applies [102]. In this study, the molecular interactions of the micro scale are not accounted for, and the macroscopic components of the fluid, such as density, viscosity, pressure, and velocity, do not display microscopic fluctuations [102].

In the simplest case, the dynamics of a fluid in the continuum (where all fluid properties are assumed to uniformly vary in time and position) is governed by the Navier-Stokes equations.

The Navier-Stokes equations are a set of partial differential equations based on the laws of conservation. These laws states that (1) mass is conserved, (2) momentum is conserved, and (3) energy is conserved [103]. For an incompressible, Newtonian fluid, the second-order nonlinear partial differential Navier-Stokes equations can be derived [104]:

$$\nabla \cdot \vec{u} = 0 \quad 2.5$$

$$\frac{\partial \vec{u}}{\partial t} + (\vec{u} \cdot \nabla) \vec{u} - \nu \nabla^2 \vec{u} = -\frac{1}{\rho} \nabla p \quad 2.6$$

where  $\vec{u}$  and  $p$  represent velocity and pressure. Equation 2.5 represents conservation of mass and equation 2.6 represents conservation of momentum.

The Poiseuille equation (see equation 2.3) can be derived from the Navier-Stokes assuming that the flow is steady and laminar, the fluid is Newtonian and incompressible, and the vessel is uniform and rigid. Poiseuille flow is seldom, if ever, seen in human circulation, and hence these approximations are only valid in relatively simple cases such as idealised arteries.

### 2.3.2 Blood Rheology

The rheological properties of whole blood, specifically non-Newtonian behaviour, is largely determined by the properties of red blood cells introduced in section 2.2.2.2. Newton's law of viscosity states that shear stress and shear rate are proportional for laminar flow, and that the proportionality constant is the viscosity,  $\mu$ , which is also the resistance of the fluid to flow [105]. Liquids that obey this law are termed Newtonian fluids (Figure 2.7). Blood, and other non-Newtonian fluids, do not follow this relationship. Instead, as the shear rate decreases, viscosity increases, and vice versa. However, beyond high shear rates ( $\dot{\gamma} > 100/\text{sec}$ ) the viscosity of blood approaches its asymptotic limit and behaves as a Newtonian fluid. This property, known as shear thinning, means that the viscosity of blood varies depending on the haemodynamic conditions and the location in the arterial tree. For example, blood near the arterial walls is Newtonian as  $\dot{\gamma}$  is greater, and non-Newtonian at the arterial centreline where  $\dot{\gamma}$  is nearer zero [106]. Hence, blood cannot be described with a single viscosity value, and instead is expressed as a function of shear rate.

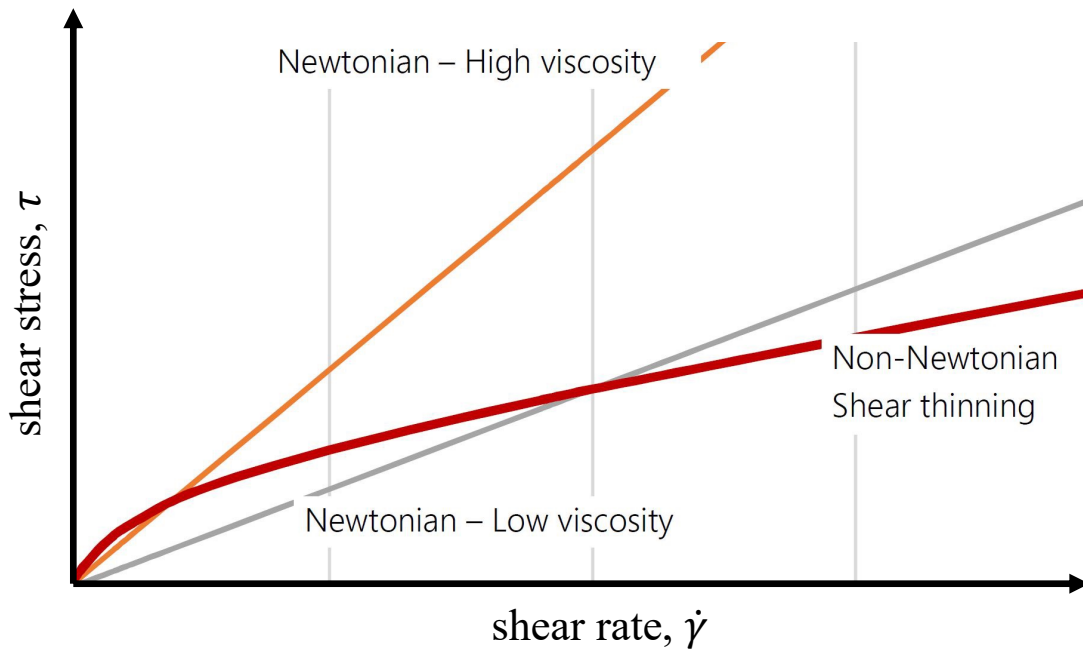


Figure 2.7 Rheological classification of fluids.

### 2.3.3 Characterisation of Different Flows

#### 2.3.3.1 Steady Laminar Flow

Steady flow is when the quantity of liquid flowing per second through any section is constant. For example, let us assume a straight tube with a uniform velocity profile at the entrance (Figure 2.8). According to the no-slip condition, the speed of the fluid layer in direct contact with the boundary is identical to the velocity of this boundary, e.g. zero when the walls are fixed and not moving. A velocity gradient is generated along the tube, where fluid particles at the middle of the tube acquire increased values of velocities while particles at layers adjacent to the wall gradually slow down. The boundary layer thickness  $\delta$  (Figure 2.8) that is formed is the effect of the viscous forces triggered by the fluid viscosity which results in a high shear stress. The velocity profile eventually develops into a parabolic or fully developed velocity profile known as Poiseuille flow profile. The Poiseuille equation was introduced in section 2.2.2.2 and further discussed in section 2.3.1. The region from the entrance of the tube until the flow is fully developed is known as the ‘entrance region’ and the length of that region is called the ‘entrance length’ (Figure 2.8). Shear stress is also gradually reduced until it is stabilised when the flow is fully developed. The entrance length can be approximated as  $L = 0.05ReD$  [107].

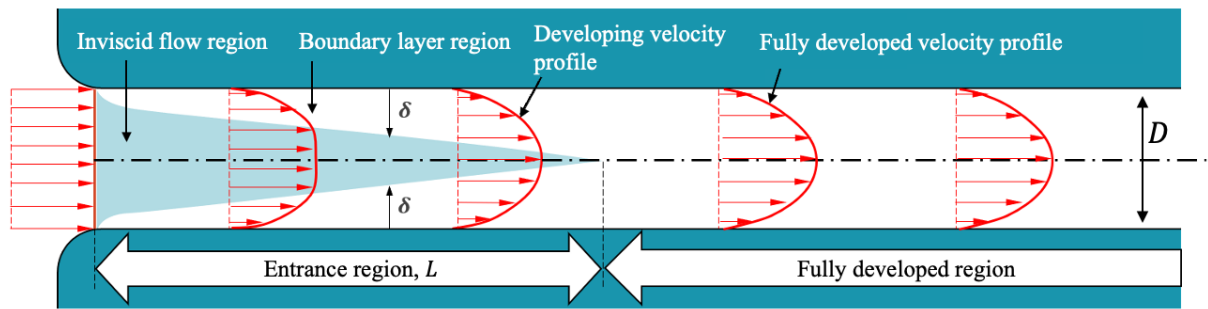


Figure 2.8 Development of laminar (Poiseuille) flow in a pipe where  $\delta$  is the boundary layer thickness.

### 2.3.3.2 Steady Turbulent Flow

In real-life flow conditions, laminar flow rarely occurs. In fact, the majority of fluids involve some form of turbulence. Contrary to the fully developed velocity profile that is observed in laminar flow (Figure 2.8 and Figure 2.9), the velocity profile in turbulent flow is flatter in the central part of the pipe (Figure 2.9). At the wall boundary, velocity of the fluid is zero due to the no-slip boundary condition. The velocity gradient which develops is large, and the turbulent boundary layer is thick and steep adjacent to the wall. The wall shear stress is greater than that seen in laminar flow as a result of this large velocity gradient.

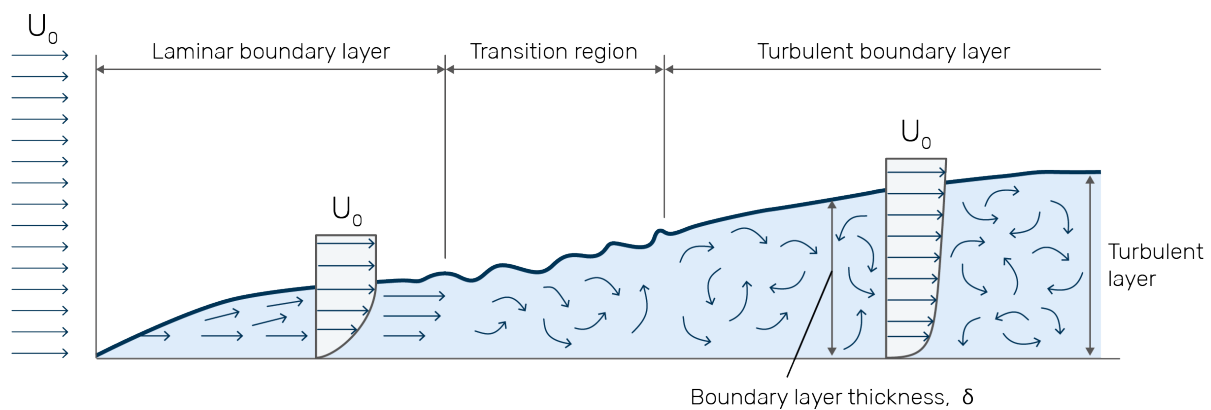


Figure 2.9 Development of turbulent flow in a pipe [108].

### 2.3.3.3 Unsteady Flow

Unlike in steady flow, the fluid properties in unsteady flow do not remain constant with respect to time. Within the circulatory system, contractions of the heart and the periodic nature of the cardiac cycle induces a pulsatile, unsteady flow environment. The simplest example of unsteady flow can be demonstrated in a long straight pipe with laminar flow. If an oscillating pressure gradient is applied to the flow, the flow will slow down, halt and reverse direction,

accelerate in this new direction, and then slow down again. The simplest form of oscillating pressure gradient that we can consider mathematically is the sinusoidal pressure gradient. The Womersley number  $Wo$  (or  $\alpha$ ) is a dimensionless parameter used to characterise unsteady flows. More specifically,  $Wo$  indicates the extent to which the velocity profile in laminar flow in a long pipe differs from the Poiseuille profile when the fluid is subjected to a sinusoidally varying pressure gradient of angular frequency  $\omega$ :

$$Wo = \frac{D}{2} \sqrt{\frac{\omega \rho}{\mu}} \quad 2.7$$

where  $D$  is the diameter of the pipe, and  $\omega$  is equal to  $2\pi f$ . At low Womersley numbers ( $Wo < 1$ ), the viscous forces dominate the inertial forces, and the flow is considered “quasi-steady”. In this case, the velocity profile remains parabolic, and is synchronous with the pressure gradient. Flow still oscillates but the instantaneous flow is determined by the instantaneous pressure gradient. At high Womersley numbers ( $Wo > 1$ ), the inertial forces dominate, the velocity profile is no longer parabolic, and the flow is asynchronous with the pressure gradient [109].

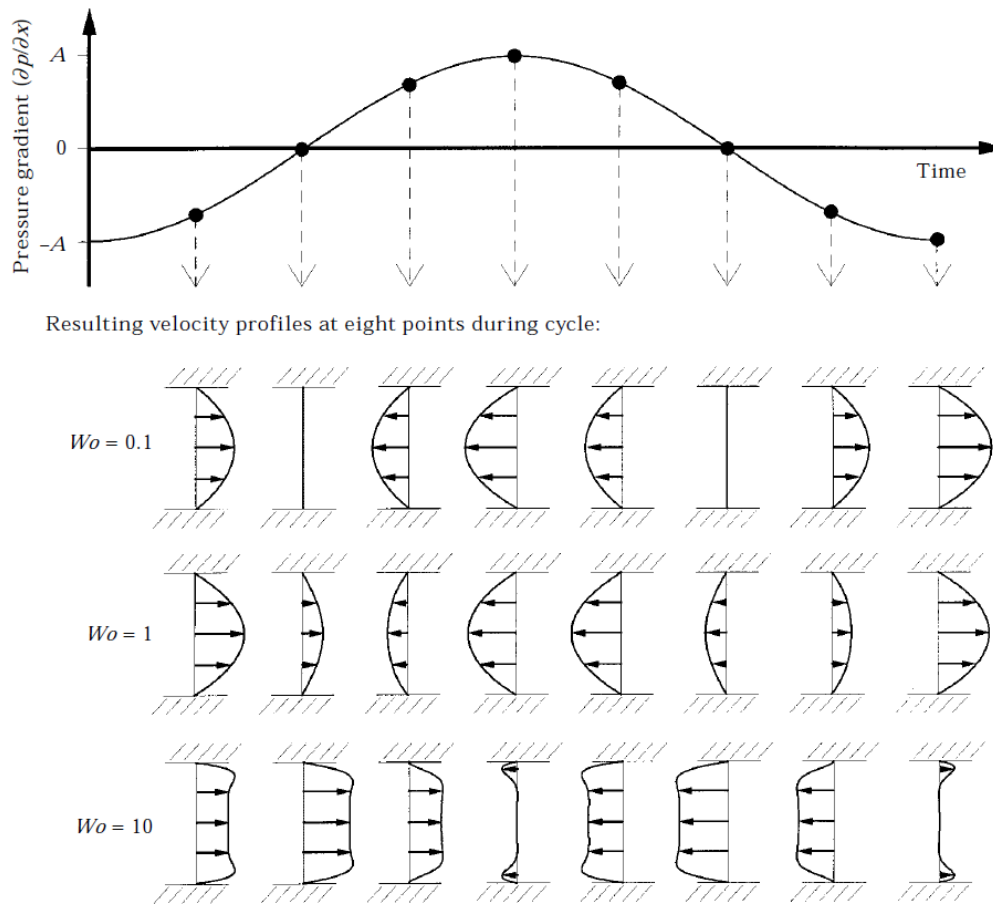


Figure 2.10 Velocity profiles for flow between two flat plates at different Womersley numbers for a sinusoidally oscillating pressure gradient [110].

This effect can be better visualised when looking at the velocity profiles of flow between two parallel plates (Figure 2.10). For  $Wo < 1$ , the flow is quasi-steady; the velocity profiles are parabolic, and velocity is in phase with pressure, while for  $Wo = 1$ , the velocity profiles are still parabolic, but the velocity exhibits a phase lag with pressure. For  $Wo > 1$ , velocity is no longer parabolic, the greatest velocities are observed closer to the walls and not at the centre, and the flow is unable to follow the rapidly changing pressure gradient [110].

## 2.4 Haemodynamics in the Aorta of Congenital Heart Disease Patients

The following text is an excerpt from a publication by L. Johnston et al. The mini-review was published in the Journal of Cardiology and Cardiovascular Sciences in June 2021 (DOI: 10.29245/2578-3025/2021/2.1213).

Congenital heart disease, which affects more than one million newborns globally each year, contributes to an increased risk of cardiovascular disease and ultimately reduced life expectancy. In this mini review, CFD methods applied to the study of congenital abnormalities, with a focus on the aorta, are discussed. The clinical relevance and future directions of CFD modelling are also reviewed.

#### 2.4.1 Congenital Abnormalities of the Aorta

Globally, an estimated 1.35 million newborns are diagnosed each year with congenital heart disease (CHD) [111], defined as structural abnormalities of the heart, and/or vessels, which are present from birth. The American Heart Association defines 21 malformations in the category of CHD [112], ranging from minor lesions, such as bicuspid aortic valve (BAV), to severe, such as coarctation of the aorta (CoA). Congenital abnormalities of the aorta contribute to an increased risk of cardiovascular disease and ultimately reduced life expectancy [113], [114].

Approximately 8% of CHD patients have coarctation of the aorta [115], defined as a narrowing of the vessel which leads to an obstruction of blood flow. If symptomatic, surgical intervention is required to widen the aortic segment and long-term monitoring is essential due to the risk of hypertension and aneurysm formation.

#### 2.4.2 CFD Studies on CHD Haemodynamics

Several groups have studied the haemodynamics behind a variety of congenital cardiovascular malformations [116], [117], [118]. Computational models of bicuspid aortic valve, which accounts for greater morbidity and mortality than all other congenital heart diseases combined, revealed turbulent jet flow through the valve and high shear stress on the aortic wall [119], [120]. In a computational analysis of a BAV patient, conducted by the authors, highly disturbed flow was found in the ascending aorta, and elevated, heterogeneous wall shear stress patterns at the inner and outer walls of the descending aorta [118]. Flow characteristics such as the Reynolds number ( $Re$ ), branch flow division and reverse flow, affect the wall shear stress patterns in the descending thoracic aorta, where increasing  $Re$  results in lower wall shear stress at the lateral sides of branch ostia [121], [122]. The impaired haemodynamics in CHD patients can lead to secondary pathologies, including aortic stenosis, dilatation, and aneurysms. In CHD patients with coarctation of the aorta, computational studies have revealed significantly altered flow dynamics, with a pressure-drop across the coarctation site, and a stenotic velocity jet

resulting in elevated wall shear stress downstream [123], [124]. We reported similar findings in a CoA patient [118]. Several authors have successfully reported the use of MRI-based CFD as an alternative to invasive diagnostic catheterisation in coarctation of the aorta [125], [126]. In 2015, Cosentino et al. [127] published a case study on the use of patient-specific modelling to optimise the intervention in an individual with complex re-coarctation of the aorta and Capelli et al. [116] utilized CFD simulations to optimise the sizing and positioning of CoA stenting. Szopos et al. [128] suggested increased surveillance of “gothic” arch patients with coarctation repair after evaluating fluid-wall interactions using CFD. Computational investigations of endovascular coarctation stent repair found negligible increases in cardiac work when compared to open surgical repair, and a greater percentage of low TAWSS along the anterior wall of the descending aorta [129].

### 2.4.3 Clinical Relevance and Future Direction

Computational fluid dynamics has increasingly driven in recent years clinical decision-making, surgical planning, and the evaluation of innovative surgical techniques by improving our understanding of congenital heart disease haemodynamics. Considering the excess of morbidity and mortality associated with CHD, and the impact of early detection and appropriate treatment in survival rates, CFD could be routinely used in the clinical management of these patients. Shear stress parameters have been linked to atherosclerosis and aneurysms, and therefore many studies have tried to evaluate the correlation between haemodynamic parameters and disease development. Endothelial cells line the vessel wall and remodel in response to variations in wall shear stress. Specifically, decreased and increased levels of WSS result in an increase in the production of endothelin-1 (ET-1) and nitric oxide (NO), respectively [130]. ET-1 is a potent vasoconstrictor and NO is a potent vasodilator, which they in turn regulate the proliferation of smooth muscle cells and collagen synthesis [130]. In addition, mixing of flow, which is found in curved and tortuous arteries, creates a beneficial environment correlated with the prevention of thrombus formation [131]. CFD tools can also be utilized for the design of medical devices, including mechanical heart valves, stents, and grafts. Placement of such devices alters the haemodynamic environment, and it is of immense importance to understand such changes and ensure the durability and proper function of them when surgically placed in patients [130]. A surgical planning tool named Advanced Surgical Planning Interactive Research Environment (ASPIRE) was developed in 1998 in order to help

clinicians assess different surgical plans [132], and similar techniques have since applied this methodology in order to evaluate various surgical procedures [133], [134]. Similarly, HeartFlow (HeartFlow Inc., CA) [135], a diagnostic tool which utilizes CFD to provide cardiologists with a haemodynamic model of the coronary arteries, facilitates customized treatment planning.

Looking towards the future, CFD modelling applied to the study of congenital heart disease should have patient outcomes at the forefront. In order to translate these methods into the clinical practice, evidence of CFD-driven treatment and patient outcomes across a variety of ages, gender, and cardiovascular conditions are essential. If these methods are to be used alongside traditional Doppler echocardiography and magnetic resonance imaging, effort should also be directed towards making these methods cost- and time-efficient as well as user-friendly.

## **2.5 Computational Fluid Dynamic Modelling of Blood flow**

The typical pipeline for patient-specific computational fluid dynamic modelling can be simplified into seven stages: (1) clinical imaging, (2) segmentation and reconstruction, (3) discretisation, (4) boundary conditions, (5) simulation, (6) post-processing, and (7) validation [136]. In the first stage, medical imaging modalities (ultrasound, CT, MRI) are used to obtain clinical data from the patient(s). The data must be of sufficient quality and provide anatomical and physiological detail to facilitate the next stage. Using segmentation software, a three-dimensional *in silico* geometry is reconstructed which defines the physical bounds of the region of interest. The geometry is then divided into a number of discrete volumetric elements in a process known as spatial discretisation or mesh generation. This is a crucial step as the mesh must be refined enough to resolve the fluid dynamics of the flow, but not so fine that there is unnecessary computational expense. The final step in the pre-processing stage is to define the conditions at the model boundaries. Boundary conditions are a set of time-varying physiological parameters that define the physical conditions at the inlets, outlets, and walls. These can be patient specific, or based on population data, physical models, or assumptions. In addition to the geometric, discretisation and boundary data, the user must provide the following information within their chosen CFD software: the density and viscosity values of blood, the initial conditions of the system, the time discretisation, and the required output data. The CFD solver can then solve the Navier-Stokes and continuity equations for blood flow through the patient-specific model. Once the solver has converged (reached a final solution), the

computational results can be interpreted using an array of post-processing methods. The velocity and pressure fields, blood flow profile, wall shear stress (WSS), oscillating shear index (OSI), and shear rate can be visualised. To confirm the accuracy of the CFD model, it is common practice to validate the simulation results with values from in vitro or in vivo assessments. For example, Steinman et al. demonstrated good agreement between computed and PC-MRI obtained in vivo velocity patterns [137]. These results can be translated to the clinical setting directly via device design and treatment planning, and indirectly by improving our understanding of health, disease, and risk stratification [138].

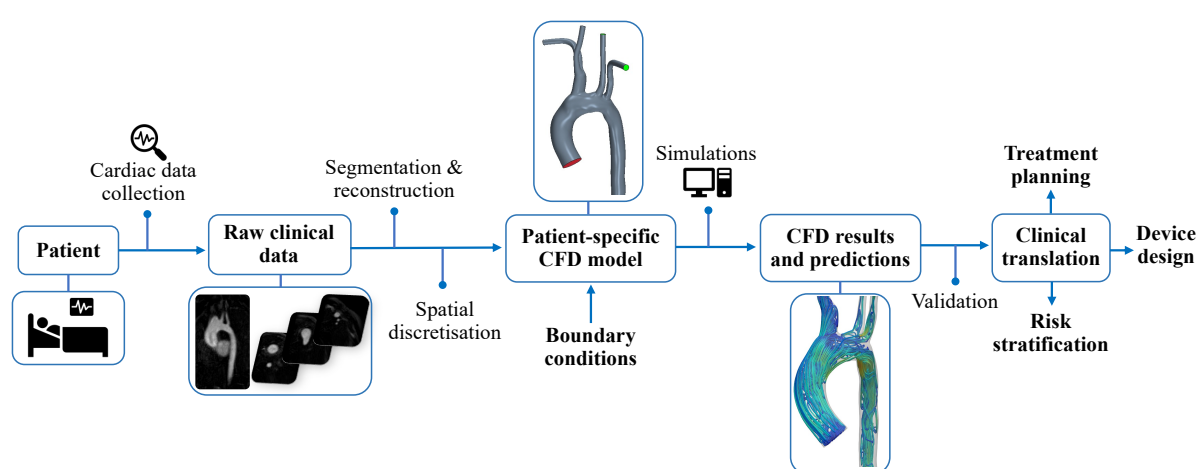


Figure 2.11. Pipeline for patient-specific computational fluid dynamic modelling.

## 2.5.1 Flow Model

### 2.5.1.1 Steady-state vs Transient Simulations

CFD simulations can be steady state, where the computed solution does not change in time, or transient, where the instantaneous values for each quantity are computed in time. For this reason, steady-state simulations are less computationally expensive and often require much simpler boundary conditions (see next section, 2.5.2). Transient simulations are more commonly used in CFD simulations as they capture the pulsatile nature of blood flow throughout the entire cardiac cycle. In these simulations the cardiac cycle period is divided into a number of timesteps. The solver then computes the solution to the governing equations at every timestep until the convergence criteria or an iteration threshold is reached, at which point the solver moves to the next timestep until the simulation is finished. Certain time-dependent haemodynamic parameters, which are important indicators of flow instability, can only be computed from transient simulations (further information in section 2.5.3).

### 2.5.1.2 Laminar vs Turbulent

Although various investigations consider blood flow to be laminar, the transition from laminar to turbulent flow can occur, particularly if aortic pathologies such as stenosis and dilatation are present [139], [140]. Laminar flow is smooth and orderly, with the fluid moving in parallel streamlines with little to no mixing. In contrast, turbulent flow is chaotic, with unpredictable fluctuations of both flow velocity and pressure. The flow regime in a system can be characterised by the dimensionless Reynolds number ( $Re$ ), defined as the ratio of the inertial forces to the viscous forces within a fluid:

$$Re = \frac{\rho u D}{\mu} \quad 2.8$$

Laminar flow occurs at low Reynolds numbers ( $< 2300$ ) where viscous forces are dominant, whereas turbulent flow occurs at higher Reynolds numbers ( $> 4000$ ), dominated by inertial forces [141]. In between laminar and turbulent flow is transitional flow ( $Re = 2300 - 4000$ ).

The majority of CFD studies on aortic haemodynamics assume laminar blood flow based on the assumption that flow in large arteries is laminar [142], [143]. While fully developed turbulence is rarely, if ever, seen in vivo, there is data to suggest that aortic flow reaches Reynolds numbers within the transitional and turbulent range [144], [145], [146], [147]. For example, Stalder et al. computed a peak Reynolds number of 3350–4500 in the aorta of young healthy volunteers [146]. In order to capture the dynamics of turbulent flow, the numerical setup requires the use of a turbulence model. Direct numerical simulation (DNS) resolves all spatial and temporal scales of the turbulence, while large eddy simulation (LES) resolves the larger turbulent eddies and models the smaller scales. Despite DNS and LES models performing well for transient and turbulent flow regimes in healthy [147] and abnormal arteries [148], [149], [150], these approaches are very computationally expensive and therefore not always feasible. Reynolds averaged Navier-Stokes (RANS) models offer a more economic approach as they require far less computational power but provide a somewhat limited representation of the flow turbulence. Nevertheless, RANS models are successful from an engineering perspective as they can predict the mean flow quantities and their interaction with the surrounding vessel in terms of wall shear stress. Commonly used RANS turbulence models are the  $k-\varepsilon$  ( $k$ -epsilon),  $k-\omega$  ( $k$ -omega), and SST (Menter's Shear Stress Transport).

## 2.5.2 Boundary Conditions

For a simulation to be fully defined, the conditions at the model inlet(s) and outlet(s) must be specified. These are known as boundary conditions (BCs) and always have a spatial component, and sometimes a time component in the case of transient flows. The choice of boundary conditions depends on a number of factors, including availability of patient-specific data, desired accuracy of the simulation, and computational power. Several authors have highlighted the sensitivity of the computed flow field when using different BCs [151], [152], [153], [154]. For patient-specific studies, non-invasive in vivo measurements of time-dependent flowrates, flow ratios or pressure waveforms should be used if possible.

### 2.5.2.1 Inlet Boundary Conditions

In arterial models, the inlet boundary condition is prescribed at the entrance to the model which will have been truncated from the remaining arterial network during the reconstruction of the geometry. Velocity profiles are the most common choice of inlet boundary condition for blood flow problems. These can be in the form of a uniform (blunt) velocity profile, a non-uniform (fully developed) velocity profile, a Womersley flow profile, or a patient-specific profile [155]

A fully developed velocity profile is parabolic in shape and can be achieved by applying a velocity profile based on an equation, or by affixing a flow extension to the inlet which allows the flow to fully develop by the time it reaches the true inlet. Typically, a uniform or non-uniform velocity profile is applied in combination with a pulsatile waveform obtained experimentally or in vivo, making the simulation transient in nature. To achieve the most realistic simulation, an in vivo velocity profile (2D or 3D) derived from phase-contrast MRI data should be used.

### 2.5.2.2 Outlet Boundary Conditions

Depending on the vessel being modelled, there could be multiple outlets requiring boundary conditions to be defined. The choice of which boundary condition to use has been a regular topic of debate as the physiological conditions of the downstream vasculature influences the haemodynamics in the vessel of interest. In the absence of patient data, the simplest approach is to apply traction free or zero pressure to each outlet. This BC defines the outlet as an opening exposed to atmospheric conditions, allowing for flow reversal if it occurs. Despite its simplicity, this BC neglects the resistance of the downstream vasculature. Several authors have

favoured Murray’s law or the splitting method over the zero-pressure boundary condition, for capturing more physiologically relevant flow features [156], [157]. In arterial bifurcations, Murray’s law states that flow in a vessel is proportional to the diameter of the vessel lumen to the power  $n$ :

$$\dot{m} \propto D^n \quad 2.9$$

This relationship has been used in several human CFD studies, and is well-known with  $n$  equal to 3, hence the name “Murray’s cube law”. However, several authors have shown that a power of 2 is more valid in the case of larger vessels such as the aorta [158], [159], [160]. The splitting method is based on the same power law relationship between diameter and flow rate as Murray’s law. At each bifurcation encountered, starting from the inlet, the splitting method assumes that the flow divides according to the following:

$$\frac{Q_1}{Q_2} = \left(\frac{D_1}{D_2}\right)^n \quad 2.10$$

where  $D_1$  and  $D_2$  are the diameters of the 2 daughter branches at the given bifurcation, and  $Q_1/Q_2$  is the bifurcation flow division [157]. Both Murray’s law and the splitting method assign a percentage of the total inlet flow rate (flow split) to each outlet boundary. When performing more complex simulations, lumped parameter or zero dimensional models can be implemented as boundary conditions (coupled with 2D or 3D models) in multi-scale models to represent the impedance of the downstream vasculature, particularly when in vivo data is not available. In lumped-parameter models the concept of a hydraulic-electrical circuit is applied, where voltage and current represent blood pressure and flow rate. They can be mono-compartmental, where the whole vascular system is represented by a single block, or multi-compartmental, where multiple blocks are connected into a network. The first, and probably the most well-known, mono-compartmental model is the two-element Windkessel model (WKM). This simple model consists of two elements in parallel: a capacitor representing the elasticity of the larger arteries, and a resistor representing the frictional losses from the smaller arteries. Despite its simplicity, the two-element WKM is used in clinical practice to estimate total arterial compliance when peripheral resistance and the aortic pressure pulse waveform are not known. More sophisticated versions of the two-element WKM have been introduced over the years, which include an additional resistor (three-element WKM) or an additional resistor in parallel with an inductor (four-element WKM). In one-dimensional (1D) models, the one-dimensional form of the

momentum and continuity equations are solved numerically to obtain pressures and flows throughout the systemic arterial tree. 1D models differ from 0D models in that they include a spatial dimension but are similar in their functionality when coupled to higher order models. These models will be discussed further in section 3.2.1.

### 2.5.3 Haemodynamic Parameters

As blood flows through the arterial system, haemodynamic forces are exerted on the arterial walls (Figure 2.12). In the arterial wall, the pressure pulse (the difference between systolic and diastolic pressure) induces distension resulting in radial ( $\sigma_{\text{radial}}$ ), circumferential ( $\sigma_{\text{circ}}$ ), and axial ( $\sigma_{\text{axial}}$ ) stresses. On the surface of the arterial wall, the frictional drag from the flow of blood induces wall shear stress ( $\sigma_{\text{shear}}$ ). The mathematical equation for wall shear stress is:

$$WSS = \mu \left( \frac{du}{dr} \right) \quad 2.11$$

where  $du/dr$  is the blood velocity gradient. WSS varies throughout the cycle due to the pulsatile nature of blood. Therefore, to analyse the WSS across the entire cycle, the time-averaged wall shear stress (TAWSS) is computed:

$$TAWSS = \frac{1}{T} \int_0^T |\overline{WSS}| dt \quad 2.12$$

where  $T$  is the cardiac cycle period,  $|WSS|$  is the magnitude of the instantaneous WSS vector, and  $t$  is time.

Endothelial cells are highly sensitive to these haemodynamic forces and mediate the regulation of vessel function and structure in response to varying wall shear stress [161]. Years of extensive research have linked the exposure of extreme wall shear stress and the development and progression of atherosclerosis.

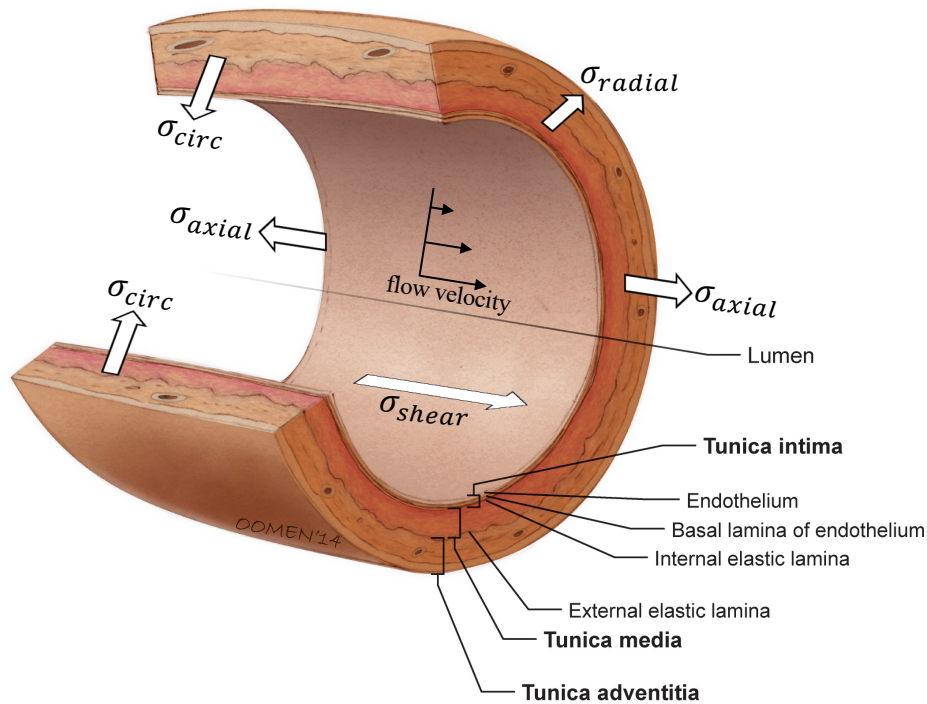


Figure 2.12. Force exerted on the vessel wall due to the flow of blood. Figure adapted from Glen Oomen [88].

In straight vessels with laminar flow, baseline wall shear stress (1.5-2.5 Pascals) promotes endothelial stability and quiescence, and an atheroprotective gene expression profile [161]. On the other hand, low wall shear stress (<1 Pascal), typically associated with complex anatomy and disturbed flow, promotes an atherogenic phenotype [162]. In fact, the distribution of atherosclerotic lesions is roughly three times greater in regions chronically exposed to low shear stresses [163]. A low WSS environment is associated with apoptosis, reduced bioavailability of nitric oxide and increased expression of adhesion molecules and chemotactic factors; thereby exposing the endothelium to the atherogenic effect of local and systemic risk factors [161], [164]. In fact, endothelial dysfunction is one of the early signs of cardiovascular disease progression [165]. This relationship explains why atherosclerotic lesions are preferentially found at bifurcations, branches, curvatures, stenoses, and dilatations, which have complex anatomy and disturbed flow [166], [167], [168]. High wall shear stress (>3 Pascals) appears to be atheroprotective based on evidence of the inhibition of platelets and leukocyte adhesion [164], as well as the destabilisation and rupture of atherosclerotic plaque at these values [169]. However, this beneficial effect is only true below levels at which the endothelium detaches (approximately >40 Pascals, although this is rare) [165].

In addition to low shear stress, disturbed flow is characterised by constantly changing gradients of shear stress, flow-separation that includes flow reversal, oscillatory flow, multidirectional secondary flows, and sometimes turbulence [165]. The degree of flow reversal (the directional change of the wall shear stress vector from the bulk flow direction) throughout the cardiac cycle can be quantified by the oscillatory shear index (OSI):

$$OSI = \frac{1}{2} \left( 1 - \frac{|\int_0^T \overline{WSS} dt|}{\int_0^T |\overline{WSS}| dt} \right) \quad 2.13$$

Proposed by Ku et al., in 1985, the OSI is a non-dimensional marker of disturbed flow with values ranging from 0, when the WSS vector does not change during the cardiac cycle, to 0.5, when the WSS vector changes its direction by 180° [167]. The endothelium is highly sensitive to oscillatory shear stress. For instance, just 20-30 minutes of experimentally-induced oscillatory shear stress was enough to disrupt endothelial cell quiescence [170]. Above an OSI value of 0.2, the flow environment is considered pro-atherogenic, and at higher values the vascular wall of the aorta and coronary arteries is susceptible to thickening [171], [172].

The specific haemodynamic environment linked to atherosclerosis, that is low and oscillatory wall shear stress, leads to an increased residence time of blood particles adjacent to the wall [161]. The relative residence time (RRT) index, defined below, combines both the TAWSS and OSI into a single parameter.

$$RRT = \frac{1}{(1-2 \cdot OSI) \cdot TAWSS} \quad 2.14$$

#### 2.5.4 Fluid Dynamics in Turner Syndrome Aortae

As of 2021, there are only three published studies on the aortic flow of TS patients: two of which employ CFD methods, and one which employs 4D flow MRI [173], [174], [175]. In 2014, Chen et al. (2014), conducted the first CFD analysis on three Turner syndrome children (age and BMI unknown) [173]. All three children had some form of aortic abnormality commonly seen in Turner syndrome (see 2.1.3.1): ascending aorta dilatation, common origin of the brachiocephalic and left common carotid arteries, elongation of the transverse aorta, and coarctation. The simulations were performed with the fluid assumed to be incompressible Newtonian, and a constant volumetric flow rate of 4.5l/min. The objective of the study was to

determine the impact of abnormal geometry on the wall shear stress (WSS), luminal surface low-density lipoproteins (LDLs) concentration, and oxygen flux along the arterial wall. Chen et al., observed weak secondary flow in the ascending aorta which became stronger throughout the transverse aorta, dean vortices in the arch of the aortic models with ETA and CoA, and remarkably different flow in the descending aorta of the three models. In terms of shear stress results: the WSS was unevenly distributed, and noticeably different when compared to healthy aortae; and low WSS was present at areas where atherosclerotic plaques develop preferentially, such as the brachiocephalic branch, the inner side of the aortic arch exit, and the entire inner wall of the descending aorta. They suggest that abnormal blood flow leads to vascular wall disease which may explain the increased cardiovascular morbidity in TS, and conclude that WSS, luminal surface low-density lipoprotein concentration, and oxygen flux are all important for the assessment of vascular disease.

In a more recent study by Wittberg et al. (2016) [176], non-Newtonian blood was simulated through four patient-specific TS geometries, three of which had an aortic abnormality (ascending aorta dilatation, ETA, CoA). As with Chen et al. (2014), similar inflow (volumetric flow rate of 5l/min) and outflow (mean static pressure) boundary conditions were applied in all cases. The main objective of Wittberg et al. (2016) was to study the flow characteristics of the TS aorta and how they are affected by anatomic anomalies. Despite the differences between the two CFD studies, Wittberg et al. (2016), also found a clear geometry effect on the flow field.

Arnold et al. (2017), characterised the aortic flow field using 4D-flow MRI in the largest cohort of TS females (n=25, mean  $\pm$  standard deviation age =  $17 \pm 4$  years) to date [174]. The authors compared the results with 16 healthy female age-matched volunteers ( $16.5 \pm 5$  years). Turner syndrome girls had significantly larger aortic diameters, increased vortices in the ascending aorta, and elevated helical flow in the ascending and descending aorta compared to healthy controls. Additionally, peak systolic wall shear stress and oscillatory shear index were significantly lower in Turner patients compared to controls.

### 2.5.5 Clinical Translation and Challenges

It is clear from the literature that CFD has many applications in the field of biomedical engineering, particularly in the cardiovascular system. Not only can CFD be used to improve

our understanding of disease processes and their progression, but it can also be used to enhance diagnostic capabilities and progress toward patient specific precision medicine. Patient-specific CFD models are being used to address aortic aneurysms, coronary stenosis, cardiac valves, and congenital heart disease through risk stratification and optimisation of surgical procedures [177]. Examples being the growing use of CFD for refining transcatheter aortic valve replacement, and improving the haemodynamic performance of medical devices (such as arterial stents and endovascular devices, prosthetic heart valves, and ventricular assist devices) to enhance their thromboresistance [178]. Currently, the management of cardiovascular conditions in Turner syndrome is the same as in the general population. This is due to a lack of understanding of the developmental origins of the cardiovascular manifestations seen specifically in TS. CFD has the potential to improve our clinical understanding of disease processes and could be used clinically to predict patients at higher risk of adverse outcomes. For CFD modelling to be translated into clinical practice, there needs to be enough evidence that these models can benefit Turner syndrome patients. As with any other methodology, longitudinal studies involving large cohorts of patients with follow-up data are necessary. Also, any computational model intended to be translated into clinical practice needs to accurately capture the relevant physiological phenomena needed to assist the decision-making process and improve prognosis, without being too complex for the average clinician.

## **2.6 Reminder of Thesis Outline**

As a reminder, a review of the literature and description of the theoretical principles was presented in this chapter to provide reader with a solid background to understand the methodologies and results presented in the subsequent chapters. In the following chapter, Chapter 3, the framework for computational fluid dynamic simulations will be presented. The proposed methodology will be explained in detail, to provide the reader with the background theory to the methodologies used in this thesis.

## Chapter 3 General Background on Methods

In the following chapter, the methodologies used throughout this thesis are presented. The specific methods will build upon the principles introduced in section 2.4, and provide the reader with a broad understanding of the processes behind each step of this research. The first section provides an introduction to computational fluid dynamic methodologies, specifically the creation and discretisation of the geometrical domain, and the numerical schemes used in computing the solution. In the second section, the application of computational fluid dynamics to cardiovascular modelling is discussed, building upon the introduction provided in chapter 2 (section 2.5). The specific methods used are presented in more detail in chapters 4-6.

### 3.1 Computational Fluid Dynamic Methodologies

The concept behind CFD is the approximation of the solution to the partial differential equations governing fluid flow (presented in section 2.3.1). In the pre-processing stage, the computational domain is discretised into a finite number of elements through a process known as mesh generation. STAR-CCM+ software was chosen to generate the computational mesh as will be discussed in section 3.1.1. Depending on the numerical problem, the user has a choice from a wide range of in-house, commercial and open-source CFD software including COMSOL, Autodesk CFD, OpenFOAM, Ansys Fluent, and STAR-CCM+. In this work, the majority of the results were obtained using the open-source software OpenFOAM. Commercial packages Ansys Fluent and STAR-CCM+ were used briefly for the purpose of verifying the results obtained from OpenFOAM simulations. Various numerical methods are employed by different solvers. These are known as the finite difference method (FDM), the finite volume method (FVM), and the finite element method (FEM). The FDM and FEM are not discussed further in this thesis as OpenFoam®, Ansys Fluent, and STAR-CCM are finite volume solvers.

#### OpenFOAM®

OpenFOAM (Open Source Field Operation And Manipulation) is an open-source CFD solver which utilised finite-volume discretisation of the domain [179]. OpenFOAM was developed in the late 1980s at Imperial College, London, and today the official OpenFOAM project is maintained by OpenCFD Ltd. OpenFOAM is a C++ library, consisting of predefined numerical solvers, utilities, and applications that can be directly used for the solution of fluid dynamic

problems. At the core of these libraries are a set of object classes that allow the programmer to manipulate meshes, geometries, and discretisation techniques at a high level of coding [179]. One of the strengths of OpenFOAM is that it offers users complete freedom to customise and extend its existing functionality, allowing for versatile modelling of various fluid dynamics phenomena. Today, over sixty customised numerical solvers are available for applications including turbulence modelling, heat transfer, combustion, and multiphase flow [180]. In this work we implemented OpenFOAM to simulate blood flow in aortic geometries. Similar examples can be seen in the literature examples for the thoracic aorta [181], [182], abdominal aorta [183], carotid artery [184], and arterial stenoses [185], [186].

The main OpenFOAM classes and their functions (Figure 3.1) represent the building blocks for the development of OpenFOAM based applications and utilities. There are five main objects in OpenFOAM®: (1) Space and time, where space is captured as computational mesh and time as a finite number of time steps; (2) Field variable, with tensors, scalars and vectors numerically approximated as list of values at pre-defined points of the mesh; (3) Matrix and linear system, that hold the results of discretisation; (4) Discretisation method, either implicit or explicit implemented through interpolation, differentiation and discretisation; (5) physical modelling libraries where the user can recognise object families that can be repeated in the physics modelling level [187].

### Anslys Fluent

Anslys Fluent is a commercial CFD software developed by a team at Sheffield University in the early 1980s and maintained by Anslys Inc. Among the commercially available CFD software, Anslys Fluent is one of, if not, the most popular across both academia and industry. Fluent was the first commercial CFD software to have a graphical user interface and workflow as opposed to the command-line input used by OpenFOAM. In fact, the entire computational modelling process (pre-processing, solving, and post-processing) can be completed in a single window. As with OpenFOAM, Fluent uses the finite volume code to find a solution such that mass, momentum, energy and other relevant quantities are conserved for each cell. The code directly solves for values of the flow variables at the cell centres, while values at other locations are obtained by suitable interpolation. More detail on the finite volume method and other numerical methods is given in this Chapter (section 3.1.2).

Objects	Type of data	OpenFOAM® Class
Interpolation	Differencing schemes	surfaceInterpolation<template>
Explicit discretization: differential operator	ddt, div, grad, curl	fvc::
Implicit discretization: differential operator	ddt, d2dt2, div, laplacian	fvm::

*Numerics and discretisation*

Objects	Type of data	OpenFOAM® Class
Variables	Primitive variables	scalar, vector, tensor
Mesh components	Point, face, cell	point, face, cell
Finite volume mesh	Computational mesh	fvMesh, polyMesh
Time	Time database	Time

*Computational domain*

Objects	Type of data	OpenFOAM® Class
Field	List of values	Field<template>
Dimensions	Dimension set up	dimensionSet
Variable field	Field + mesh + boundaries + dimension	GeometricField<template>
Algebra	+, -, pow, =, sin, cos...	field operators

*Field operation*

Objects	Type of data	OpenFOAM® Class
Sparse matrix	Matrix coefficients and manipulation	lduMatrix, fvMatrix
Iterative solver	Iterative matrix solvers	lduMatrix::solver
Preconditioner	Matrix preconditioner	lduMatrix::preconditioner

*Linear equation systems and solvers*

Figure 3.1. List of the main OpenFOAM classes and their functions. Figure adapted from Moukalled, 2016 [179].

### STAR-CCM+

The other most popular commercial CFD software, and Ansys Fluent’s competitor, is Simcenter STAR-CCM+. STAR-CCM+, previously known as STAR-CD, was originally developed during the late 1980s by a spin-off company from Imperial College London and acquired by Siemens in 2016. Like most continuum-based CFD codes, STAR-CCM+ uses the finite volume method to discretise the Navier-Stokes equations. Similar to Ansys Fluent, STAR-CCM+ operates through a graphical user interface, offering the user pre-processing, simulation, and post-processing tasks from within a single window.

For more information beyond the scope of this thesis, see “Notes on Computational Fluid Dynamics”, a recently published book co-authored by the core developer of OpenFOAM [188]. In this book the authors “offer a modern perspective on CFD with the finite volume method, as implemented in OpenFOAM and other popular general-purpose CFD software”.

### 3.1.1 Geometrical Domain and Mesh Generation

The first stage in a computational fluid dynamic simulation is to define the geometrical space. The definition of this space depends on the problem of interest and the physics involved. For example, in external aerodynamics, the flow is simulated around a geometrical object (e.g., an aeroplane), therefore the computational domain is a volume of adequate dimensions around the geometry of interest. Meanwhile, in internal flows, the computational domain is defined by the confines of the geometry itself, e.g., flow within a blood vessel. Computer aided design (CAD) software, such as SOLIDWORKS and Autodesk, are often used to build such geometries. Again, these can be two-dimensional or three-dimensional, depending on the nature of the problem. In section 3.2 the creation of geometries specific to cardiovascular modelling will be discussed. In all cases, the product will be a closed flow volume i.e., a non-discretised volume enclosed by a rigid surface boundary.

Now that the geometrical domain is defined, to compute the simulated flow field, the CFD software requires the computational domain to be discretised into a finite number of subdomains (also called elements or cells) in which the mathematical equations are solved. The quality of the mesh is critical to the success of the numerical simulation as it determines numerical accuracy and stability. In fact, it is often said that the numerical solution is only as good as the mesh behind it.

Computational meshes can be broadly classified into two categories: structured and unstructured. A structured mesh is defined as a set of elements with an implicit connectivity, while an unstructured mesh is defined as a set of elements with an explicitly defined connectivity. The most common element types used in structured meshes are 2D quadrilateral and 3D hexahedral elements, and in unstructured meshes are 2D triangle and 3D tetrahedral elements (Figure 3.2, A). The decision of which mesh type is most suitable depends on the complexity of the physical problem. In most biomedical problems the geometries are complex and generally unstructured meshes are favoured [189].

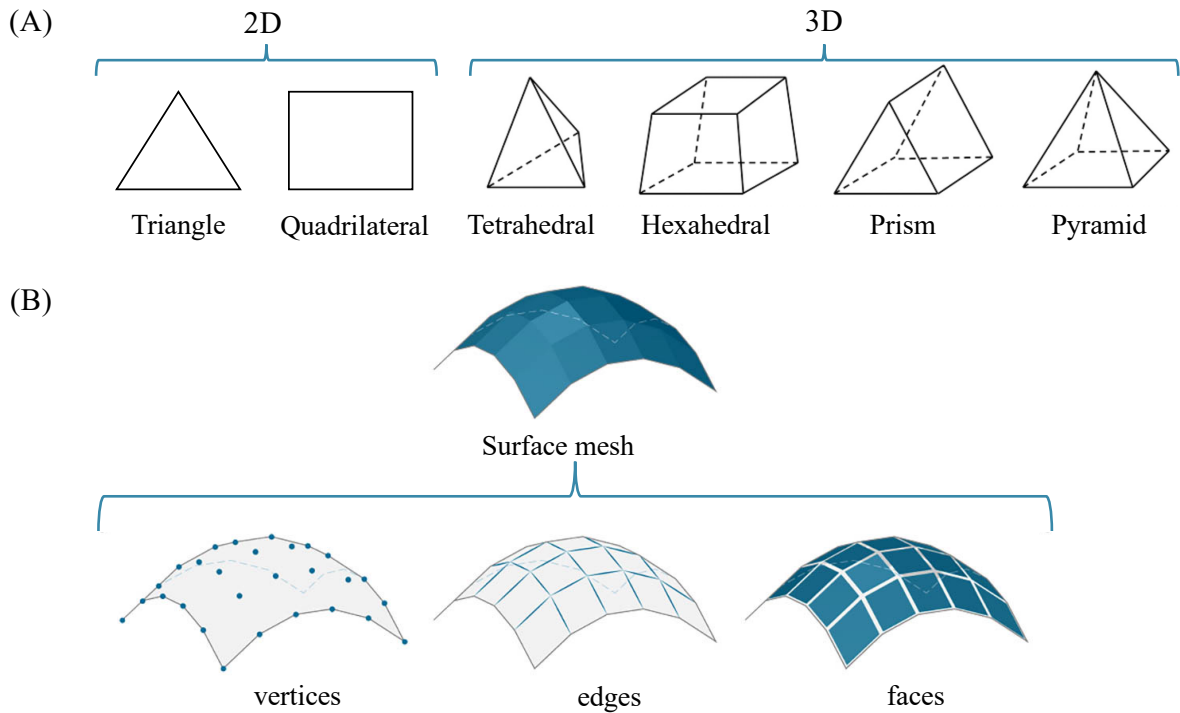


Figure 3.2 Components of computational meshes. (A) Two- and three-dimensional element types, and (B) mesh structure including the vertices, edges, and faces that collectively create the surface mesh. Figure adapted from COMSOL® and Autodesk® user manuals [190].

The mesh generation process begins with the creation of vertices, lines, and faces which together form the surface mesh (Figure 3.2, B). In unstructured mesh generation, the most common methodologies are Octree, Delaunay, and advancing front. Using the Octree method, an initial bounding cube is divided into eight congruent cubes, each of which is split recursively, until a desired resolution threshold is achieved. Alternatively, using the Delaunay method, new points are iteratively inserted into the domain while maintaining the Delaunay criterion: a node must not be contained within the sphere passing through all four vertices of the tetrahedron within the mesh. The third is the advancing front method, where tetrahedra are built progressively inward, until the front (the region separating the meshed and unmeshed) is empty and the surface is meshed. Using either of these methods, the surface mesh is generated and the next step is to fill the enclosed computational domain to form the volume mesh [191]. This bottom-up approach is common in mesh generation. All geometries presented in this study were meshed using STAR-CCM+ software.

### 3.1.1.1 Polyhedral Mesh

Traditionally, the task of automatically generating meshes for complex three-dimensional patient-specific geometries has favoured the use of tetrahedral elements (Figure 3.2, A). However, recently polyhedral elements have emerged as an alternative option as they offer the same automatic meshing benefits as tetrahedral meshes but with greater potential for numerical stability. The first major advantage of polyhedral elements is that each individual element has multiple neighbours (typically of the order of 10, compared to four for tetrahedral elements), even along wall edges and at corners [192]. This allows for better approximation of both scalar gradients and local flow distribution. The second advantage of polyhedral elements is that they are less sensitive to stretching than tetrahedral cells. Mesh comparison studies have verified that the same level of accuracy can be achieved with polyhedral meshes of approximately four times fewer cells (therefore half the computing memory and a tenth to a fifth the computing time) than a tetrahedral mesh [192]. To that end, several authors have utilised polyhedral meshing in vascular geometries [142], [193], [194].

STAR-CCM+ offers an automated mesh generator which can be used in combination with the following tools [196]:

- Surface remeshing: A surface preparation tool used to generate a closed, manifold and nonintersecting surface to improve the overall quality of the existing surface
- Polyhedral mesher: An unstructured, general-purpose mesher for complex geometries which utilises an arbitrary polyhedral cell shape to build the core mesh
- Prism Layer mesher: Used in combination with the core volume mesh to generate prismatic cells adjacent to wall surfaces to accurately capture the boundary layer (see section 3.1.1.2)

Polyhedral mesh generation in STAR-CCM+ utilises a dualisation technique, where polyhedral cells are created from existing tetrahedral cells. Specifically, the centroids of each tetrahedron are marked along with the centre of cell edges at the boundaries, and the polyhedral cells grow from the boundary and merge towards the centre of the domain.

### 3.1.1.2 Boundary Layer

The boundary layer refers to the region near the geometric wall where the viscous forces are dominant. In this case, the near-wall mesh was generated by first defining the minimum

distance ( $\Delta y_1$ ) between the first element of the boundary layer and the wall. The quality of the boundary layer mesh is represented by the  $y^+$  value, a non-dimensional distance from the wall to the first element node. Refining the near-wall mesh with an appropriate  $y^+$  value is crucial for resolving flow in the viscous sublayer of the boundary layer. Satisfying a  $y^+$  value of 1, the height of the first layer ( $\Delta y_1$ ) can be computed from the following equation [197]

$$\Delta y_1 = \frac{\mu y^+}{\rho U_T} \quad 3.1$$

where the friction velocity ( $U_T$ ) is:

$$U_T = \sqrt{\tau_w / \rho} \quad 3.2$$

where  $\tau_w$  is the wall shear stress:

$$\tau_w = \frac{1}{2} C_f \rho U_{mean}^2 \quad 3.3$$

and  $C_f$ , the skin friction coefficient, is computed using the Churchill equation which relates pipe friction loss to Reynolds number for laminar, transitional, and turbulent flows [198]:

$$C_f = 2 \left[ \left( \frac{8}{Re} \right)^{12} + \left( \left( 2.457 \ln \left( \left( \frac{Re}{7} \right)^{0.9} \right) \right)^{16} + \left( \frac{37530}{Re} \right)^{16} \right)^{-1.5} \right]^{1/12} \quad 3.4$$

The boundary layer usually consists of multiple layers, created using the advancing-layers method [199]. Subsequent layers were added to the first layer by connecting new nodes in the direction of the model centre, progressively increasing by a specified growth factor rate, until the desired layer thickness was reached (see Figure 3.3).

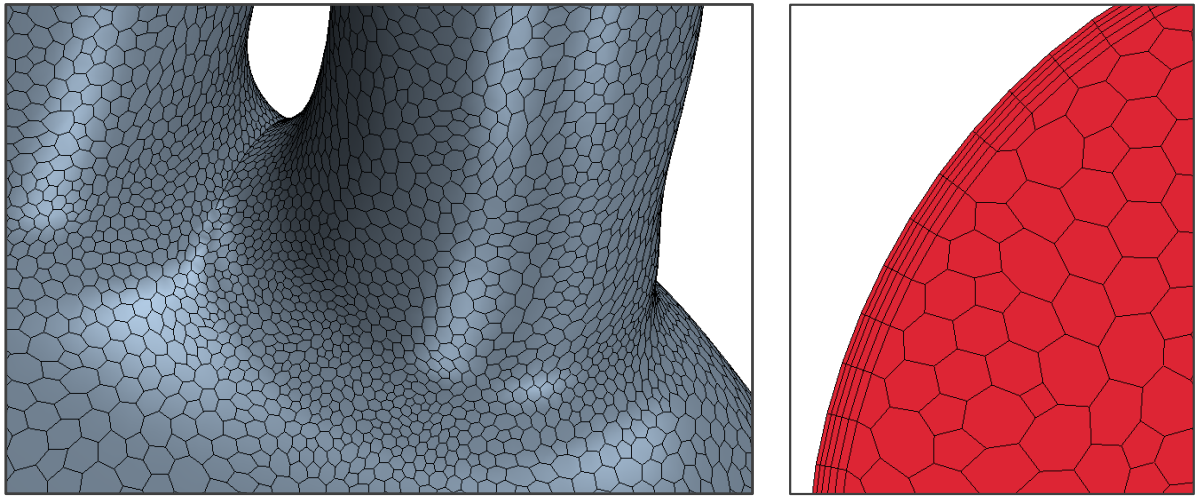


Figure 3.3 STAR-CCM+ polyhedral mesh generated on a patient-specific aortic model (left) with zoomed views of the polyhedral surface mesh and the boundary layer mesh (right).

### 3.1.2 Numerical Methods

Numerical methods are used to approximate a solution to the partial differential equations (introduced in section 2.3.1) which describe the fluid flow. This involves the discretisation of the continuous problem domain (see section 3.1.1) where each flow variable is defined at specific grid points as opposed to every point in the domain. As previously mentioned, most commercial CFD solvers today employ the finite element or finite volume method which have proven efficient and robust in modelling flow in complex geometries.

#### 3.1.2.1 Boundary Conditions in Numerical Methods

As with all numerical methods, particular attention should be given to the boundary conditions assigned at the boundary faces of the geometric domain. To evaluate the fluxes at the boundary faces, the Dirichlet and Neumann boundary conditions are most commonly used. In the first case, a specific scalar value is assigned at the boundary face, while in the second case, the derivative of the scalar is the known quantity which is specified [200]. The effect and the importance of different boundary conditions was previously discussed in section 2.5.2.

#### 3.1.2.2 Finite Element Method

The finite element method is the most commonly applied method in numerical analysis [201] Initially, FEM was developed for solving solid-state mechanical problems where the deformations and stresses of solid structures under mechanical loads are predicted. Today,

finite element discretisation is used across a range of applications, namely computational fluid dynamics. In simple terms, the concept of FEM is as follows: first, the fluid domain is divided into a finite number of sub-domains (elements) over which the algebraic equations are solved, and then the individual solutions are combined to obtain a global solution [201]. In FEM, only the list of vertices is needed for which the solution is approximated. In between these points the solution is linearly interpolated [201]. For example, in a two-dimensional case the domain is divided into a finite number of triangles, and the corner point of each triangle is a vertice. Each element in the domain is defined using the Lagrangian coordinate system, a local coordinate system that is valid only within the element itself, as opposed to the global coordinate system (see Figure 3.4) [201].

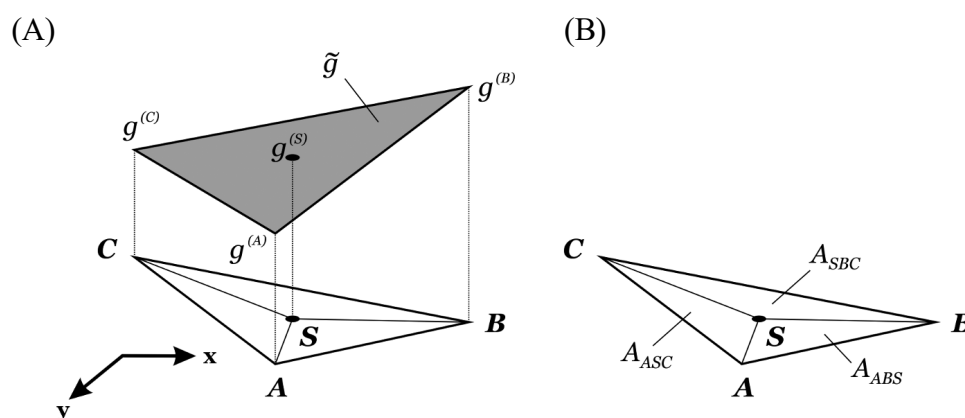


Figure 3.4 Lagrangian coordinate system illustrated on a single element in a finite element mesh. (A) Approximation of the dependent function,  $g$ , using  $\tilde{g}$ . (B) Definition of the Lagrangian coordinates using the area of the sub triangles created by the point  $S$  [201].

### 3.1.2.3 Finite Volume Method

The finite element and finite volume method share many similarities as both describe a numerical method for solving partial differential equations. However, it is the fundamental conservation property of the finite volume method that makes this method different from other methods (FEM and FDM). The basic concept of the finite volume method is the solution to the partial differential equations of the laws of conservation (see chapter 2.3.1) through discretisation into algebraic equations over finite volumes. Specifically, such algebraic equations are solved at every single element in the geometric domain to compute the value of the dependent variables of velocity and pressure. The values of the dependent variables are stored at the centre of each cell (cell-centred method). The conservation property of the FVM

is maintained by monitoring the fluxes of the dependent variable across the boundary of the cells and adjusting the quantity of the change of the dependent variable within the control volume accordingly [201].

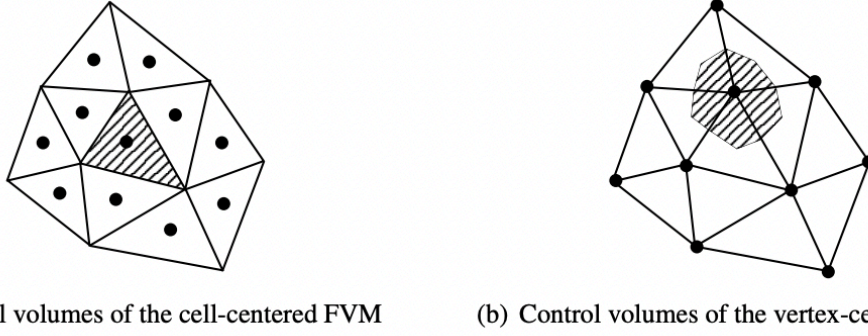


Figure 3.5 (a) cell-centered and (b) vertex-centered arrangements where the unknown variables are associated to the black nodes [202].

The governing equations (see section 2.3.1) describing the conservation of mass, momentum and energy are written in terms of specific quantities. The form of the general conservation equation for a scalar  $\varphi$  is expressed as:

$$\int \frac{\partial \rho \varphi}{\partial t} dV + \int \nabla \cdot (\rho \mathbf{u} \varphi) dV - \int \nabla \cdot (\Gamma^\varphi \nabla \varphi) dV = \int Q^\varphi dV \quad 3.5$$

where  $\frac{\partial \rho \varphi}{\partial t}$  is the transient term,  $\nabla \cdot (\rho \mathbf{u} \varphi)$  the convective term,  $\nabla \cdot (\Gamma^\varphi \nabla \varphi)$  the diffusion term, and  $Q^\varphi$  the source term [179].

Following the integration of the governing equations over the finite volumes and for a steady state form, in which case the transient term is removed (equation 3.6), the volume integrals are transformed using the Gauss theorem into surface integrals for the convection and diffusion terms of the conservation equation (equation 3.7) [179]. The Gauss simply states that the outward flux of a vector field through a closed surface is equal to the volume integral of the divergence over the region inside the surface.

$$\int_\Omega \nabla \cdot (\rho \mathbf{u} \varphi) d\Omega = \int_\Omega \nabla \cdot (\Gamma^\varphi \nabla \varphi) d\Omega + \int_\Omega Q^\varphi d\Omega \quad 3.6$$

$$\int_S (\rho \mathbf{u} \varphi) \cdot dS = \int_\Omega (\Gamma^\varphi \nabla \varphi) \cdot dS + \int_V Q^\varphi dV \quad 3.7$$

Integration points are used along the surface (for the convection and diffusion fluxes), or volume (for the source term), of the elements, in which the discrete form of the surface and volume integrals are numerically integrated, and the number of points affect the accuracy of the solution. The majority of finite volume methods use a single integration point for a simple mean value integration, allowing a second-order accurate approximation, which is found adequate in terms of accuracy and computational cost for most biofluid mechanics problems. Increasing the number of points along the surface or volume of the element, increases the accuracy of the solution, respectively [179]. Once the convection and diffusion fluxes and the source term are discretised with a specified number of integration points, the next step in the discretisation process is to convert the finite volume equations of each element into an algebraic equation and relate the face and volume fluxes with the values of the variables of the neighbouring cells. Flux linearisation is used in the second discretisation process and the evaluation of the fluxes depends on the boundary conditions assumed.

#### 3.1.2.4 Properties of Numerical Methods

During the discretisation process, there are properties that the user must consider to ensure that the numerical solution obtained is accurate [200], [203]. These properties are introduced below and are presented in more detail in the book by Moukalled et al. (2016) [179]:

- Conservation: for the numerical solution to be realistic, the numerical scheme should respect the conservation laws discussed in section 2.3.1.
- Accuracy: the numerical solution should be as close as possible to the exact solution. However, in many cases the exact solution to the problem is unknown and a direct comparison between the obtained and exact solution cannot be made.
- Convergence: the numerical solution converges as it tends towards the true analytical solution. Starting with an initial guess, solutions are obtained by repeatedly applying a solution algorithm with the solution at the end of an iteration used as an initial guess for the following iteration. Ideally, a solution is converged when the value does not change with further iterations. In reality, a solution is considered converged when changes between two consecutive iterations fall below a certain quantity. Often, the term “converged” is also used when a solution is independent of further mesh refinement.

- Consistency: refers to a condition on the Numerical Scheme, and the approximation scheme must tend towards the differential equation when both spatial and time steps tend to zero.
- Stability: refers to a condition on the Numerical Solution. The numerical errors must be bounded during the computational iteration process. Essentially, the error between the computed solution and the exact solution of the discretised equation should be minimal.

### 3.1.3 Implicit and Explicit Methods

The numerical scheme used to solve the equations in each of the discretised elements can be either implicit or explicit. In an explicit numerical method, the dependent variables are computed directly via already known values. In this case any discretisation operator can be directly evaluated based on the actual variable values. On the other hand, in an implicit numerical method the dependent variables are treated as unknowns and assembled to form a coupled set of equations which are then solved via numerical tools using either a direct or an iterative solution algorithm [179]. In computational fluid dynamics, the nonlinear conservation equations are often solved using the implicit approach. While implicit methods are more complex and computationally expensive, they facilitate larger time steps and are known to be more stable [179].

## 3.2 Cardiovascular Computational Fluid Dynamics Methodologies

In section 3.1 the general principles of computational modelling were discussed which are applicable to any industry. Building on this understanding, this section will introduce further methodologies which should be considered when modelling cardiovascular flows.

### 3.2.1 Zero-, One-, Two-, and Three-Dimensional Models

In computational fluid dynamics, the domain can be defined by zero- (0D), one- (1D), two- (2D) or three- (3D) dimensional models. The appropriate dimensionality in a model representation depends on the aims and required accuracy of the numerical problem. Zero-dimensional, or lumped-parameter, models are based on simplified representations of the cardiovascular system and generally feature the major components such as the heart and heart valves. These models are governed by ordinary differential equations, and assume a uniform

distribution of pressure, flow, and volume at any instant in time. Modelling the cardiovascular system using 0D-models is analogous to a hydraulic electric system where the volumetric blood flow rate is represented by an electric current. Both Kirchhoff's current law and Ohm's law are used in 0D-modelling for the conservation of mass and momentum. Kirchhoff's current law states that the current entering a node must be equal to the sum of currents exiting the node, while Ohm's law states that the current in an electric circuit is equal to the voltage divided by the resistance.

The first and most simple 0D model is the two-element Windkessel model which describes the haemodynamics of the arterial system in terms of resistance and compliance [204]. Since the introduction of the two-element Windkessel model in 1899, further models have been introduced. This includes the three-element Windkessel model, which has an additional resistor, and the four-element Windkessel model, which has an additional inductor [205], [205], [206], [207].

One-dimensional models use the conservation of mass and momentum to describe the blood flow using the 1D form of the Navier-Stokes equations in combination with equations for the forces acting on the vessel wall. They are most often used to represent wave transmission and to improve the boundary conditions for 3D models in order to capture arterial wave reflections [208]. The unstressed radius of the domain, the length and the wall thickness of the vessel and the Young's modulus are the initial parameters needed, while the radius of the vessel, pressure and flow are information that can be obtained from the 1D analysis [209].

Two-dimensional and three-dimensional models are governed by the partial differential Navier-Stokes equations. Two-dimensional models provide information on the radial variation of local flow in an axisymmetric domain, while three-dimensional models predict flow in all directions [208]. Such higher dimensional models can predict in more detail the haemodynamic parameters of the vessels, but due to the higher complexity, modelling is usually limited to smaller segments [210]. In cardiovascular modelling, the gold standard models are three-dimensional, patient-specific models, which are reconstructed from clinical imaging data.

### 3.2.2 Image-based Models

Cardiac imaging modalities enable the acquisition of cardiac images which can be used to reconstruct the computational domain based on a patient's anatomy. The most common modalities for obtaining cardiac images of the heart and surrounding blood vessels are magnetic resonance imaging (MRI) and computed tomography (CT). Cardiac computed tomography uses multiple x-ray beams from a CT scanner at various angles to create cross-sectional images. The x-ray beams pass through the body and are collected by a detector array that can generate an image. Depending on the path of the beam through tissues of varying densities, a grey scale is created where bone appears white, air black, and blood various shades of grey. To better differentiate the cardiac chambers from the vascular structures, contrast is often used. These images can also be used to produce a three-dimensional image of the heart [211]. In cardiac magnetic resonance imaging, an MRI machine creates a magnetic field and alters the spin of the protons present in hydrogen molecules. Depending on the surroundings, the frequencies of the spins change. These frequencies are detected, and an image is reconstructed. The cardiac structure is very well-visualized with MRI, and the contrast between tissue and vasculature is more pronounced than in CT images.

The clinical images obtained are a stack of two-dimensional slices, with each slice consisting of a matrix of pixels with different intensities of a grayscale value. To segment the area of interest from these images, open-access or commercial software can be used which employ automatic, semi-automatic or manual segmentation tools. The Insight Segmentation and Registration Tool Kit, ITK-Snap ([www.itksnap.org](http://www.itksnap.org)), SimVascular ([www.simvascular.github.io](http://www.simvascular.github.io)) and Mimics ([www.materialise.com/en/healthcare/mimics-innovation-suite/mimics](http://www.materialise.com/en/healthcare/mimics-innovation-suite/mimics)) are some of the most frequently used modalities. In manual segmentation, the user progresses slice-by-slice and draws the region of interest with suitable tools. In semi-automatic segmentation, ITK-Snap implements the Geodesic Active Contours [212], [213] and the Region Competition methods [214]. In this work, semi-automatic segmentation based on the Region Competition method was adopted, and the segmentation was manually checked slice by slice and corrected where appropriate. The segmented models were exported as surface mesh, using the marching cube algorithm that processes 3D medical data and creates triangle vertices of constant density surfaces using linear interpolation [215].

### 3.2.3 Coupled Models

Coupling of the 0D models to higher dimensional models was introduced in cardiovascular modelling in order to overcome one of the main limitations of zero pressure at the outlets of the models. 0D models can be coupled at the boundary outlets to represent, with reduced complexity, the downstream peripheral circulation which is neglected in the 3D modes [210]. Applications of this methodology can be found in many studies, especially in cases of virtual surgeries, to test different surgical plans and optimise the anatomical configuration of the region. Several studies of univentricular circulation and cavopulmonary anastomosis, a congenital heart disease where one ventricular chamber is absent and an operation is performed to bypass the absent ventricle, named cavopulmonary anastomosis, have utilised such methods [216], [217], [218], [219], [220], [221]. Nevertheless, lower- order models can be coupled either upstream or downstream of the higher-order models, depending on the availability of data, and the information to be acquired through the model [222].

#### 3.2.3.1 Fluid Structure Interaction

Fluid structure interaction (FSI) refers to the co-simulation of a fluid and a solid structure. In cardiovascular modelling, it can be used to simulate the motion of the vascular walls or the heart valves [130]. Although it has been found that neglecting vessel compliance the regional shear stress is overestimated [223], it is more computationally expensive, and the vessel's mechanical properties, need to be specified [224].

FSI simulations require the coupling of the fluid and the solid domain, and two of the most well-known techniques adopted are the Arbitrary Lagrangian Eulerian (ALE) and the Immersed Boundary Method (IBM). A brief description of each method is provided here, but more details can be found on Donea et al., 2004, and Peskin, 1972, for the ALE and IBM methods, respectively [225], [226].

The ALE method is a body-fitted, also known as body-conforming method, where a structured/unstructured mesh is generated, with the grid being updated in each time step. The fluid domain is moving according to the motion of the vascular interface, and therefore the Navier-Stokes equations need to be solved on a moving reference system. For the solid domain, the equations are usually solved based on a Lagrangian reference system. Finally, the flow for

the grid points of the fluid domain which are not at the interface with the moving solid domain need to be defined [227], [228].

There are two approaches for solving FSI problems, the monolithic (or non-modular) and the partitioned (or modular). In the partitioned approach, the equations governing the fluid and the solid domain are solved separately, allowing more specialised solvers to be used for each domain. However, a coupling algorithm is required to allow the interaction of the two and the acquisition of a solution for the coupled problem. These algorithms exhibit stability issues and poor convergence due to the “added mass effect”, related to the mass density of the fluid versus the solid structure. In the monolithic approach, the fluid and the solid equations are solved simultaneously, which has the advantage of stability and faster solution of the problem [130], [228], [229].

The IBM was introduced by Peskin (1972) and is a non-body-fitted, also known as fixed-grid method which does not require the computational grid of the fluid domain to be changed or deformed [226]. IBM instead uses two sets of independent grids, a fixed Eulerian and a moving structured or unstructured grid, for the fluid and the solid domains, respectively. The advantage of this method is that it does not involve the update of the mesh and therefore, is more effective in handling arbitrarily large deformations. Additional external forces are incorporated in the governing equations of motion to account for the moving body in the fixed computational domain [226]. Some of the challenges are related to the application of boundary conditions and the more accurate definition of the moving body. In addition, IBM requires increased spatial resolution due to the delta function which is introduced to avoid numerical instabilities [230]. The immersed interface method [231] and the hybrid Cartesian/immersed boundary method are two approaches to overcome these limitations [232].

### **3.3 Reminder of Thesis Outline**

As a reminder, in this chapter the computational fluid dynamic methodology was explained in detail to provide the reader with the background theory to the following chapters (4-6) in this thesis.

## Chapter 4

# Morphological Characterisation of Turner Syndrome Aorta

In this chapter, the work detailed in “Morphological Characterisation of Paediatric Turner Syndrome Aortae: Insights from a small cohort study” is presented. This work was published in the Medical Engineering and Physics Journal (doi: 10.1016/j.medengphy.2023.104045), with co-authors Asimina Kazakidi (Department of Biomedical Engineering, University of Strathclyde), Ruth Allen and Avril Mason (Royal Hospital for Children, Queen Elizabeth University Hospital).

### 4.1 Abstract

Cardiovascular disease, either congenital or acquired, is widespread in girls and women living with Turner syndrome (TS) today and is a major reason for premature death in this population. The evaluation of aortic diameter and other morphological dimensions is the established clinical practice for cardiovascular risk assessment in TS. However, risk evaluation using the current guidelines have seen life-threatening aortic events occurring at dimensions classified within the normal threshold. In this study, we aim to characterize the aortic geometries of Turner syndrome children, in comparison to age-matched healthy counterparts, and to evaluate various morphological parameters, such as diameter, curvature, and torsion. The aortic geometries were reconstructed in three-dimensions (3D) from cardiac imaging data, and the aortic centrelines were identified to determine morphological differences between TS and healthy aortae. It was found that the Turner syndrome girls had overall greater values in ten out of fifteen parameters examined (although not statistically significant,  $p > 0.05$ ), as compared to the healthy children: the aortic arch height and width; the ascending aorta, aortic arch (2 locations), and descending aorta diameters; the ratio of the ascending to descending aorta diameter; average curvature; average torsion; and average curvature-torsion score. These parameters may explain the abnormal haemodynamics seen previously in some of the Turner syndrome patients, as reported in Johnston et al. 2021, namely vortical flow, flow separation,

and flow disturbances, when compared to anatomically normal aortae [6]. In addition, within the TS group, a significant association was found between body surface area and arch height ( $p = 0.03$ ), as well as the arch height to width ratio ( $p = 0.05$ ). A significant association was also found between aortic arch diameter and both body surface area ( $p = 0.04$ ) and weight ( $p = 0.04$ ). No significant association ( $p > 0.05$ ) was found between any morphological parameter and systolic blood pressure. The results of this study contribute to an improved understanding of the morphological parameters affecting the haemodynamic environment in TS, and the clinical assessment of the increased cardiovascular risk in this population.

## 4.2 Introduction

Turner syndrome females have an increased predisposition for hypertension, atherosclerosis, and obesity, and Turner syndrome itself has been proposed as an independent risk marker for cardiovascular disease. In fact, approximately half of TS women are born with a congenital cardiovascular defect [18], [19], [20]. The spectrum of congenital heart disease ranges from minor abnormalities to severe and highly complex disorders, predominantly involving the left side of the heart. Throughout the literature of Turner syndrome children (aged 2-19 years), the most common congenital heart defects were bicuspid aortic valve (29%), a dilated ascending aorta (19-22%), and aortic coarctation (11%) [22], [233]. Congenital abnormalities of the aorta are discussed in more detail in a previous publication of ours [234]. Turner syndrome is associated with substantial morbidity, and a 3-fold (standardised mortality ratio, SMR = 3.0) higher mortality rate than the general population [2], [70], with cardiovascular disease accounting for approximately half of all deaths [69]. Even when congenital heart disease is excluded, there remains an excess mortality attributable to acquired cardiovascular disease [2], [70]. Hypertension, the most easily treatable cardiovascular risk factor, is also exacerbated in Turner syndrome due to an underlying predisposition to metabolic abnormalities such as diabetes and obesity [63].

Given the increased prevalence of cardiovascular disease in TS, clinical guidelines recommend a thorough cardiovascular examination of the heart and aorta at diagnosis, [1]. Non-invasive cardiac imaging modalities, namely, transthoracic echocardiography (TTE), cardiovascular magnetic resonance imaging (CMR), and computed tomography (CT), are used to identify, diagnose, and monitor structural abnormalities of the heart. If initial imaging is normal, then NHS guidelines suggest this should be repeated every 5 years in children and every 10 years

in adults [1]. If there is evidence of abnormalities such as bicuspid aortic valve, coarctation of the aorta, or dilatation of the ascending thoracic aorta, then annual imaging or follow-up imaging is advised [235]. Cardiovascular screening is also recommended when the patient is transitioning from paediatric to adult care, is considering pregnancy, or has suspected hypertension [1], [9].

Despite European [236] and American [1] guidelines, the cardiovascular risk stratification in Turner syndrome is challenging [237]. For example, aortic dissection (AoD), a severe cardiovascular complication that occurs more frequently and at a younger age in Turner syndrome females, has been described in TS girls as young as 4 years of age [238]. Currently, the aortic size index (ASI = aortic diameter (cm)/body surface area (m<sup>2</sup>)) is the primary method for estimating aortic dissection probability in TS patients and is routinely employed for clinical and operative decision making. In adult women (> 18 years of age) with TS, the proposed threshold for aortic dissection risk is an ascending ASI greater than 2.5 cm/m<sup>2</sup> [51], [239]. However, the characteristic short stature seen in TS complicates the assessment of AoD risk as the relationship of body size to aortic dimensions is different in Turner syndrome compared to the general population. ASI is also age-dependent and has been proven unreliable in younger children, with or without TS, due to the non-constant variance associated with rapid somatic growth [240]. In fact, ASI in the ascending aorta is often >2.5 cm/m<sup>2</sup> in healthy girls with TS. Other studies predict AoD risk using the ratio of ascending to descending aortic diameter, with a value of > 1.5 indicating aortic dilatation [241]. However, this method does not consider that the descending aorta may be abnormal in TS females.

Cardiovascular risk assessment and prediction using the current guidelines has seen life-threatening aortic events occurring at dimensions classified as normal according to conventional size criteria [12]. This is due to a limited understanding of the pathophysiology of cardiovascular disease in TS and unreliable markers to predict cardiovascular risk. Among the list of cardiovascular research priorities in TS specified by the American Heart Association were to: “characterize the most accurate tool to define aortic enlargement and aneurysm”, “characterize the most accurate approach to measure the aortic diameter”, and “characterize and reduce the risk for aortic dissection with aortic enlargement in TS, including the use of specific biomarkers and functional imaging tools” [1]. Prior to the American Heart Association 2018 statement, other authors had identified the importance of fully characterising the

cardiovascular anatomy in TS patients [22]. Therefore, in this study we aim to perform morphometric analysis to obtain a comprehensive set of geometric parameters for a dataset of eight Turner syndrome, and four healthy, paediatric patients. The goal is to characterize the three-dimensional aortae of Turner syndrome children to improve our understanding of cardiovascular disease in this population.

### 4.3 Materials and methods

In the following work, Full Ethical approval was awarded by the UK Health Research Authority (IRAS Project ID: 252,866, REC Reference: 18/LO/2052).

#### 4.3.1 Patient Cohorts

Ethical approval was obtained for a retrospective review of patients attending the paediatric Turner syndrome clinic at the Royal Hospital for Children, Queen Elizabeth University Hospital, Glasgow, UK (see appendix 3-4). To be considered for this study, the patient had to have karyotypically proven Turner syndrome and retrospective cardiac imaging data obtained before the age of 18 years. Eight patients ( $n=8$ ,  $14.3 \pm 2.1$  years, mean  $\pm$  standard deviation) were identified that met the criteria (Table 4.1). Three patients were identified as having previous surgical intervention, none of which affected our analysis of aortic morphology: in TS3 the aortic operation (to repair neonatal coarctation) took place a decade prior to scanning for the present study, and in TS4 and TS5 the operation was related to vessels not including the aorta. Patient-specific volumetric image and geometrical data from four ( $n=4$ ) gender- and age-matched ( $12.5 \pm 5.8$  years, mean  $\pm$  standard deviation) females was purchased from the Vascular Model Repository ([www.vascularmodel.com](http://www.vascularmodel.com)). These models had no aortic abnormalities, and although BMI and blood pressure information was not provided, it is expected that these were within the normal range of a healthy child.

Of all TS girls, four were of a normal weight (TS3, TS5, TS6, TS8), one was overweight (TS1), and three were obese (TS2, TS4, TS7). All but one (TS6) Turner syndrome girl had some form of aortic arch abnormality, when including the anatomy of the supra-aortic vessels. These were ascending aorta dilatation (TS1 and TS8), elongated transverse arch (TS2 and TS7), coarctation of the aorta (TS3), common origin of the brachiocephalic and left common carotid branches (TS4) (bovine arch), a triangular-shaped ‘gothic’ arch (TS5), and an aberrant right subclavian

artery, arising from the posterior arch, distal to the left common carotid artery (TS7). In TS3, the left subclavian artery was not visible due to neonatal coarctation repair which involved a left subclavian flap aortoplasty. An abnormal bicuspid aortic valve was reported in TS1, TS6, TS7 and TS8, accounting for half of the girls.

Table 4.1. Healthy and Turner syndrome baseline characteristics. Data shown as mean  $\pm$  standard deviation. Hypertension was defined as systolic blood pressure  $\geq$  95<sup>th</sup> percentile for patient age and height. BMI category defined as normal weight (0 – 85<sup>th</sup> percentile), overweight (86<sup>th</sup> – 95<sup>th</sup> percentile), and obese (>95<sup>th</sup> percentile). \*Information available for one healthy patient only from the Vascular Model Repository ([www.vascularmodel.com](http://www.vascularmodel.com)).

	<b>Healthy (n = 4)</b>	<b>Turner syndrome (n = 8)</b>
<b>Age (years)</b>	12.5 $\pm$ 5.8	14.3 $\pm$ 2.1
<b>Height (cm)</b>	146*	142.4 $\pm$ 5.1
<b>Weight (kg)</b>	40.1*	54.2 $\pm$ 20.7
<b>BSA (m<sup>2</sup>)</b>	1.2*	1.4 $\pm$ 0.2
<b>BMI</b>	19*	26.5 $\pm$ 9.1
<b>Normal weight</b>	4 (100%)	4 (50.0%) [TS3, TS5, TS6, TS8]
<b>Overweight</b>	0 (0.0%)	1 (12.5%) [TS1]
<b>Obese</b>	0 (0.0%)	3 (37.5%) [TS2, TS4, TS7]
<b>SBP (mmHg)</b>	-	115 $\pm$ 15
<b>DBP (mmHg)</b>	-	66 $\pm$ 13
<b>Hypertensive</b>	0 (0.0%)	2 (25.0%) [TS4, TS8]
<b>Bicuspid aortic valve</b>	0 (0.0%)	4 (50.0%) [TS1, TS6, TS7, TS8]
<b>Dilatation</b>	0 (0.0%)	2 (25.0%) [TS1, TS8]
<b>Coarctation</b>	0 (0.0%)	1 (12.5%) [TS3]
<b>Elongated arch</b>	0 (0.0%)	2 (25.0%) [TS2, TS7]
<b>Gothic arch</b>	0 (0.0%)	1 (12.5%) [TS5]
<b>Unconventional branching</b>	0 (0.0%)	2 (25.0%) [TS4, TS7]

#### 4.3.2 Image Acquisition and Geometry Segmentation

Retrospective, anonymous, cardiac imaging data was obtained from each of the Turner syndrome girls outlined in section 4.3.1. All cardiac imaging was performed between 2014-2018 on either a 1.5 Tesla diagnostic magnetic resonance imaging (MRI) scanner (MAGNATOM Aera/Avanto, Siemens Healthcare, GmbH), or a diagnostic revolution computed tomography (CT) scanner (GE Healthcare). Raw files in the digital imaging and

communications in medicine (DICOM) format were then exported into ITK-SNAP software ([www.itksnap.org](http://www.itksnap.org)) for segmentation.

Image segmentation of the aorta from the cardiac imaging data was performed using the semi-automatic active contour-based algorithm implemented in ITK-SNAP. The aortic geometries were reconstructed such that only the ascending aorta (from above the location of the aortic root), aortic arch, descending aorta (to the end of the thoracic aorta), and the supra-aortic branches (brachiocephalic, left common carotid, and left and right subclavian branches) were kept. The output from the automated segmentation was visually inspected slice by slice and any artifacts were corrected with the manual segmentation tool within ITK-SNAP. This same methodology has been applied previously to segment aortic geometries from cardiac imaging data [6], [242]. After segmentation, the surface models (stereolithography (STL) file-format) were smoothed in Autodesk Meshmixer ([www.meshmixer.org](http://www.meshmixer.org)) to remove surface artefacts, particularly staircase artefacts which occur due to subsampling of the voxel grid.

## 4.4 Morphometric Analysis

### 4.4.1 Geometric Centreline

Morphometric analysis was performed for all aortic geometries within the Vascular Modelling Toolkit (VMTK) ([www.vmtk.org](http://www.vmtk.org)) software [243], an open-source collection of tools and libraries intended for geometric analysis of blood vessels. VMTK has previously been used to characterise geometrical changes in longitudinal studies of adults with Turner syndrome [244] and abdominal aortic aneurysms [245]. First, the geometric centreline was generated as this provided the baseline for three-dimensional analysis. In VMTK, the centreline is automatically extracted in the form of a set of discrete points in space (computed as the centres of maximal spheres inscribed in the vessel lumen) between the source and target point(s). In the case of the aorta, the centreline was computed from the ascending aorta (the source point) to the descending aorta (target point) using automatic end point detection (Figure 4.1A). Piccinelli et al. (2009) provide a more detailed description of the methodology used to estimate centrelines [246]. Before any analysis can be performed, the centreline coordinate data requires smoothing to remove any spurious values which may have been present as an artefact of voxel size or the segmentation process. Current approaches include the inbuilt VMTK centreline smoothing tool which employs a moving average filter and was employed in Turner syndrome aortae by

Subramaniam et al. [244], or the fitting of splines, specifically regression splines, as used by Gallo et al. [242] in the aorta of patients with diastolic dysfunction. In our case, smoothing of the vessel centreline was undertaken in MATLAB<sup>®</sup>, using a similar method to Gallo et al [242], by fitting a smoothing spline to the data which is a piecewise polynomial defined by a smoothing parameter value between 0 and 1.

#### 4.4.2 Morphological Parameters

Morphometric analysis was performed for the full aortic geometry, and for anatomical subregions defined in the following paragraph (Figure 4.1). Analysis of all parameters was performed in VMTK, unless otherwise stated. First, colourmaps of the Euclidean distance, defined as the distance between the centreline and lumen wall, were computed. The Euclidean distance is useful in that it provides visual information on the dimensional (circumferential and axial) variation within and between patients. Previous studies have also employed this variable to visualize aortic growth in Turner syndrome women [244] and patients with small abdominal aortic aneurysms [245]. Single values were then computed for two- and three-dimensional parameters: vessel volume (V), surface area (SA), centreline length (l), arch height ( $H_{\text{arch}}$ ), arch width ( $W_{\text{arch}}$ ), and the subsequent ratio of height to width ( $H_{\text{arch}}/W_{\text{arch}}$ ) (Figure 4.1). Arch width was defined as the distance between the two centrelines in the ascending and descending aorta, at the cranial edge of the pulmonary artery, and height as the distance between the imaginary line  $W_{\text{arch}}$  and the peak centreline point in the arch (Figure 4.1B). Arch height and width are often computed in morphological studies of the aorta [247], [248], [249]. Finally, vessel curvature (k) and torsion ( $\tau$ ) were calculated, which at a given point on the centreline are the inverse of the radius of the osculating circle and the local deviation from the osculating plane, respectively. In other words, curvature measures the deviation of the centreline from an imaginary straight line, while torsion measures how sharp the centreline twists in 3D space [246], [250].

$$k = \frac{|C'(s) \times C''(s)|}{|C'(s)|^3} \quad 4.1$$

$$\tau = \frac{|C'(s) \times C''(s) \cdot C'''(s)|}{|C'(s) \times C''(s)|^2} \quad 4.2$$

where C is the centerline curve and s the curvilinear abscissa, while C' and C'' indicate the first and second derivatives of the curve with respect to the curvilinear abscissa. Both parameters are of interest considering their influence on the haemodynamics in the vasculature

[251], [252], [253], [254]. A third parameter which accounts for both curvature and torsion simultaneously is the combined curvature score (CC) proposed by O’Flynn [255]:

$$CC = \sqrt{k^2 + \tau^2} \quad 4.3$$

Computation of the vessel curvature, torsion, and combined curvature score is performed for every point along the centreline length; therefore, results were presented as minimum, maximum, and mean values. In addition, vessel tortuosity (T) defined as the ratio between centreline length (l) and the Euclidean distance between endpoints (d) was given as a single value for each geometry:

$$T = \frac{l}{d} - 1 \quad 4.4$$

For a more detailed, regional, analysis, the centreline length was divided at five locations relative to the individual model inlet diameter ( $D_{inlet}$ ) and local landmarks (Figure 4.1A). These were: in the ascending aorta, midway between the inlet and the aortic arch ( $D_{asc}$ ); at the entrance to the aortic arch, proximal to the origin of the brachiocephalic branch ( $D_{bca}$ ); in the transverse arch, midway between the left common carotid and left subclavian branches ( $D_{trans}$ ); at the aortic isthmus, distal to the left subclavian branch ( $D_{isth}$ ); and in the descending aorta, one inlet diameter downstream from the left subclavian branch ( $D_{desc}$ ). The ascending aorta (AscAo) was defined as the region between the model inlet and  $D_{bca}$ , the arch as the region between  $R_{bca}$  and  $R_{isth}$ , and the descending aorta (DescAo) as the region from  $R_{isth}$  to the model end. The average and maximum values for diameter, curvature, torsion, and the combined curvature score were compared at each of these three regions.

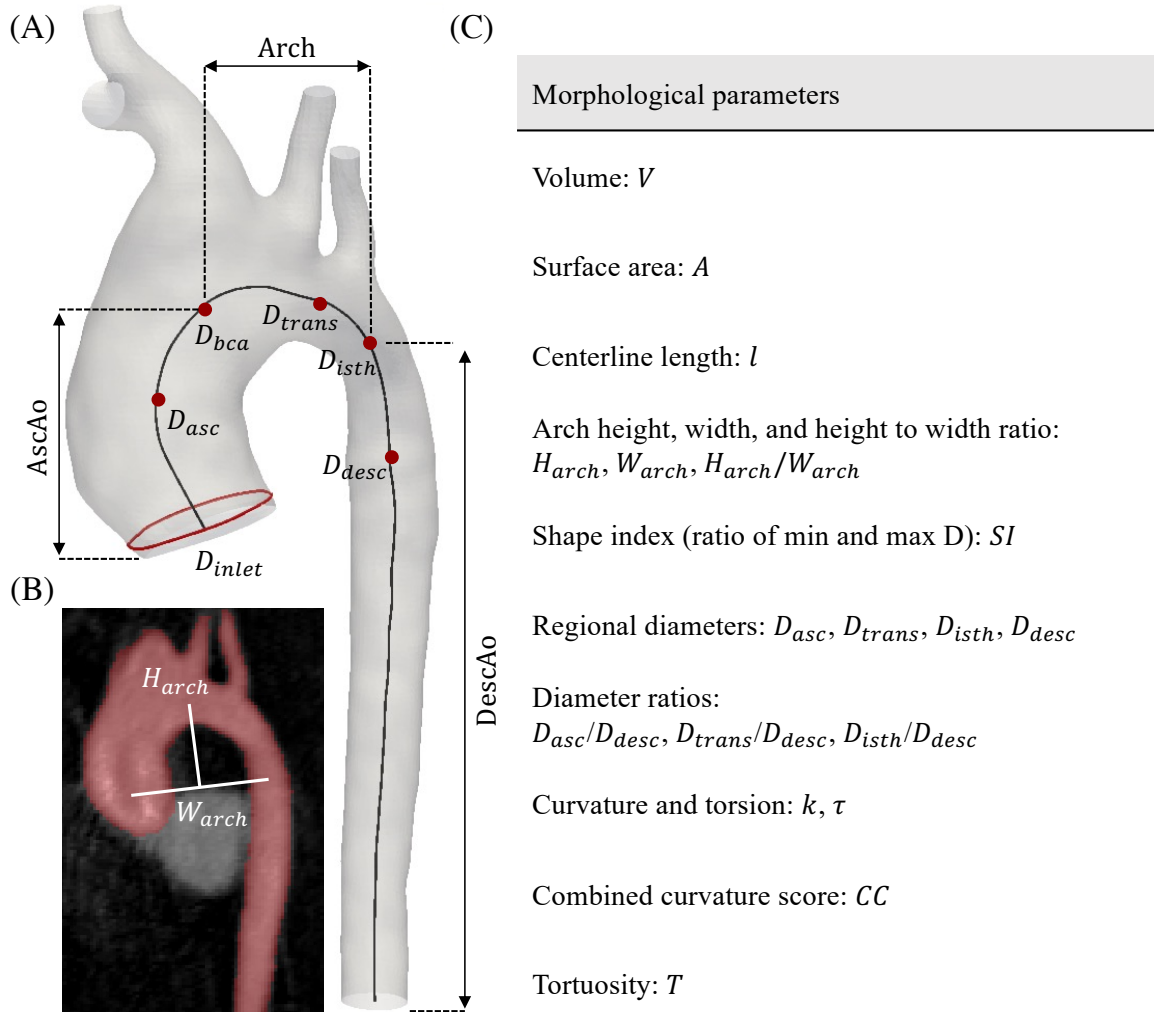


Figure 4.1 Morphometric parameters exemplified (A, B) and listed (C) for the three-dimensional aorta of TS1. (A) Model centreline shown with regional points  $D_{asc}$ ,  $D_{bca}$ ,  $D_{trans}$ ,  $D_{isth}$ , and  $D_{desc}$  as described in the text. (B) MRI slice showing the location of the arch width ( $W_{arch}$ ) and height ( $H_{arch}$ ) measurements, taken relative to the cranial edge of the pulmonary artery. (C) List of full morphological parameters.

#### 4.4.3 Statistical Analysis

Statistical analysis (Table 4.2) was performed on the morphometric parameters using OriginPro (version 2021b, OriginLab Corporation, USA) and Minitab Express (version 1.5.3, Minitab Inc, USA) software. To test for differences between the healthy and Turner syndrome groups, the univariate Mann–Whitney non-parametric U test was applied with the Significance level set at  $\rho \leq 0.05$  [242]. This was chosen as the sample size was small, and the data was not normally distributed. As multiple analyses were performed for the same sample of data, the

Bonferroni correction was considered, but not deemed necessary as few results were statistically significant. For the Turner syndrome group only (due to a lack of data for the healthy girls), Pearson's correlation analysis was performed with the measured geometric parameters indexed to both body mass index (BMI) and body surface area (BSA).

#### 4.5 Results

The complete set ( $n=12$ ) of in-scale three-dimensional aortic geometries is presented in Figure 4.2A. The surface of the geometries is coloured according to the Euclidean distance (the distance between the centreline and the lumen wall) which allows for a direct visual comparison of the vessel radius. As expected, and true for all geometries, the aortic diameter was greatest in the ascending aorta region and smallest at the aortic branches. The ascending aortic diameter was profoundly greater than the remainder of the aorta in TS1, TS6 and TS8. Note that TS1 and TS8 were diagnosed with aortic dilatation as per their clinical notes (Table 4.1). The maximum diameters seen within the healthy group ranged from 14.82 – 22.62 mm, whereas in the TS group these ranged from 17.72 – 32.56 mm (see Appendix 2). The vessel diameter was then plotted along the centreline length, where it was clear the healthy group (Figure 4.2B, H1-H4) displayed less variation in aortic diameter than the Turner syndrome group (Figure 4.2C, TS1-TS8). Among the healthy group, the largest variation in aortic diameter was seen in H2 ( $D_{\min} = 15.00$  mm and  $D_{\max} = 22.62$  mm), compared to an average variation of  $6.97 \pm 0.93$  mm ( $n=4$ , mean  $\pm$  standard deviation). Meanwhile in the TS group, the largest variation was seen in TS1 ( $D_{\min} = 12.72$  mm and  $D_{\max} = 32.56$  mm), compared to an average variation of  $10.27 \pm 4.67$  mm ( $n=8$ , mean  $\pm$  standard deviation).

For each individual, the three-dimensional curvature and torsion were visualized in Figure 4.3A and B respectively. Local curvature and torsion profiles highlight the non-uniformity and non-planarity of the aortic geometries. From Figure 4.3A, peak curvature values ( $0.05$  to  $0.1$   $\text{mm}^{-1}$  depending on the individual) were clearly concentrated in the ascending aorta and arch regions, distal to the aortic valve. For all geometries, low curvature values ( $< 0.05$   $\text{mm}^{-1}$ ) were found in the descending aorta (Figure 4.3A). Inversely, there appeared to be less measured torsion ( $\tau \sim 0$ ) in the proximal aorta (Figure 4.3B). This was especially true for the healthy girls (H1-H4). Peak minimum ( $0$  to  $-2$   $\text{mm}^{-1}$ ) and maximum ( $0$  to  $2$   $\text{mm}^{-1}$ ) torsion was predominantly visualized along the length of the descending aorta.

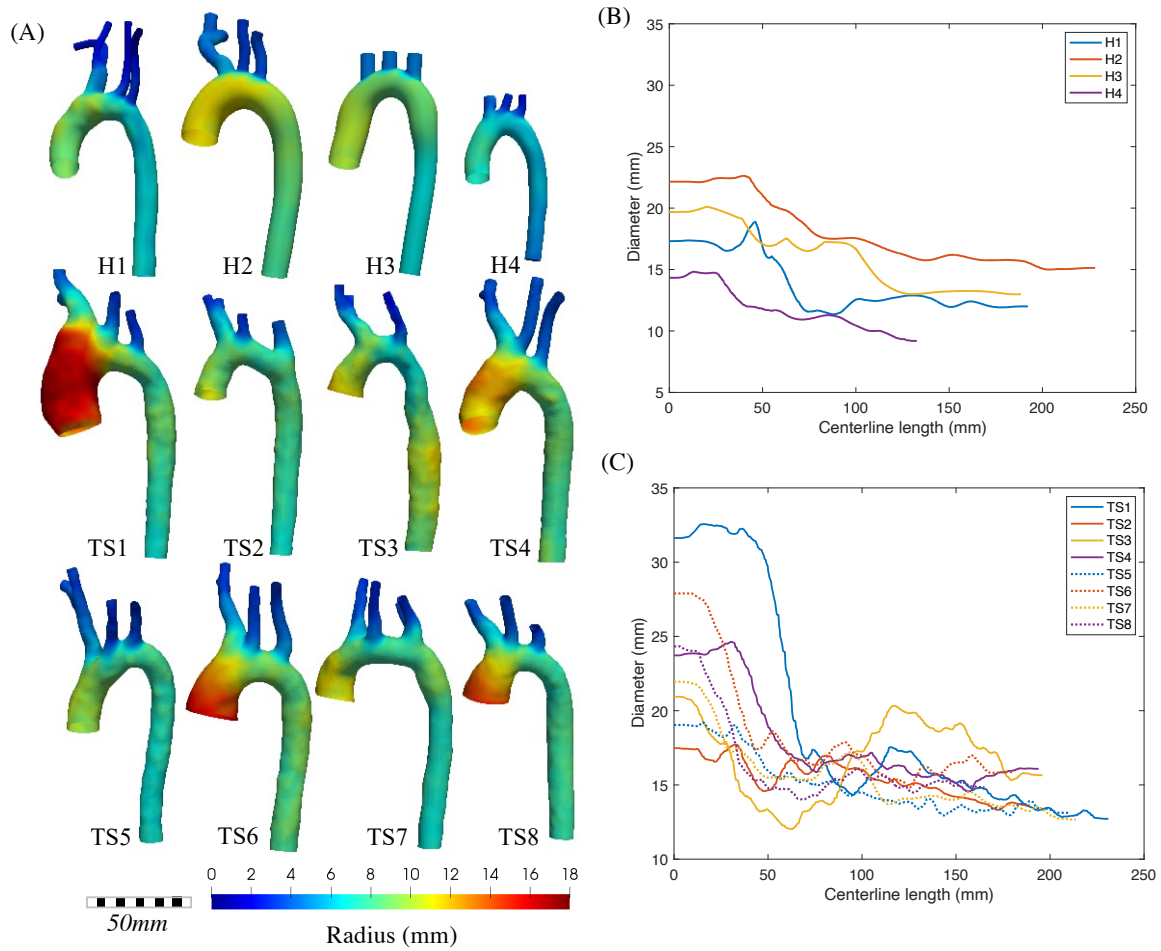


Figure 4.2 (A) Colourmap distributions of the aortic radius and (B-C) line plots of the aortic diameter for the (H1-H4) healthy and (TS1-TS8) Turner syndrome (TS) girls. Geometries in (A) are shown in scale. All values are in millimetres.

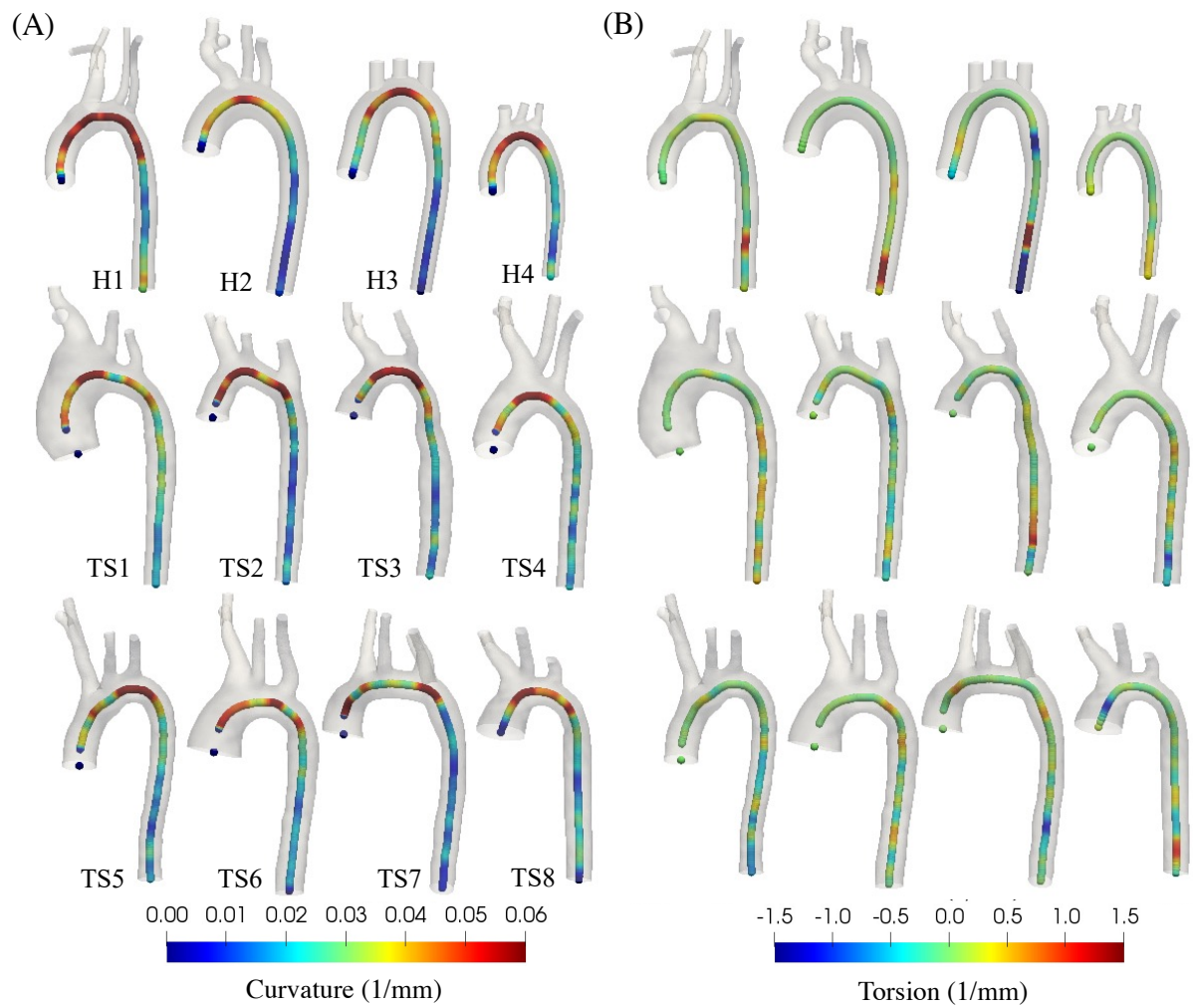


Figure 4.3. Anterior view of the (A) curvature and (B) torsion for the (H1-H4) healthy and (TS1-TS8) Turner syndrome girls. Geometries are in scale. All values are in millimetres<sup>-1</sup>.

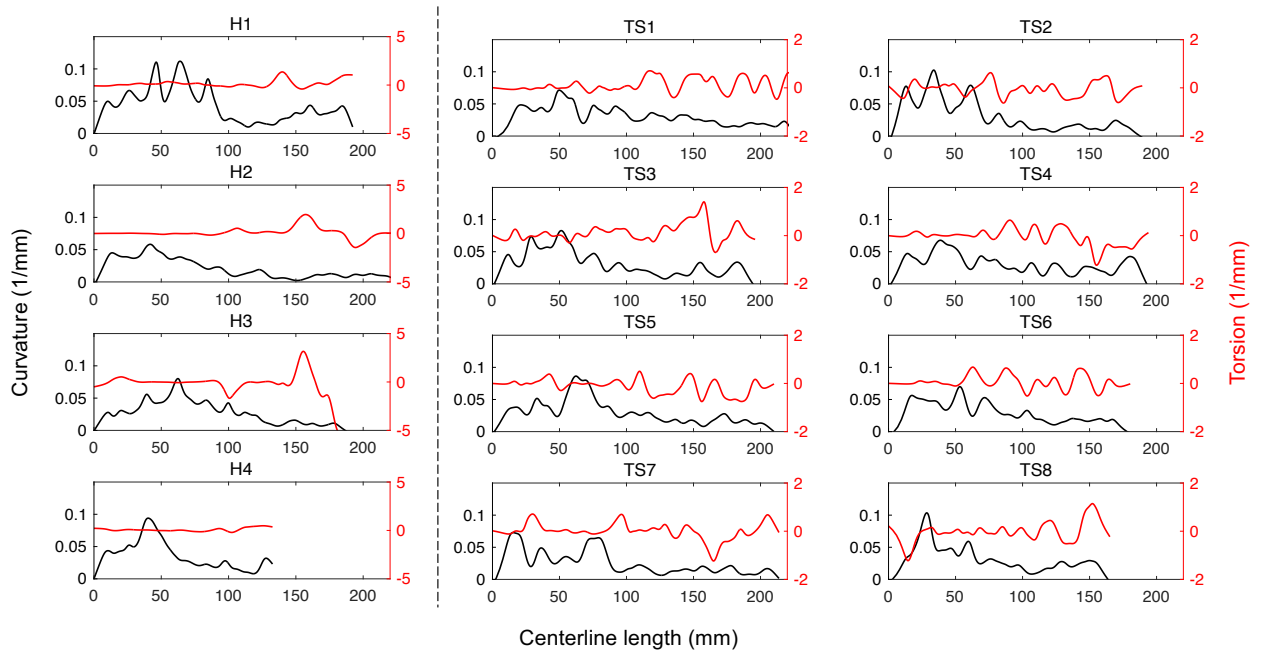


Figure 4.4. Plots of the curvature (black line, primary y-axis) and torsion (red line, secondary y-axis) along the centreline length for each healthy (H1-H4) and Turner syndrome (TS1-TS8) girl. Note the difference in the torsion scale between the healthy ( $-5$  to  $5$   $\text{mm}^{-1}$ ) and TS ( $-2$  to  $2$   $\text{mm}^{-1}$ ) groups.

To directly compare the healthy and Turner syndrome data presented in Figure 4.4, the diameter, curvature, torsion, and centreline length were non-dimensionalised. Aortic diameter was normalised with respect to the individual patient-specific inlet diameter, and centreline length, curvature, and torsion were normalised with respect to the maximum values. The average plus standard deviation was plotted for each group for the respective parameters: normalised diameter (Figure 4.5A), curvature, (Figure 4.5B), and torsion (Figure 4.5C). Figure 4.5A revealed a greater average normalised diameter among the healthy group, for all points along the centreline length. In other words, the average diameter throughout the aortic length was closer in value to the model inlet diameter for the healthy group. The difference between the two groups was most apparent in the ascending aorta and arch regions (normalised centreline length =  $0.2 - 0.4$ ) and least apparent in the descending aorta (normalised centreline length  $> 0.6$ ). The variation around the group average (i.e., the standard deviation represented by the shaded region) was far greater among the Turner syndrome group, indicating larger variances in aortic diameter between each girl. The average normalised curvature presented in Figure 4.5B shows a similar pattern for both patient groups: gradually increasing curvature directly distal to the aortic root (Figure 4.5B, normalised centreline length:  $0 - 0.1$ ), followed

by fluctuating higher curvature in the ascending aorta and arch (Figure 4.5B, normalised centreline length: 0.1 – 0.4), and fluctuating lower curvature in the descending aorta (Figure 4.5B, normalised centreline length = 0.4 – 1). The normalised curvature was greater, on average, for the TS girls in the ascending and descending aorta, but not in the aortic arch. Figure 4.5C presents the average pattern of normalised torsion, which was defined by small fluctuations around the zero value in the proximal aorta, and larger fluctuations in the distal descending aorta, for both patient groups. The average normalised torsion along the centreline length was predominantly greater for the healthy group, albeit both groups reached similar peak values for average torsion.

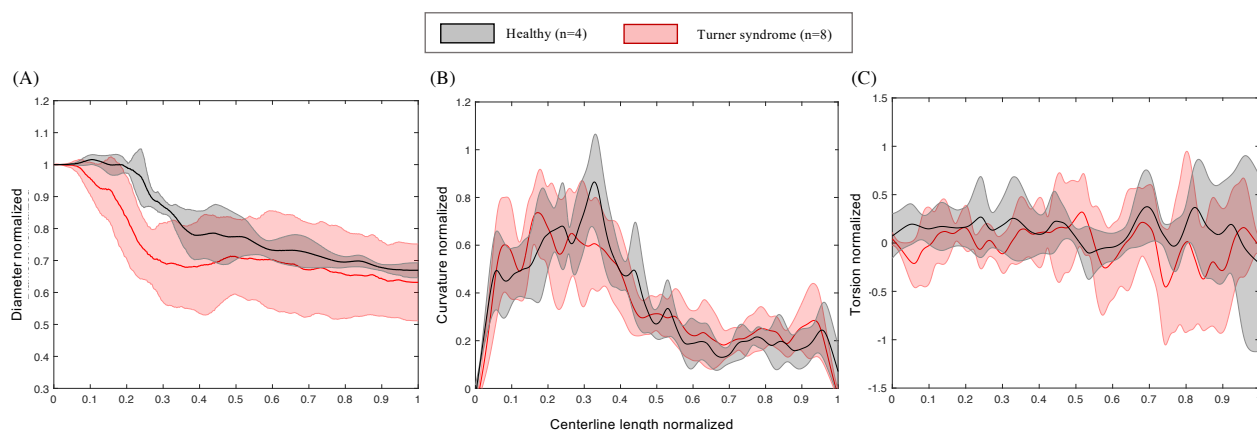


Figure 4.5. Non-dimensional, normalised, data for (A) diameter, (B) curvature, and (C) torsion, plotted against the non-dimensional normalised centreline length for the healthy and Turner syndrome groups. Group average and standard deviation represented by the solid line and shaded region respectively. Diameter normalised with respect to the model inlet diameter, and centreline length, curvature, and torsion normalised with respect to the maximum values for each parameter.

Statistical analysis was performed on three morphometric parameters known to influence haemodynamics, these being aortic diameter, curvature, and torsion (Figure 4.6). Specifically, the average and maximum diameter (Figure 4.6A, E), curvature (Figure 4.6B, F), torsion (Figure 4.6C, G), and the combined curvature torsion score (Figure 4.6D, H), at three regions along the aorta (ascending aorta, aortic arch, and descending aorta, as seen in Figure 4.1A), and along the full centreline length, were presented for both the healthy and TS groups. Boxplots allowed the differences between the two groups to be evaluated and are presented with the median (horizontal line), interquartile range (box), and values for 95% coverage of the

data (whiskers). Median average (Figure 4.6A) and maximum (Figure 4.6E) diameter were greater in the TS group along the entire centreline length, and for each individual region. Almost all (5-95% as indicated by plot whiskers) of the healthy diameters were within approximately 5 millimetres of the median value (Figure 4.6A, E), unlike in the TS group where variability of diameter values was clearly greater (in Figure 4.6A the ascending aorta and in Figure 4.6E the ascending aorta, aortic arch, and the full model). Median average curvature (Figure 4.6B) values were comparable between both groups at the ascending and descending aorta, and the full model. At the aortic arch region, median average curvature was marginally greater in the healthy group (Figure 4.6B: 0.05 vs 0.045 1/mm). In the plot of maximum curvature (Figure 4.6F), the median values were distinctly greater for the healthy group at all regions investigated except for the ascending aorta where the difference was only marginal. For both groups, the average and maximum curvature was greatest in the aortic arch. Both average and maximum values for torsion (Figure 4.6C, G) were greater for the healthy group at all regions considered with the exception of the average torsion in the ascending aorta (Figure 4.6C). For both groups, the greatest torsion was seen in the descending aortic region (Figure 4.6G). The distribution of combined curvature-torsion (CC) score followed a similar pattern for the average (Figure 4.6D) and maximum results (Figure 4.6H). That is, for the healthy group, the average and maximum CC values were greater at all regions considered. This difference was more pronounced in the descending region and for the full model, and less in the aortic arch and ascending aorta. The CC score results (Figure 4.6D, H) were dominated by the respective torsion (Figure 4.6C, G) values, which were substantially higher than the respective curvature values (Figure 4.6B, F).

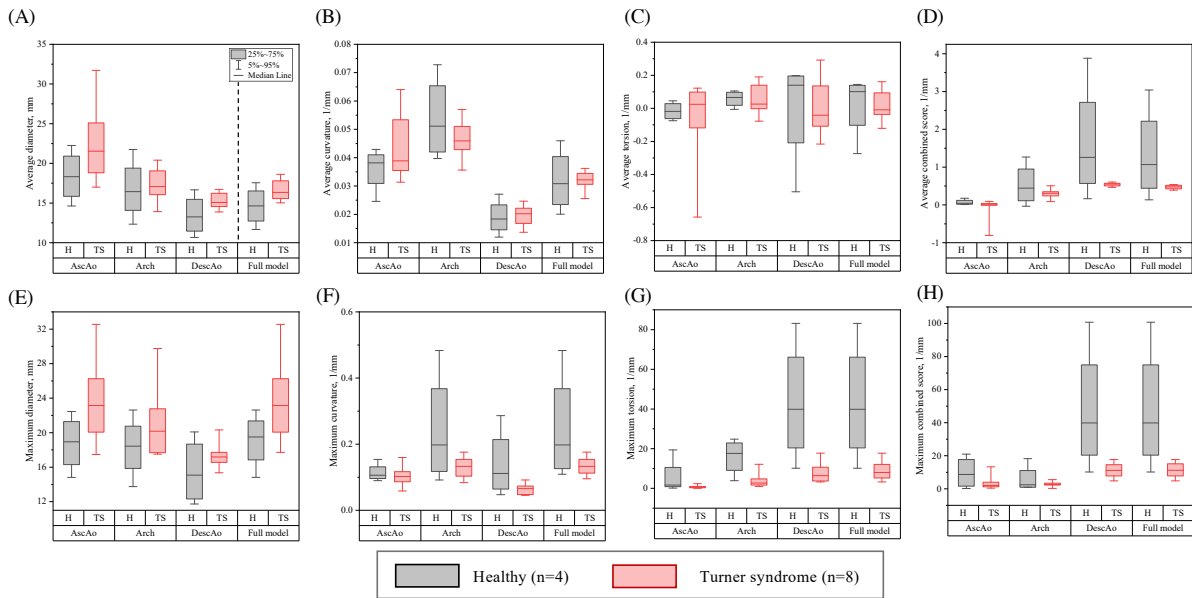


Figure 4.6. Boxplots of average and maximum values for diameter (A, E), curvature (B, F), torsion (C, G), and the combined curvature torsion score (D, H) at four locations: ascending aorta, aortic arch, descending aorta, and the entire model. Results presented as the mean of the healthy (H1-H4) and Turner syndrome (TS1-TS8) groups, with the median value (horizontal line), interquartile range (box), and values for 95% coverage of the data (whiskers).

The parameters of interest (Figure 4.1C) were averaged over the healthy (n=4) and Turner syndrome groups (n=8) and presented as the mean  $\pm$  standard deviation in Table 4.2. The Mann-Whitney U test was then performed to determine if the values for both the healthy and Turner syndrome groups were statistically different ( $p \leq 0.05$ ) (Table 4.2). Global parameters, these being the centreline length ( $l$ ), arch height ( $H_{\text{arch}}$ ), and arch width ( $W_{\text{arch}}$ ), were greater in the Turner syndrome girls, but not significantly different (Table 4.2,  $p = 0.37-0.57$ ) from the healthy group. The ratio of arch height to arch width ( $H_{\text{arch}}/W_{\text{arch}}$ ) was greater in the healthy group, but not significantly different from the TS result (Table 4.2,  $p = 0.39$ ). Further analysis was performed on the regional diameters ( $D_{\text{asc}}$ ,  $D_{\text{trans}}$ ,  $D_{\text{isth}}$  and  $D_{\text{desc}}$ ) and the ratio of these diameters to the descending aorta ( $D_{\text{asc}/\text{desc}}$ ,  $D_{\text{trans}/\text{desc}}$ ,  $D_{\text{isth}/\text{desc}}$ ) (Table 4.2). At all four regions, the Turner syndrome group had the greatest diameter, with the greatest difference between the two groups seen in the ascending aorta (Table 4.2,  $D_{\text{asc}} = 23.18$  vs  $18.54$  mm). However, this difference was not statistically significant (Table 4.2,  $p = 0.15$ ), nor was it for the other regional diameters ( $D_{\text{trans}}$ ,  $D_{\text{isth}}$  and  $D_{\text{desc}}$ :  $p = 0.68-0.93$ ). When the regional diameters were indexed to the descending diameter,  $D_{\text{asc}/\text{desc}}$  was greater ( $p = 0.21$ ) in the TS

group but  $D_{trans/desc}$  and  $D_{isth/desc}$  were lower ( $p = 0.15$ ). This was unsurprising as the TS group featured cases (Table 4.1) of ascending aortic dilatation, which would result in a higher  $D_{asc/desc}$  ratio, and aortic coarctation, resulting in a lower  $D_{trans/desc}$  and  $D_{isth/desc}$  ratio. The same was true for the shape index (SI), the ratio of minimum to maximum diameter, where the larger diameters seen in the TS group resulted in a smaller SI value. Again, the statistical difference between the healthy and TS groups was not significant ( $p = 0.20$ ). Finally, statistical analysis revealed that mean curvature ( $0.03$  vs  $0.02$   $\text{mm}^{-1}$ ) and torsion magnitude  $\tau_{mean}$  ( $0.02$  vs  $-0.01$   $\text{mm}^{-1}$ ) were greater in the Turner syndrome group, while tortuosity  $T$  was lower ( $0.79$  vs  $1.04$   $\text{mm}^{-1}$ ). The mean curvature-torsion score  $CC_{mean}$  was also greater in the TS group ( $0.47$  vs  $0.31$   $\text{mm}^{-1}$ ), which was expected as cumulative torsion was the dominant contributor. The healthy and TS values for  $k_{mean}$  were significantly different ( $p = 0.07$ ) while for  $\tau_{mean}$ ,  $CC_{mean}$  and  $T$  there was no significant difference between the two groups (Table 4.2).

Further statistical analysis quantified the correlation between the investigated morphological parameters (Figure 4.1 Morphometric parameters exemplified (A, B) and listed (C) for the three-dimensional aorta of TS1. (A) Model centreline shown with regional points  $D_{asc}$ ,  $D_{bca}$ ,  $D_{trans}$ ,  $D_{isth}$ , and  $D_{desc}$  as described in the text. (B) MRI slice showing the location of the arch width ( $W_{arch}$ ) and height ( $H_{arch}$ ) measurements, taken relative to the cranial edge of the pulmonary artery. (C) List of full morphological parameters.) and clinical parameters such as body mass index, body surface area, weight, and systolic blood pressure (Table 4.3). This investigation was performed for the Turner syndrome group only due to a lack of data for the healthy group. When indexed to BMI, no statistically significant correlations were found. However, the result for  $D_{trans}$  (the diameter at the location of the transverse arch, midway between the left common carotid and left subclavian) was very close with  $p = 0.06$  (Table 4.3). When indexed to BSA, three parameters produced statistically significant correlations. These were  $H_{arch}$ ,  $H_{arch}/W_{arch}$  and  $D_{trans}$  with  $p$  values of 0.03, 0.05 and 0.04 respectively (Table 4.3). Similarly, a significant correlation was found between  $D_{trans}$  and weight ( $p = 0.04$ ). No significant correlations were found between systolic blood pressure and the investigated parameters (Table 4.3).

Table 4.2. Comparison of clinical and morphometric parameters averaged over the healthy (n=4) and Turner syndrome groups (n=8). Data presented as mean  $\pm$  standard deviation. The Mann-Whitney U test was performed to determine if the values for each parameter were significantly different ( $p \leq 0.05$ ) between the healthy and Turner syndrome groups. Note, there was not enough data available to perform this analysis for height or weight.

	Healthy (n=4)	Turner syndrome (n=8)	Mann-Whitney U test P value
Age (years)	12.5 $\pm$ 5.8	14.25 $\pm$ 2.12	0.31
Height (cm)	146.00	142.41 $\pm$ 5.08	-
Weight (kg)	40.10	54.21 $\pm$ 20.71	-
SBP (mmHg)	102 $\pm$ 2	115 $\pm$ 15	0.12
DBP (mmHg)	58 $\pm$ 3	66 $\pm$ 13	0.18
Volume (mm <sup>3</sup> )	37457 $\pm$ 17023	59725 $\pm$ 15737	0.05
Surface area (mm <sup>2</sup> )	11207 $\pm$ 4253	14100 $\pm$ 2134	0.28
l (mm)	185.40 $\pm$ 39.48	197.45 $\pm$ 20.59	0.57
H <sub>arch</sub> (mm)	20.85 $\pm$ 5.10	21.31 $\pm$ 11.02	0.57
W <sub>arch</sub> (mm)	38.88 $\pm$ 6.44	42.13 $\pm$ 9.70	0.37
H <sub>arch</sub> /W <sub>arch</sub>	0.54 $\pm$ 0.10	0.49 $\pm$ 0.20	0.39
D <sub>asc</sub> (mm)	18.54 $\pm$ 3.21	23.18 $\pm$ 4.94	0.15
D <sub>trans</sub> (mm)	16.18 $\pm$ 4.12	16.60 $\pm$ 1.77	0.79
D <sub>isth</sub> (mm)	15.19 $\pm$ 4.03	15.56 $\pm$ 1.55	0.93
D <sub>desc</sub> (mm)	14.24 $\pm$ 3.50	15.70 $\pm$ 1.62	0.68
D <sub>asc</sub> /desc	1.32 $\pm$ 0.14	1.47 $\pm$ 0.24	0.21
D <sub>trans</sub> /desc	1.14 $\pm$ 0.11	0.91 $\pm$ 0.38	0.15
D <sub>isth</sub> /desc	1.06 $\pm$ 0.05	0.99 $\pm$ 0.10	0.15
SI (D <sub>min</sub> /D <sub>max</sub> )	0.63 $\pm$ 0.03	0.58 $\pm$ 0.10	0.20
k <sub>mean</sub> (mm <sup>-1</sup> )	0.02 $\pm$ 0.01	0.03 $\pm$ 0.00	0.07
$\tau$ <sub>mean</sub> (mm <sup>-1</sup> )	-0.01 $\pm$ 0.01	0.02 $\pm$ 0.09	0.93
CC <sub>mean</sub> (mm <sup>-1</sup> )	0.31 $\pm$ 0.19	0.47 $\pm$ 0.05	0.21
T	1.04 $\pm$ 0.37	0.79 $\pm$ 0.20	0.35

Table 4.3. Univariate regression of Turner syndrome parameters and body mass index (BMI), body surface area (BSA), weight, and systolic blood pressure (SBP). Significance level of  $P \leq 0.05$ .

	Indexed with BMI P-value	Indexed with BSA P-value	Indexed with weight P-value	Indexed with SBP P-value
Volume (mm <sup>3</sup> )	0.83	0.98	0.92	1.00
Surface area (mm <sup>2</sup> )	0.28	0.39	0.32	0.97
l (mm)	0.92	0.72	0.90	0.43
H <sub>arch</sub> (mm)	0.11	0.03	0.07	0.53
W <sub>arch</sub> (mm)	0.20	0.15	0.16	0.27
H <sub>arch</sub> /W <sub>arch</sub>	0.13	0.05	0.11	0.66
D <sub>asc</sub> (mm)	0.69	0.66	0.69	0.51
D <sub>trans</sub> (mm)	0.06	0.04	0.04	0.31
D <sub>isth</sub> (mm)	0.18	0.31	0.24	0.84
D <sub>desc</sub> (mm)	0.52	0.75	0.64	0.88
D <sub>asc</sub> /desc	0.89	0.69	0.81	0.32
D <sub>trans</sub> /desc	0.47	0.59	0.51	0.34
D <sub>isth</sub> /desc	0.57	0.53	0.54	0.75
SI (D <sub>min</sub> /D <sub>max</sub> )	0.81	0.70	0.78	0.68
k <sub>mean</sub> (mm <sup>-1</sup> )	0.56	0.50	0.52	0.76
τ <sub>mean</sub> (mm <sup>-1</sup> )	0.95	0.88	0.98	0.57
CC <sub>mean</sub> (mm <sup>-1</sup> )	0.67	0.77	0.68	0.60
T	0.50	0.31	0.43	0.69

#### 4.6 Discussion

In girls and women with Turner syndrome, congenital cardiovascular defects and acquired cardiovascular disease is common. As a result, the morphology of the ascending aorta, aortic arch, and descending aorta can be highly variable from patient to patient, in addition to varying incidences of dilatation, coarctation, non-uniformity, and non-planarity. Haemodynamic factors have been linked to the initiation and development of cardiovascular disease for over a century, and the relationship between anatomical and haemodynamic factors is well known [139], [173], [256], [257], [258]. In this study, 3D models of the aortic arch were reconstructed from patient cardiac data, and morphometric parameters, defined by anatomical landmarks,

were analysed to quantitatively define the three-dimensional morphology in a patient group with categorically abnormal aortic morphologies. This study complements a previous study [6] on the same patients which utilised computational fluid dynamic methods commonly used to analyse blood flow behaviour [259], [260], [261]

#### 4.6.1 Findings and Clinical Significance

Dimensional differences were observed both within the TS group and between the TS and healthy girls. The Euclidean distance maps (Figure 4.2A) provided information on the variation in vessel radius, and highlighted areas with the greatest asymmetry. At all locations, Turner syndrome diameter was greater than respective healthy diameters (Figure 4.6A, E and Table 4.2), which reflected the findings of similar studies on Turner syndrome children and adults [244], [262]. The enlarged aortic diameters seen in this group may be due to the intrinsic abnormality of the intimal layer in the vascular wall, which is also observed in other genetic disorders (such as Marfan and Loeys-Dietz syndrome) where it is proven to lead to progressive dilation of the ascending aorta [49], [263]. Identifying and/or diagnosing aortic dilatation in TS females is an important clinical step as it has been significantly associated with hypertension, even when age and BMI are accounted for [67]. Additionally, a similar link between ascending aorta dilatation and hypertension has been reported in disease-free individuals [264]. Two of the eight TS girls included in this study were clinically diagnosed with aortic dilatation (Table 4.1: TS1 and TS8). Of these two girls, only one (TS8) was also classed as hypertensive (138/88 mmHg). While TS1 did not have high blood pressure (116/75 mmHg), the severity of ascending aorta dilatation (even in comparison with other TS girls) may require prophylactic medical therapies earlier than what has been recommended for other conditions [1]. Interestingly, while TS4 was not diagnosed with aortic dilatation, this girl had the third largest ascending aorta diameter (Figure 4.2A, C), a BMI of 47.4 and a systolic blood pressure of 136 mmHg (hypertensive). Aortic dilatation is also known to have an influence on flow rate, arterial resistance, and the presence of helical flow, especially in the ascending aorta [265]. The link between dilatation and disturbed blood flow was shown in our previous computational fluid dynamic study [6] which included some of the patient geometries presented here. Specifically, we observed highly disturbed flow with low velocity values in the dilated ascending aorta of TS1 along with low time-averaged wall shear stress at the proximal ascending aortic wall [6]. Furthermore, the degree of aortic dilatation and aortic growth rate are known to be risk factors

for aortic dissection in similar genetic disorders such as the Marfan syndrome. Although it is uncertain whether the TS patients in this study would be more at risk for aortic dissection, patients with a high BMI (TS1, TS2, TS4 and TS7) and/or hypertension (TS4 and TS8) should probably be screened even if they do not meet the aortic size index criteria indicating a risk of dissection. Based on these risk factors, five of the eight Turner syndrome patients presented in this study would be flagged for dissection risk. When accounting for the common presence of bicuspid aortic valve in cases of TS dissection, TS6 would also be included in this higher-risk category [1], [239].

#### 4.6.2 Comparison With Other Studies

Aortic arch morphology has been investigated in previous TS studies [23], [36], [67], where a significant association between either aortic arch morphology and hypertension [67], or abnormal arch morphology and blood pressure [23], have been reported. In the study by De Groote et al. (44), aortic arch abnormality was quantified, through a novel parameter, according to the position of the highest point of the aortic arch. In this study, we quantified arch morphology according to aortic arch height, width, and the corresponding ratio, which are often computed in anatomical studies of the aorta [247], [248], [249]. Aortic arch height, width, and the ratio between the two ( $H_{\text{arch}}/W_{\text{arch}}$ ) have been identified by several authors to influence pulse pressure and pulse wave velocity (PWV) in the aortic arch. Redheuil et al. [248] reported the significant relationship between increased arch width ( $W_{\text{arch}}$ ), which we also saw in the TS group (Table 4.2) and increased PWV. Ou et al. [266] reported a similar positive relationship between an increased  $H_{\text{arch}}/W_{\text{arch}}$  (reminder: a higher  $H_{\text{arch}}/W_{\text{arch}}$  ratio is defined by a gothic shaped arch) and increased central aortic stiffness, as well as enhanced systolic wave reflection. Both increased central aortic stiffness and enhanced systolic wave reflection are well-known contributors to the development of hypertension [267], [268]. The average ratio of aortic arch height to width was greater for the healthy group ( $0.54 \pm 0.1$ ) than the TS group ( $0.49 \pm 0.2$ ), however the maximum value across all individuals was seen in TS5 ( $H_{\text{arch}}/W_{\text{arch}} = 0.92$ ). This was due to the abnormal angulation associated with a gothic shaped arch in TS5.

In this study, curvature and torsion averaged over the entire aortic centreline were greater in the TS group (Table 4.2). Subramaniam et al. [244], reported similar trends in their study measuring aortic dimensions in Turner syndrome adults. When looking at each region

individually, median curvature values in the ascending and descending regions were greater in the TS group, meanwhile median curvature values in the arch were higher in the healthy group (Figure 4.6B). The normalised curvature data followed a similar trend (Figure 4.5B). On the other hand, median torsion values in the ascending aorta were greater in the TS group, and in the aortic arch and descending aorta, higher in the healthy group (Figure 4.6C). While there does not appear to be any specific studies on aortic curvature and/or torsion in Turner syndrome, conclusions can be drawn from studies on patients with a similar genetic disorder. Like Turner syndrome, Marfan syndrome (MS) is genetic disorder in which abnormal connective tissue composition predisposes the individual to aortic complications. A study by Poullis et al. [269] on Marfan syndrome patients, reported that aortic curvature had major effects on the forces exerted on the aortic wall. In fact, they suggested that aortic curvature was relatively more important than aortic diameter, blood pressure, cardiac output, and patient size with regard to the force acting on the aortic wall [269]. Given the predisposition of atherosclerotic lesions along the inner wall of curved segments, and the importance that flow-induced wall shear stress plays in the localisation of atherogenesis [121], [122], [155], [161], [270], aortic curvature could be an important parameter to consider in risk stratification of Turner syndrome girls and women.

#### 4.6.3 Limitations

There are some limitations present in this study. Firstly, we recognise that the sample size of 12 patients (4 healthy and 8 TS) included in this study is relatively small and it is likely that we did not account for the full range of morphological variability seen in the TS population. However, despite our small sample size, each TS aorta had some form of aortic abnormality, and we are therefore confident that the group of 8 TS girls provided a good representation of the population. Also, we can still extract statistically significant results even if the group was small. Secondly, due to a lack of healthy clinical details with regards to height, weight, BMI, BSA, and blood pressure, unfortunately comparisons between the two groups could not be made for these parameters using the Mann-Whitney U test.

#### 4.7 Conclusions

In conclusion, we performed morphometric analysis of the aorta and supra-aortic branches in both healthy and Turner syndrome girls. Our aim was to identify differences between the two

groups, and to understand the clinical implications of morphologically abnormal aortic geometries. Turner syndrome girls had overall greater values in ten out of fifteen parameters examined (although not statistically significant,  $p > 0.05$ ), when compared to an age- and sex-matched healthy group, that is: the aortic arch height and width; the ascending aorta, aortic arch (2 locations), and descending aorta diameters; the ratio of the ascending to descending aorta diameter; average curvature; average torsion; and average curvature-torsion score. These parameters may explain the abnormal haemodynamics seen in Turner syndrome patients, namely vortical flow, flow separation, and flow disturbances, when compared to anatomically normal aortae, as shown in our previous study [6]. In addition, in the TS group a significant association between clinical (body surface area and weight) and morphological parameters (arch diameter, arch height and arch height-width ratio) was found. Clinically, an improved understanding of the morphological parameters contributing to changes in the haemodynamic environment enhances our understanding of the increased risk of cardiovascular disease in this population. We recommend that future work should aim to increase the database of Turner syndrome geometries to evaluate the risk stratification potential of these morphometric parameters. This would also allow statistical shape modelling to quantify a representative aortic model for this patient group that considers the anatomical variation associated with TS.

# Chapter 5

## Personalised Haemodynamic Simulations of Paediatric Aorta

The work presented in this chapter was published in the journal of *Frontiers in Cardiovascular Medicine* under the title “Hemodynamic Abnormalities in the Aorta of Turner Syndrome Girls” (June 2021) with co-authors Ruth Allen, Pauline Hall-Barrientos, Avril Mason, and Asimina Kazakidi (doi: 10.3389/fcvm.2021.670841).

### 5.1 Abstract

Congenital abnormalities in girls and women with Turner syndrome (TS), alongside an underlying predisposition to obesity and hypertension, contribute to an increased risk of cardiovascular disease and ultimately reduced life expectancy. We observe that children with TS present a greater variance in aortic arch morphology than their healthy counterparts and hypothesise that their haemodynamics are also different. In this study, computational fluid dynamic (CFD) simulations were performed for four TS girls, and three age-matched healthy girls, using patient-specific inlet boundary conditions, obtained from phase-contrast MRI data. The visualisation of multidirectional blood flow revealed an increase in vortical flow in the arch, supra-aortic vessels, and descending aorta, and a correlation between the presence of aortic abnormalities and disturbed flow. Compared to the relatively homogeneous pattern of time-averaged wall shear stress (TAWSS) on the healthy aortae, a highly heterogeneous distribution with elevated TAWSS values was observed in the TS geometries. Visualisation of further shear stress parameters, such as oscillatory shear index (OSI), relative residence time (RRT), and transverse WSS (transWSS), revealed dissimilar heterogeneity in the oscillatory and multidirectional nature of the aortic flow. Taking into account the young age of our TS cohort (average age  $13 \pm 2$  years) and their obesity level (75% were obese or overweight), which is believed to accelerate the initiation and progression of endothelial dysfunction, these findings may be an indication of atherosclerotic disease manifesting earlier in life in TS patients. Age, obesity, and aortic morphology may, therefore, play a key role in assessing cardiovascular risk in TS children.

## 5.2 Introduction

Turner syndrome (TS) is a rare genetic disorder where the second sex chromosome in females is partially or completely absent and can affect all or only a percentage of cells (mosaicism). Although rare, TS is the most common chromosomal abnormality among females [3], [9], [271]. The clinical characteristics of TS are highly variable, however, with congenital heart abnormalities estimated to occur in as many as half of individuals [272]. These defects predominantly affect the left side of the heart, with the most commonly reported being an elongated transverse aortic arch (ETA) [273], [274]. Defined as an increased distance between the second (LCCA) and third (LSA) supra-aortic branch origins, ETA is reported in 49% of TS adults [273], [274]. Bicuspid aortic valve (BAV) is the second most common abnormality in TS, affecting approximately 30%, closely followed by aortic dilatation with a prevalence of 27% [273], [275], [276]. Coarctation of the aorta (CoA) is reported in around 16% of TS females, most commonly at the site between the third supra-aortic branch and the descending aorta [273], [275], [276]. Aberrant right subclavian artery is an anatomical variation of the RSA which atypically originates from the arch as a separate fourth branch and has a prevalence of 8% in the TS [274]. These congenital abnormalities, alongside an underlying predisposition to obesity and hypertension, contribute to a greater risk of cardiovascular disease and ultimately reduced life expectancy in TS [277].

Haemodynamic factors have been linked to the initiation and development of cardiovascular disease for over a century [278]. However, the exact nature of pro-atherogenic flow is uncertain with researchers proposing contradicting theories [279], [280]. Fry suggested that high wall shear stress (WSS) preceded endothelial dysfunction, one of the early biological markers for atherosclerotic lesions that underlie most cardiovascular diseases [279]. Soon after, Caro et al. suggested that high WSS regions are in fact spared from disease, with low WSS areas prone to develop atherosclerosis [280], [281]. The oscillatory shear index (OSI) was then put forward by Ku et al. [282] to characterize regions of reversing flow, and today the combined low and/or oscillatory WSS theory is generally accepted as the biological mechanism for atherosclerosis. However, atherosclerotic lesions appear to depend on and vary with age [283]: studies in human fetuses, newborns, and children have demonstrated the development of sudanophilic lesions downstream of branch ostia in the thoracic aorta [284]; in young adults, lesions are observed laterally of such branch origins, while in middle age, upstream [285], [286]; last, in older people, atherosclerotic lesions develop around the origins of intercostal arteries [287].

Some aspects of such distinct lesion distributions have been described before haemodynamically and were correlated with strikingly varied WSS patterns calculated numerically around aortic branches [288], [289], [290].

In recent decades, computational fluid dynamic (CFD) modelling has gradually replaced traditional experimental methods in the study of cardiovascular diseases, largely due to its ability to quantify variables not measurable *in-vivo*, particularly at a temporal and spatial resolution exceeding all other methodologies [291]. Increasingly complex models of arterial vessels have improved our understanding of the relationship between anatomical and haemodynamic factors [292], [293], [294], [295], [296], [297], [298], [299]. However, the accuracy of these models is dependent on several assumptions. The assumption of blood as an incompressible, Newtonian fluid is common in the case of larger arteries. While this assumption is not physiologically correct, qualitative wall shear stress patterns have proven to be comparable between Newtonian and non-Newtonian simulations [300]. Multiple studies ignore the pulsatile nature of blood flow, assuming instead a steady-state condition [293], [294]. This assumption is computationally-efficient when only considering the mean WSS result, but pulsatility is crucial for capturing time-dependent parameters such as instantaneous velocities and WSS, time-averaged wall shear stress (TAWSS), transverse WSS (transWSS), oscillatory shear index (OSI), and relative residence time (RRT) [301]. In addition to the above assumptions, the computational result is highly sensitive to the assigned boundary conditions (BCs) [300], [301], [302], [303], [304]. Madhavan and Kemmerling [300] compared five different inlet velocity profiles on human aortae and found only small differences in the flow solution approximately two diameters downstream from the aortic inlet. In a similar study on mice, Van Doormaal et al. [305] used realistic MRI-derived aortic root velocity profiles and suggested that idealized inflow profiles should be avoided. Pirola et al. [296] recommended the use of a 3D inlet velocity profile for haemodynamic analysis of the ascending aorta and arch, but a 1D inlet velocity profile was acceptable for evaluating flow in the descending aorta. Outlet BCs impact a greater percentage of the solution domain, but often *in-vivo* data is not available, which is a hurdle in patient-specific simulations [300]. In the absence of *in-vivo* data, most studies apply either an outflow boundary condition, in which a percentage of the total flow is specified at each outlet, or a simple downstream resistance or the Windkessel model, in which the resistance and capacitance of the downstream vasculature are modelled [306]. However, implementation of the Windkessel model is particularly challenging for children,

due to the lack of values for the Windkessel parameters in the literature, especially for children with TS. In the absence of patient information, Murray's Law or the splitting method, both established from the power law relationship between branch diameter and flow rate, could be used [307], [308]. Several authors have favoured Murray's law over the zero-pressure boundary condition, for capturing more physiologically relevant flow features [301], [307].

In Turner syndrome, deviations from an anatomically healthy aorta are common, and therefore changes in blood flow may exacerbate the risk of cardiovascular disease. Understanding the pathogenesis of the increased cardiovascular morbidity and mortality in Turner syndrome, and determining the contributions of atherosclerotic disease, hypertension, and obesity was made a key cardiovascular research priority by the American Heart Association [272]. To this end, our research primarily aims at providing new evidence for the aortic arch haemodynamics in the TS children population, with categorically abnormal aortic morphologies. Comparison with three age- and gender-matched, anatomically healthy cases is also made to highlight the differences with normal anatomies. The haemodynamic environment of each patient was studied, and the relationship between aortic morphology and flow was analysed. Moreover, this study provides further evidence on understanding the aortic flow development generally in children and attempts to find correlations between haemodynamics and clinical significance in TS patients.

## **5.3 Materials and Methods**

### **5.3.1 Magnetic Resonance Imaging (MRI) and Patient Cohort**

In this study, retrospective MRI scans were obtained from four ( $n=4$ ) girls (average age  $13 \pm 2$  years) with karyotypically proven Turner syndrome (Table 5.1), attending the paediatric TS clinic at the Royal Hospital for Children, Queen Elizabeth University Hospital (RHC, QEUH). TS3 underwent anomalous pulmonary venous drainage repair approximately 6 years prior to MRI imaging, and TS4 underwent left congenital diaphragmatic hernia repair at birth (13 years before the MRI scan). Both surgical corrections were unrelated to the region of interest, being the proximal aorta.

All cardiac imaging was performed between 2014-2018 on a 1.5 Tesla diagnostic MRI scanner (MAGNATOM Aera/Avanto, Siemens Healthcare, GmbH). The scans were acquired with both

ECG and respiratory gating. Additional 2D time-resolved phase-contrast MRI (PC-MRI) data was acquired at the aortic root of each individual over a cardiac cycle, oriented axially and centred on the anatomical position of the pulmonary artery. Flow in the through-plane direction was measured with PC-MRI imaging using a velocity encoding (VENC) of 150-400 cm/s and TE = 2.66-3.33 ms, TR = 9.94 ms (slice thickness of 3.5-5 mm; FOV = 300 x 300 mm), for all data, resulting in a 256 x 256 pixel matrix and resolution of 1.17x1.17x3.5-5 mm.

Table 5.1 Biometric and anatomical data for the Turner syndrome (TS) girls (n=4). Age, height, weight, and blood pressure (BP) obtained from the patient electronic clinical records, as well as body surface area (BSA) and body mass index (BMI). The cardiac output (CO) and heart rate (HR) was obtained from within Medviso Segment software (<http://medviso.com/segment>).

	TS 1	TS 2	TS 3	TS 4
<b>Age, y</b>	14	10	14	13
<b>Height, cm</b>	136.60	134.70	143.70	138.30
<b>Weight, kg</b>	47.85	44.15	60.20	33.00
<b>BSA, m<sup>2</sup></b>	1.3	1.27	1.53	1.2
<b>BMI</b>	25.6	24.3	29.2	17.3
<b>BMI percentile</b>	92 <sup>nd</sup>	97 <sup>th</sup>	99 <sup>th</sup>	27 <sup>th</sup>
<b>BMI category</b>	over-weight	obese	obese	healthy
<b>BP<sub>syst</sub>/BP<sub>diast</sub>, mmHg</b>	116/75	102/61	104/43	111/69
<b>CO, l/min</b>	4.58	5.40	4.97	3.34
<b>HR, bpm</b>	88	105	84	83
<b>Anatomical abnormality</b>	dilatation	ETA	aberrant RSA	none

Biometric data (height, weight and blood pressure, BP) was obtained within one month of the cardiac imaging data and body mass index (BMI) and BMI percentile were computed according to the 1990 British childhood standards (Table 5.1) [309]. The cardiac output (CO) and heart rate (HR) were obtained from the PC-MRI data. Patient-specific volumetric image and

geometrical data from three gender-matched (average age  $13 \pm 6.8$  years) patients ( $n=3$ ), with no known aortic abnormalities, were purchased from the Vascular Model Repository ([www.vascularmodel.com](http://www.vascularmodel.com)). The average CO and HR of the healthy group were  $3.77 \pm 1$  l/min (mean  $\pm$  SD), and  $81.33 \pm 22.59$  bpm (mean  $\pm$  SD) respectively. Even though detailed BMI information was not included as part of the purchased data, it is expected that all healthy cases were within the normal BMI range, in accordance with the standard of the repository.

### 5.3.2 Anatomical Reconstruction and Mesh Generation

The three-dimensional geometries of the TS group were segmented and reconstructed from the MRI data, from above the location of the aortic valve to the end of the thoracic aorta, including the brachiocephalic, left common carotid, and subclavian arteries, using the medical-imaging software ITK-SNAP ([www.itksnap.org](http://www.itksnap.org)). In Figure 5.1 the anterior view of the reconstructed aortic models of the healthy (H1-H3) and Turner syndrome girls (TS1-TS4) is shown, with the geometries being in scale for direct comparison.

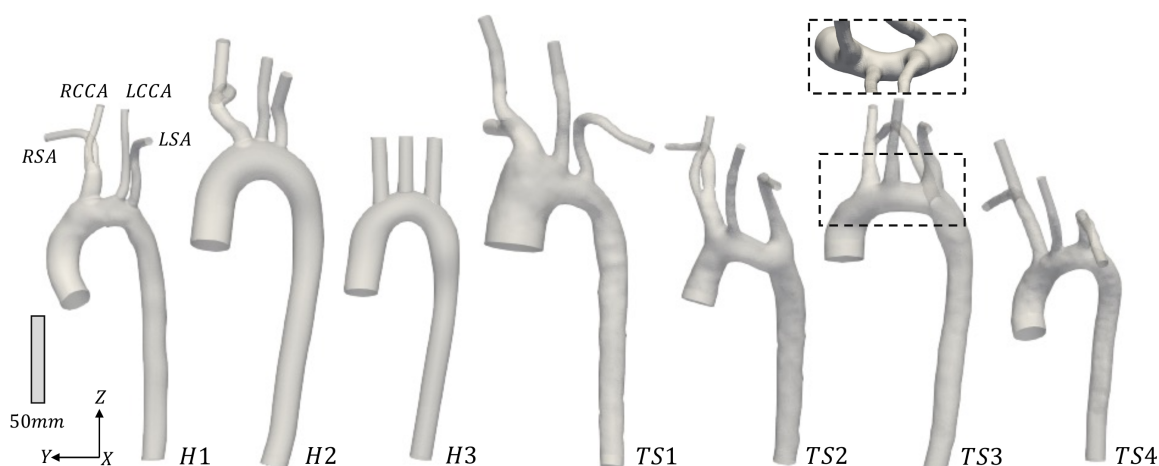


Figure 5.1. Anterior view of the reconstructed aortic models from the (H1-H3) healthy and (TS1-TS4) Turner syndrome (TS) girls. RSA: Right subclavian artery; RCCA: right common carotid artery; LCCA: left common carotid artery; LSA: left subclavian artery. Inset: Superior view of TS3 to highlight the origin of the aberrant RSA. Geometries are in scale.

The healthy controls had aortic diameters ( $D$ ) of 17.53-22.48 mm at the sinotubular junction (Table 5.2), similar to the mean diameter of 17.5 mm (range=11.1-26.4 mm) found in healthy children of a related age ( $n=53$ , range=2-20 years) [310]. Ascending aorta diameters in women with TS are generally about 10% greater than in healthy women [311]. In our cohort, the TS girls had aortic diameters of 18.99-33.77 mm (Table 5.2). The excessively large aortic diameter

in TS1 was expected due to the dilated ascending aorta. Among the Turner syndrome models were aortic abnormalities commonly reported in the literature, such as ascending aorta dilatation (TS1), elongated transverse arch (TS2 and TS3), and an aberrant right subclavian artery (TS3), as stated in the patient clinical records. Arch morphology in TS4 was suggestive of a triangular-shaped ‘gothic’ arch, although this was not recorded in the clinical records. Both TS1 and TS3 had a bicuspid aortic valve, while TS2 and TS4 had a normal functioning tricuspid aortic valve. TS girls 1, 2, and 4 exhibited the conventional anatomy of three supra-aortic vessels arising from the arch. In TS3, the right subclavian artery arose from the posterior arch, distal to the left common carotid artery (Figure 5.1, inset). There were no aortic abnormalities in the healthy cases (H1-H3).

Table 5.2. Haemodynamic information for healthy (H1-H3) and Turner syndrome (TS1-TS4) patients.  $T$ : cardiac cycle period;  $Q_{\text{mean}}$ ,  $Q_{\text{peak}}$ : mean and peak flow rates, respectively, and  $Re_{\text{mean}}$ ,  $Re_{\text{peak}}$  the corresponding Reynolds numbers;  $Wo$ : Womersley number;  $\Delta y_1$ : first boundary layer height;  $\Delta y_{n=5}$ : total boundary layer height (Eq. 1 – 4).

	H1	H2	H3	TS 1	TS 2	TS 3	TS 4
$D$ [mm]	17.53	22.48	19.68	33.77	19.30	22.56	18.99
$T$ [s]	0.57	1.00	0.76	0.68	0.57	0.71	0.72
$Q_{\text{mean}}$ $\left[\frac{\text{ml}}{\text{s}}\right]$	48	82	56	77	90	83	56
$Q_{\text{peak}}$ $\left[\frac{\text{ml}}{\text{s}}\right]$	197	302	223	254	294	320	207
$Re_{\text{mean}}$	1046	1394	1106	871	1782	1406	1127
$Re_{\text{peak}}$	4292	5145	4336	2873	5820	5418	4164
$Wo$	16	15	16	28	18	18	15
$\Delta y_1$ [mm]	0.19	0.21	0.21	0.40	0.16	0.21	0.20
$\Delta y_{n=5}$ [mm]	1.43	1.59	1.56	3.01	1.21	1.59	1.49

After segmentation, the surface models were smoothed in Autodesk Meshmixer ([www.meshmixer.org](http://www.meshmixer.org)) to reduce post-segmentation staircase artefacts, and flow extensions were added normal to all boundary faces in VMTK ([www.vmtk.org](http://www.vmtk.org)). An extension of half

aortic diameter in length was added at each patient-specific inlet, which was fitted to a circular inlet of the same area. The domain was then discretized in STAR-CCM+ software (Siemens PLM, USA, [www.plm.automation.siemens.com/global/en/products/simcenter/STAR-CCM.html](http://www.plm.automation.siemens.com/global/en/products/simcenter/STAR-CCM.html)) using polyhedral elements for the internal mesh, and prismatic elements for the boundary layer (Figure 5.2). While tetrahedral meshing is a more common approach, often a larger number of elements are required to limit element skewness and achieve acceptable mesh quality. Polyhedral meshing, introduced in STAR-CCM+, has two major benefits resulting in better numerical stability: one, each individual element has multiple neighbours, and two, the elements are less sensitive to stretching [195], [312]. As a result, an accurate solution can be achieved with a much lower cell count of polyhedral elements than tetrahedral. Quantitative grid convergence was investigated on three meshes of increasing density (each grid was further refined by a factor of 2) and assessed using the Grid Convergence Index ( $GCI = F_s(e/(r^p - 1))$  where  $F_s$  is a safety factor, taken as 1.25,  $e$  the relative error, and  $r$  the mesh refinement ratio, and  $p$  the order of convergence) [313]. The results confirmed that wall shear stress accuracy was suitably achieved with 1.5 million polyhedral elements ( $GCI \cong 11\%$ ). Mesh generation with polyhedral elements is a promising discretisation approach to reduce the computational time of simulations while retaining accuracy.

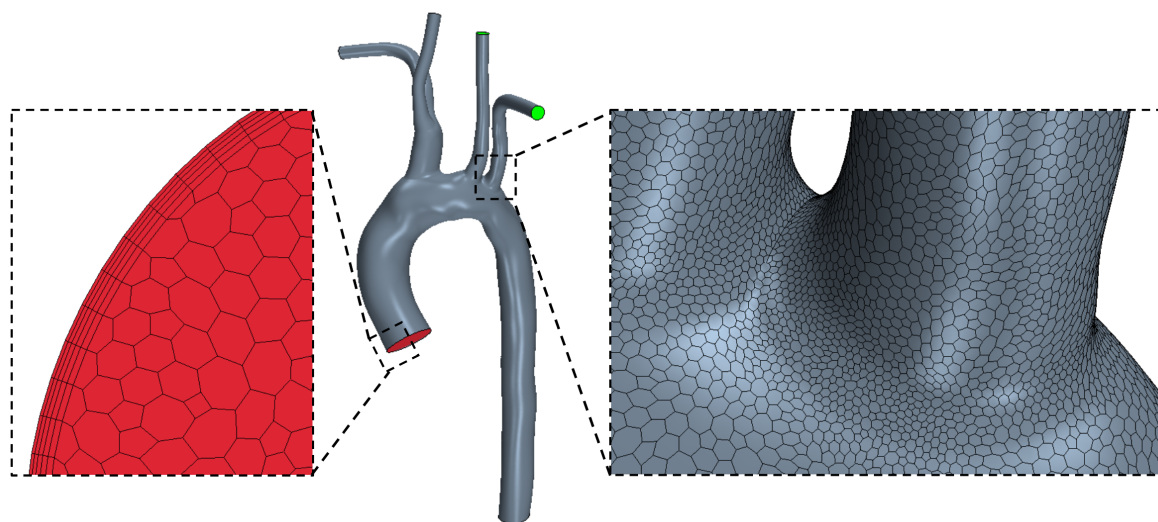


Figure 5.2. STAR-CCM+ polyhedral mesh shown on a healthy (H1) model with zoomed views of the inlet mesh with a prism boundary layer (left) and the arch surface mesh (right).

To accurately resolve the flow adjacent to the wall, the boundary layer mesh was generated using a total of 5 layers, with the height of the first layer ( $\Delta y_1$ ) satisfying a  $y^+$  value of 1 with the fluid viscosity and density, taken as  $3.5 \times 10^{-3}$  Pa s and  $1050 \text{ kg/m}^3$ , respectively [293] [314].

The  $y^+$  value describes a non-dimensional distance from the wall to the first element node and therefore characterizes near-wall mesh quality. Refining the near-wall mesh with an appropriate  $y^+$  value is crucial for resolving flow in the viscous sublayer of the boundary layer. The values of the first boundary layer height ( $\Delta y_1$ ) and total boundary layer height ( $\Delta y_{n=5}$ ) are shown in Table 5.2. The adequacy of the  $y^+$  value was further confirmed based on the directly calculated maximum WSS values, which led to a  $y^+$  value much smaller than 1.

### 5.3.3 Boundary Conditions

The flow exiting the aortic valve was segmented from the two-dimensional time-resolved PC-MRI data with the use of Medviso Segment software (<http://medviso.com/segment>), as detailed by Heiberg et al., resulting in a series of time-dependent flow waveforms (Figure 5.3) [315]. The highest peak flow rate was found for TS2 and TS3, and the lowest peak flow rate for H1 (Figure 5.3a). To account for diameter and cardiac cycle variability, the normalised flow rates were calculated (Figure 5.3b), where two of the healthy girls demonstrated higher peak flow rates than the TS girls. The subject-specific volumetric flow waveforms (Figure 5.3a) were applied at the inlet boundary, which was defined at the location of the sinotubular junction.

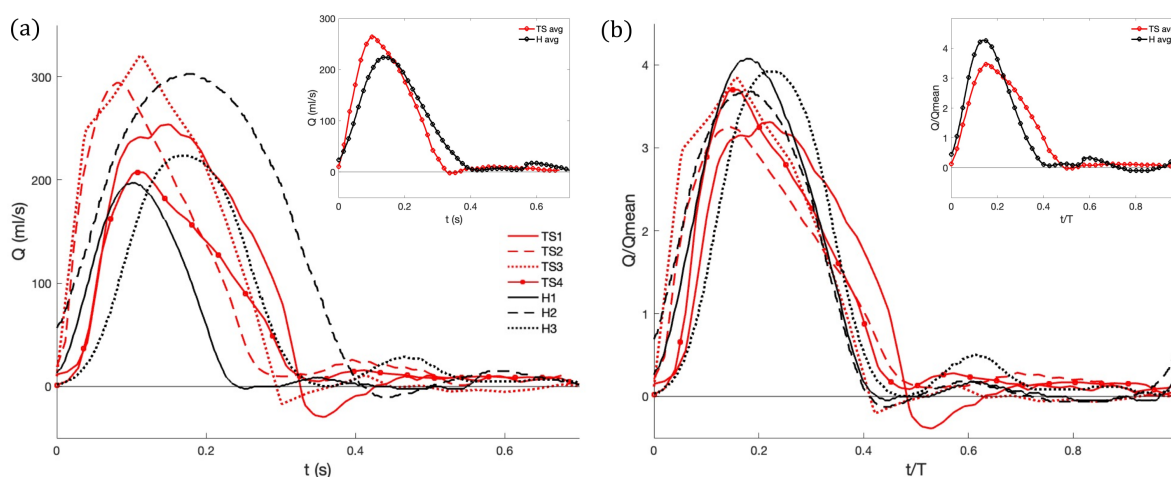


Figure 5.3. PC-MRI derived (a) volumetric flow rate and (b) normalised waveforms at the aortic root during one cardiac cycle for healthy (H) and Turner syndrome (TS) girls. Insets: average data calculated from H1-H3 (black line) and TS1-TS4 (red line). Flow rate and time normalised by the mean flow rate and cardiac cycle period (see Table 5.2 for values).

The cardiac cycle period ( $T$ ) and mean and peak flow rates ( $Q_{\text{mean}}$ ,  $Q_{\text{peak}}$ , respectively) were extracted from the location of the aortic valve from the PC-MRI data, while the Reynolds and Womersley numbers were calculated post-segmentation using the patient-specific inlet diameter ( $D$ ) and the cardiac cycle period (Table 5.2). The mean and peak Reynolds number ( $Re = 4Q\rho / (\pi D\mu)$ ) in TS patients varied, although the mean value for the TS group ( $Re_{\text{mean}}=1296$ ) was greater than the healthy group ( $Re_{\text{mean}}=1182$ ). Available  $Re_{\text{peak}}$  data in the literature for TS children reported a range of 3980-6560 in the ascending aorta, meaning that the average value for our cohort ( $Re_{\text{peak}}=4568$ ) was at the lower end of this range [176].

The Womersley number is a non-dimensional expression of the pulsatile nature of blood flow. The expected Womersley number in the abdominal aorta of a young healthy adult is 13 [316]. At large Womersley numbers (above 10), the shape of the velocity profile is relatively flat or plug-like, with the maximum velocity no longer at the center [317]. The computed Womersley number (Table 5.2) for the healthy aortae ( $Wo=15-16$ ) is within the range of TS2-TS4 ( $Wo=15-18$ ). For TS1, with the largest aortic diameter, the Womersley number is the highest with a value of 28.

The percentage of the total flow rate distributed to each outlet was calculated using Murray's law due to the shortage of patient-specific or literature values for children. In arterial bifurcations, Murray's law states that the flow is proportional to the diameter of that vessel raised to a power,  $n$  [307]. For the right subclavian branch, it can be expressed as:

$$\frac{Q_{RSA}}{Q_{RSA} + Q_{RCCA} + Q_{LCCA} + Q_{LSA} + Q_{DescAO}} = \frac{D_{RSA}^n}{D_{RSA}^n + D_{RCCA}^n + D_{LCCA}^n + D_{LSA}^n + D_{DescAO}^n} \quad 5.1$$

where  $Q_{RSA}$ ,  $Q_{RCCA}$ ,  $Q_{LCCA}$ ,  $Q_{LSA}$ ,  $Q_{DescAO}$  are the flow rates, and  $D_{RSA}$ ,  $D_{RCCA}$ ,  $D_{LCCA}$ ,  $D_{LSA}$ ,  $D_{DescAO}$  the diameters at the corresponding vessels. This relationship has been used in several human CFD studies, and is well-known with an exponential power of 3, hence the name "Murray's cube law". However, several authors have shown that a power of 2 is more valid in the case of larger vessels such as the aorta [318], [319], [320]. Using a power of 2, the calculated combined flow percentage to the aortic branches was 34%-59% for the healthy aortae and 32%-55% for the TS aortae, with the remaining flow distributed to the descending aorta (Table 5.3).

Table 5.3. Outlet flow percentages for each individual case calculated using Murray’s Law (exponential power of 2, equation 5.1).

	H1	H2	H3	TS 1	TS 2	TS 3	TS 4
$Q_{RSA}$	9%	14%	19%	20%	6%	8%	10%
$Q_{RCCA}$	9%	14%		14%	9%	12%	17%
$Q_{LCCA}$	7%	9%	19%	13%	9%	12%	10%
$Q_{LSA}$	9%	12%	21%	8%	8%	5%	15%
$Q_{DescAo}$	66%	51%	41%	45%	68%	63%	48%

In line with other CFD studies in the aortic arch, the arterial wall was presumed non-deformable and the no-slip BC was assigned [292], [293], [295], [296], [298], [299].

#### 5.3.4 Numerical Methods

Throughout this study, the fluid was considered incompressible and Newtonian, with a constant density and viscosity. The fluid was governed by the time-dependent Navier-Stokes equations previously introduced in section 2.3.1.

Flow simulations were performed in the open-source software, OpenFOAM© (www.openfoam.org, version 6), using the combined pressure-implicit split-operator and semi-implicit method for pressure-linked equations (PIMPLE) solver for incompressible, transient flow. The flow was computed using the wall-adapted local eddy-viscosity (WALE) large eddy simulation (LES) model, with temporal and spatial discretisation performed using second order accurate schemes (backward Euler and central differencing, respectively). As the peak Reynolds numbers (Table 5.2) are in the transitional to turbulent range, an investigation was made with a pulsatile laminar model, a k-omega SST model, and the LES (WALE) model for the same mesh (TS2). The wall shear stress results were qualitatively similar for all three models, and marginally different quantitatively (0.14% difference in the integral of the WSS between the LES and laminar models, and 6% difference between the LES and k-omega SST models). However, the LES model more accurately captured the flow features, especially during systole and early diastole. The motivation for the use of the LES turbulence model was further reinforced by other published studies on blood flow [321], [322]. Blood flow was simulated until time-periodicity was reached at approximately five cardiac cycles with a time

step ( $\Delta t$ ) of  $1 \times 10^{-3}$  s (satisfying mean Courant number  $< 1$ ). Residual control for the convergence criteria was set to  $1 \times 10^{-5}$  [323] for both pressure and velocity.

### 5.3.5 Shear Stress Parameters

The characterisation of shear stress during pulsatile flow is commonly described with haemodynamic parameters such as the instantaneous wall shear stress (WSS) at various time points in the cardiac cycle, the time-averaged WSS (TAWSS), the oscillatory shear index (OSI), the relative residence time (RRT) and the transverse WSS (transWSS), (equations 5.2-5.5 respectively). Such shear stress parameters can be used to identify areas where flow departs from a laminar, unidirectional pattern.

$$TAWSS = \frac{1}{T} \int_0^T |\vec{\tau}_w| dt \quad 5.2$$

$$OSI = \frac{1}{2} \left( 1 - \frac{\frac{1}{T} \int_0^T \vec{\tau}_w dt}{\frac{1}{T} \int_0^T |\vec{\tau}_w| dt} \right) \quad 5.3$$

$$RRT = [(1 - 2 OSI) \times TAWSS]^{-1} \quad 5.4$$

$$transWSS = \frac{1}{T} \int_0^T \left| \vec{\tau}_w \cdot \left( \vec{n} \times \frac{\int_0^T \vec{\tau}_w dt}{\int_0^T |\vec{\tau}_w| dt} \right) \right| dt \quad 5.5$$

where  $|\vec{\tau}_w|$  is the magnitude of the wall shear stress vector, and  $\vec{n}$  is the surface normal. In this study, the TAWSS, OSI, RRT and transWSS were taken over the fifth cardiac cycle, and both the WSS and TAWSS were normalised with respect to the mean WSS at the inlet for each individual case. The OSI describes the degree of oscillatory flow ranging from zero, representing unidirectional flow, to 0.5, representing reversing flow with no mean shear direction [324]. The RRT provides information on the residence time of flow particles in close proximity to the wall and is elevated in regions of low magnitude and high oscillatory WSS [325]. The transWSS quantifies multidirectional flow, with low values indicating that flow remains approximately parallel to a single axis throughout the cardiac cycle and high values indicating large changes in flow direction [326].

## 5.4 Results

### 5.4.1 Blood Flow in the Aorta

Blood flow was visualized in the geometries of Figure 5.1, using a combination of 3D streamlines (Figure 5.4) at three time points in the cardiac cycle, peak velocity ( $t_1$ ), maximum

deceleration ( $t_2$ ), and mid-diastole ( $t_3$ ), and 2D and 3D vector-fields (Figure 5.5) at peak velocity ( $t_1$ ). Maximum deceleration was defined as the minimum rate of change of the velocity with respect to time.

#### 5.4.1.1 Velocity Streamlines

In Figure 5.4a, the non-dimensional velocity streamlines in the aortic arch were visualized at peak velocity ( $t_1$ ). In all three healthy cases (H1-H3), the flow at peak systole was laminar throughout the aortic arch, the descending aorta, and the three major branches arising from the arch. A similar flow pattern was observed for TS patients 1 and 4. In TS2 and TS3, the streamlines at peak systole were, for the most part, laminar throughout the aorta, except at the entrance to the LSA in both geometries, and the aberrant RSA in TS3, where small zones of recirculation were formed. In the ascending aorta of all cases, the velocity magnitude was greater at the inner wall. The majority of flow within the arch of H1-H2, and to some extent in H3 and TS2, was of lower magnitude than in the ascending aorta. In all TS aortae, the velocity magnitude for the majority of the arch was similar to, or greater than, the flow in the ascending aorta. In the majority of TS aortic models, flow velocity in the descending aorta was high, with the exception of TS2.

In Figure 5.4b, the non-dimensional velocity streamlines in the aortic arch were visualized at maximum deceleration ( $t_2$ ). In the healthy aortae, flow was relatively laminar with the exception of the entrance to the LCCA and LSA branches in H3. In contrast, a complex flow pattern with significant secondary flows was observed for all TS aortic models. In the ascending aorta of TS girls 2-4, the flow at maximum deceleration was laminar. However, in the TS girl with ascending aortic dilatation (TS1), the flow was highly disturbed in this region with significantly low velocity values. In the aortic arch of TS3-TS4, vortical flow developed along the lesser curvature and extended to the entrance of the descending aorta, while in TS1 and TS2 the region of vortical flow filled the majority of the aortic arch. In the descending aorta of the TS girls, with the exception of TS1, vortical flow was present at the proximal wall with undisturbed streamlines at the distal wall, with the inverse true for TS1. Unlike in the healthy geometries, the pattern of flow entering the TS aortic branches was unpredictable and highly disturbed. Strong vortical flow patterns were observed in the brachiocephalic branch of

TS1, and recirculation regions at the proximal wall of TS2-TS4. The left common carotid artery of TS1 and TS3, and the left subclavian branch of TS1-TS3 further exhibit disturbed flow.

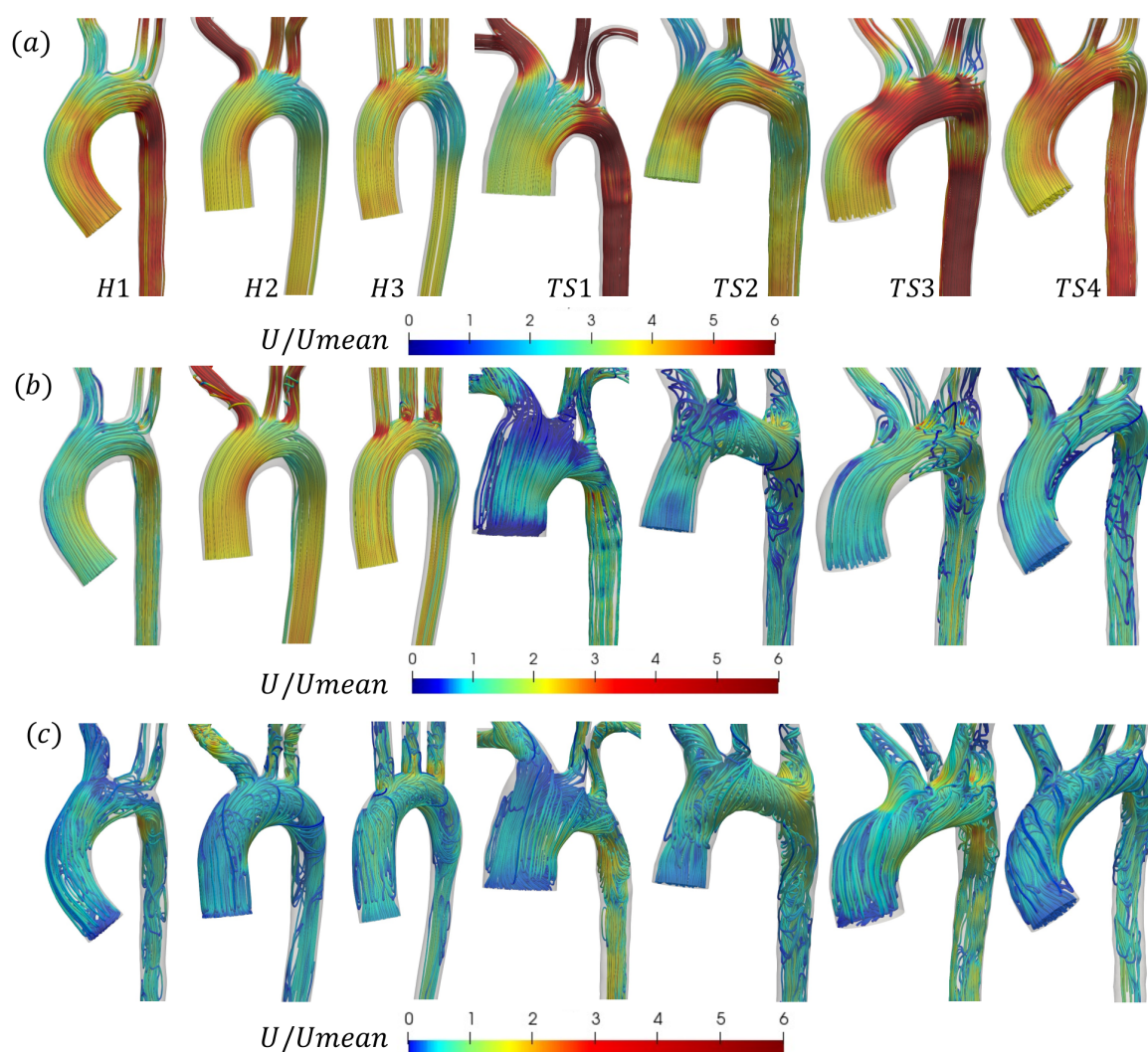


Figure 5.4. Velocity streamlines in the aortic arch of the healthy (H1-H3) and Turner syndrome (TS1-TS4) girls at (a) peak velocity ( $t_1$ ), (b) maximum deceleration ( $t_2$ ), and (c) mid-diastole ( $t_3$ ), colored by non-dimensional velocity magnitude that is normalised according to the average inlet velocity ( $U_{\text{mean}}$ ), derived from patient PC-MRI data (anterior view). Note that the colour legends in (b) and (c) were shifted compared to (a) to enhance visualisation. For interpretation of the coloured legends, please refer to the online version of the paper.

In Figure 5.4c, the non-dimensional velocity streamlines in the aortic arch were visualized at mid-diastole ( $t_3$ ). For the healthy aortae, the predominantly laminar flow pattern seen at maximum deceleration (Figure 5.4b) was replaced with strong, slow-moving vortical motion

throughout the entire vessel at mid-diastole (Figure 5.4c). For TS1-TS2, there was little visible difference in the flow patterns between  $t_2$  (Figure 5.4b) and  $t_3$  (Figure 5.4c), albeit with lower velocity values and a slight increase in vortical flow in the ascending aorta of TS2 and descending aorta of TS1. For TS3, flow throughout all regions of the aorta and aortic branches was clearly more disturbed in mid-diastole than in systole. Similar observations could be made for TS4, with the greatest flow disturbance seen in the ascending aorta and arch.

#### 5.4.1.2 Through-plane and In-plane Velocities

Furthermore, the through-plane and in-plane velocities were calculated for seven cross-sectional slices ( $\alpha$ - $\alpha'$  to  $\eta$ - $\eta'$ , Figure 5.5) of all models, at peak velocity ( $t_1$ ). The 3D through-plane velocity profiles were shown only for a healthy (H1) case, in the corresponding geometry (left side of Figure 5.5), while the cross-sections, colored by through-plane velocity contours and overlaid by in-plane velocity streamlines, were shown to the right side of Figure 5.5 for all models. The cross-sectional slices were considered at the same relative locations for all cases, perpendicular to the aortic centerline and relative to the individual model inlet diameter,  $D$ : slice  $\alpha$ - $\alpha'$  was taken  $1D$  upstream from the inlet; slice  $\beta$ - $\beta'$  was assumed midway between the LCCA and LSA branches;  $\gamma$ - $\gamma'$ ,  $1D$  downstream from the LSA (TS3: from the LCCA);  $\delta$ - $\delta'$ ,  $2D$  downstream from the LSA (TS3: from the LCCA);  $\varepsilon$ - $\varepsilon'$ ,  $0.5D$  upstream from the brachiocephalic junction;  $\zeta$ - $\zeta'$ ,  $0.5D$  upstream from the LCCA origin; and  $\eta$ - $\eta'$ ,  $0.5D$  upstream from the LSA ostium. The slices in Figure 5.5 are oriented so that the top and bottom edges correspond to the anterior and posterior sides of the aorta, respectively, while the left and right points correspond to the greater and lesser curvature of the arch, respectively, for slices  $\alpha$ - $\alpha'$  to  $\delta$ - $\delta'$ , and to the outer and inner walls of the branches, for slices  $\varepsilon$ - $\varepsilon'$  to  $\eta$ - $\eta'$ . That is, all cross-sections are oriented looking downstream. In all figures, the velocity values were normalised according to the corresponding mean inlet velocity magnitude.

As the velocity increases to a maximum during peak systole (Figure 5.5), blood flow accelerates along the curvature of the arch, with a tendency to skew towards the inner wall of the ascending aorta ( $\alpha'$ ) as seen in TS1 and TS3, and to a lesser extent in H1 and TS4. In H2 and TS2 the flow was skewed anterolaterally, and in H3 the flow was uniform. In slice  $\beta$ - $\beta'$ , the flow was skewed laterally or posterolaterally for all healthy aortae, posteriorly for TS1 and TS3, laterally for TS4, and posteromedially for TS2. At the entrance to the descending aorta,

flow in the healthy aortae was only slightly skewed: towards the outer curvature wall ( $\gamma$ ) in H1 and H3, and towards the inner curvature wall ( $\gamma'$ ) in H2. In the TS aortae, flow was more visibly skewed, specifically towards the outer curvature wall in TS1 and TS3, and the anterior wall in TS2. In the remainder of the descending aorta ( $\delta$ - $\delta'$ ), the flow field was well-structured with little asymmetry, except in TS2 where a region of higher velocity flow was located near the anteromedial wall. For slices  $\varepsilon$ - $\varepsilon'$  to  $\eta$ - $\eta'$ , the individual branch anatomy of each aorta influenced the axial and transverse flow fields. When asymmetry of the axial flow was present, it tended to be skewed towards a region of the lateral wall, as seen in the brachiocephalic branch ( $\varepsilon$ - $\varepsilon'$ ) of TS2 and TS4, the left common carotid branch ( $\zeta$ - $\zeta'$ ) of H3 and TS2, and the left subclavian branch ( $\eta$ - $\eta'$ ) of H1. In the left common carotid branch ( $\zeta$ - $\zeta'$ ) of TS3, the flow velocity was greatest posterior to the vessel center.

Figure 5.5 also revealed further information on the presence of secondary flows at peak velocity that were not visible in Figure 5.4a. In the ascending aorta ( $\alpha$ - $\alpha'$ ), even though the flow was laminar for all cases presented (Figure 5.4a), the direction of secondary flow differed among the patients, although it was never in the direction of the posterior wall. By the time the flow reached the distal end of the aortic arch ( $\beta$ - $\beta'$ ), the secondary flow direction changed for all geometries, except for H3 and TS1, while recirculatory flow was present along the anterior, lateral, or anterolateral walls in TS2-TS4 respectively. Secondary flow in the first descending aortic slice ( $\gamma$ - $\gamma'$ ) of the healthy aortae was present as a single recirculation zone at the posterolateral wall of H3 exclusively. The same region of recirculating flow was present in the first descending aortic slice of TS1. In TS2-TS4, secondary flow in slice  $\gamma$ - $\gamma'$  presented as a pair of counter-rotating vortices at the posterior wall of TS2, the posterolateral wall of TS3, and the anterolateral wall of TS4. An additional region of recirculating flow was present at the anterior wall of TS3. In slice  $\delta$ - $\delta'$ , taken further downstream in the descending aorta, secondary flow direction changed from slice  $\gamma$ - $\gamma'$  in all geometries except for H2, but remained laminar in all. In the majority of healthy aortic branches, excluding the BCA ( $\varepsilon$ - $\varepsilon'$ ) and LSA ( $\eta$ - $\eta'$ ) in H2 and H3 respectively, in-plane velocities were laminar. The same was true for all aortic branches of TS1 and TS4. In TS2, flow recirculation was present in the brachiocephalic branch ( $\varepsilon$ - $\varepsilon'$ ) near the anterior wall, and in the left subclavian branch ( $\eta$ - $\eta'$ ) near the anteromedial wall. A single recirculation region was present between the vessel center and medial wall in the LCCA branch ( $\zeta$ - $\zeta'$ ), and between the vessel center and anterior wall in the LSA branch ( $\eta$ - $\eta'$ ) of TS3.

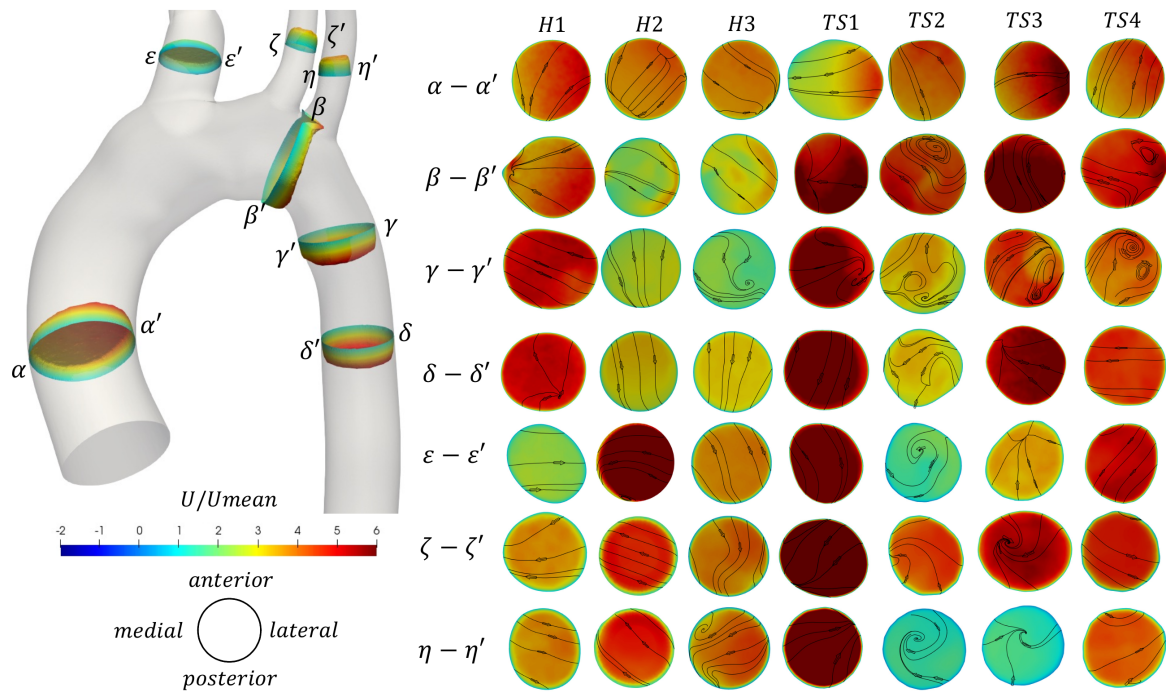


Figure 5.5. (left) Through-plane velocity profiles and (right) contours of through-plane velocity overlaid by vectors of in-plane velocity (components calculated normal to the vessel centreline in Paraview) on seven cross-sections  $\alpha-\alpha'$  to  $\eta-\eta'$  along the aorta (locations shown on the 3D healthy (H1) model). Contours coloured by non-dimensional axial velocity at peak velocity for the healthy (H1-H3) and Turner syndrome (TS1-TS4) girls. Cross-sections are oriented looking downstream, with the top and bottom edges corresponding to the anterior and posterior sides of the aorta, respectively, and the left and right points as shown on the left. Cross-sections are not to scale.

#### 5.4.2 Other Haemodynamic Metrics

The distribution of instantaneous normalised wall shear stress (WSS<sub>n</sub>) at peak systole ( $t_1$ ) and maximum deceleration ( $t_2$ ) are shown, respectively, in Figure 5.6a and b. Figure 5.6c displays the normalised time-averaged wall shear stress (TAWSS<sub>n</sub>) for all models. Additionally, the oscillatory shear index (OSI), relative residence time (RRT), and transverse WSS (transWSS) are presented in Figure 5.7a-c. A further analysis on the regional TAWSS<sub>n</sub> is provided in Figure 5.8.

The WSS<sub>n</sub> distribution differed throughout the cardiac cycle for all models but was most visible at peak systole (Figure 5.6a) due to the lower values at maximum deceleration (Figure 5.6b). At peak systole (Figure 5.6a), each TS aortic geometry presented a highly heterogeneous wall

shear stress pattern compared to the less diversified distribution on the aortic wall of the healthy cases. The  $WSS_n$  pattern at maximum deceleration (Figure 5.6b) was less clear, with values  $<20$  throughout the majority of the H2, H3, and TS2-TS4 aorta. The peak systolic  $WSS_n$  had evidently the greatest influence throughout the cardiac cycle, as the  $TAWSS_n$  (Figure 5.6c) results were to a large degree similar in character to the  $WSS_n$  patterns at  $t_1$  (Figure 5.6a). In the healthy (H1-H3) geometries the majority of the aortic body was exposed to relatively low  $TAWSS_n$  (0-5) values (Figure 5.6c), with additional higher  $TAWSS_n$  regions at the inner ascending aortic wall, and the proximal entrance to the descending aorta in H1. In general, for H1-H3, along the greater arch curvature  $TAWSS_n$  was highest upstream of the branch junctions and lowest downstream. Along the lesser arch curvature,  $TAWSS_n$  was lowest at the arch entrance and highest at the proximal entrance to the descending aorta.  $TAWSS_n$  on the three healthy branching arteries was lowest on the proximal walls. In the descending aorta, low  $TAWSS_n$  was observed on the downstream proximal wall and higher  $TAWSS_n$  on the distal wall. Of the regions identified on the healthy aortae with the lowest  $TAWSS_n$  (the inner arch curvature wall, the proximal walls of the three branches, downstream of branch junctions, and the downstream proximal wall of the descending aorta), all were accompanied by elevated OSI and RRT values (Figure 5.7a-b). The  $transWSS$  (Figure 5.7c), which provides information on the multi-directionality of WSS, was greater in H1 than H2-H3, with the exception of the brachiocephalic branch in H2. This indicates that the direction of flow in H1 is not parallel to a single axis and experiences fluctuations.

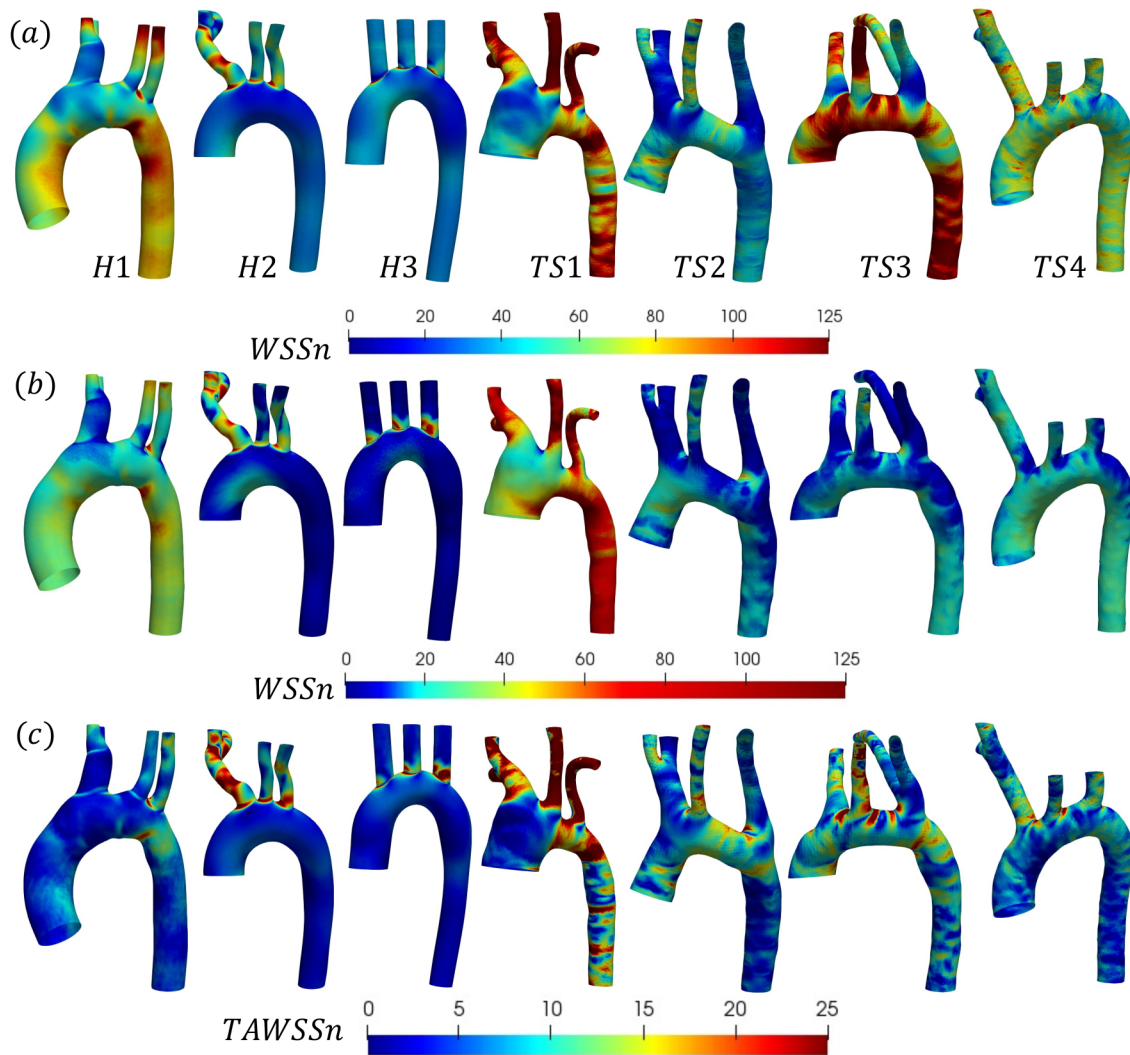


Figure 5.6. (a-b) Instantaneous normalised wall shear stress ( $WSS_n$ ), and (c) normalised time-averaged wall shear stress ( $TAWSS_n$ ) distributions shown (anterior view) for the (H1-H3) healthy, and (TS1-T4) Turner syndrome cases. (a) Peak systole and (b) maximum deceleration. WSS and TAWSS were normalised with respect to the mean WSS at the inlet for each individual case.

The relatively homogenous distribution of  $TAWSS_n$  on the healthy aortae was replaced with higher  $TAWSS_n$  values and highly heterogeneous patterns on the walls of the Turner syndrome geometries (Figure 5.6c). In the dilated aorta of TS1, low  $TAWSS_n$  values (0-5) were concentrated at the proximal wall of the ascending aorta, downstream of the three branch junctions, and at the proximal wall of the left subclavian artery. Irregular low shear stresses were also found along the proximal wall of the descending aorta among high shear stress regions. Very high  $TAWSS_n$  values dominated the three aortic branches and almost

circumferentially at two locations along the aorta, the first being between the left common carotid and left subclavian branch, and the second at the transition from the arch to the descending aorta. OSI values were highest at the proximal walls of the ascending and descending aorta, and downstream of the three branch junctions, more specifically at the anterior side. As low magnitude and high oscillatory wall shear stress leads to an increase in the residence time of the blood adjacent to the arterial wall, particularly elevated RRT values were observed at the ascending and descending aorta, and the distal wall of the brachiocephalic branch for TS1 (Figure 5.7b). The magnitude of transWSS in TS1 was overall very low, with higher values concentrated to the lesser curvature of the proximal arch and the aortic branches (Figure 5.7c). Case TS2 was defined by moderate-high TAWSS<sub>n</sub> and transWSS values (Figure 5.6c and Figure 5.7c), extending from the distal wall of the ascending aorta and throughout the majority of the elongated arch. The lowest TAWSS<sub>n</sub> (Figure 5.6c), accompanied by high OSI (Figure 5.7a) and RRT (Figure 5.7b), and low transWSS (Figure 5.7c), was found along the proximal wall of the descending aorta. TS3 had a very heterogeneous time-averaged wall shear stress pattern throughout the entire geometry, with the highest values concentrated to the outer curvature of the arch, near branch junctions, and at the transition from the arch to the descending aorta, as seen in TS1 and TS2. As expected, the OSI and RRT distributions on the surface of TS3 were also highly heterogeneous, with elevated values dominating the descending aorta (Figure 5.7a-b). TransWSS (Figure 5.7c) was highest along the anterior wall of the ascending aorta and arch, as was the case for TS2. TAWSS<sub>n</sub> heterogeneity in TS4 was concentrated to the outer walls of the ascending aorta, arch, and descending aorta, with low TAWSS<sub>n</sub> and elevated OSI and RRT transcending from the lateral wall of the ascending aorta, through the lesser curvature of the arch, to the proximal wall of the descending aorta. The transWSS in TS4 was of lower magnitude than that of TS2-TS3, although the highest values were again found along the anterior wall of the ascending aorta and arch.

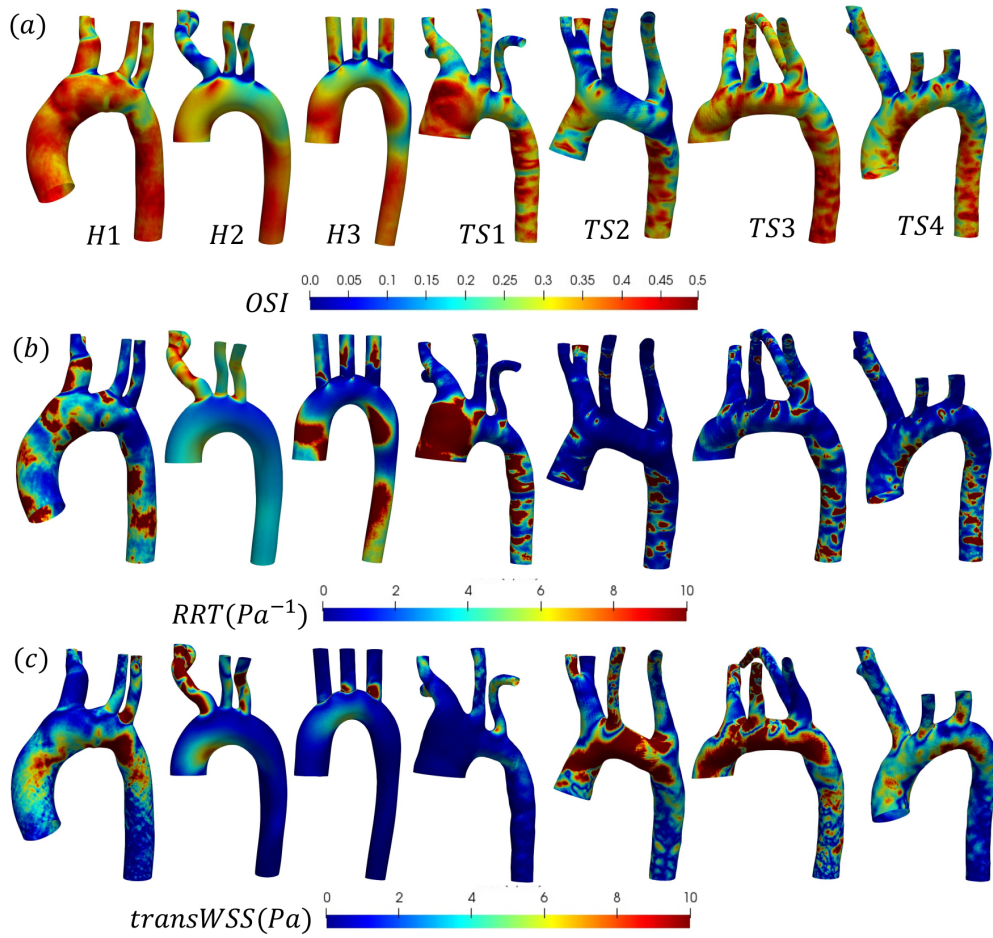


Figure 5.7 (a) Oscillatory shear index (OSI), (b) relative residence time (RRT), and (c) transverse wall shear stress (transWSS) distributions shown (anterior view) for the (H1-H3) healthy and (TS1-T4) Turner syndrome cases.

A detailed, comparative analysis of the TAWSS and  $TAWSS_n$  was performed at eight circumferential points of the selected aortic slices for the Turner syndrome group, taken as an average, and compared with those of the healthy group. This investigation revealed distinctly higher  $TAWSS_n$  values at all eight points of all cross-sections for the TS group (Figure 5.8). The only regions of the aorta that did not fit this trend were at points  $\epsilon$  and  $\epsilon'$  of the brachiocephalic trunk. Cross-sections  $\zeta$ - $\zeta'$ , and  $\eta$ - $\eta'$  in the left common carotid and left subclavian branches showed the greatest  $TAWSS_n$  variation between the healthy and TS groups. When comparing the dimensional TAWSS and non-dimensional  $TAWSS_n$  values averaged over each analysis plane for both groups (Table 5.4), the TS group had higher average values at every aortic location for both TAWSS and  $TAWSS_n$ , with the exception of the brachiocephalic branch ( $\epsilon$ - $\epsilon'$ ) for TAWSS.

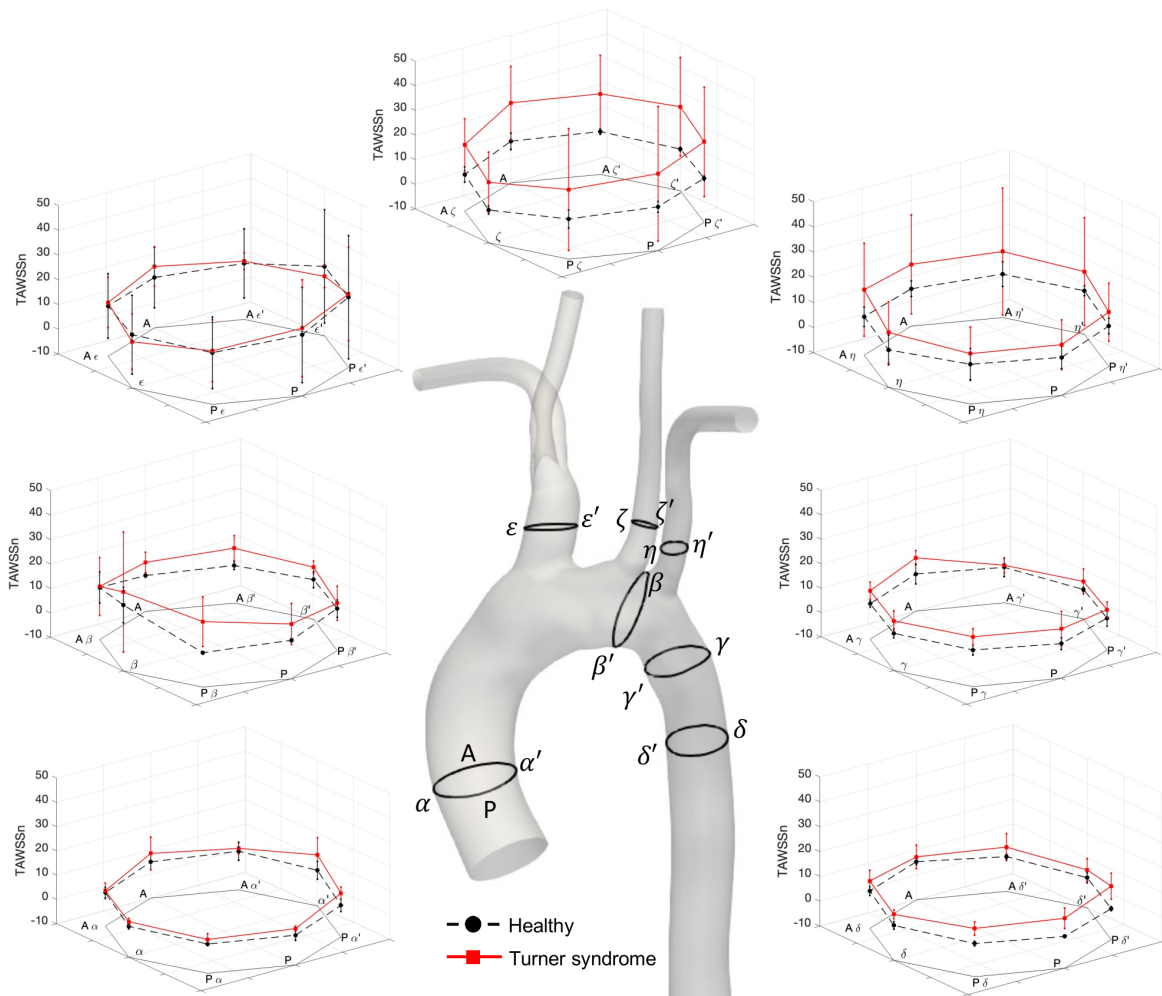


Figure 5.8. Normalised time-averaged wall shear stress ( $TAWSS_n$ ) values at seven cross-sections along the aorta of the healthy (black, dotted lines, as average of H1-H3) and Turner syndrome girls (red, solid lines, as average of TS1-TS4). Cross-sections are located as shown on the 3D model of a healthy (H1) case. Standard deviation shown as error bars at each point.

## 5.5 Discussion

In our study, patient-specific blood flow simulations were performed through the aortae of four Turner syndrome girls and three healthy girls. In healthy aortae, blood flow patterns range greatly throughout the systolic period [327], [328]. The TS girls included in this study had on average larger aortic root diameters ( $23.66 \pm 6.93$  mm) and higher peak flow rates ( $269 \pm 49$  ml/s, mean  $\pm$  SD) than the healthy group ( $19.90 \pm 2.48$  mm and  $241 \pm 55$  ml/s respectively, mean  $\pm$  SD). At peak systole, the velocity streamlines revealed the highest flow velocities in the descending aorta of the TS geometries with the largest diameters (TS1 and TS3), but no

vortical flow, except at some small recirculation areas in the distal branches of TS3 (Figure 5.4a). The evolution of helical flow throughout peak to late systole is influenced by the curvature and non-planarity of the arch [329]. The visualisation of multidirectional blood flow at maximum deceleration (Figure 5.4b), revealed increased vortical flow in the arch, supra-aortic branches, and descending aorta of the TS patients compared to the healthy controls. This is likely due to the anatomical variants of the TS aortae, rather than the transition from peak systolic flow to diastolic flow, as the peak deceleration value was higher for the healthy group ( $-13.73 \text{ m/s}^2 \pm 1.52$ ) than the TS group ( $-7.98 \pm 1.40 \text{ m/s}^2$ , mean  $\pm$  SD).

Table 5.4. Time-averaged wall shear stress (TAWSS), expressed in Pascals (Pa), and normalised time-averaged wall shear stress (TAWSS<sub>n</sub>) averaged over each analysis plane ( $\alpha$ - $\alpha'$  to  $\eta$ - $\eta'$ ) for the healthy (n=3) and the turner syndrome groups (n=4).

Analysis plane	TAWSS, Pa		TAWSS <sub>n</sub>	
	H1-H3*	TS1-TS4*	H1-H3*	TS1-TS4*
$\alpha$ - $\alpha'$	$1.04 \pm 0.40$	$1.86 \pm 0.63$	$3.65 \pm 1.40$	$6.55 \pm 2.49$
$\beta$ - $\beta'$	$2.19 \pm 1.22$	$2.86 \pm 0.71$	$7.70 \pm 4.33$	$13.29 \pm 4.24$
$\gamma$ - $\gamma'$	$1.23 \pm 0.33$	$2.08 \pm 0.58$	$4.24 \pm 1.11$	$8.74 \pm 2.55$
$\delta$ - $\delta'$	$1.03 \pm 0.35$	$1.94 \pm 0.46$	$3.63 \pm 1.18$	$8.60 \pm 1.90$
$\varepsilon$ - $\varepsilon'$	$3.50 \pm 0.86$	$2.52 \pm 0.81$	$13.38 \pm 3.32$	$13.94 \pm 3.45$
$\zeta$ - $\zeta'$	$1.79 \pm 0.44$	$3.83 \pm 0.98$	$6.42 \pm 1.58$	$20.36 \pm 3.39$
$\eta$ - $\eta'$	$1.59 \pm 0.29$	$1.97 \pm 0.25$	$5.81 \pm 0.99$	$13.13 \pm 2.55$

\* Values are given as mean  $\pm$  standard deviation

Atherosclerosis has a non-uniform distribution within the arterial system and shows a predilection for arterial curvatures and branch junctions. However, it is yet unclear why the endothelium is at times prone or immune to disease, particularly with increasing age. One of our key findings in this study was that compared to the relatively homogeneous distribution of time-averaged wall shear stress on the healthy aortae, there was a highly heterogeneous pattern on the walls of the Turner syndrome geometries. Taking into account the young age of our TS cohort (average age  $13 \pm 2$  years) and their obesity level (75% of the TS girls examined here were obese or overweight, Table 5.1), which is believed to accelerate the initiation and progression of endothelial dysfunction [330], the higher heterogeneity of WSS distribution

found in TS girls may be an indication of atherosclerotic disease manifesting earlier in life in these patients.

Wall shear stress is a biomechanical force, predetermined by fluid flow and arterial geometry, and a key player in the pathogenesis of atherosclerosis [331]. Aortic sites where blood flow departs from a laminar, unidirectional pattern, and wall shear stresses are low and/or oscillatory, are often associated with locations of atherosclerosis development [295], [329]. However, this link has primarily been established in the literature for adults [295], [329]. Studies on other species of younger age (e.g. mice and rabbits) do not necessarily follow the low and/or oscillatory WSS theory [290], [305] and the underlying flow mechanisms related to children are not well known in general. In our study, there appeared to be a correlation between the presence of aortic abnormalities, as seen in the TS group, and overall elevated TAWSSn. Higher TAWSS values and increased vortical flows may indicate a less atheroprotective environment in the young TS patient cohort studied here, thus not showing complete consistency with the above theory. However, the time-averaged WSS that we used here as part of our conclusions may not be the best indicator of disease predisposition, since atherogenesis may also be associated with the time that endothelial cells are exposed to WSS, rather than TAWSS, during the cardiac cycle [305]. Additionally, atherogenesis may not depend only on low and/or oscillatory WSS. Mass transfer of molecules such as Low Density Lipoproteins (LDL) or Nitric Oxide (NO) between the blood and the endothelium may also play a role in the mechanism of atherogenesis, even though they might be related to WSS [305].

### 5.5.1 Comparison With Other Studies

As far as we are aware, there are only three published studies on the aortic flow of TS patients. In the 2014 study by Chen et al. [293], a steady flow rate of 4.5l/min was simulated through three patient-specific Turner syndrome aortae (without patient age information), with aortic abnormalities common to two aortic geometries (TS1 and TS2) in our study. Although our study includes more complex simulations, accounting for patient-specific transient flow, similarities can be made with Chen et al. [293] regarding the flow patterns: weak secondary flow in the ascending aorta (Figure 5.5 slice  $\alpha$ - $\alpha'$ ) became stronger throughout the transverse aorta (Figure 5.5 slice  $\beta$ - $\beta'$ ); vortical flow was present in the arch of the aortic model with ETA (TS2) (Figure 5.5 slice  $\beta$ - $\beta'$ ); and the flow in the descending aorta was remarkably different between TS models (Figure 5.5 slices  $\gamma$ - $\gamma'$ ,  $\delta$ - $\delta'$ ). While we report a large variation in the flow

patterns of the descending aorta among TS1-TS4, we further found much greater asymmetry in the through-plane velocities and stronger secondary flow, especially at maximum deceleration, than Chen et al [293]. In the same study, the authors determined three locations with low WSS ( $<0.5$  Pa): (1) the brachiocephalic artery, (2) the inner side of the aortic arch exit, and (3) the entire inner wall of the descending aorta, which is in agreement with our results of low TAWSS<sub>n</sub> values, across all healthy and TS aortae.

In a more recent study by Wittberg et al. [176], a non-patient-specific flow rate of 5L/min was simulated through four different TS geometries using a non-Newtonian flow model (no patient age information provided). The authors found recirculation zones in all TS geometries, specifically at a cross-section in the descending aorta, which was most prominent (in length and width) in the aorta with ETA. This is in good agreement with Figure 5.5, where in-plane vectors revealed secondary flow in the descending aorta (slice  $\gamma$ - $\gamma'$ ) of all TS geometries, as well as H3. While a prominent region of recirculating flow was seen in TS2 with ETA, this region was of a similar length and width to that seen in TS3 and TS4 (Figure 5.5). In the arch of a TS geometry with ETA, Wittberg et al. [176] reported a single recirculation zone, as did our results for TS2 at peak systole ( $t_1$ ) (Figure 5.5 slice  $\beta$ - $\beta'$ ). At the entrance to the left subclavian branch in the ETA model, Wittberg et al. [176] visualized recirculating flow, which we also observed anteromedially to the vessel centre in TS2 (Figure 5.5 slice  $\eta$ - $\eta'$ ). The low-velocity recirculatory regions identified by Wittberg et al. [176] were accompanied by low TAWSS ( $<0.5$  Pa) and high OSI values. Additionally, the authors identified high TAWSS (3 Pa) on the walls of the supra-aortic branches in their normal, dilated, and ETA geometries, and very high TAWSS (5-10 Pa) in the arch of the dilated and ETA models [176]. We found similar TAWSS values on the brachiocephalic walls of both the healthy ( $3.50 \pm 0.86$  Pa) and TS groups ( $2.52 \pm 0.86$  Pa), on the left common carotid walls of the TS group ( $3.83 \pm 0.98$  Pa) (Table 5.4), and on the arch cross-section of TS2 ( $5.28 \pm 1.73$  Pa).

The 4D-flow MRI study in the aorta of both healthy and Turner syndrome girls by Arnold et al. [332] found significant differences between the two cohorts (mean age patient group  $16 \pm 5$  years for TS,  $17 \pm 4$  years for healthy controls). Specifically, during early and late systole, and early diastole, helical flow was increased in the ascending and descending regions of TS individuals with significantly larger diameters. Peak systolic velocities did not vary significantly between the TS and control group. In our study, the TS geometries with the largest

aortic diameters were TS1 and TS3, for which we demonstrated a similar trend, particularly at mid-diastole (Figure 5.4c). Additionally, Arnold et al. [332] reported decreased peak systolic WSS throughout the body of the aorta in TS girls, especially at larger diameter regions, when compared to healthy controls. Compared with Figure 5.6a, we observed a similar pattern on the ascending aortic wall of TS1, but not for TS2-TS4 which had only marginally larger diameters than the healthy controls. Also, our regional TAWSS results (Table 5.4, Figure 5.8), averaged over each cross-section, and extended to the supra-aortic branches, concluded that TS girls generally have higher TAWSS and TAWSS<sub>n</sub> than their healthy counterpart.

### 5.5.2 Study Limitations

There are some limitations in this study considering the assumptions made in sections 2.3-2.4. The assumptions of the arterial wall as rigid and blood as Newtonian are reasonable as the deformation of the arterial wall is relatively small in the proximal aorta and the effects of non-Newtonian blood can be ignored in larger vessels [333]. In this study, the applied inlet boundary condition is the volumetric waveform and so information on the spatial profile of the inlet velocity is lost. This was because the 3D velocity profile was not available for the healthy cases. The Murray's law, utilized here to predict the outflow percentages, is based on fully developed laminar Poiseuille flow which is not the case for larger arteries where turbulence occurs [334], [335]. However, in the case of absent patient data at the model outlets, and a lack of Windkessel parameter values from the literature, especially for children with Turner syndrome, Murray's law was considered the most appropriate method for the outlet boundary conditions. Furthermore, it was difficult to validate the results of this study since the patient data was obtained retrospectively. Prospective MRI data obtained alongside Doppler ultrasound measurements of blood velocity would allow the validation of the numerical results. Nonetheless, our numerical methodology has been used extensively in the past by our group and other researchers for biomedical engineering problems increasing our confidence in the obtained results [288], [289], [305], [336]. Finally, due to the limited availability of retrospective MRI data, this study examined only a small cohort of TS patients at a specific age range, which undoubtedly limits the statistical significance of our results.

## 5.6 Clinical Significance

Computational fluid dynamics can be a very powerful tool in cardiovascular medicine. The evaluation of haemodynamic parameters of patient-specific aortic models that are challenging to measure *in vivo* can improve our understanding of cardiovascular disease processes, thus enhancing diagnostic capabilities, and progressing toward patient-specific precision medicine. TS girls and women face a lifelong battle with a broad spectrum of cardiovascular concerns, from congenital heart abnormalities to an increased risk of hypertension, ultimately reducing life expectancy. The current management of cardiovascular conditions in TS is the same as in the general population, due to a lack of understanding of the developmental origins of the cardiovascular manifestations seen specifically in TS [272]. The key clinical question is whether any of the cardiovascular risk in TS patients is modifiable. Currently, known modifiable risk factors are hypertension and obesity and therefore the treatment of hypertension and avoidance of being overweight and obese is necessary for this group of patients. This begs the question - would this alter the flow dynamics more favourably too? In this study, the anatomical abnormalities observed in the aortae of young TS girls, the majority (75%) of which were obese or overweight, were accompanied by abnormal flow patterns and highly non-uniform distribution of wall shear stresses, which may promote the development of cardiovascular diseases earlier in life. The type of analysis presented in this study could be used clinically to predict patients at higher risk and therefore be more pro-active in lifestyle measures. Aortic dilatation, although rare, is more common in TS patients and is catastrophic, associated with high mortality. Other risk factors are bicuspid aortic valves, hypertension, and previous aortic surgeries, as well as pregnancy. It is still very difficult to predict even if aortic size index, a criterion to estimate the probability for aortic dissection in TS patients, has been evaluated correctly [337]. Pregnancy in some recommendations is contraindicated in all of TS due to this risk. CFD modelling could help in this direction. Considering the excess of morbidity and mortality, the early diagnosis of cardiovascular changes associated with Turner syndrome is essential and given the advantages of CFD in monitoring these changes, this method should be used alongside the standard Doppler echocardiography and magnetic resonance imaging in the clinical assessment of these patients.

## 5.7 Conclusions

Personalized flow in seven patient-specific aortic geometries (four TS, three healthy) was investigated in a comprehensive investigation of Turner syndrome children, using

computational fluid dynamic methods. The visualisation of multidirectional blood flow revealed increased vortical flow in the arch, supra-aortic branches, and descending aorta of the TS girls compared to the healthy controls, but no significant difference was found in the ascending aorta. This study found that young Turner syndrome patients, at about 13 years of age, exhibit markedly elevated TAWSS values when compared to age-and gender-matched healthy controls, suggesting a correlation with the presence of aortic abnormalities. The Turner syndrome girls, 75% of whom were obese or overweight, also display a highly heterogeneous pattern of TAWSS on the aorta, compared to the relatively homogeneous distribution of the healthy aortae, which may be an indication of atherosclerotic disease manifesting earlier in life in these patients. These results are not fully consistent with the low and/or oscillatory WSS theory of atherogenesis, which nonetheless may depend also on other factors, e.g. age, endothelial cells' exposure time to WSS and not TAWSS, and mass transfer of LDL and NO molecules to the endothelium, as explained here. For TS children, age, obesity, and aortic morphology may, therefore, play a key role in assessing cardiovascular risk. Further investigations are required on the role of mechanobiological factors on atherogenesis in healthy and diseased children, and the haemodynamics in different age groups of TS patients in particular.

# Chapter 6

## Personalised Haemodynamic Simulations of Adults

The work presented in this chapter was in collaboration with Negin Shahbazian, David Romero, and Cristina Amon at the Department of Mechanical and Industrial Engineering, University of Toronto, Canada. This work, titled “Computational Fluid Dynamics Study of Pre- and Post-Thoracic Endovascular Repair (TEVAR) in Patients with Thoracic Aortic Aneurysm”, is currently being reviewed for publication by the Journal of Vascular Surgery - Vascular Science.

### 6.1 Abstract

Thoracic Endovascular Aortic Repair is an established treatment for a range of thoracic aortic diseases, including aortic aneurysm and dissection, and is favoured in acutely unstable patients or individuals with a high operative risk. For treatment planning and long-term outcomes of TEVAR, both the vascular morphology and the consequent haemodynamic environment are crucial. In this study, we applied computational fluid dynamic (CFD) analysis in the aortae of five patients who underwent elective TEVAR for thoracic aortic aneurysm repair. Numerical simulations were performed for the pre- and post-operative geometries to explore the complex interplay between vascular morphology and blood flow after surgical intervention. Analysis of morphological parameters before and after TEVAR revealed that the stenting procedure had a significant impact on remodelling the aortic vessel. The radius at the aneurysm site, aortic curvature, torsion, and the combined curvature-torsion score were all reduced in the post-TEVAR geometries. In addition, we observed a favourable return to more physiological flow structures and a decrease in the aortic time-averaged wall shear stress ( $TAWSS_{pre} = 0.0266$  Pa and  $TAWSS_{post} = 0.0202$  Pa) post-TEVAR. Overall, this study highlights both the morphological and haemodynamic changes induced in the thoracic aorta with the placement of a stent graft, and the statistical differences between the pre- and post-environments.

## 6.2 Introduction

The thoracic aorta is prone to diseases such as aneurysms and dissections, which are characterised by a growing annual incidence and considerable morbidity and mortality [338]. Open-chest surgical repair of aortic disease has progressively been replaced by minimally invasive thoracic endovascular repair (Figure 6.1). The procedure involves the deployment of one or more stent-grafts (self-expanding metal scaffolds covered by a polymeric skirt) into the diseased site, through a catheter-guided endovascular delivery system (initially discussed in section 2.1.5.1) [339]. Traditionally, aortic diameter was used as a metric to base decisions for surgical intervention of aortic aneurysms. The concept of “one size fits all” for predicting adverse aortic events has become less favourable among surgeons, and new metrics have arisen that account for the influence of age, sex, and body size on aortic diameter. One such metric is the aortic size index (ASI) which indexes aortic diameter to body surface area (BSA) [340]. Davies et al., used this metric to stratify patients into three risk categories: those with an ASI  $< 2.75 \text{ cm/m}^2$  who were at low risk for rupture (4% per year), an ASI of 2.75 to 4.25  $\text{cm/m}^2$  was considered moderate risk (8% per year), and those with an ASI  $> 4.25 \text{ cm/m}^2$  were at high risk (20%–25% per year) [340]. Using this metric, surgical intervention is recommended for patients before they reach an ASI  $> 2.75 \text{ cm/m}^2$  [340]. Clinically, TEVAR aims to (a) exclude aneurysm pressurisation, thus minimizing the risk of rupture, and (b) seal the proximal entry tear of dissection, triggering a positive remodelling of the diseased aorta. While TEVAR is attractive for its low invasiveness, long-term efficacy remains a matter of clinical debate due to associated in-hospital mortality and neurological complications [339].

For successful post-surgical thoracic endovascular aortic repair outcomes, achieving a complete seal of the proximal landing zone is essential [342]. However, both the stiffness of the stent-graft and the complex anatomy of the aortic arch mean achieving a complete seal can be challenging [343]. A wedge-shaped breach between the aortic wall and the stent-graft, known as a bird-beak deformity, can develop from failure in sealing at the proximal zone along the lesser aortic arch curvature [344]. Morphological characteristics of the aorta recognised as potential causes of bird-beak formation include high angulation and curvature of the arch [345] [346].

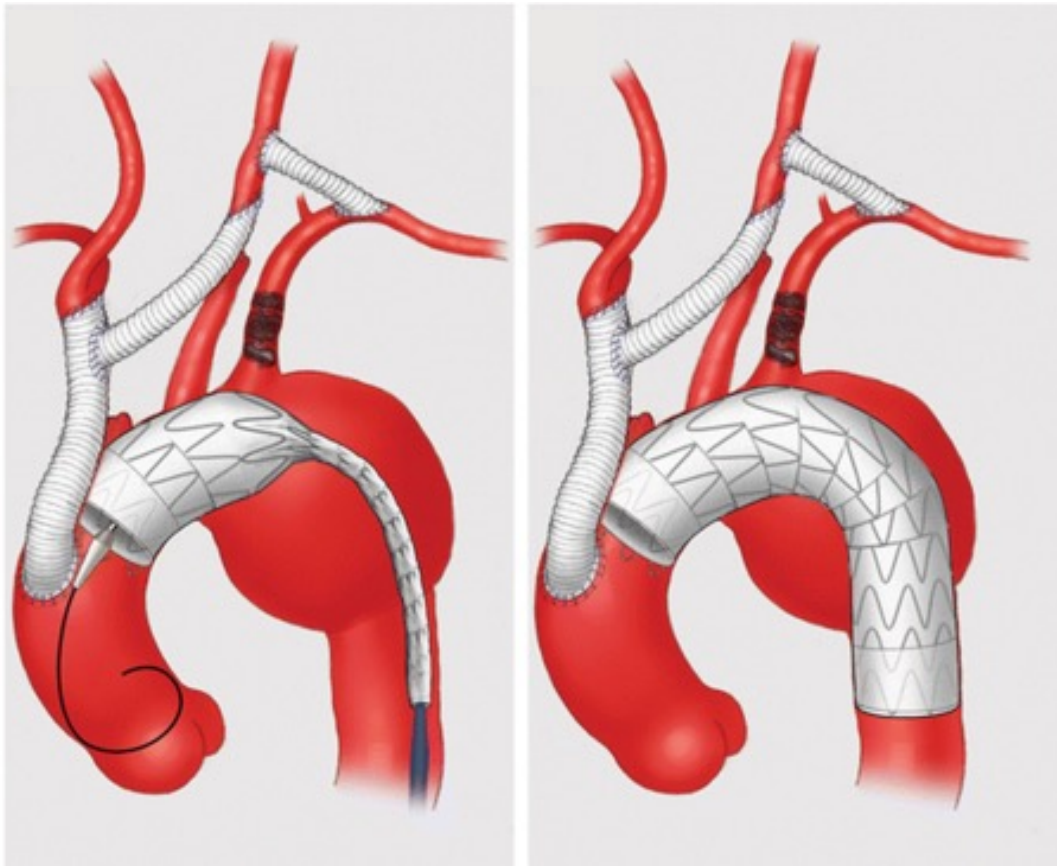


Figure 6.1. Deployment of an endovascular stent graft introduced via trans-femoral approach to repair a thoracic aneurysm. Figure reprinted from [341].

Earlier studies have utilized computational tools to analyse the blood flow in patients with thoracic aortic aneurysms pre and/or post-operatively and calculate the wall shear stresses developed. Karmonik et al. [348] applied CFD methods to a single patient to quantify haemodynamic forces pre- and post-endovascular aortic repair of an aortic dissection extending from the subclavian artery to the femoral artery. Treatment included placement of a stent graft with the proximal point at the aortic arch between the left carotid and the subclavian artery, and the distal point at the descending aorta ending at T7. They demonstrated that after TEVAR, the flow was undisturbed in the true lumen during systole and wall shear stress was lowered, suggesting a reduction of potential expansion or rupture. In 2012, Midulla et al. [349] combined MRI and CFD to perform four-dimensional mapping of velocity and wall shear stress in 20 patients post-TEVAR. Blood flow distribution varied from undisturbed to complex, with turbulent flow patterns depicted as “corkscrew” patterns present in the distal descending aorta. Wall shear stress alterations were observed in the arch and thoracic-abdominal aorta, at the

proximal end of the stent-graft. In a CFD study validated with ultrasonography, Polanczyk et al. [338], reported that post-operative remodelling of the aorta improved the haemodynamic patterns in a group of 5 patients with aortic dissection. Specifically, they observed an increase in the flow rate through the thoracic trunk and a decrease in the overall aortic wall shear stress values post-TEVAR. In a combined fluid-structure interaction study, Romarowski et al. [339] concluded that the presence of the stent-graft did not disturb the flow proximally or distally to the implant, as the velocity streamlines in the ascending and descending aortas followed an organised pattern.

More recently, Midulla et al. [349] quantified the WSS and vorticity profiles in pre- and post-TEVAR models with different thoracic aortic pathologies. They concluded that TEVAR induces changes in the native aorta, but the significance of these is not yet known. Sengupta et al. [350] investigated the aortic haemodynamics following TEVAR treatment with a single-branched endograft. They compared the pre-, post- and follow-up models and although found normal flow patterns post-operatively, the wall shear stress and displacement forces acting on the graft increased, which could contribute to device migration or endoleaks. Finally, Zhang et al. [351] very recently evaluated morphological and functional changes in three patients with aortic arch aneurysms that were treated with embedded modular branched stent graft, both before and after the stent graft implantation. They found an increase in flow velocity and low relative residence time after treatment, indicating promising short-term results of the stenting technique. Area reduction and curvature changes were also notable in two out of the three patients.

In this study, computational fluid dynamic simulations were applied to five patient-specific clinical cases (n=5) of pre- and post-TEVAR. These patients have also been used as part of the control group in the study of Shahbazian et al. [352] where they performed patient-specific simulation to predict the formation of bird-beak pre-operatively. All patients underwent elective TEVAR for thoracic aortic aneurysm repair. The local vascular morphological features such as curvature, torsion and area variations were evaluated in both the pre- and post-operative geometries for each patient, with an average follow-up time of 21 months. For all geometries, numerical simulations were performed, and both near-wall and intravascular haemodynamics were considered. The novelty of this study lies in the analysis of the haemodynamic parameters and the correlation to the geometric changes pre- and post-operatively in patients with thoracic

aortic aneurysms. The complex interplay between vascular morphology and blood flow after surgical intervention is explored.

## 6.3 Materials and methods

### 6.3.1 Clinical cases and medical image acquisition

Patients who received elective TEVAR for thoracic aortic aneurysm repair at Toronto General Hospital between 2015 to 2017 were identified and compared against a set of inclusion/exclusion criteria as approved by the University of Toronto Research Ethics Board, as follows: Inclusion Criteria: All elective TEVAR cases for thoracic aortic aneurysm repair that do not meet any of the exclusion criteria; Exclusion Criteria: (a) Lack of pre-operative and post-operative imaging data or scans without sufficient resolution/contrast to be able to segment the aorta; (b) Patients with previous surgical history; (c) Patients with a genetic disorder affecting the aorta (e.g., Marfan syndrome); (d) patients with genetic history including connective tissue disorders (e.g. Marfan's syndrome, Ehlers-Danlos syndrome and Loey-Dietz syndrome); (e) patients with myotic thoracic aortic aneurysm; (f) TEVAR patients treated for aortic dissection and blunt thoracic aortic injury.

A total of five patients (3 male, 2 female) met the above criteria and were therefore included in this study (Table 6.1). The average age at surgical intervention was  $63.8 \pm 13.0$  years (mean  $\pm$  standard deviation) with an average follow-up time of 21 months between pre-operative and post-operative imaging (T). Anonymised computed tomography angiography (CTA) images (pre- and post-operative), demographic data (age, gender), and basic information about the surgery (type of stent graft, TEVAR treatment landing zone and post-operative complications) were collected for each individual. According to the medical notes and pre-operative images, all patients had at least one of the following aortic abnormalities requiring TEVAR intervention: dilatation of the ascending (patient 004) and/or the descending aorta (patients 001 – 005), descending aneurysm (patients 001 and 003), and coarctation of the aorta (patients 003 – 005). All five patients were treated with a Zenith Alpha Thoracic Endovascular Graft (Cook Medical, USA), the details of which are presented in Table 6.1. The Zenith Alpha Graft is constructed of woven polyester fabric sewn to self-expanding nitinol stents which provide the necessary attachment and seal of the graft to the vessel wall. At both the distal and proximal

ends of the stent are fixation barbs which protrude through the graft material for added fixation and sealing.

Table 6.1. Summary of the patient details including sex and age (years) at the time of surgical intervention and post-operative follow-up imaging, as well as the implanted stent details.

Case	Patient Demographics			Zenith Alpha stent-graft Details
	Sex (M/F)	Age at surgery (pre-operative) (years)	Age at follow-up (post-operative) (years)	Stent graft diameter (mm)
001	F	45	46	28
002	M	57	58	34
003	F	78	79	36
004	M	67	68	32 – 40
005	M	72	72	36

### 6.3.2 Reconstruction of patient-specific geometries

Segmentation of the aorta from the cardiac imaging data was performed using the semi-automatic active contour-based algorithm implemented in ITK-SNAP ([www.itksnap.org](http://www.itksnap.org)). The aortic geometries were reconstructed such that only the ascending aorta (from above the location of the aortic root), aortic arch, descending aorta (including the aneurysm site), and the supra-aortic branches (brachiocephalic, left common carotid, and left and right subclavian branches) were included. The output from the automated segmentation was visually inspected slice by slice and any artifacts were corrected with the manual segmentation tool within ITK-SNAP. This same methodology has been applied previously to segment geometries from cardiac imaging data [5], [6], [242]. After segmentation, the surface models (stereolithography, STL, file-format) were smoothed in Autodesk Meshmixer ([www.meshmixer.org](http://www.meshmixer.org)) to remove unwanted staircase surface artefacts, and flow extensions were added normal to all boundary faces in VMTK ([www.vmtk.org](http://www.vmtk.org)) [259]. The complete set of pre- and post-operative geometries for patients 001-005 is shown in Figure 6.2A and B, respectively. Sensitivity analysis was

performed on the segmentation process by two independent users to ensure user independence (See Appendix 8).

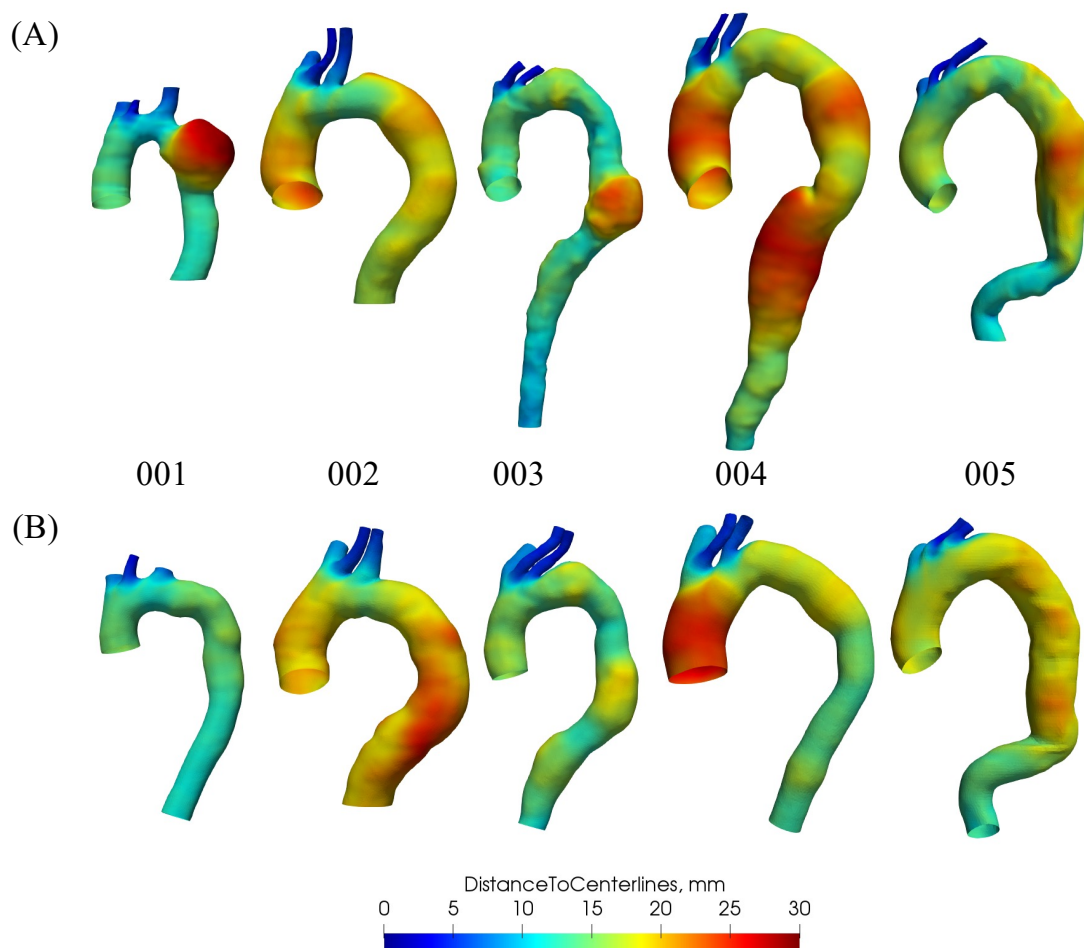


Figure 6.2 (A) Pre-operative and (B) post-operative geometries of the thoracic aorta for patients 001 – 005 coloured by the Euclidean distance (the distance between the centreline and the lumen) in millimetres. All geometries are in scale.

### 6.3.2.1 Aortic Morphological Parameters

Morphometric analysis was performed for both the pre- and post-operative geometries within the Vascular Modelling Toolkit (VMTK) ([www.vmtk.org](http://www.vmtk.org)), unless otherwise stated [243]. VMTK is an open-source collection of tools and libraries intended for geometric analysis of blood vessels, and has previously been used to characterise geometrical changes in abdominal aortic aneurysms [245]. Further details on the steps taken in VMTK can be found in Appendix 9, and for a more detailed description of the methodology used in VMTK, the work of Piccinelli et al. (2009) is recommended [246].

First, single values for vessel volume ( $V$ ) and surface area ( $SA$ ) were obtained, followed by colourmaps of the Euclidean distance, defined as the distance between the centreline and lumen boundary. The Euclidean distance is useful in that it provides visual information on the dimensional (circumferential and axial) variation within and between patients. Previous studies have also employed this variable to visualize aortic growth in patients with small abdominal aortic aneurysms [245]. Additionally, vessel curvature ( $k$ ) and torsion ( $\tau$ ) were calculated, the definitions given in equations 4.1 and 4.2. respectively [250]. Both parameters give a detailed insight into the morphological characteristics of the vessel and are of interest given their influence on the flow field [251], [252], [253], [254]. The combined curvature and (absolute) torsion score ( $CC$ ) proposed by O’Flynn et al. [255] was also computed, see equation 4.3.

### 6.3.2.2 Aneurysm Morphological Parameters (Pre-operative geometries only)

The minimum, average, and maximum diameters at the aneurysmal site were computed for the pre-operative geometries (Table 6.2).

Table 6.2. Minimum, average, and maximum aneurysmal diameters for the pre-operative geometries of patients 001 – 005.

Case	$D_{minimum}$ , mm	$D_{average}$ , mm	$D_{maximum}$ , mm
001	20	31	41
002	27	36	40
003	24	31	38
004	33	44	51
005	24	32	38
Mean $\pm$ SD	25.6 $\pm$ 4.83	34.8 $\pm$ 5.54	41.6 $\pm$ 5.41

Both patients 001 and 002 presented with saccular aneurysms at the distal end of the aortic arch of reasonably large diameter (maximum diameter = 41mm and 40mm respectively). Patients 003-005 presented with aneurysms in the thoracic aorta with maximum diameters of 38 mm, 51 mm, and 38 mm, respectively.

### 6.3.3 Mesh Generation

The patient geometries were discretised using ANSYS ICEM CFD software with tetrahedral elements adopted for the internal mesh, and prismatic elements for the boundary layer. A mesh

independence test was performed for the pre-operative patient 001 using 0.5, 1, 2, 4, and 8 million elements and the resulting wall shear stress was compared. The mesh independence study confirmed that wall shear stress accuracy was achieved with 1 million elements, showing a 1.46% difference when compared to an 8 million element mesh. The average number of elements used was 1,157,531 (Figure 6.3, see Appendix 10 for the individual values), which was in line with similar studies by Pasta et al., Rinaudo et al., Polanczyk et al., and Romarowski et al. [338], [339], [353], [354].

To reliably compute the wall shear stress, the mesh at the boundary wall needs to be highly refined to accurately resolve the adjacent flow, as detailed by Soudah et al. [345]. Since the boundary layer thickness is small, the distance for the first element node ( $y$ ) should be in the order of micrometres to millimetres. This distance from the wall is represented as the non-dimensional  $y^+$  value. A low  $y^+$  value ( $< 1$ ) is crucial to resolve flow in the viscous sublayer of the boundary layer. In their respective aortic meshes, Soudah et al. [345] utilised a distance in the order of micrometres ( $10^{-6}$  m) for  $y$ , and Tan et al. [355] created a mesh satisfying a  $y^+$  value less than 2.

In the aortic geometries presented here (Figure 6.2), the boundary layer was generated using five nodes (i.e., five layers) with a total boundary layer height of  $5 \times 10^{-4}$  m. The corresponding  $y$  and  $y^+$  values were computed for each geometry (Appendix 10).

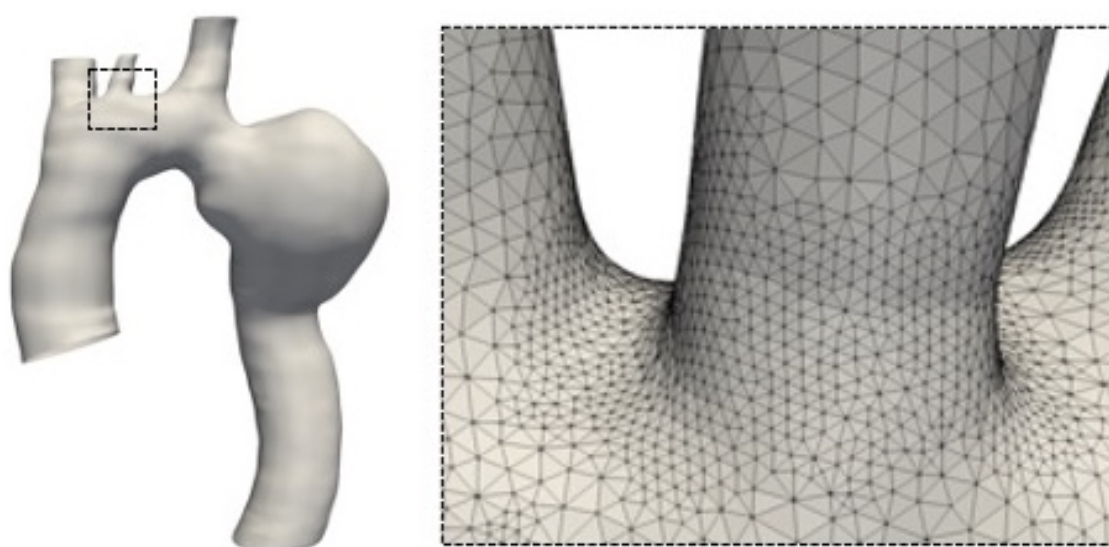


Figure 6.3. Mesh generation displayed on the pre-operative geometry of patient 001. Boundary layer and branch junction meshes shown in insets.

### 6.3.4 Boundary Conditions

For this study, only patient CT data was available for the extraction of anatomical information. Therefore, phase-contrast MRI data at one-year post-TEVAR from a 51-year-old male with an asymptomatic post-dissecting thoracic aortic aneurysm was applied as the inlet boundary condition to all geometries (Figure 6.4A) [356]. The time-dependent velocity waveform was then adjusted for each patient, relative to the respective inlet boundary surface area (Figure 6.4B). The decision to apply an identical inlet BC for all geometries (pre- and post-operative) was based on the investigation by Gallo et al. [356], where near-wall haemodynamics and WSS-based descriptors were not markedly affected by the applied flow rate waveform shape and average value. This methodology was also similar to that of Qiao et al. [357].

The flow was distributed between the outlet boundaries, these being the supra-aortic vessels (brachiocephalic, left common carotid, and left subclavian) and the descending aorta, using resistance boundary conditions. The specific flow ratio used was 40%:60% to the branches and descending aorta, as implemented previously by Pasta et al. [353]. In line with other CFD studies in the aortic arch, the arterial wall was presumed non-deformable and the no-slip boundary condition was assigned [292], [293], [295], [296], [298], [299].

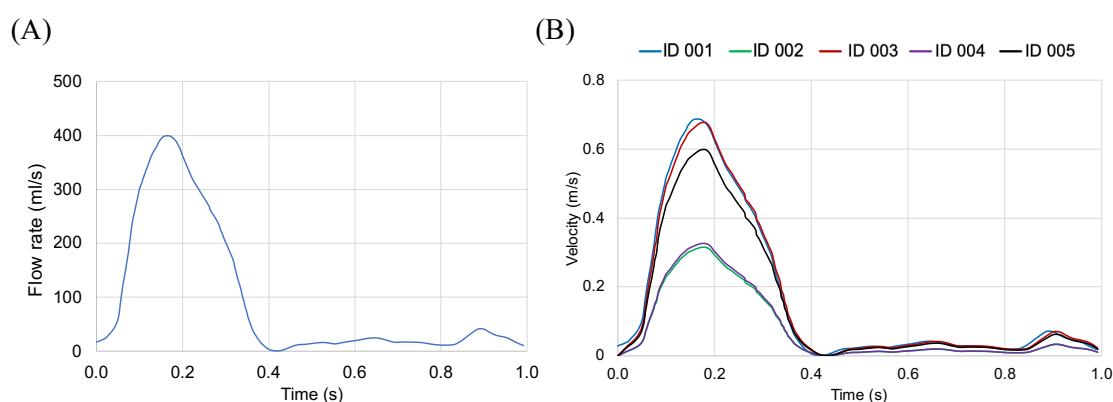


Figure 6.4. Pulsatile waveform applied as the inlet boundary condition to the aortic geometries. (A) Patient-specific flow rate waveform from a 51-year-old with a thoracic aortic aneurysm post TEVAR [356], and (B) corresponding velocity waveforms for each pre-operative patient.

### 6.3.5 Numerical Method

For all cases (pre- and post-operative), the governing equations of fluid motion were solved where the fluid was assumed to be Newtonian and incompressible. The assumption of blood as an incompressible, Newtonian fluid is common in the case of larger arteries, and while this assumption is not physiologically correct, qualitative wall shear stress patterns have proven to be comparable between Newtonian and non-Newtonian simulations [358]. The density and viscosity were set to  $1060 \text{ kg/m}^3$  and  $0.00371 \text{ Pa s}$ , respectively. Transient flow simulations were performed in Ansys Fluent (version 16.2) which utilises the finite-volume method to numerically solve the time-dependent Navier-Stokes equations.

### 6.3.6 Haemodynamic Parameters

The impact of elective thoracic endovascular repair on aortic haemodynamics was evaluated using several haemodynamic parameters. Wall shear stress, a biomechanical force influenced by fluid flow and arterial geometry, is a known factor in the pathogenesis of atherosclerosis [331]. Several studies have associated aortic sites where blood flow departs from a laminar, unidirectional pattern, and wall shear stresses are low and oscillatory, with locations of atherosclerosis development [290], [295], [305], [321], [359], [360]. The presence of disturbed shear was investigated in terms of luminal distributions of time averaged WSS (TAWSS), see equation 5.2. For all cases, the TAWSS was taken over the fifth and final cardiac cycle, and both the WSS and TAWSS were normalised with respect to the mean WSS at the inlet for each individual case.

## 6.4 Results

### 6.4.1 Morphological Characterisation

Analysis of morphological parameters before and after TEVAR provided a clear representation of the impact that the stenting procedure had in remodelling the aortic vessel. Dimensional (circumferential and axial) variation within and between patients was visualised through the use of Euclidean distance colourmaps (Figure 6.2). As expected, for all geometries, the Euclidean distance reduced at the site of the aneurysm after stent implantation (Figure 6.2B). Visually, this was most notable in patients 001, 003, and 004. Figure 6.5 demonstrates in more quantitative detail the changes in the normalised vessel radius along the centreline length of the five cases (Figure 6.5A, B). The radius and distance were normalised with respect to the maximum values. The pre-operative aorta was widest halfway along the vessel length with the

exception of patient 004. This indicated that in the majority of the patients (4 out of 5) the aneurysmal site was approximately halfway along the aorta. In patient 004, the aneurysm was located further downstream, approximately two thirds along the centreline length. For the post-operative cases (Figure 6.5B, D), there was clearly less disparity between the radius of the previous aneurysm site and the remainder of the aorta, with the exception of patient 004 where indications of ascending aorta dilatation remained. The peak in the average aortic radius (Figure 6.5C) averaged across the pre-operative patient group, reflecting the bulging aneurysm(s), corresponds to a peak in curvature at approximately 0.5 times the centreline length. Finally, the mean values for all morphological parameters, as presented in Table 6.3, were found to be lower post-operatively.

Table 6.3. Morphological analysis of the pre- and post-operative aorta of patients 001 – 005. The mean  $\pm$  standard deviation of the aortic surface area, curvature, torsion, and combined curvature-torsion score are provided.

	Surface area, mm <sup>2</sup>	Curvature, mm <sup>-1</sup>	Torsion, mm <sup>-1</sup>	Curvature-torsion score, mm <sup>-1</sup>
Pre-operative Mean $\pm$ SD	42,881 $\pm$ 15,884	0.0237 $\pm$ 0.0039	0.0193 $\pm$ 0.0196	0.2289 $\pm$ 0.1076
Post-operative Mean $\pm$ SD	40,064 $\pm$ 9235	0.0171 $\pm$ 0.0029	0.0160 $\pm$ 0.0089	0.0600 $\pm$ 0.0188

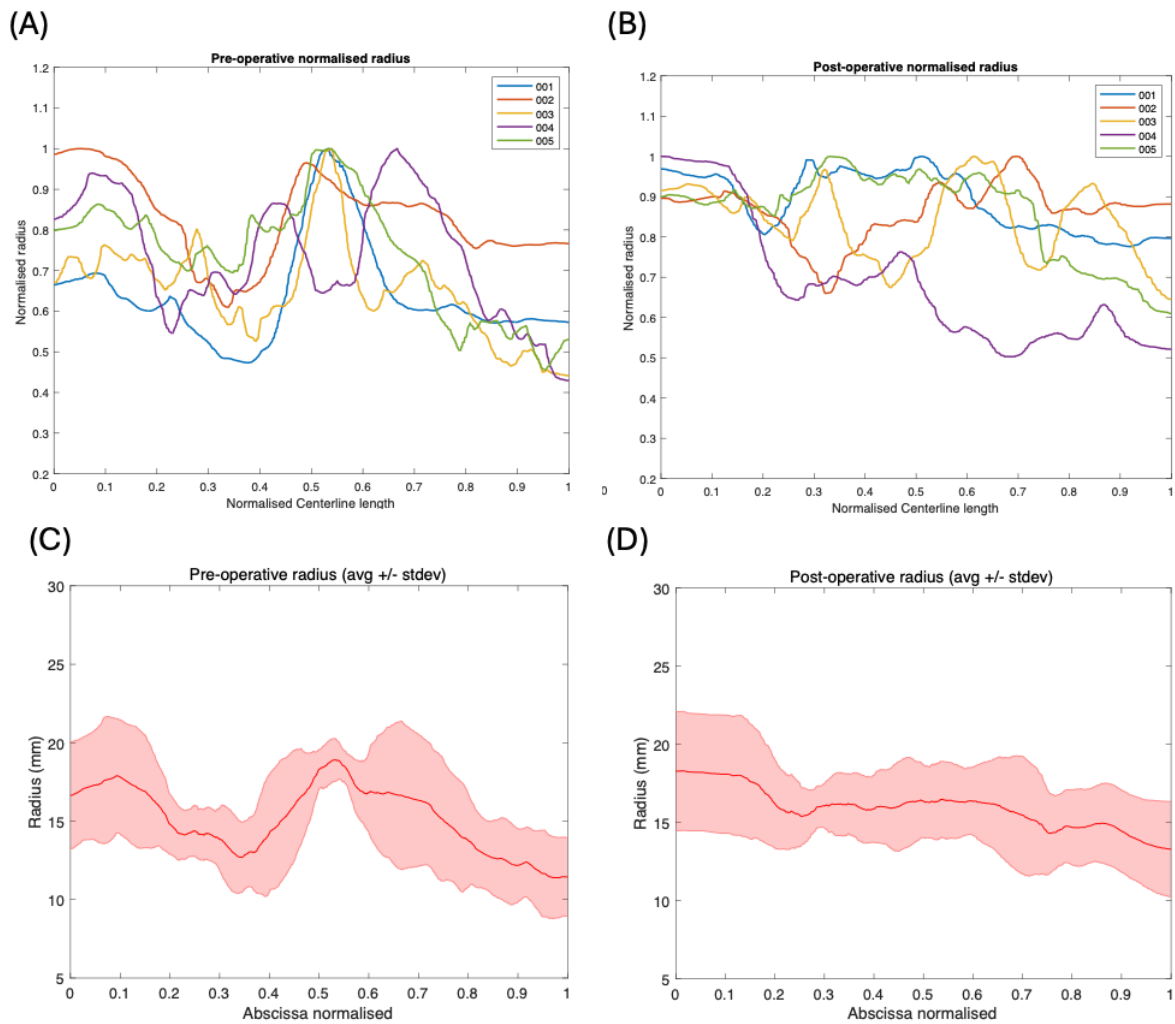


Figure 6.5. Non-dimensional vessel radius along the length of the aortic centreline for patients 001 – 005 both pre- (A) and post-operatively (B). Values normalised with respect to the maximum centreline length and radius. Pre-operative (C) and post-operative (D) radius plotted as patient average (solid line) and standard deviation (shaded area) (n=5).

## 6.4.2 Haemodynamic Parameters

### 6.4.2.1 Flow patterns

Instantaneous velocity streamlines pre- and post-surgical intervention (Figure 6.6A and B respectively) were compared for all models at peak systole (approximately 0.18 s). Blood flow patterns in the pre-operative models (Figure 6.6) were disturbed, particularly at the aneurysmal site. In patients 1 and 3, the aneurysm on the outer aortic wall led to localized low velocity and recirculating flow. In patients 4 and 5, the aneurysmal bulge was most prominent on the inner aortic wall and affected a larger length of the descending aorta. This resulted in a larger volume of flow defined by low velocity values as shown in Figure 6.6A. Patient 2 was the only

exception, where the fluid pre-operatively did not show any flow recirculation. After TEVAR, aortic flow patterns altered significantly in response to changes in vessel morphology, with the exception of patient 2 (Figure 6.6B). In all post-operative models, undisturbed blood flow patterns were observed. This was especially true at the site of aneurysm repair in the descending aorta of patients 001 and 003.

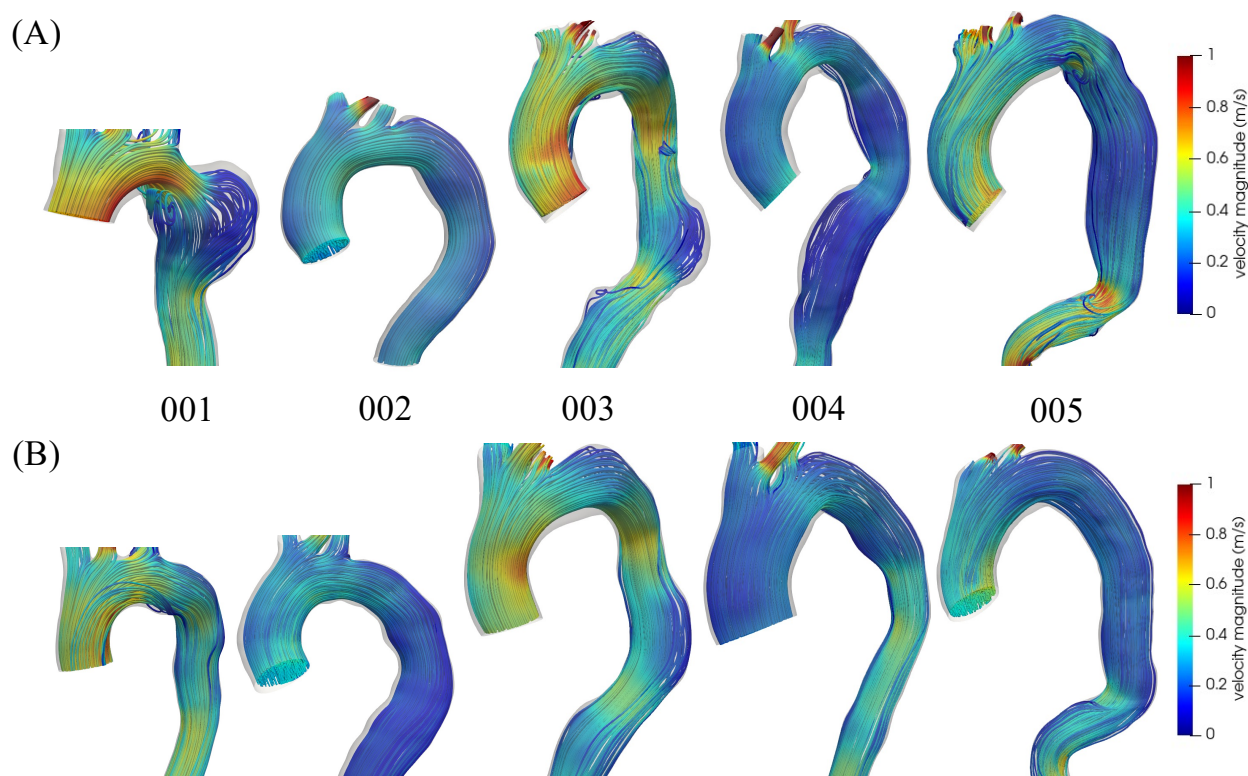


Figure 6.6. (A) Pre- operative and (B) post-operative instantaneous velocity streamlines at peak systole (0.18 s) in the cardiac cycle. Velocity streamlines coloured according to magnitude (0 – 1 m/s). Geometries not to scale.

For a detailed analysis of peak-systolic flow in the aneurysm, a cross-sectional plane was taken at the location of maximum aneurysmal diameter in the pre-operative geometries (see example for patient 1 in Figure 6.7), and along the corresponding centreline length in the post-operative geometries (Figure 6.7B). In-plane velocity vectors were compared before and after TEVAR, where the left- and right-hand side of each cross-section corresponds to the inner and outer curvature of the aorta, and the top and bottom correspond to the posterior and anterior wall respectively. The velocity magnitude scale was reduced to 0 – 0.15 m/s to account for the lower velocity values at the aneurysm site. Before surgical intervention, multiple regions of vortical flow were present in the aortic aneurysm of all patients, with the exception of patient 2 (Figure

6.7). In patient 1, vortices were found at both the inner and anterior walls, separated by a region of high velocity in the centre of the aneurysm. In patient 3, vortices were located at the outer wall with high velocity flow at the inner wall. In patient 4, a pair of small counter-rotating vortices were seen near the posterior wall and the cross-section centre. In patient 5, a large region of near-zero recirculating flow was present at the posterior-outer wall. In contrast to patients 1 and 3, the overall cross-sectional velocities seen in patients 4 and 5 were very low (0 – 0.05 m/s). Post-TEVAR, the vortical in-plane flow patterns at the aneurysmal site were replaced with predominantly undisturbed flow. In patient 3, a small region of recirculatory flow remained near the anterior vessel wall. For patient 2, there was no visible difference between the pre- and post-operative flow in the cross-sectional slice (Figure 6.7).

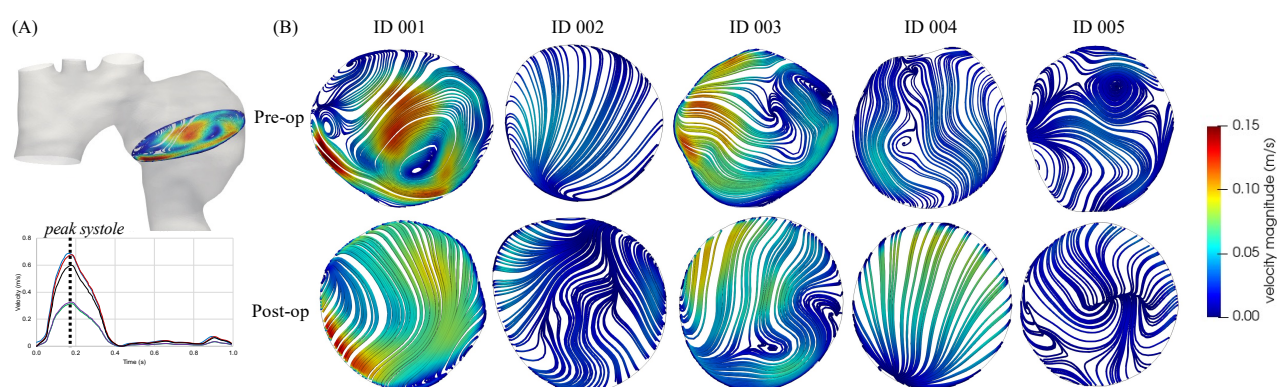


Figure 6.7. Pre- and post-operative in-plane velocity streamlines (B) at a cross-sectional slice of maximum diameter in the aneurysm (exemplified on patient 1) at peak systole (A). Velocity streamlines coloured according to magnitude (0 – 0.15 m/s). Cross-sections not to scale.

#### 6.4.2.2 Time-averaged wall shear stress

The time-averaged wall shear stress contours pre- and post-TEVAR are shown in Figure 6.8A and B respectively. At first glance, the TAWSS distribution on the pre-operative aortae was highly heterogenous (Figure 6.8A) when compared to the post-operative aortae (Figure 6.8B). This was especially true for patients 1 and 3 with the smallest overall vessel diameters. For all pre-operative geometries, very low TAWSS values (0 – 0.5 Pa) were localized at the aneurysm site (Figure 6.8A), immediately followed by a region of higher TAWSS at the distal end of the aneurysm. This pattern coincided with the large increase in vessel diameter (due to the aneurysm) and the sharp return to the true vessel diameter. In the ascending aorta and arch of the pre-operative geometries, TAWSS values were greater at the inner wall and around the

branch junctions. In the remainder of the descending aorta, TAWSS was highly varied in both distribution and values.

Post-operatively, higher TAWSS remained at the inner wall of the ascending aorta and arch, and at the proximal side of branch junctions, in patient 1 (Figure 6.8B). A visible difference was seen in the descending aorta of patient 1, where the reduction in vessel diameter in response to TEVAR was accompanied by less extreme TAWSS values ( $> 2$  Pa) (Figure 6.8B). The trends seen between the pre- and post-operative geometries of patient 1 were almost mirrored in patient 3 (Figure 6.8B). Very little change was seen between the pre- and post-operative geometries (Figure 6.8A and B) of patient 4 in the ascending aorta, arch, and branch regions, albeit the overall TAWSS magnitude was marginally lower post-operatively. However, a notable difference was seen in the descending aorta of patient 4 where very low TAWSS ( $\sim 0$  Pa) was replaced with more moderate values ( $0 - 1$  Pa). In patient 5, TAWSS values were reduced in the ascending, distal descending, and arch regions post-operatively, but remained largely unchanged in the proximal descending aorta (Figure 6.8B).

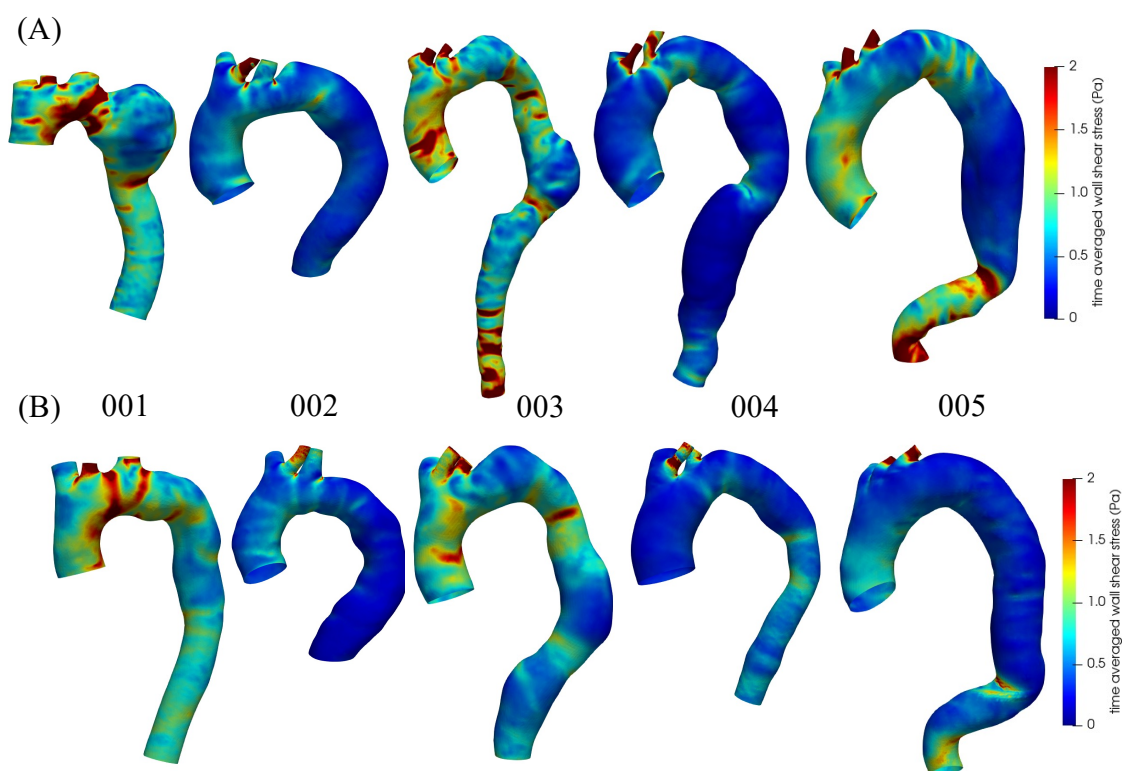


Figure 6.8. Anterior view of the (A) pre-operative and (B) post-operative time-averaged wall shear stress ( $0 - 2$  Pa). Geometries not to scale.

Quantitatively, a decrease in the average luminal surface wall shear stress at peak systole was observed for the majority of the post-TEVAR patients: patient 2 (0.0473 vs 0.0586 Pa), patient 3 (0.0702 vs 0.1185 Pa), patient 4 (0.0618 vs 0.0776 Pa), and patient 5 (0.0682 vs 0.1035 Pa). When comparing the pre- and post-operative group averages (0.0825 and 0.0633 Pa respectively), the post-operative wall shear stress was lower but not statistically significant ( $p = 0.183$ ). As expected, the same trend was seen for the time-averaged wall shear stress with pre- and post-operative averages of 0.0266 Pa and 0.0202 Pa ( $p = 0.117$ ) respectively.

## 6.5 Discussion

Technological advancements in the field of endovascular surgery have resulted in increased application of thoracic endovascular repair for a variety of thoracic aortic diseases. In particular, TEVAR has become an established alternative to open surgery in patients with a high operative risk and unclear overall life expectancy, or in the acutely unstable patient to achieve rapid aortic stabilisation [361]. For treatment planning and long-term outcomes of TEVAR, a crucial role is played by both the vascular morphology and the consequent haemodynamic environment [361]. To that end, we combined quantitative morphometry with a detailed analysis of local haemodynamic parameters to improve our understanding of the medium- and long-term outcome of patients undergoing TEVAR and support future clinical decisions.

In this study of five patients (3 males/2 females) with an average follow-up time of 21 months, our findings showed that after endovascular repair: (a) remodeling of the aortic vessel occurred in an extended area of the thoracic aorta, with the progressive return to more moderate diameters and changes in local curvature and torsion; (b) the aortic haemodynamics progressively returned to more physiological flow patterns, with vortical flow structures being reduced in the aneurysmal site; (c) TEVAR intervention had clear beneficial effects in reducing the luminal surface exposed to extremes of time-averaged wall shear stress, particularly in the descending aorta, but areas of very low TAWSS were present suggesting the risk of thrombosis inside the graft.

Previous studies have found a reduction in the wall shear stress and turbulent flow patterns post stent implantation [260], [362], and that post-operative remodelling of the aorta improved the

haemodynamic patterns in patients with aortic dissection [338]. In this study, we have shown a favourable return to more physiological flow structures and a decrease in the overall aortic wall shear stress post-TEVAR, in agreement with previous literature [260], [338], [362]. Moreover, we have demonstrated the post-operatively remodelling of the extended thoracic aorta, reflected in the decrease in the radius, surface area, curvature and torsion parameters. Overall, the present work has shown a clear correlation between the remodelling of the aorta post TEVAR, the return to undisturbed flow and the reduction in the TAWSS developed.

Clinically, our results complement the MRI images obtained post-operatively, providing information on hemodynamic parameters not available in routine clinical imaging. This study presents further evidence in favour of TEVAR for aortic aneurysms, however, and the use of CFD in pre-operative treatment planning, and post-operative investigation. However, these computational models would require additional refining before they could be fully implemented in clinical practice.

There are some limitations to this study including the choice of boundary conditions. As phase-contrast MRI data was not available for any patient, pre- or post-stent implantation, a pulsatile flow waveform was extracted from the literature for a 51-year-old male who underwent PC-MRI after elected TEVAR [356] and the time-dependent velocity waveform was derived for each patient relative to the inlet boundary surface area. Although not ideal, Gallo et al. [356], showed that the near-wall haemodynamics of a patient who underwent TEVAR were not significantly affected by different inflow waveforms. In addition, the effect of boundary conditions has been extensively studied in previous work [260], [363]. The second limitation was the assumptions of the arterial wall as rigid and blood as Newtonian, however these are reasonable as the deformation of the arterial wall is relatively small in the proximal aorta and the effects of non-Newtonian blood can be ignored in larger vessels [234], [261].

## 6.6 Conclusions

This study aims to address the complex interplay between vascular anatomy and blood flow, by investigating the pre- and post- operative environment in patient-specific models with abdominal aortic aneurysm. In summary, our results indicate that post-operative remodelling of the aorta (including decreased aortic curvature and torsion) after elective TEVAR for

thoracic aortic aneurysm repair improved haemodynamic patterns, reflected by undisturbed flow velocity and wall shear stress. The novelty of this study lies in the combined analysis of geometric and haemodynamic parameters in this group of patients. Future work would be to consider the stent structure in the computational analysis, and to extend this study to Turner syndrome patients.

# Chapter 7 Conclusions & Future Work

## 7.1 Conclusions

The aim of this thesis was to investigate morphological and haemodynamic features in healthy and diseased aortae, using computational fluid dynamic methods. Two patient groups were investigated throughout this research, the first being Turner syndrome children who are known to have a variety of aortic and cardiovascular abnormalities, and the second being adults with abdominal aortic aneurysms. The former was in collaboration with a local hospital (Queen Elizabeth University Hospital, Glasgow, UK), and the latter with the Advanced Thermofluids Optimization, Modelling, and Simulation (ATOMS) Laboratory (University of Toronto, Toronto, Canada). The work undertaken at the University of Toronto was through the UKRI-Canada Globalink Doctoral Exchange Scheme which was a competitive grant award.

The novelty of this work lies:

- (i) in the application of computational fluid dynamic methods to paediatric Turner syndrome patients. To the best of the authors knowledge, this thesis presents the first in-depth fluid dynamic analysis of Turner syndrome aorta, with reference to healthy age-matched females. The timing of this research is in line with the 2018 American Heart Association declaration of key research priorities surrounding Turner syndrome.
- (ii) the combined analysis of geometric and haemodynamic parameters in patients with TEVAR.

The objectives of this research were, first, to acquire cardiac imaging data at the location of the aorta for both patient groups, and to extract the three-dimensional geometric and flow information from this data to create patient-specific geometries and boundary conditions. Secondly, to characterise the morphology of the aortic arch geometries and perform statistical analysis on the morphological parameters. Thirdly, to solve the complex haemodynamic environment in three-dimensional patient-specific geometries of the aorta through computational fluid dynamic simulations, and to analyse the flow patterns and wall shear stresses. Finally, to determine the differences in morphology and haemodynamics between

healthy and Turner syndrome in Chapters 4 and 5, and between pre- and post-operative adults in Chapter 6.

This thesis contributes towards a better understanding of the haemodynamics in the aorta of Turner syndrome children as follows:

- (1) It highlights the importance of patient-specificity in numerical models of Turner syndrome haemodynamics.
- (2) It demonstrates the variation in aortic morphology in Turner syndrome girls, with all patients diagnosed with some form of structural and/or functional aortic abnormality.
- (3) It clearly shows the differences in morphological features between healthy volunteers and TS patients. Turner syndrome girls had overall greater values in ten out of fifteen parameters morphological parameters examined, as compared to the healthy children.
- (4) It correlates the higher curvature and torsion seen in Turner syndrome aorta with areas of complex secondary flow patterns and increased wall shear stress.
- (5) It highlights the association between obesity and aortic morphology in TS. The following measures of obesity and indicators of aortic morphology were significantly associated in Turner syndrome girls: body surface area and arch height ( $p = 0.03$ ), body surface area and arch height to width ratio ( $p = 0.05$ ), body surface area and aortic arch diameter ( $p = 0.04$ ), and weight and aortic arch diameter ( $p = 0.04$ ).
- (6) It qualitatively and quantitatively highlights the difference in wall shear stress patterns between healthy and TS girls. On TS aorta, wall shear stress patterns were elevated and highly heterogeneous, while on healthy aorta, wall shear stress patterns were relatively homogeneous.
- (7) It revealed a correlation between the presence of aortic abnormalities and disturbed flow in Turner syndrome girls, with the visualisation of multidirectional blood flow and wall shear stress (WSS) revealing an increase in vortical flow in the arch, supra-aortic vessels, and descending aorta.

The thesis further contributes to the field of haemodynamics in TEVAR as follows:

- (1) It aims to address the complex interplay between vascular anatomy and blood flow, by investigating the pre- and post- operative environment in patient-specific models with abdominal aortic aneurysm.

- (2) The results indicate that post-operative remodelling of the aorta (including decreased aortic curvature and torsion) after elective TEVAR for thoracic aortic aneurysm repair improved haemodynamic patterns, reflected by undisturbed flow velocity and wall shear stress.

## 7.2 Future Work

Several proposals can be made for future work that would increase the complexity of the simulations and could add to the flow characterisation of the aorta. In addition, including the wall motion could potentially produce different flow patterns in the patient-specific simulations, even though studies in large vessels have shown that the effect of wall motion is small [364]. Further studies could validate, and further extend, the findings presented in this thesis.

Similarly, aortic vascular resistance, compliance and inductance could be used in the outlets of the models to better represent the downstream conditions. That also requires optimisation of these values for every patient-specific model, so that flow diverted to each branch matches the clinically observed flow splits. Clinical data are therefore essential both for the reconstruction of the models, but also for the extraction of flow information. Computational results can greatly vary based on the boundary conditions, and therefore, it is important to have appropriate BCs to characterise the flow environment. In addition, clinical data are required to validate the computational outcomes. Further studies could compare clinical data with computational results and identify the model which better captures the flow development in the aorta.

Finally, this study is limited to a small number of subjects, and it could be extended to a larger cohort, and perhaps of different gender and age groups, to identify intraspecies variability. Longitudinal data are also missing and could be included in future studies.

The findings of this thesis may help clinicians understand the haemodynamic environment of each patient's particular anatomy and potentially disease progression. Furthermore, this work is hoped to benefit future research studies in the field.

# List of References

- [1] M. Silberbach *et al.*, ‘Cardiovascular Health in Turner Syndrome: A Scientific Statement From the American Heart Association’, *Circ. Genomic Precis. Med.*, vol. 11, no. 10, p. e000048, Oct. 2018, doi: 10.1161/HCG.0000000000000048.
- [2] K. Stochholm, S. Juul, K. Juel, R. W. Naeraa, and C. Højbjerg Gravholt, ‘Prevalence, Incidence, Diagnostic Delay, and Mortality in Turner Syndrome’, *J. Clin. Endocrinol. Metab.*, vol. 91, no. 10, pp. 3897–3902, Oct. 2006, doi: 10.1210/jc.2006-0558.
- [3] J. Nielsen and M. Wohler, ‘Chromosome abnormalities found among 34,910 newborn children: results from a 13-year incidence study in Aarhus, Denmark’, *Hum. Genet.*, vol. 87, no. 1, pp. 81–83, May 1991, doi: 10.1007/BF01213097.
- [4] J. Nielsen and I. Sillesen, ‘Incidence of chromosome aberrations among 11148 newborn children’, *Humangenetik*, vol. 30, no. 1, pp. 1–12, Oct. 1975, doi: 10.1007/BF00273626.
- [5] L. Johnston, R. Allen, A. Mason, and A. Kazakidi, ‘Morphological characterisation of pediatric Turner syndrome aortae: Insights from a small cohort study’, *Med. Eng. Phys.*, vol. 120, p. 104045, Oct. 2023, doi: 10.1016/j.medengphy.2023.104045.
- [6] L. Johnston, R. Allen, P. Hall Barrientos, A. Mason, and A. Kazakidi, ‘Hemodynamic Abnormalities in the Aorta of Turner Syndrome Girls’, *Front. Cardiovasc. Med.*, vol. 8, p. 670841, Jun. 2021, doi: 10.3389/fcvm.2021.670841.
- [7] H. H. Turner, ‘A SYNDROME OF INFANTILISM, CONGENITAL WEBBED NECK, AND CUBITUS VALGUS1’, *Endocrinology*, vol. 23, no. 5, pp. 566–574, Nov. 1938, doi: 10.1210/endo-23-5-566.
- [8] C. E. Ford, K. W. Jones, P. E. Polani, J. C. De Almeida, and J. H. Briggs, ‘A sex-chromosome anomaly in a case of gonadal dysgenesis (Turner’s syndrome)’, *Lancet Lond. Engl.*, vol. 1, no. 7075, pp. 711–713, Apr. 1959, doi: 10.1016/s0140-6736(59)91893-8.
- [9] C. A. Bondy and Turner Syndrome Study Group, ‘Care of girls and women with Turner syndrome: a guideline of the Turner Syndrome Study Group’, *J. Clin. Endocrinol. Metab.*, vol. 92, no. 1, pp. 10–25, Jan. 2007, doi: 10.1210/jc.2006-1374.
- [10] P. Saenger, ‘Turner’s syndrome’, *N. Engl. J. Med.*, vol. 335, no. 23, pp. 1749–1754, Dec. 1996, doi: 10.1056/NEJM199612053352307.
- [11] N. Shankar Kikkeri and S. Nagalli, ‘Turner Syndrome’, in *StatPearls*, Treasure Island (FL): StatPearls Publishing, 2021. Accessed: Nov. 02, 2021. [Online]. Available: <http://www.ncbi.nlm.nih.gov/books/NBK554621/>
- [12] K. H. Mortensen, N. H. Andersen, and C. H. Gravholt, ‘Cardiovascular phenotype in Turner syndrome--integrating cardiology, genetics, and endocrinology’, *Endocr. Rev.*, vol. 33, no. 5, pp. 677–714, Oct. 2012, doi: 10.1210/er.2011-1059.
- [13] Q. Zhong and L. C. Layman, ‘Genetic considerations in the patient with Turner syndrome-45,X with or without mosaicism’, *Fertil. Steril.*, vol. 98, no. 4, pp. 775–779, Oct. 2012, doi: 10.1016/j.fertnstert.2012.08.021.
- [14] M. B. Ranke and P. Saenger, ‘Turner’s syndrome’, *Lancet Lond. Engl.*, vol. 358, no. 9278, pp. 309–314, Jul. 2001, doi: 10.1016/S0140-6736(01)05487-3.
- [15] M. Ibarra-Ramírez and L. E. Martínez-de-Villarreal, ‘Clinical and genetic aspects of Turner’s syndrome’, *Med. Univ.*, vol. 18, no. 70, pp. 42–48, Jan. 2016, doi: 10.1016/j.rmu.2016.03.003.

- [16] K. Oktay *et al.*, ‘Fertility Preservation in Women with Turner Syndrome: A Comprehensive Review and Practical Guidelines’, *J. Pediatr. Adolesc. Gynecol.*, vol. 29, no. 5, pp. 409–416, Oct. 2016, doi: 10.1016/j.jpag.2015.10.011.
- [17] D. J. Wolff, D. L. Van Dyke, C. M. Powell, and Working Group of the ACMG Laboratory Quality Assurance Committee, ‘Laboratory guideline for Turner syndrome’, *Genet. Med. Off. J. Am. Coll. Med. Genet.*, vol. 12, no. 1, pp. 52–55, Jan. 2010, doi: 10.1097/GIM.0b013e3181c684b2.
- [18] T. M. K. Völkl, K. Degenhardt, A. Koch, D. Simm, H. G. Dörr, and H. Singer, ‘Cardiovascular anomalies in children and young adults with Ullrich-Turner syndrome the Erlangen experience’, *Clin. Cardiol.*, vol. 28, no. 2, pp. 88–92, Feb. 2005, doi: 10.1002/clc.4960280209.
- [19] L. Mazzanti and E. Cacciari, ‘Congenital heart disease in patients with Turner’s syndrome. Italian Study Group for Turner Syndrome (ISGTS)’, *J. Pediatr.*, vol. 133, no. 5, pp. 688–692, Nov. 1998, doi: 10.1016/s0022-3476(98)70119-2.
- [20] V. P. Sybert, ‘Cardiovascular malformations and complications in Turner syndrome’, *Pediatrics*, vol. 101, no. 1, p. E11, Jan. 1998, doi: 10.1542/peds.101.1.e11.
- [21] C. H. Gravholt, M. H. Viuff, S. Brun, K. Stochholm, and N. H. Andersen, ‘Turner syndrome: mechanisms and management’, *Nat. Rev. Endocrinol.*, vol. 15, no. 10, pp. 601–614, Oct. 2019, doi: 10.1038/s41574-019-0224-4.
- [22] K. McCarthy and C. A. Bondy, ‘Turner syndrome in childhood and adolescence’, *Expert Rev. Endocrinol. Metab.*, vol. 3, no. 6, pp. 771–775, Nov. 2008, doi: 10.1586/17446651.3.6.771.
- [23] V. B. Ho *et al.*, ‘Major vascular anomalies in Turner syndrome: prevalence and magnetic resonance angiographic features’, *Circulation*, vol. 110, no. 12, pp. 1694–1700, Sep. 2004, doi: 10.1161/01.CIR.0000142290.35842.B0.
- [24] V. Sachdev *et al.*, ‘Aortic valve disease in Turner syndrome’, *J. Am. Coll. Cardiol.*, vol. 51, no. 19, pp. 1904–1909, May 2008, doi: 10.1016/j.jacc.2008.02.035.
- [25] A.-S. Sillesen *et al.*, ‘Prevalence of Bicuspid Aortic Valve and Associated Aortopathy in Newborns in Copenhagen, Denmark’, *JAMA*, vol. 325, no. 6, p. 561, Feb. 2021, doi: 10.1001/jama.2020.27205.
- [26] S. Nistri, C. Basso, C. Marzari, P. Mormino, and G. Thiene, ‘Frequency of Bicuspid Aortic Valve in Young Male Conscripts by Echocardiogram’, *Am. J. Cardiol.*, vol. 96, no. 5, pp. 718–721, Sep. 2005, doi: 10.1016/j.amjcard.2005.04.051.
- [27] E. Klásková *et al.*, ‘Increased prevalence of bicuspid aortic valve in Turner syndrome links with karyotype: the crucial importance of detailed cardiovascular screening’, *J. Pediatr. Endocrinol. Metab. JPEM*, vol. 30, no. 3, pp. 319–325, Mar. 2017, doi: 10.1515/jpem-2016-0301.
- [28] Y. Dulac, C. Pienkowski, S. Abadir, M. Tauber, and P. Acar, ‘Cardiovascular abnormalities in Turner’s syndrome: what prevention?’, *Arch. Cardiovasc. Dis.*, vol. 101, no. 7–8, pp. 485–490, Aug. 2008, doi: 10.1016/j.acvd.2008.05.007.
- [29] G. M. Novaro, M. Mishra, and B. P. Griffin, ‘Incidence and echocardiographic features of congenital unicuspid aortic valve in an adult population’, *J. Heart Valve Dis.*, vol. 12, no. 6, pp. 674–678, Nov. 2003.
- [30] K. van Engelen *et al.*, ‘Bicuspid aortic valve morphology and associated cardiovascular abnormalities in fetal Turner syndrome: a pathomorphological study’, *Fetal Diagn. Ther.*, vol. 36, no. 1, pp. 59–68, 2014, doi: 10.1159/000357706.
- [31] L. J. Olivieri *et al.*, ‘Spectrum of aortic valve abnormalities associated with aortic dilation across age groups in Turner syndrome’, *Circ. Cardiovasc. Imaging*, vol. 6, no. 6, pp. 1018–1023, Nov. 2013, doi: 10.1161/CIRCIMAGING.113.000526.

- [32] M. G. D'Alfonso, A. Oddo, P. Stefano, and F. Mori, 'Unicuspid aortic valve in Turner syndrome, detected by 3D transoesophageal echocardiography: The usefulness of 3D echo in challenge diagnosis', *Echocardiogr. Mt. Kisco N*, vol. 37, no. 10, pp. 1691–1693, Oct. 2020, doi: 10.1111/echo.14854.
- [33] M. Essandoh, K. Castellon-Larios, A. Zuleta-Alarcon, J. G. Portillo, and J. A. Crestanello, 'Unicuspid Aortic Stenosis in a Patient with Turner Syndrome: A Case Report', *Front. Cardiovasc. Med.*, vol. 1, p. 14, 2014, doi: 10.3389/fcvm.2014.00014.
- [34] A. Bansal, S. Arora, D. Traub, and D. Haybron, 'Unicuspid aortic valve and aortic arch aneurysm in a patient with Turner syndrome', *Asian Cardiovasc. Thorac. Ann.*, vol. 16, no. 3, pp. 266–267, Jun. 2008, doi: 10.1177/021849230801600321.
- [35] B. Ece, H. Yiğit, E. Ergün, and P. N. Koşar, 'Elongated transverse aortic arch in subjects without turner syndrome: A preliminary computed tomography study', *Clin. Anat. N. Y. N*, vol. 31, no. 6, pp. 887–890, Sep. 2018, doi: 10.1002/ca.23209.
- [36] H. K. Kim *et al.*, 'Cardiovascular anomalies in Turner syndrome: spectrum, prevalence, and cardiac MRI findings in a pediatric and young adult population', *AJR Am. J. Roentgenol.*, vol. 196, no. 2, pp. 454–460, Feb. 2011, doi: 10.2214/AJR.10.4973.
- [37] K. H. Mortensen *et al.*, 'Abnormalities of the major intrathoracic arteries in Turner syndrome as revealed by magnetic resonance imaging', *Cardiol. Young*, vol. 20, no. 2, pp. 191–200, Apr. 2010, doi: 10.1017/S1047951110000041.
- [38] M. D. Kelly, 'Endoscopy and the aberrant right subclavian artery', *Am. Surg.*, vol. 73, no. 12, pp. 1259–1261, Dec. 2007.
- [39] V. Bastianon *et al.*, 'Mitral valve prolapse in Turner syndrome', *Eur. J. Pediatr.*, vol. 148, no. 6, pp. 533–534, Apr. 1989, doi: 10.1007/BF00441551.
- [40] R. Dalla Pozza *et al.*, 'QTc interval prolongation in children with Ulrich-Turner syndrome', *Eur. J. Pediatr.*, vol. 165, no. 12, pp. 831–837, Dec. 2006, doi: 10.1007/s00431-006-0194-0.
- [41] I. Noordman *et al.*, 'Phenotype in girls and women with Turner syndrome: Association between dysmorphic features, karyotype and cardio-aortic malformations', *Eur. J. Med. Genet.*, vol. 61, no. 6, pp. 301–306, Jun. 2018, doi: 10.1016/j.ejmg.2018.01.004.
- [42] J. E. Ostberg, J. A. S. Brookes, C. McCarthy, J. Halcox, and G. S. Conway, 'A comparison of echocardiography and magnetic resonance imaging in cardiovascular screening of adults with Turner syndrome', *J. Clin. Endocrinol. Metab.*, vol. 89, no. 12, pp. 5966–5971, Dec. 2004, doi: 10.1210/jc.2004-1090.
- [43] M. M. Fuchs *et al.*, 'Cardiovascular surgery in Turner syndrome - early outcome and long-term follow-up', *World J. Cardiol.*, vol. 12, no. 3, pp. 97–106, Mar. 2020, doi: 10.4330/wjc.v12.i3.97.
- [44] K. S. Zanjani, B. D. Thanopoulos, A. Peirone, L. Alday, and G. Giannakoulas, 'Usefulness of stenting in aortic coarctation in patients with the Turner syndrome', *Am. J. Cardiol.*, vol. 106, no. 9, pp. 1327–1331, Nov. 2010, doi: 10.1016/j.amjcard.2010.06.063.
- [45] H. R. Ravelo *et al.*, 'Coarctation resection in children with Turner's syndrome: a note of caution', *J. Thorac. Cardiovasc. Surg.*, vol. 80, no. 3, pp. 427–430, Sep. 1980.
- [46] R. Simsolo *et al.*, 'Long-term systemic hypertension in children after successful repair of coarctation of the aorta', *Am. Heart J.*, vol. 115, no. 6, pp. 1268–1273, Jun. 1988, doi: 10.1016/0002-8703(88)90020-8.
- [47] L. K. Bickerstaff *et al.*, 'Thoracic aortic aneurysms: a population-based study', *Surgery*, vol. 92, no. 6, pp. 1103–1108, Dec. 1982.

- [48] C. Højbjerg Gravholt *et al.*, ‘Clinical and epidemiological description of aortic dissection in Turner’s syndrome’, *Cardiol. Young*, vol. 16, no. 5, pp. 430–436, Oct. 2006, doi: 10.1017/S1047951106000928.
- [49] A. E. Lin *et al.*, ‘Aortic dilation, dissection, and rupture in patients with Turner syndrome’, *J. Pediatr.*, vol. 109, no. 5, pp. 820–826, Nov. 1986, doi: 10.1016/s0022-3476(86)80700-4.
- [50] W. H. Price and J. Wilson, ‘Dissection of the aorta in Turner’s syndrome’, *J. Med. Genet.*, vol. 20, no. 1, pp. 61–63, Feb. 1983, doi: 10.1136/jmg.20.1.61.
- [51] L. A. Matura, V. B. Ho, D. R. Rosing, and C. A. Bondy, ‘Aortic dilatation and dissection in Turner syndrome’, *Circulation*, vol. 116, no. 15, pp. 1663–1670, Oct. 2007, doi: 10.1161/CIRCULATIONAHA.106.685487.
- [52] S. Thunström, E. Krantz, E. Thunström, C. Hanson, I. Bryman, and K. Landin-Wilhelmsen, ‘Incidence of Aortic Dissection in Turner Syndrome’, *Circulation*, vol. 139, no. 24, pp. 2802–2804, Jun. 2019, doi: 10.1161/CIRCULATIONAHA.119.040552.
- [53] A. J. Asch, ‘Turner’s syndrome occurring with Horner’s syndrome. Seen with coarctation of the aorta and aortic aneurysm’, *Am. J. Dis. Child. 1960*, vol. 133, no. 8, pp. 827–830, Aug. 1979.
- [54] T. Fukui, ‘Management of acute aortic dissection and thoracic aortic rupture’, *J. Intensive Care*, vol. 6, p. 15, 2018, doi: 10.1186/s40560-018-0287-7.
- [55] P. G. Hagan *et al.*, ‘The International Registry of Acute Aortic Dissection (IRAD): new insights into an old disease’, *JAMA*, vol. 283, no. 7, pp. 897–903, Feb. 2000, doi: 10.1001/jama.283.7.897.
- [56] M. Carlson and M. Silberbach, ‘Dissection of the aorta in Turner syndrome: two cases and review of 85 cases in the literature’, *J. Med. Genet.*, vol. 44, no. 12, pp. 745–749, Dec. 2007, doi: 10.1136/jmg.2007.052019.
- [57] S. C. Wong, M. Cheung, and M. Zacharin, ‘Aortic dilatation and dissection in Turner syndrome: what we know, what we are unclear about and what we should do in clinical practice?’, *Int. J. Adolesc. Med. Health*, vol. 26, no. 4, pp. 469–488, 2014, doi: 10.1515/ijamh-2013-0336.
- [58] L. Cleemann *et al.*, ‘Aortic dimensions in girls and young women with turner syndrome: a magnetic resonance imaging study’, *Pediatr. Cardiol.*, vol. 31, no. 4, pp. 497–504, May 2010, doi: 10.1007/s00246-009-9626-8.
- [59] B. Donadille *et al.*, ‘Prevalence and progression of aortic dilatation in adult patients with Turner syndrome: a cohort study’, *Eur. J. Endocrinol.*, vol. 183, no. 4, pp. 463–470, Oct. 2020, doi: 10.1530/EJE-20-0284.
- [60] M. J. Roman, R. B. Devereux, R. Kramer-Fox, and J. O’Loughlin, ‘Two-dimensional echocardiographic aortic root dimensions in normal children and adults’, *Am. J. Cardiol.*, vol. 64, no. 8, pp. 507–512, Sep. 1989, doi: 10.1016/0002-9149(89)90430-x.
- [61] J. van den Berg, E. M. Bannink, P. A. Wielopolski, P. M. Pattynama, S. M. de Muinck Keizer-Schrama, and W. A. Helbing, ‘Aortic distensibility and dimensions and the effects of growth hormone treatment in the turner syndrome’, *Am. J. Cardiol.*, vol. 97, no. 11, pp. 1644–1649, Jun. 2006, doi: 10.1016/j.amjcard.2005.12.058.
- [62] C. A. Bondy, ‘Congenital cardiovascular disease in Turner syndrome’, *Congenit. Heart Dis.*, vol. 3, no. 1, pp. 2–15, Feb. 2008, doi: 10.1111/j.1747-0803.2007.00163.x.
- [63] E. Los, E. Quezada, Z. Chen, J. Lapidus, and M. Silberbach, ‘Pilot Study of Blood Pressure in Girls With Turner Syndrome: An Awareness Gap, Clinical Associations, and New Hypotheses’, *Hypertens. Dallas Tex 1979*, vol. 68, no. 1, pp. 133–136, Jul. 2016, doi: 10.1161/HYPERTENSIONAHA.115.07065.

- [64] B. E. Hjerrild *et al.*, ‘Thoracic aortopathy in Turner syndrome and the influence of bicuspid aortic valves and blood pressure: a CMR study’, *J. Cardiovasc. Magn. Reson. Off. J. Soc. Cardiovasc. Magn. Reson.*, vol. 12, p. 12, Mar. 2010, doi: 10.1186/1532-429X-12-12.
- [65] R. Sivasubramanian and K. E. Meyers, ‘Hypertension in Children and Adolescents with Turner Syndrome (TS), Neurofibromatosis 1 (NF1), and Williams Syndrome (WS)’, *Curr. Hypertens. Rep.*, vol. 23, no. 4, p. 18, Mar. 2021, doi: 10.1007/s11906-021-01136-7.
- [66] E. M. Freel and A. Mason, ‘Turner Syndrome: Unique Insights Into Estrogen Replacement and Cardiovascular Risk in a Unique Condition’, *Hypertension*, vol. 73, no. 1, pp. 42–44, Jan. 2019, doi: 10.1161/HYPERTENSIONAHA.118.12029.
- [67] K. De Groote *et al.*, ‘Abnormal aortic arch morphology in Turner syndrome patients is a risk factor for hypertension’, *Heart Vessels*, vol. 30, no. 5, pp. 618–625, Sep. 2015, doi: 10.1007/s00380-014-0529-0.
- [68] J. Wen *et al.*, ‘Impaired aortic distensibility and elevated central blood pressure in Turner Syndrome: a cardiovascular magnetic resonance study’, *J. Cardiovasc. Magn. Reson. Off. J. Soc. Cardiovasc. Magn. Reson.*, vol. 20, no. 1, p. 80, Dec. 2018, doi: 10.1186/s12968-018-0497-0.
- [69] C. H. Gravholt, S. Juul, R. W. Naeraa, and J. Hansen, ‘Morbidity in Turner syndrome’, *J. Clin. Epidemiol.*, vol. 51, no. 2, pp. 147–158, Feb. 1998, doi: 10.1016/s0895-4356(97)00237-0.
- [70] M. J. Schoemaker, A. J. Swerdlow, C. D. Higgins, A. F. Wright, P. A. Jacobs, and United Kingdom Clinical Cytogenetics Group, ‘Mortality in women with turner syndrome in Great Britain: a national cohort study’, *J. Clin. Endocrinol. Metab.*, vol. 93, no. 12, pp. 4735–4742, Dec. 2008, doi: 10.1210/jc.2008-1049.
- [71] P. W. Franks, R. L. Hanson, W. C. Knowler, M. L. Sievers, P. H. Bennett, and H. C. Looker, ‘Childhood obesity, other cardiovascular risk factors, and premature death’, *N. Engl. J. Med.*, vol. 362, no. 6, pp. 485–493, Feb. 2010, doi: 10.1056/NEJMoa0904130.
- [72] J. C. Han, D. A. Lawlor, and S. Y. S. Kimm, ‘Childhood obesity’, *Lancet Lond. Engl.*, vol. 375, no. 9727, pp. 1737–1748, May 2010, doi: 10.1016/S0140-6736(10)60171-7.
- [73] M. Elsheikh and G. S. Conway, ‘The impact of obesity on cardiovascular risk factors in Turner’s syndrome’, *Clin. Endocrinol. (Oxf.)*, vol. 49, no. 4, pp. 447–450, Oct. 1998, doi: 10.1046/j.1365-2265.1998.00552.x.
- [74] Y. Lebenthal *et al.*, ‘The Natural History of Metabolic Comorbidities in Turner Syndrome from Childhood to Early Adulthood: Comparison between 45,X Monosomy and Other Karyotypes’, *Front. Endocrinol.*, vol. 9, p. 27, 2018, doi: 10.3389/fendo.2018.00027.
- [75] K. Hanew, T. Tanaka, R. Horikawa, T. Hasegawa, K. Fujita, and S. Yokoya, ‘Women with Turner syndrome are at high risk of lifestyle-related disease -From questionnaire surveys by the Foundation for Growth Science in Japan’, *Endocr. J.*, vol. 63, no. 5, pp. 449–456, May 2016, doi: 10.1507/endocrj.EJ15-0288.
- [76] T. Reinehr, A. Lindberg, C. Toschke, J. Cara, D. Chrysis, and C. Camacho-Hübner, ‘Weight gain in Turner Syndrome: association to puberty induction? - longitudinal analysis of KIGS data’, *Clin. Endocrinol. (Oxf.)*, vol. 85, no. 1, pp. 85–91, Jul. 2016, doi: 10.1111/cen.13044.
- [77] C. H. Gravholt *et al.*, ‘Body composition is distinctly altered in Turner syndrome: relations to glucose metabolism, circulating adipokines, and endothelial adhesion molecules’, *Eur. J. Endocrinol.*, vol. 155, no. 4, pp. 583–592, Oct. 2006, doi: 10.1530/eje.1.02267.

- [78] R. L. Rosenfield, N. Devine, J. J. Hunold, N. Mauras, T. Moshang, and A. W. Root, 'Salutary effects of combining early very low-dose systemic estradiol with growth hormone therapy in girls with Turner syndrome', *J. Clin. Endocrinol. Metab.*, vol. 90, no. 12, pp. 6424–6430, Dec. 2005, doi: 10.1210/jc.2005-1081.
- [79] D. Nation and G. Wang, 'TEVAR: Endovascular Repair of the Thoracic Aorta', *Semin. Interv. Radiol.*, vol. 32, no. 03, pp. 265–271, Aug. 2015, doi: 10.1055/s-0035-1558824.
- [80] L. G. Svensson *et al.*, 'Expert Consensus Document on the Treatment of Descending Thoracic Aortic Disease Using Endovascular Stent-Grafts\*\*Expert Consensus Document on the Treatment of Descending Thoracic Aortic Disease Using Endovascular Stent-Grafts has been supported by Unrestricted Educational Grants from Cook, Inc and Medtronic, Inc.', *Ann. Thorac. Surg.*, vol. 85, no. 1, pp. S1–S41, Jan. 2008, doi: 10.1016/j.athoracsur.2007.10.099.
- [81] A. Le Huu *et al.*, 'Endovascular therapy for patients with heritable thoracic aortic disease', *Ann. Cardiothorac. Surg.*, vol. 11, no. 1, pp. 31–36, Jan. 2022, doi: 10.21037/acs-2021-taes-109.
- [82] D. Berdajs and M. I. Turina, 'Surgical Anatomy of the Aorta', in *Operative Anatomy of the Heart*, Berlin, Heidelberg: Springer Berlin Heidelberg, 2011, pp. 455–513. doi: 10.1007/978-3-540-69229-4\_11.
- [83] G. Oomen, *Anatomy of the human aortic arch*. 2016. [Online]. Available: <https://www.glenoomen.com/medical-scientific-illustration>
- [84] T. Krüger *et al.*, 'Ascending aortic elongation and the risk of dissection', *Eur. J. Cardiothorac. Surg.*, vol. 50, no. 2, pp. 241–247, Aug. 2016, doi: 10.1093/ejcts/ezw025.
- [85] M. Bäck, T. C. Gasser, J.-B. Michel, and G. Caligiuri, 'Biomechanical factors in the biology of aortic wall and aortic valve diseases', *Cardiovasc. Res.*, vol. 99, no. 2, pp. 232–241, Jul. 2013, doi: 10.1093/cvr/cvt040.
- [86] H. F. Galley and N. R. Webster, 'Physiology of the endothelium', *Br. J. Anaesth.*, vol. 93, no. 1, pp. 105–113, Jul. 2004, doi: 10.1093/bja/ae163.
- [87] Z. Tonar, P. Tomášek, P. Loskot, J. Janáček, M. Králíčková, and K. Witter, 'Vasa vasorum in the tunica media and tunica adventitia of the porcine aorta', *Ann. Anat. - Anat. Anz.*, vol. 205, pp. 22–36, May 2016, doi: 10.1016/j.aanat.2016.01.008.
- [88] G. Oomen, *Cross-section of the aorta*. 2014. [Online]. Available: <https://www.glenoomen.com/medical-scientific-illustration>
- [89] J. L. Cavalcante, J. A. C. Lima, A. Redheuil, and M. H. Al-Mallah, 'Aortic Stiffness', *J. Am. Coll. Cardiol.*, vol. 57, no. 14, pp. 1511–1522, Apr. 2011, doi: 10.1016/j.jacc.2010.12.017.
- [90] A. I. Moens, 'Over de voortplantingssnelheid van den pols', University of Leiden, 1877.
- [91] D. Korteweg, 'Over voortplantings-snelheid van golven in elastische buizen', University of Amsterdam, 1878.
- [92] K. C. Harris *et al.*, 'Biophysical Properties of the Aorta and Left Ventricle and Exercise Capacity in Obese Children', *Am. J. Cardiol.*, vol. 110, no. 6, pp. 897–901, Sep. 2012, doi: 10.1016/j.amjcard.2012.05.019.
- [93] G. S. Kassab, 'Biomechanics of the cardiovascular system: the aorta as an illustratory example', *J. R. Soc. Interface*, vol. 3, no. 11, pp. 719–740, Dec. 2006, doi: 10.1098/rsif.2006.0138.
- [94] D. A. Fox *et al.*, 'Non-invasive assessment of aortic stiffness and blood pressure in young Turner syndrome patients', *J. Pediatr. Endocrinol. Metab. JPEM*, vol. 32, no. 5, pp. 489–498, May 2019, doi: 10.1515/jpem-2018-0346.

- [95] M. Schäfer *et al.*, ‘Aortic stiffness in adolescent Turner and Marfan syndrome patients’, *Eur. J. Cardiothorac. Surg.*, vol. 54, no. 5, pp. 926–932, Nov. 2018, doi: 10.1093/ejcts/ezy168.
- [96] D. G. H. Devos *et al.*, ‘Proximal aortic stiffening in Turner patients may be present before dilation can be detected: a segmental functional MRI study’, *J. Cardiovasc. Magn. Reson.*, vol. 19, no. 1, p. 27, Dec. 2017, doi: 10.1186/s12968-017-0331-0.
- [97] Y. J. Heo, H. W. Jung, Y. A. Lee, C. H. Shin, and S. W. Yang, ‘Arterial stiffness in young women with Turner syndrome using cardio-ankle vascular index’, *Ann. Pediatr. Endocrinol. Metab.*, vol. 24, no. 3, pp. 158–163, Sep. 2019, doi: 10.6065/apem.2019.24.3.158.
- [98] H. W. Jung, S. M. Kim, H. Y. Kim, Y. A. Lee, S. W. Yang, and C. H. Shin, ‘A study of arterial stiffness in turner syndrome patients using cardio-ankle vascular index’, *Int. J. Pediatr. Endocrinol.*, vol. 2015, no. S1, pp. P82, 1687-9856-2015-S1-P82, Dec. 2015, doi: 10.1186/1687-9856-2015-S1-P82.
- [99] K. Hill *et al.*, ‘Blood Rheology’, in *Encyclopedia of Exercise Medicine in Health and Disease*, F. C. Mooren, Ed., Berlin, Heidelberg: Springer Berlin Heidelberg, 2012, pp. 128–131. doi: 10.1007/978-3-540-29807-6\_315.
- [100] G. S. Ohm, ‘Die galvanische Kette, mathematisch bearbeitet’, Berlin, 1827.
- [101] E. Nader *et al.*, ‘Blood Rheology: Key Parameters, Impact on Blood Flow, Role in Sickle Cell Disease and Effects of Exercise’, *Front. Physiol.*, vol. 10, p. 1329, Oct. 2019, doi: 10.3389/fphys.2019.01329.
- [102] D. Drikakis, M. Frank, and G. Tabor, ‘Multiscale Computational Fluid Dynamics’, *Energies*, vol. 12, no. 17, p. 3272, Aug. 2019, doi: 10.3390/en12173272.
- [103] J. D. Anderson, ‘Governing Equations of Fluid Dynamics’, in *Computational Fluid Dynamics*, J. F. Wendt, Ed., Berlin, Heidelberg: Springer Berlin Heidelberg, 1992, pp. 15–51. doi: 10.1007/978-3-662-11350-9\_2.
- [104] F. M. White, *Fluid mechanics*, 6th ed. in McGraw-Hill series in mechanical engineering. New York, NY: McGraw-Hill, 2009.
- [105] I. Newton, ‘Philosophiae Naturalis Principia Mathematica’, 1687.
- [106] R. L. Fournier, *Basic transport phenomena in biomedical engineering*, 2nd ed. New York: Taylor & Francis, 2007.
- [107] D. Ting, ‘Forced convection’, in *Thermofluids*, Elsevier, 2022, pp. 319–356. doi: 10.1016/B978-0-323-90626-5.00010-0.
- [108] Y. A. Çengel and J. M. Cimbala, *Fluid mechanics: fundamentals and applications*, 3. ed. New York, NY: McGraw-Hill, 2014.
- [109] C. G. Caro, Ed., *The Mechanics of the circulation*. Oxford; New York: Oxford University Press, 1978.
- [110] C. Loudon and A. Tordesillas, ‘The use of the dimensionless Womersley number to characterize the unsteady nature of internal flow’, *J. Theor. Biol.*, vol. 191, no. 1, pp. 63–78, Mar. 1998, doi: 10.1006/jtbi.1997.0564.
- [111] D. van der Linde *et al.*, ‘Birth Prevalence of Congenital Heart Disease Worldwide’, *J. Am. Coll. Cardiol.*, vol. 58, no. 21, pp. 2241–2247, Nov. 2011, doi: 10.1016/j.jacc.2011.08.025.
- [112] D. Mozaffarian *et al.*, ‘Heart Disease and Stroke Statistics—2015 Update: A Report From the American Heart Association’, *Circulation*, vol. 131, no. 4, Jan. 2015, doi: 10.1161/CIR.000000000000152.
- [113] T. Wang *et al.*, ‘Congenital Heart Disease and Risk of Cardiovascular Disease: A Meta-Analysis of Cohort Studies’, *J. Am. Heart Assoc.*, vol. 8, no. 10, p. e012030, May 2019, doi: 10.1161/JAHA.119.012030.

- [114] M. E. Oster *et al.*, ‘Comorbidities Among Young Adults with Congenital Heart Defects: Results from the Congenital Heart Survey To Recognize Outcomes, Needs, and well-being — Arizona, Arkansas, and Metropolitan Atlanta, 2016 – 2019’, *MMWR Morb. Mortal. Wkly. Rep.*, vol. 70, no. 6, pp. 197–201, Feb. 2021, doi: 10.15585/mmwr.mm7006a3.
- [115] S. S. Virani *et al.*, ‘Heart Disease and Stroke Statistics—2021 Update: A Report From the American Heart Association’, *Circulation*, vol. 143, no. 8, Feb. 2021, doi: 10.1161/CIR.0000000000000950.
- [116] C. Capelli *et al.*, ‘Patient-specific simulations for planning treatment in congenital heart disease’, *Interface Focus*, vol. 8, no. 1, p. 20170021, Feb. 2018, doi: 10.1098/rsfs.2017.0021.
- [117] M. Boumpouli, A. Kazakidi, M. Danton, and T. Gourlay, ‘Hemodynamics in the pulmonary bifurcation in relation to adults with congenital heart disease: effect of branching angle and origin’, *6th Eur. Conf. Comput. Mech.-7th Eur. Conf. Comput. Fluid Dyn.*, pp. 1–12, 2018.
- [118] L. Johnston, R. Allen, P. Hall Barrientos, A. Mason, and A. Kazakidi, ‘Computational haemodynamics in turner syndrome patient-specific aortae with PC-MRI obtained boundary conditions’, *Heart*, p. 106, Feb. 2020.
- [119] E. Girდაuskas, M. A. Borger, M.-A. Secknus, G. Girდაuskas, and T. Kuntze, ‘Is aortopathy in bicuspid aortic valve disease a congenital defect or a result of abnormal hemodynamics? A critical reappraisal of a one-sided argument’, *Eur. J. Cardiothorac. Surg.*, vol. 39, no. 6, pp. 809–814, Jun. 2011, doi: 10.1016/j.ejcts.2011.01.001.
- [120] S. Mei, F. S. N. de Souza Júnior, M. Y. S. Kuan, N. C. Green, and D. M. Espino, ‘Hemodynamics through the congenitally bicuspid aortic valve: a computational fluid dynamics comparison of opening orifice area and leaflet orientation’, *Perfusion*, vol. 31, no. 8, pp. 683–690, Nov. 2016, doi: 10.1177/0267659116656775.
- [121] A. Kazakidi, S. J. Sherwin, and P. D. Weinberg, ‘Effect of Reynolds number and flow division on patterns of haemodynamic wall shear stress near branch points in the descending thoracic aorta’, *J. R. Soc. Interface*, vol. 6, no. 35, pp. 539–548, Jun. 2009, doi: 10.1098/rsif.2008.0323.
- [122] A. Kazakidi, A. M. Plata, S. J. Sherwin, and P. D. Weinberg, ‘Effect of reverse flow on the pattern of wall shear stress near arterial branches’, *J. R. Soc. Interface*, vol. 8, no. 64, pp. 1594–1603, Nov. 2011, doi: 10.1098/rsif.2011.0108.
- [123] A. Arzani, P. Dyverfeldt, T. Ebbers, and S. C. Shadden, ‘In Vivo Validation of Numerical Prediction for Turbulence Intensity in an Aortic Coarctation’, *Ann. Biomed. Eng.*, vol. 40, no. 4, pp. 860–870, Apr. 2012, doi: 10.1007/s10439-011-0447-6.
- [124] A. Menon, T. J. Eddinger, H. Wang, D. C. Wendell, J. M. Toth, and J. F. LaDisa, ‘Altered hemodynamics, endothelial function, and protein expression occur with aortic coarctation and persist after repair’, *Am. J. Physiol. Heart Circ. Physiol.*, vol. 303, no. 11, pp. H1304–1318, Dec. 2012, doi: 10.1152/ajpheart.00420.2012.
- [125] L. Goubergrits *et al.*, ‘MRI-based computational fluid dynamics for diagnosis and treatment prediction: Clinical validation study in patients with coarctation of aorta: MRI-Based CFD Diagnosis’, *J. Magn. Reson. Imaging*, vol. 41, no. 4, pp. 909–916, Apr. 2015, doi: 10.1002/jmri.24639.
- [126] K. Ralovich *et al.*, ‘Noninvasive hemodynamic assessment, treatment outcome prediction and follow-up of aortic coarctation from MR imaging: Noninvasive assessment of coarctation from MRI’, *Med. Phys.*, vol. 42, no. 5, pp. 2143–2156, Apr. 2015, doi: 10.1118/1.4914856.

- [127] D. Cosentino *et al.*, ‘Patient-specific computational models to support interventional procedures: a case study of complex aortic re-coarctation’, *EuroIntervention*, vol. 11, no. 6, pp. 669–672, Oct. 2015, doi: 10.4244/EIJY15M09\_03.
- [128] M. Szopos *et al.*, ‘Computational modeling of blood flow in the aorta—insights into eccentric dilatation of the ascending aorta after surgery for coarctation’, *J. Thorac. Cardiovasc. Surg.*, vol. 148, no. 4, pp. 1572–1582, Oct. 2014, doi: 10.1016/j.jtcvs.2013.11.055.
- [129] J. S. Coogan, F. P. Chan, C. A. Taylor, and J. A. Feinstein, ‘Computational fluid dynamic simulations of aortic coarctation comparing the effects of surgical- and stent-based treatments on aortic compliance and ventricular workload’, *Catheter. Cardiovasc. Interv.*, vol. 77, no. 5, pp. 680–691, Apr. 2011, doi: 10.1002/ccd.22878.
- [130] C. A. Taylor and C. A. Figueroa, ‘Patient-Specific Modeling of Cardiovascular Mechanics’, *Annu. Rev. Biomed. Eng.*, vol. 11, no. 1, pp. 109–134, Aug. 2009, doi: 10.1146/annurev.bioeng.10.061807.160521.
- [131] A. N. Cookson, D. J. Doorly, and S. J. Sherwin, ‘Mixing Through Stirring of Steady Flow in Small Amplitude Helical Tubes’, *Ann. Biomed. Eng.*, vol. 37, no. 4, pp. 710–721, Apr. 2009, doi: 10.1007/s10439-009-9636-y.
- [132] C. A. Taylor *et al.*, ‘Predictive medicine: computational techniques in therapeutic decision-making’, *Comput. Aided Surg. Off. J. Int. Soc. Comput. Aided Surg.*, vol. 4, no. 5, pp. 231–247, 1999, doi: 10.1002/(SICI)1097-0150(1999)4:5<231::AID-IGS1>3.0.CO;2-Z.
- [133] E. L. Bove, M. R. de Leval, F. Migliavacca, R. Balossino, and G. Dubini, ‘Toward optimal hemodynamics: computer modeling of the Fontan circuit’, *Pediatr. Cardiol.*, vol. 28, no. 6, pp. 477–481, 2007, doi: 10.1007/s00246-007-9009-y.
- [134] A. L. Marsden *et al.*, ‘Evaluation of a novel Y-shaped extracardiac Fontan baffle using computational fluid dynamics’, *J. Thorac. Cardiovasc. Surg.*, vol. 137, no. 2, pp. 394–403.e2, Feb. 2009, doi: 10.1016/j.jtcvs.2008.06.043.
- [135] C. A. Taylor, T. A. Fonte, and J. K. Min, ‘Computational Fluid Dynamics Applied to Cardiac Computed Tomography for Noninvasive Quantification of Fractional Flow Reserve’, *J. Am. Coll. Cardiol.*, vol. 61, no. 22, pp. 2233–2241, Jun. 2013, doi: 10.1016/j.jacc.2012.11.083.
- [136] P. D. Morris *et al.*, ‘Computational fluid dynamics modelling in cardiovascular medicine’, *Heart*, vol. 102, no. 1, pp. 18–28, Jan. 2016, doi: 10.1136/heartjnl-2015-308044.
- [137] D. A. Steinman, J. B. Thomas, H. M. Ladak, J. S. Milner, B. K. Rutt, and J. D. Spence, ‘Reconstruction of carotid bifurcation hemodynamics and wall thickness using computational fluid dynamics and MRI’, *Magn. Reson. Med.*, vol. 47, no. 1, pp. 149–159, Jan. 2002, doi: 10.1002/mrm.10025.
- [138] R. A. Gray and P. Pathmanathan, ‘Patient-Specific Cardiovascular Computational Modeling: Diversity of Personalization and Challenges’, *J Cardiovasc. Transl. Res.*, vol. 11, no. 2, pp. 80–88, Apr. 2018, doi: 10.1007/s12265-018-9792-2.
- [139] S. Numata *et al.*, ‘Blood flow analysis of the aortic arch using computational fluid dynamics’, *Eur. J. Cardiothorac. Surg.*, vol. 49, no. 6, pp. 1578–1585, Jun. 2016, doi: 10.1093/ejcts/ezv459.
- [140] E. L. Manchester, S. Pirola, M. Y. Salmasi, D. P. O’Regan, T. Athanasiou, and X. Y. Xu, ‘Analysis of Turbulence Effects in a Patient-Specific Aorta with Aortic Valve Stenosis’, *Cardiovasc. Eng. Technol.*, vol. 12, no. 4, pp. 438–453, Aug. 2021, doi: 10.1007/s13239-021-00536-9.

- [141] A. D. Caballero and S. Laín, ‘A Review on Computational Fluid Dynamics Modelling in Human Thoracic Aorta’, *Cardiovasc. Eng. Technol.*, vol. 4, no. 2, pp. 103–130, Jun. 2013, doi: 10.1007/s13239-013-0146-6.
- [142] J. Febina, M. Y. Sikkandar, and N. M. Sudharsan, ‘Wall Shear Stress Estimation of Thoracic Aortic Aneurysm Using Computational Fluid Dynamics’, *Comput. Math. Methods Med.*, vol. 2018, pp. 1–12, Jun. 2018, doi: 10.1155/2018/7126532.
- [143] W. Jeong and J. Seong, ‘Comparison of effects on technical variances of computational fluid dynamics (CFD) software based on finite element and finite volume methods’, *Int. J. Mech. Sci.*, vol. 78, pp. 19–26, Oct. 2013, doi: <https://doi.org/10.1016/j.ijmecsci.2013.10.017>.
- [144] K. A. Barbee, ‘Role of Subcellular Shear–Stress Distributions in Endothelial Cell Mechanotransduction’, *Ann. Biomed. Eng.*, vol. 30, no. 4, pp. 472–482, Apr. 2002, doi: 10.1114/1.1467678.
- [145] K. M. Saqr *et al.*, ‘Physiologic blood flow is turbulent’, *Sci. Rep.*, vol. 10, no. 1, p. 15492, Dec. 2020, doi: 10.1038/s41598-020-72309-8.
- [146] A. F. Stalder *et al.*, ‘Assessment of flow instabilities in the healthy aorta using flow-sensitive MRI’, *J. Magn. Reson. Imaging*, vol. 33, no. 4, pp. 839–846, Apr. 2011, doi: 10.1002/jmri.22512.
- [147] J. Lantz, R. Gårdhagen, and M. Karlsson, ‘Quantifying turbulent wall shear stress in a subject specific human aorta using large eddy simulation’, *Med. Eng. Phys.*, vol. 34, no. 8, pp. 1139–1148, Oct. 2012, doi: 10.1016/j.medengphy.2011.12.002.
- [148] V. Mancini, A. W. Bergersen, J. Vierendeels, P. Segers, and K. Valen-Sendstad, ‘High-Frequency Fluctuations in Post-stenotic Patient Specific Carotid Stenosis Fluid Dynamics: A Computational Fluid Dynamics Strategy Study’, *Cardiovasc. Eng. Technol.*, vol. 10, no. 2, pp. 277–298, Jun. 2019, doi: 10.1007/s13239-019-00410-9.
- [149] R. M. Lancellotti, C. Vergara, L. Valdetaro, S. Bose, and A. Quarteroni, ‘Large eddy simulations for blood dynamics in realistic stenotic carotids: LES for hemodynamics in stenotic carotids’, *Int. J. Numer. Methods Biomed. Eng.*, vol. 33, no. 11, p. e2868, Nov. 2017, doi: 10.1002/cnm.2868.
- [150] C. Vergara, D. Le Van, M. Quadrio, L. Formaggia, and M. Domanin, ‘Large eddy simulations of blood dynamics in abdominal aortic aneurysms’, *Med. Eng. Phys.*, vol. 47, pp. 38–46, Sep. 2017, doi: 10.1016/j.medengphy.2017.06.030.
- [151] U. Morbiducci *et al.*, ‘Outflow Conditions for Image-Based Hemodynamic Models of the Carotid Bifurcation: Implications for Indicators of Abnormal Flow’, *J. Biomech. Eng.*, vol. 132, no. 9, p. 091005, Sep. 2010, doi: 10.1115/1.4001886.
- [152] U. Morbiducci, R. Ponzini, D. Gallo, C. Bignardi, and G. Rizzo, ‘Inflow boundary conditions for image-based computational hemodynamics: Impact of idealized versus measured velocity profiles in the human aorta’, *J. Biomech.*, vol. 46, no. 1, pp. 102–109, Jan. 2013, doi: 10.1016/j.jbiomech.2012.10.012.
- [153] D. Gallo *et al.*, ‘On the Use of In Vivo Measured Flow Rates as Boundary Conditions for Image-Based Hemodynamic Models of the Human Aorta: Implications for Indicators of Abnormal Flow’, *Ann. Biomed. Eng.*, vol. 40, no. 3, pp. 729–741, Mar. 2012, doi: 10.1007/s10439-011-0431-1.
- [154] I. C. Campbell, J. Ries, S. S. Dhawan, A. A. Quyyumi, W. R. Taylor, and J. N. Oshinski, ‘Effect of Inlet Velocity Profiles on Patient-Specific Computational Fluid Dynamics Simulations of the Carotid Bifurcation’, *J. Biomech. Eng.*, vol. 134, no. 5, p. 051001, May 2012, doi: 10.1115/1.4006681.

- [155] M. A. Van Doormaal *et al.*, ‘Haemodynamics in the mouse aortic arch computed from MRI-derived velocities at the aortic root’, *J. R. Soc. Interface*, vol. 9, no. 76, pp. 2834–2844, Nov. 2012, doi: 10.1098/rsif.2012.0295.
- [156] M. McElroy and A. Keshmiri, ‘Impact of Using Conventional Inlet/Outlet Boundary Conditions on Haemodynamic Metrics in a Subject-Specific Rabbit Aorta’, *Proc. Inst. Mech. Eng. [H]*, vol. 232, no. 2, pp. 103–113, Feb. 2018, doi: 10.1177/0954411917699237.
- [157] C. Chnafa, O. Brina, V. M. Pereira, and D. A. Steinman, ‘Better Than Nothing: A Rational Approach for Minimizing the Impact of Outflow Strategy on Cerebrovascular Simulations’, *Am. J. Neuroradiol.*, vol. 39, no. 2, pp. 337–343, Feb. 2018, doi: 10.3174/ajnr.A5484.
- [158] C. Cheng *et al.*, ‘Large variations in absolute wall shear stress levels within one species and between species’, *Atherosclerosis*, vol. 195, no. 2, pp. 225–235, Dec. 2007, doi: 10.1016/j.atherosclerosis.2006.11.019.
- [159] R. S. Reneman and A. P. G. Hoeks, ‘Wall shear stress as measured in vivo: consequences for the design of the arterial system’, *Med. Biol. Eng. Comput.*, vol. 46, no. 5, pp. 499–507, May 2008, doi: 10.1007/s11517-008-0330-2.
- [160] M. Zamir, P. Sinclair, and T. H. Wonnacott, ‘Relation between diameter and flow in major branches of the arch of the aorta’, *J. Biomech.*, vol. 25, no. 11, pp. 1303–1310, Nov. 1992, doi: 10.1016/0021-9290(92)90285-9.
- [161] A. M. Malek, S. L. Alper, and S. Izumo, ‘Hemodynamic shear stress and its role in atherosclerosis’, *JAMA*, vol. 282, no. 21, pp. 2035–2042, Dec. 1999, doi: 10.1001/jama.282.21.2035.
- [162] J. M. Dolan, J. Kolega, and H. Meng, ‘High Wall Shear Stress and Spatial Gradients in Vascular Pathology: A Review’, *Ann. Biomed. Eng.*, vol. 41, no. 7, pp. 1411–1427, Jul. 2013, doi: 10.1007/s10439-012-0695-0.
- [163] C. G. Caro, J. M. Fitz-Gerald, and R. C. Schroter, ‘Arterial wall shear and distribution of early atheroma in man’, *Nature*, vol. 223, no. 5211, pp. 1159–1160, Sep. 1969, doi: 10.1038/2231159a0.
- [164] Y. S. Chatzizisis, A. U. Coskun, M. Jonas, E. R. Edelman, C. L. Feldman, and P. H. Stone, ‘Role of endothelial shear stress in the natural history of coronary atherosclerosis and vascular remodeling: molecular, cellular, and vascular behavior’, *J. Am. Coll. Cardiol.*, vol. 49, no. 25, pp. 2379–2393, Jun. 2007, doi: 10.1016/j.jacc.2007.02.059.
- [165] P. F. Davies, ‘Hemodynamic shear stress and the endothelium in cardiovascular pathophysiology’, *Nat. Clin. Pract. Cardiovasc. Med.*, vol. 6, no. 1, pp. 16–26, Jan. 2009, doi: 10.1038/ncpcardio1397.
- [166] C. K. Zarins, D. P. Giddens, B. K. Bharadvaj, V. S. Sottiurai, R. F. Mabon, and S. Glagov, ‘Carotid bifurcation atherosclerosis. Quantitative correlation of plaque localization with flow velocity profiles and wall shear stress’, *Circ. Res.*, vol. 53, no. 4, pp. 502–514, Oct. 1983, doi: 10.1161/01.res.53.4.502.
- [167] D. N. Ku, D. P. Giddens, D. J. Phillips, and D. E. Strandness, ‘Hemodynamics of the normal human carotid bifurcation: in vitro and in vivo studies’, *Ultrasound Med. Biol.*, vol. 11, no. 1, pp. 13–26, Feb. 1985, doi: 10.1016/0301-5629(85)90003-1.
- [168] M. H. Friedman, O. J. Deters, C. B. Barger, G. M. Hutchins, and F. F. Mark, ‘Shear-dependent thickening of the human arterial intima’, *Atherosclerosis*, vol. 60, no. 2, pp. 161–171, May 1986, doi: 10.1016/0021-9150(86)90008-0.
- [169] J. J. Wentzel, Y. S. Chatzizisis, F. J. H. Gijssen, G. D. Giannoglou, C. L. Feldman, and P. H. Stone, ‘Endothelial shear stress in the evolution of coronary atherosclerotic plaque

- and vascular remodelling: current understanding and remaining questions’, *Cardiovasc. Res.*, vol. 96, no. 2, pp. 234–243, Nov. 2012, doi: 10.1093/cvr/cvs217.
- [170] N. T. Jenkins, J. Padilla, L. J. Boyle, D. P. Credeur, M. H. Laughlin, and P. J. Fadel, ‘Disturbed Blood Flow Acutely Induces Activation and Apoptosis of the Human Vascular Endothelium’, *Hypertension*, vol. 61, no. 3, pp. 615–621, Mar. 2013, doi: 10.1161/HYPERTENSIONAHA.111.00561.
- [171] C.-Y. Wen, A.-S. Yang, L.-Y. Tseng, and J.-W. Chai, ‘Investigation of Pulsatile Flowfield in Healthy Thoracic Aorta Models’, *Ann. Biomed. Eng.*, vol. 38, no. 2, pp. 391–402, Feb. 2010, doi: 10.1007/s10439-009-9835-6.
- [172] L. Goubergrits, U. Kertzsch, B. Schöneberg, E. Wellnhofer, C. Petz, and H.-C. Hege, ‘CFD analysis in an anatomically realistic coronary artery model based on non-invasive 3D imaging: comparison of magnetic resonance imaging with computed tomography’, *Int. J. Cardiovasc. Imaging*, vol. 24, no. 4, pp. 411–421, Apr. 2008, doi: 10.1007/s10554-007-9275-z.
- [173] J. Chen, E. Gutmark, G. Mylavarapu, P. F. Backeljauw, and I. Gutmark-Little, ‘Numerical investigation of mass transport through patient-specific deformed aortae’, *J. Biomech.*, vol. 47, no. 2, pp. 544–552, Jan. 2014, doi: 10.1016/j.jbiomech.2013.10.031.
- [174] R. Arnold, M. Neu, D. Hirtler, C. Gimpel, M. Markl, and J. Geiger, ‘Magnetic resonance imaging 4-D flow-based analysis of aortic hemodynamics in Turner syndrome’, *Pediatr. Radiol.*, vol. 47, no. 4, pp. 382–390, Apr. 2017, doi: 10.1007/s00247-016-3767-8.
- [175] L. Prah Wittberg, S. van Wyk, L. Fuchs, E. Gutmark, P. Backeljauw, and I. Gutmark-Little, ‘Effects of aortic irregularities on blood flow’, *Biomech. Model. Mechanobiol.*, vol. 15, no. 2, pp. 345–360, Apr. 2016, doi: 10.1007/s10237-015-0692-y.
- [176] L. Prah Wittberg, S. van Wyk, L. Fuchs, E. Gutmark, P. Backeljauw, and I. Gutmark-Little, ‘Effects of aortic irregularities on blood flow’, *Biomech. Model. Mechanobiol.*, vol. 15, no. 2, pp. 345–360, 2016, doi: 10.1007/s10237-015-0692-y.
- [177] R. A. Gray and P. Pathmanathan, ‘Patient-Specific Cardiovascular Computational Modeling: Diversity of Personalization and Challenges’, *J Cardiovasc. Transl. Res.*, vol. 11, no. 2, pp. 80–88, Apr. 2018, doi: 10.1007/s12265-018-9792-2.
- [178] D. Bluestein, ‘Utilizing Computational Fluid Dynamics in Cardiovascular Engineering and Medicine-What You Need to Know. Its Translation to the Clinic/Bedside: Invited Editorial’, *Artif. Organs*, vol. 41, no. 2, pp. 117–121, Feb. 2017, doi: 10.1111/aor.12914.
- [179] F. Moukalled, L. Mangani, and M. Darwish, *The Finite Volume Method in Computational Fluid Dynamics: An Advanced Introduction with OpenFOAM® and Matlab*, vol. 113. in Fluid Mechanics and Its Applications, vol. 113. Cham: Springer International Publishing, 2016. doi: 10.1007/978-3-319-16874-6.
- [180] G. Chen, Q. Xiong, P. J. Morris, E. G. Paterson, A. Sergeev, and Y.-C. Wang, ‘OpenFOAM for Computational Fluid Dynamics’, *Not. Am. Math. Soc.*, vol. 61, no. 4, p. 354, Apr. 2014, doi: 10.1090/noti1095.
- [181] A. Fuchs, N. Berg, and L. Prah Wittberg, ‘Pulsatile Aortic Blood Flow - a Critical Assessment of Boundary Conditions’, *J. Eng. Sci. Med. Diagn. Ther.*, Oct. 2020, doi: 10.1115/1.4048978.
- [182] J. Casacuberta, *Hemodynamics in the thoracic aorta using OpenFOAM: 4d PCMRI versus CFD*. Barcelona: International Center for Numerical Methods in Engineering, 2015.
- [183] Z. Malecha *et al.*, ‘GPU-based simulation of 3D blood flow in abdominal aorta using OpenFOAM’, *Arch. Mech.*, vol. 63, no. 2, pp. 137–161, 2011.

- [184] M. Lui, S. Martino, M. Salerno, and M. Quadrio, 'On the Turbulence Modeling of Blood Flow in a Stenotic Vessel', *J. Biomech. Eng.*, vol. 142, no. 1, p. 011009, Jan. 2020, doi: 10.1115/1.4044029.
- [185] S. I. S. Pinto, E. Doutel, J. B. L. M. Campos, and J. M. Miranda, 'Blood Analog Fluid Flow in Vessels with Stenosis: Development of an Openfoam Code to Simulate Pulsatile Flow and Elasticity of the Fluid', *APCBEE Procedia*, vol. 7, pp. 73–79, 2013, doi: 10.1016/j.apcbee.2013.08.015.
- [186] S. Srinivasan and D. Madathil, '3-dimensional computational study of blood flow in pathophysiologically affected arteries simulated in OpenFOAM', in *2016 8th Cairo International Biomedical Engineering Conference (CIBEC)*, Cairo, Egypt: IEEE, Dec. 2016, pp. 35–38. doi: 10.1109/CIBEC.2016.7836114.
- [187] H. Jasak, 'OpenFOAM : Open source CFD in research and industry', *Int. J. Nav. Archit. Ocean Eng.*, vol. 1, no. 2, pp. 89–94, Dec. 2009, doi: 10.3744/JNAOE.2009.1.2.089.
- [188] C. J. Greenshields and H. G. Weller, *Notes on computational fluid dynamics: general principles*. Reading, UK: CFD Direct Limited, 2022.
- [189] E. Makris, P. Neofytou, S. Tsangaris, and C. Housiadas, 'A novel method for the generation of multi-block computational structured grids from medical imaging of arterial bifurcations', *Med. Eng. Phys.*, vol. 34, no. 8, pp. 1157–1166, Oct. 2012, doi: 10.1016/j.medengphy.2011.12.004.
- [190] 'COMSOL Multiphysics: Reference Manual'. [Online]. Available: [https://doc.comsol.com/5.5/doc/com.comsol.help.comsol/COMSOL\\_ReferenceManual.pdf](https://doc.comsol.com/5.5/doc/com.comsol.help.comsol/COMSOL_ReferenceManual.pdf)
- [191] A. Lintermann, 'Computational Meshing for CFD Simulations', in *Clinical and Biomedical Engineering in the Human Nose*, K. Inthavong, N. Singh, E. Wong, and J. Tu, Eds., in *Biological and Medical Physics, Biomedical Engineering.*, Singapore: Springer Singapore, 2021, pp. 85–115. doi: 10.1007/978-981-15-6716-2\_6.
- [192] A. Field, 'What is the benefit of a polyhedral mesh?' Accessed: Apr. 02, 2022. [Online]. Available: <https://community.sw.siemens.com/s/article/JC-4-332>
- [193] M. Menut *et al.*, 'Comparison between a generalized Newtonian model and a network-type multiscale model for hemodynamic behavior in the aortic arch: Validation with 4D MRI data for a case study', *J. Biomech.*, vol. 73, pp. 119–126, May 2018, doi: 10.1016/j.jbiomech.2018.03.038.
- [194] C. Karmonik *et al.*, 'Longitudinal computational fluid dynamics study of aneurysmal dilatation in a chronic DeBakey type III aortic dissection', *J. Vasc. Surg.*, vol. 56, no. 1, pp. 260-263.e1, Jul. 2012, doi: 10.1016/j.jvs.2012.02.064.
- [195] J. Febina, M. Y. Sikkandar, and N. M. Sudharsan, 'Wall Shear Stress Estimation of Thoracic Aortic Aneurysm Using Computational Fluid Dynamics', *Comput. Math. Methods Med.*, vol. 2018, 2018, doi: 10.1155/2018/7126532.
- [196] 'Simcenter STAR-CCM+ meshing solutions'. Accessed: Apr. 02, 2022. [Online]. Available: <https://www.cosmositalia.it/wp-content/software/doc/siemens/starccm/Siemens%20SW%20Simcenter%20STAR%20CCM+%20meshing%20solutions%20Fact%20Sheet.pdf>
- [197] H. Schlichting and K. Gersten, *Boundary-layer theory*, 8th rev. and enl. Ed. Berlin ; New York: Springer, 2000.
- [198] S. W. Churchill, 'Friction factor equation spans all fluid-flow regimes', *Chem Eng*, vol. 84, no. 24, pp. 91–92, 1997.
- [199] H. Ye, J. Chen, Y. Pang, Y. Liu, and Y. Zheng, 'Fast advancing layer method for viscous mesh generation', *Chin. J. Aeronaut.*, vol. 36, no. 9, pp. 133–150, Sep. 2023, doi: 10.1016/j.cja.2023.05.018.

- [200] J. H. Ferziger and M. Perić, *Computational methods for fluid dynamics*, 3rd, rev. ed ed. Berlin ; New York: Springer, 2002.
- [201] B. E. Rapp, ‘Finite Element Method’, in *Microfluidics: Modelling, Mechanics and Mathematics*, Elsevier, 2017, pp. 655–678. doi: 10.1016/B978-1-4557-3141-1.50032-0.
- [202] L. Chen, ‘Finite-Volume Methods’, in *Computational Engineering — Introduction to Numerical Methods*, Berlin/Heidelberg: Springer-Verlag, 2011, pp. 77–105. doi: 10.1007/3-540-30686-2\_4.
- [203] J. Peiró and S. Sherwin, ‘Finite Difference, Finite Element and Finite Volume Methods for Partial Differential Equations’, in *Handbook of Materials Modeling*, S. Yip, Ed., Dordrecht: Springer Netherlands, 2005, pp. 2415–2446. doi: 10.1007/978-1-4020-3286-8\_127.
- [204] F. Otto, ‘Die Grundform des arteriellen Pulses.’, in *Z Biol.*, 1899, pp. 483–526.
- [205] G. Landes, ‘Einige untersuchungen an elektrischen analogieschaltungen zum kreislaufsystem’, *Z Biol*, 1943, pp. 418–429.
- [206] G. N. Jager, N. Westerhof, and A. Noordergraaf, ‘Oscillatory Flow Impedance in Electrical Analog of Arterial System:: Representation of Sleeve Effect and Non-Newtonian Properties of Blood’, *Circ. Res.*, vol. 16, no. 2, pp. 121–133, Feb. 1965, doi: 10.1161/01.RES.16.2.121.
- [207] N. Stergiopoulos, B. E. Westerhof, and N. Westerhof, ‘Total arterial inertance as the fourth element of the windkessel model’, *Am. J. Physiol.-Heart Circ. Physiol.*, vol. 276, no. 1, pp. H81–H88, Jan. 1999, doi: 10.1152/ajpheart.1999.276.1.H81.
- [208] Y. Shi, P. Lawford, and R. Hose, ‘Review of Zero-D and 1-D Models of Blood Flow in the Cardiovascular System’, *Biomed. Eng. OnLine*, vol. 10, no. 1, p. 33, Dec. 2011, doi: 10.1186/1475-925X-10-33.
- [209] J. Alastruey Arimon, ‘Numerical modelling of pulse wave propagation in the cardiovascular system: development, validation and clinical applications’, Imperial College London, 2006.
- [210] S. Malatos, ‘Advances in Low-Dimensional Mathematical Modeling of the Human Cardiovascular System’, *J. Hypertens. Manag.*, vol. 2, no. 2, Dec. 2016, doi: 10.23937/2474-3690/1510017.
- [211] R. Rehman, V. S. Yelamanchili, and A. N. Makaryus, ‘Cardiac Imaging’, in *StatPearls*, Treasure Island (FL): StatPearls Publishing, 2023. Accessed: May 19, 2023. [Online]. Available: <http://www.ncbi.nlm.nih.gov/books/NBK448128/>
- [212] V. Caselles, F. Cattani, T. Coll, and F. Dibos, ‘A geometric model for active contours in image processing’, *Numer. Math.*, vol. 66, no. 1, pp. 1–31, Dec. 1993, doi: 10.1007/BF01385685.
- [213] V. Caselles, R. Kimmel, and G. Sapiro, ‘Geodesic Active Contours’, *Int. J. Comput. Vis.*, vol. 22, no. 1, pp. 61–79, 1997, doi: 10.1023/A:1007979827043.
- [214] Song Chun Zhu and A. Yuille, ‘Region competition: unifying snakes, region growing, and Bayes/MDL for multiband image segmentation’, *IEEE Trans. Pattern Anal. Mach. Intell.*, vol. 18, no. 9, pp. 884–900, Sep. 1996, doi: 10.1109/34.537343.
- [215] W. E. Lorensen and H. E. Cline, ‘Marching cubes: A high resolution 3D surface construction algorithm’, *ACM SIGGRAPH Comput. Graph.*, vol. 21, no. 4, pp. 163–169, Aug. 1987, doi: 10.1145/37402.37422.
- [216] G. Pennati, F. Migliavacca, G. Dubini, R. Pietrabissa, and M. R. De Leval, ‘A mathematical model of circulation in the presence of the bidirectional cavopulmonary anastomosis in children with a univentricular heart’, *Med. Eng. Phys.*, vol. 19, no. 3, pp. 223–234, Apr. 1997, doi: 10.1016/S1350-4533(96)00071-9.

- [217] F. Migliavacca, M. R. de Leval, G. Dubini, R. Pietrabissa, and R. Fumero, ‘Computational fluid dynamic simulations of cavopulmonary connections with an extracardiac lateral conduit’, *Med. Eng. Phys.*, vol. 21, no. 3, pp. 187–193, Apr. 1999, doi: 10.1016/s1350-4533(99)00042-9.
- [218] F. Migliavacca *et al.*, ‘Multiscale modelling in biofluidynamics: application to reconstructive paediatric cardiac surgery’, *J. Biomech.*, vol. 39, no. 6, pp. 1010–1020, 2006, doi: 10.1016/j.jbiomech.2005.02.021.
- [219] K. Laganà *et al.*, ‘Multiscale modeling of the cardiovascular system: application to the study of pulmonary and coronary perfusions in the univentricular circulation’, *J. Biomech.*, vol. 38, no. 5, pp. 1129–1141, May 2005, doi: 10.1016/j.jbiomech.2004.05.027.
- [220] E. L. Bove *et al.*, ‘Use of mathematic modeling to compare and predict hemodynamic effects of the modified Blalock–Taussig and right ventricle–pulmonary artery shunts for hypoplastic left heart syndrome’, *J. Thorac. Cardiovasc. Surg.*, vol. 136, no. 2, pp. 312–320.e2, Aug. 2008, doi: 10.1016/j.jtcvs.2007.04.078.
- [221] A. Baretta *et al.*, ‘Virtual surgeries in patients with congenital heart disease: a multi-scale modelling test case’, *Philos. Transact. A Math. Phys. Eng. Sci.*, vol. 369, no. 1954, pp. 4316–4330, Nov. 2011, doi: 10.1098/rsta.2011.0130.
- [222] F. N. Van De Vosse, ‘Mathematical modelling of the cardiovascular system’, *J. Eng. Math.*, vol. 47, no. 3/4, pp. 175–183, Dec. 2003, doi: 10.1023/B:ENGI.0000007986.69547.5a.
- [223] Y. Bazilevs, M.-C. Hsu, D. J. Benson, S. Sankaran, and A. L. Marsden, ‘Computational fluid–structure interaction: methods and application to a total cavopulmonary connection’, *Comput. Mech.*, vol. 45, no. 1, pp. 77–89, Dec. 2009, doi: 10.1007/s00466-009-0419-y.
- [224] K. S. Hunter, J. A. Feinstein, D. D. Ivy, and R. Shandas, ‘Computational Simulation of the Pulmonary Arteries and its Role in the Study of Pediatric Pulmonary Hypertension’, *Prog. Pediatr. Cardiol.*, vol. 30, no. 1–2, pp. 63–69, Dec. 2010, doi: 10.1016/j.ppedcard.2010.09.008.
- [225] J. Donea, A. Huerta, J.-P. Ponthot, and A. Rodríguez-Ferran, ‘Arbitrary Lagrangian-Eulerian Methods’, in *Encyclopedia of Computational Mechanics Second Edition*, E. Stein, R. De Borst, and T. J. R. Hughes, Eds., Chichester, UK: John Wiley & Sons, Ltd, 2017, pp. 1–23. doi: 10.1002/9781119176817.ecm2009.
- [226] C. S. Peskin, ‘Flow patterns around heart valves: A numerical method’, *J. Comput. Phys.*, vol. 10, no. 2, pp. 252–271, Oct. 1972, doi: 10.1016/0021-9991(72)90065-4.
- [227] T. J. R. Hughes, W. K. Liu, and T. K. Zimmermann, ‘Lagrangian-Eulerian finite element formulation for incompressible viscous flows’, *Comput. Methods Appl. Mech. Eng.*, vol. 29, no. 3, pp. 329–349, Dec. 1981, doi: 10.1016/0045-7825(81)90049-9.
- [228] H. H. Hu, ‘Direct simulation of flows of solid-liquid mixtures’, *Int. J. Multiph. Flow*, vol. 22, no. 2, pp. 335–352, Apr. 1996, doi: 10.1016/0301-9322(95)00068-2.
- [229] Bhakade, Suraj, S. Kumbhar, Y. Mohite, and P. Kengar, ‘A Review on Fluid Structure Interaction Analysis Methodology.’, *Int. J. Trend Res. Dev.*, pp. 2394–9333, 2016.
- [230] A. Kazakidi, D. P. Tsakiris, D. Angelidis, F. Sotiropoulos, and J. A. Ekaterinaris, ‘CFD study of aquatic thrust generation by an octopus-like arm under intense prescribed deformations’, *Comput. Fluids*, vol. 115, pp. 54–65, Jul. 2015, doi: 10.1016/j.compfluid.2015.03.009.
- [231] R. J. LeVeque and Z. Li, ‘Immersed Interface Methods for Stokes Flow with Elastic Boundaries or Surface Tension’, *SIAM J. Sci. Comput.*, vol. 18, no. 3, pp. 709–735, May 1997, doi: 10.1137/S1064827595282532.

- [232] A. Gilmanov and F. Sotiropoulos, ‘A hybrid Cartesian/immersed boundary method for simulating flows with 3D, geometrically complex, moving bodies’, *J. Comput. Phys.*, vol. 207, no. 2, pp. 457–492, Aug. 2005, doi: 10.1016/j.jcp.2005.01.020.
- [233] F. Chalard, S. Ferey, C. Teinturier, and G. Kalifa, ‘Aortic dilatation in Turner syndrome: the role of MRI in early recognition’, *Pediatr. Radiol.*, vol. 35, no. 3, pp. 323–326, Mar. 2005, doi: 10.1007/s00247-004-1359-5.
- [234] L. Johnston, M. Boumpouli, and A. Kazakidi, ‘Hemodynamics in the Aorta and Pulmonary Arteries of Congenital Heart Disease Patients: A Mini Review’, *J. Cardiol. Cardiovasc. Sci.*, vol. 5, no. 2, pp. 1–5, Jun. 2021, doi: 10.29245/2578-3025/2021/2.1213.
- [235] WRITING COMMITTEE MEMBERS *et al.*, ‘2010 ACCF/AHA/AATS/ACR/ASA/SCA/SCAI/SIR/STS/SVM Guidelines for the Diagnosis and Management of Patients With Thoracic Aortic Disease: Executive Summary: A Report of the American College of Cardiology Foundation/American Heart Association Task Force on Practice Guidelines, American Association for Thoracic Surgery, American College of Radiology, American Stroke Association, Society of Cardiovascular Anesthesiologists, Society for Cardiovascular Angiography and Interventions, Society of Interventional Radiology, Society of Thoracic Surgeons, and Society for Vascular Medicine’, *Circulation*, vol. 121, no. 13, pp. 1544–1579, Apr. 2010, doi: 10.1161/CIR.0b013e3181d47d48.
- [236] C. H. Gravholt *et al.*, ‘Clinical practice guidelines for the care of girls and women with Turner syndrome: proceedings from the 2016 Cincinnati International Turner Syndrome Meeting’, *Eur. J. Endocrinol.*, vol. 177, no. 3, pp. G1–G70, Sep. 2017, doi: 10.1530/EJE-17-0430.
- [237] A. Marin, J. R. Weir-McCall, D. J. Webb, E. J. R. van Beek, and S. Mirsadraee, ‘Imaging of cardiovascular risk in patients with Turner’s syndrome’, *Clin. Radiol.*, vol. 70, no. 8, pp. 803–814, Aug. 2015, doi: 10.1016/j.crad.2015.03.009.
- [238] B. M. Lippe and M. D. Kogut, ‘Aortic rupture in gonadal dysgenesis’, *J. Pediatr.*, vol. 80, no. 5, p. 895, May 1972, doi: 10.1016/S0022-3476(72)80162-8.
- [239] M. Carlson, N. Airhart, L. Lopez, and M. Silberbach, ‘Moderate aortic enlargement and bicuspid aortic valve are associated with aortic dissection in Turner syndrome: report of the international turner syndrome aortic dissection registry’, *Circulation*, vol. 126, no. 18, pp. 2220–2226, Oct. 2012, doi: 10.1161/CIRCULATIONAHA.111.088633.
- [240] H. Corbitt, C. Maslen, S. Prakash, S. A. Morris, and M. Silberbach, ‘Allometric considerations when assessing aortic aneurysms in Turner syndrome: Implications for activity recommendations and medical decision-making’, *Am. J. Med. Genet. A.*, vol. 176, no. 2, pp. 277–282, Feb. 2018, doi: 10.1002/ajmg.a.38584.
- [241] L. Lanzarini *et al.*, ‘Aortic dimensions in Turner’s syndrome: two-dimensional echocardiography versus magnetic resonance imaging’, *J. Cardiovasc. Med.*, vol. 8, no. 6, pp. 428–437, Jun. 2007, doi: 10.2459/01.JCM.0000269716.33435.d3.
- [242] D. Gallo *et al.*, ‘Cardiovascular morphometry with high-resolution 3D magnetic resonance: First application to left ventricle diastolic dysfunction’, *Med. Eng. Phys.*, vol. 47, pp. 64–71, Sep. 2017, doi: 10.1016/j.medengphy.2017.03.011.
- [243] L. Antiga, M. Piccinelli, L. Botti, B. Ene-Iordache, A. Remuzzi, and D. A. Steinman, ‘An image-based modeling framework for patient-specific computational hemodynamics’, *Med. Biol. Eng. Comput.*, vol. 46, no. 11, p. 1097, Nov. 2008, doi: 10.1007/s11517-008-0420-1.
- [244] D. R. Subramaniam *et al.*, ‘Continuous measurement of aortic dimensions in Turner syndrome: a cardiovascular magnetic resonance study’, *J. Cardiovasc. Magn. Reson. Off.*

- J. Soc. Cardiovasc. Magn. Reson.*, vol. 19, no. 1, p. 20, Feb. 2017, doi: 10.1186/s12968-017-0336-8.
- [245] A. Arzani, G.-Y. Suh, R. L. Dalman, and S. C. Shadden, ‘A longitudinal comparison of hemodynamics and intraluminal thrombus deposition in abdominal aortic aneurysms’, *Am. J. Physiol.-Heart Circ. Physiol.*, vol. 307, no. 12, pp. H1786–H1795, Dec. 2014, doi: 10.1152/ajpheart.00461.2014.
- [246] M. Piccinelli, A. Veneziani, D. A. Steinman, A. Remuzzi, and L. Antiga, ‘A Framework for Geometric Analysis of Vascular Structures: Application to Cerebral Aneurysms’, *IEEE Trans. Med. Imaging*, vol. 28, no. 8, pp. 1141–1155, Aug. 2009, doi: 10.1109/TMI.2009.2021652.
- [247] M. Boufi *et al.*, ‘Morphological Analysis of Healthy Aortic Arch’, *Eur. J. Vasc. Endovasc. Surg.*, vol. 53, no. 5, pp. 663–670, May 2017, doi: 10.1016/j.ejvs.2017.02.023.
- [248] A. Redheuil *et al.*, ‘Age-Related Changes in Aortic Arch Geometry’, *J. Am. Coll. Cardiol.*, vol. 58, no. 12, pp. 1262–1270, Sep. 2011, doi: 10.1016/j.jacc.2011.06.012.
- [249] J. Sugawara, K. Hayashi, T. Yokoi, and H. Tanaka, ‘Age-Associated Elongation of the Ascending Aorta in Adults’, *JACC Cardiovasc. Imaging*, vol. 1, no. 6, pp. 739–748, Nov. 2008, doi: 10.1016/j.jcmg.2008.06.010.
- [250] G. Choi, C. P. Cheng, N. M. Wilson, and C. A. Taylor, ‘Methods for Quantifying Three-Dimensional Deformation of Arteries due to Pulsatile and Nonpulsatile Forces: Implications for the Design of Stents and Stent Grafts’, *Ann. Biomed. Eng.*, vol. 37, no. 1, pp. 14–33, Jan. 2009, doi: 10.1007/s10439-008-9590-0.
- [251] N. L. Browse, A. E. Young, and M. L. Thomas, ‘The effect of bending on canine and human arterial walls and on blood flow.’, *Circ. Res.*, vol. 45, no. 1, pp. 41–47, Jul. 1979, doi: 10.1161/01.RES.45.1.41.
- [252] M. Prosi, K. Perktold, Z. Ding, and M. H. Friedman, ‘Influence of curvature dynamics on pulsatile coronary artery flow in a realistic bifurcation model’, *J. Biomech.*, vol. 37, no. 11, pp. 1767–1775, Nov. 2004, doi: 10.1016/j.jbiomech.2004.01.021.
- [253] Ö. Smedby and L. Bergstrand, ‘Tortuosity and atherosclerosis in the femoral artery: What is cause and what is effect?’, *Ann. Biomed. Eng.*, vol. 24, no. 4, pp. 474–480, Jul. 1996, doi: 10.1007/BF02648109.
- [254] N. B. Wood *et al.*, ‘Curvature and tortuosity of the superficial femoral artery: a possible risk factor for peripheral arterial disease’, *J. Appl. Physiol.*, vol. 101, no. 5, pp. 1412–1418, Nov. 2006, doi: 10.1152/jappphysiol.00051.2006.
- [255] P. M. O’Flynn, G. O’Sullivan, and A. S. Pandit, ‘Methods for Three-Dimensional Geometric Characterization of the Arterial Vasculature’, *Ann. Biomed. Eng.*, vol. 35, no. 8, pp. 1368–1381, Jul. 2007, doi: 10.1007/s10439-007-9307-9.
- [256] X. Liu, F. Pu, Y. Fan, X. Deng, D. Li, and S. Li, ‘A numerical study on the flow of blood and the transport of LDL in the human aorta: the physiological significance of the helical flow in the aortic arch’, *Am. J. Physiol.-Heart Circ. Physiol.*, vol. 297, no. 1, pp. H163–H170, Jul. 2009, doi: 10.1152/ajpheart.00266.2009.
- [257] E. Sundström *et al.*, ‘Effects of Normal Variation in the Rotational Position of the Aortic Root on Hemodynamics and Tissue Biomechanics of the Thoracic Aorta’, *Cardiovasc. Eng. Technol.*, vol. 11, no. 1, pp. 47–58, Feb. 2020, doi: 10.1007/s13239-019-00441-2.
- [258] S. Pirola *et al.*, ‘Computational study of aortic hemodynamics for patients with an abnormal aortic valve: The importance of secondary flow at the ascending aorta inlet’, *APL Bioeng.*, vol. 2, no. 2, p. 026101, Jun. 2018, doi: 10.1063/1.5011960.
- [259] M. Boumpouli, E. L. Sauvage, C. Capelli, S. Schievano, and A. Kazakidi, ‘Characterization of Flow Dynamics in the Pulmonary Bifurcation of Patients With

- Repaired Tetralogy of Fallot: A Computational Approach', *Front. Cardiovasc. Med.*, vol. 8, p. 703717, Sep. 2021, doi: 10.3389/fcvm.2021.703717.
- [260] M. Boumpouli, M. H. D. Danton, T. Gourlay, and A. Kazakidi, 'Blood flow simulations in the pulmonary bifurcation in relation to adult patients with repaired tetralogy of Fallot', *Med. Eng. Phys.*, vol. 85, pp. 123–138, Nov. 2020, doi: 10.1016/j.medengphy.2020.09.014.
- [261] G. Hyde-Linaker, P. H. Barrientos, S. Stoumpos, D. B. Kingsmore, and A. Kazakidi, 'Patient-specific computational haemodynamics associated with the surgical creation of an arteriovenous fistula', *Med. Eng. Phys.*, vol. 105, p. 103814, Jul. 2022, doi: 10.1016/j.medengphy.2022.103814.
- [262] J.-P. Baguet, S. Douchin, H. Pierre, A.-M. Rossignol, M. Bost, and J.-M. Mallion, 'Structural and functional abnormalities of large arteries in the Turner syndrome', *Heart Br. Card. Soc.*, vol. 91, no. 11, pp. 1442–1446, Nov. 2005, doi: 10.1136/hrt.2004.048371.
- [263] D. Gomez *et al.*, 'Syndromic and non-syndromic aneurysms of the human ascending aorta share activation of the Smad2 pathway: Smad2 activation in ascending aortic aneurysm', *J. Pathol.*, vol. 218, no. 1, pp. 131–142, May 2009, doi: 10.1002/path.2516.
- [264] C. Chrysohoou *et al.*, 'Aortic artery distensibility shows inverse correlation with heart rate variability in elderly non-hypertensive, cardiovascular disease-free individuals: the Ikaria Study', *Heart Vessels*, vol. 28, no. 4, pp. 467–472, Jul. 2013, doi: 10.1007/s00380-012-0267-0.
- [265] A. Frydrychowicz *et al.*, 'Interdependencies of aortic arch secondary flow patterns, geometry, and age analysed by 4-dimensional phase contrast magnetic resonance imaging at 3 Tesla', *Eur. Radiol.*, vol. 22, no. 5, pp. 1122–1130, May 2012, doi: 10.1007/s00330-011-2353-6.
- [266] P. Ou *et al.*, 'Angular (Gothic) aortic arch leads to enhanced systolic wave reflection, central aortic stiffness, and increased left ventricular mass late after aortic coarctation repair: Evaluation with magnetic resonance flow mapping', *J. Thorac. Cardiovasc. Surg.*, vol. 135, no. 1, pp. 62–68, Jan. 2008, doi: 10.1016/j.jtcvs.2007.03.059.
- [267] G. M. London, 'Large artery function and alterations in hypertension', *J. Hypertens. Suppl. Off. J. Int. Soc. Hypertens.*, vol. 13, no. 2, pp. S35-38, Aug. 1995, doi: 10.1097/00004872-199508001-00006.
- [268] T. Willeum-Hansen *et al.*, 'Prognostic value of aortic pulse wave velocity as index of arterial stiffness in the general population', *Circulation*, vol. 113, no. 5, pp. 664–670, Feb. 2006, doi: 10.1161/CIRCULATIONAHA.105.579342.
- [269] M. P. Poullis, R. Warwick, A. Oo, and R. J. Poole, 'Ascending aortic curvature as an independent risk factor for type A dissection, and ascending aortic aneurysm formation: a mathematical model☆', *Eur. J. Cardiothorac. Surg.*, vol. 33, no. 6, pp. 995–1001, Jun. 2008, doi: 10.1016/j.ejcts.2008.02.029.
- [270] T. Karino, T. Asakura, and S. Mabuchi, 'Role of Hemodynamic Factors in Atherogenesis', in *Vascular Endothelium in Health and Disease*, vol. 242, S. Chien, Ed., in *Advances in Experimental Medicine and Biology*, vol. 242. , Boston, MA: Springer US, 1988, pp. 51–57. doi: 10.1007/978-1-4684-8935-4\_7.
- [271] A. Cockwell, M. MacKenzie, S. Youings, and P. Jacobs, 'A cytogenetic and molecular study of a series of 45,X fetuses and their parents.', *J. Med. Genet.*, vol. 28, no. 3, pp. 151–155, Mar. 1991, doi: 10.1136/jmg.28.3.151.
- [272] M. Silberbach *et al.*, 'Cardiovascular Health in Turner Syndrome: A Scientific Statement From the American Heart Association', 2018. doi: 10.1161/HCG.0000000000000048.

- [273] I. Gutmark-Little and P. F. Backeljauw, 'Cardiac magnetic resonance imaging in turner syndrome', 2013. doi: 10.1111/cen.12157.
- [274] V. B. Ho *et al.*, 'Major vascular anomalies in Turner syndrome: Prevalence and magnetic resonance angiographic features', *Circulation*, vol. 110, no. 12, pp. 1694–1700, 2004, doi: 10.1161/01.CIR.0000142290.35842.B0.
- [275] A. V. B. de Castro *et al.*, 'Cardiovascular assessment of patients with Ullrich-Turner's Syndrome on Doppler echocardiography and magnetic resonance imaging.', *Arq. Bras. Cardiol.*, vol. 78, no. 1, pp. 51–58, 2002, doi: 10.1590/S0066-782X2002000100005.
- [276] H. K. Kim *et al.*, 'Cardiovascular anomalies in turner syndrome: Spectrum, prevalence, and cardiac MRI findings in a pediatric and young adult population', *Am. J. Roentgenol.*, vol. 196, no. 2, pp. 454–460, 2011, doi: 10.2214/AJR.10.4973.
- [277] K. De Groote *et al.*, 'Arterial hypertension in turner syndrome: A review of the literature and a practical approach for diagnosis and treatment', 2015. doi: 10.1097/HJH.0000000000000599.
- [278] &NA; W F N, *A Text-book of Pathological Histology. An Introduction to the Study of Pathological Anatomy*, vol. 64, no. 127. Lindsay and Blakiston, 1872. doi: 10.1097/00000441-187207000-00017.
- [279] D. L. FRY, 'Certain Chemorheologic Considerations Regarding the Blood Vascular Interface with Particular Reference to Coronary Artery Disease', *Circulation*, vol. 40, no. 5s4, 1969, doi: 10.1161/01.cir.40.5s4.iv-38.
- [280] C. G. Caro, J. M. Fitz-Gerald, and R. C. Schroter, 'Atheroma and arterial wall shear. Observation, correlation and proposal of a shear dependent mass transfer mechanism for atherogenesis.', *Proc. R. Soc. Lond. B Biol. Sci.*, vol. 177, no. 46, pp. 109–159, 1971, doi: 10.1098/rspb.1971.0019.
- [281] C. G. Caro, T. J. Pedley, R. C. Schroter, W. A. Seed, and K. H. Parker, *The mechanics of the circulation, second edition*, vol. 9780521151. Cambridge University Press, 2011. doi: 10.1017/CBO9781139013406.
- [282] D. N. Ku, D. P. Giddens, C. K. Zarins, and S. Glagov, 'Pulsatile flow and atherosclerosis in the human carotid bifurcation. Positive correlation between plaque location and low and oscillating shear stress', *Arteriosclerosis*, vol. 5, no. 3, pp. 293–302, 1985, doi: 10.1161/01.atv.5.3.293.
- [283] P. D. Weinberg, 'Disease patterns at arterial branches and their relation to flow', *Biorheology*, vol. 39, pp. 533–537, 2002.
- [284] H. Sinzinger, K. Silberbauer, and W. Auerswald, 'Paradoxical relaxation of arterial strips induced by vasoconstrictive agents', *J. Vasc. Res.*, vol. 17, no. 1, pp. 44–52, 1980, doi: 10.1159/000158233.
- [285] G. D. Sloop, R. S. Perret, J. S. Brahney, and M. Oalman, 'A description of two morphologic patterns of aortic fatty streaks, and a hypothesis of their pathogenesis', *Atherosclerosis*, vol. 141, no. 1, pp. 153–160, 1998, doi: 10.1016/S0021-9150(98)00167-1.
- [286] A. Svindland and L. Walløe, 'Distribution pattern of sudanophilic plaques in the descending thoracic and proximal abdominal human aorta', *Atherosclerosis*, vol. 57, no. 2–3, pp. 219–224, 1985, doi: 10.1016/0021-9150(85)90035-8.
- [287] M. H. Simms, J. H. N. Welfe, and W. B. Campbell, *Arterial disease*, vol. 75, no. 5. Oxford: Blackwell Scientific Publications, 1988. doi: 10.1002/bjs.1800750545.
- [288] A. Kazakidi, S. J. Sherwin, and P. D. Weinberg, 'Effect of Reynolds number and flow division on patterns of haemodynamic wall shear stress near branch points in the descending thoracic aorta', *J. R. Soc. Interface*, vol. 6, no. 35, pp. 539–548, 2009, doi: 10.1098/rsif.2008.0323.

- [289] A. Kazakidi, A. M. Plata, S. J. Sherwin, and P. D. Weinberg, ‘Effect of reverse flow on the pattern of wall shear stress near arterial branches’, *J. R. Soc. Interface*, vol. 8, no. 64, pp. 1594–1603, 2011, doi: 10.1098/rsif.2011.0108.
- [290] P. E. Vincent, A. M. Plata, A. A. E. Hunt, P. D. Weinberg, and S. J. Sherwin, ‘Blood flow in the rabbit aortic arch and descending thoracic aorta’, *J. R. Soc. Interface*, vol. 8, no. 65, pp. 1708–1719, 2011, doi: 10.1098/rsif.2011.0116.
- [291] P. D. Morris *et al.*, ‘Computational fluid dynamics modelling in cardiovascular medicine’, *Heart*, vol. 102, no. 1, pp. 18–28, 2016, doi: 10.1136/heartjnl-2015-308044.
- [292] L. Antiga, ‘Patient-specific modeling of geometry and blood flow in large arteries’, *Politec. Milano*, 2002.
- [293] J. Chen, E. Gutmark, G. Mylavarapu, P. F. Backeljauw, and I. Gutmark-Little, ‘Numerical investigation of mass transport through patient-specific deformed aortae’, *J. Biomech.*, vol. 47, no. 2, pp. 544–552, 2014, doi: 10.1016/j.jbiomech.2013.10.031.
- [294] X. Liu, F. Pu, Y. Fan, X. Deng, D. Li, and S. Li, ‘A numerical study on the flow of blood and the transport of LDL in the human aorta: The physiological significance of the helical flow in the aortic arch’, *Am. J. Physiol. - Heart Circ. Physiol.*, vol. 297, no. 1, 2009, doi: 10.1152/ajpheart.00266.2009.
- [295] S. Numata *et al.*, ‘Blood flow analysis of the aortic arch using computational fluid dynamics’, *Eur. J. Cardiothorac. Surg.*, vol. 49, no. 6, pp. 1578–1585, 2016, doi: 10.1093/ejcts/ezv459.
- [296] S. Pirola *et al.*, ‘Computational study of aortic hemodynamics for patients with an abnormal aortic valve: The importance of secondary flow at the ascending aorta inlet’, *APL Bioeng.*, vol. 2, no. 2, 2018, doi: 10.1063/1.5011960.
- [297] E. Sundström *et al.*, ‘Effects of Normal Variation in the Rotational Position of the Aortic Root on Hemodynamics and Tissue Biomechanics of the Thoracic Aorta’, *Cardiovasc. Eng. Technol.*, vol. 11, no. 1, pp. 47–58, 2020, doi: 10.1007/s13239-019-00441-2.
- [298] P. Youssefi, A. Gomez, C. Arthurs, R. Sharma, M. Jahangiri, and C. A. Figueroa, ‘Impact of patient-specific inflow velocity profile on hemodynamics of the thoracic aorta’, *J. Biomech. Eng.*, vol. 140, no. 1, 2018, doi: 10.1115/1.4037857.
- [299] Y. Zhu *et al.*, ‘Clinical validation and assessment of aortic hemodynamics using computational fluid dynamics simulations from computed tomography angiography’, *Biomed. Eng. Online*, vol. 17, no. 1, 2018, doi: 10.1186/s12938-018-0485-5.
- [300] S. Madhavan and E. M. C. Kemmerling, ‘The effect of inlet and outlet boundary conditions in image-based CFD modeling of aortic flow’, *Biomed. Eng. Online*, vol. 17, no. 1, 2018, doi: 10.1186/s12938-018-0497-1.
- [301] M. McElroy and A. Keshmiri, ‘Impact of Using Conventional Inlet/Outlet Boundary Conditions on Haemodynamic Metrics in a Subject-Specific Rabbit Aorta’, *Proc. Inst. Mech. Eng. [H]*, vol. 232, no. 2, pp. 103–113, 2018, doi: 10.1177/0954411917699237.
- [302] D. Gallo *et al.*, ‘On the use of in vivo measured flow rates as boundary conditions for image-based hemodynamic models of the human aorta: Implications for indicators of abnormal flow’, *Ann. Biomed. Eng.*, vol. 40, no. 3, pp. 729–741, 2012, doi: 10.1007/s10439-011-0431-1.
- [303] U. Morbiducci *et al.*, ‘Outflow conditions for image-based hemodynamic models of the carotid bifurcation: Implications for indicators of abnormal flow’, *J. Biomech. Eng.*, vol. 132, no. 9, 2010, doi: 10.1115/1.4001886.
- [304] U. Morbiducci, R. Ponzini, D. Gallo, C. Bignardi, and G. Rizzo, ‘Inflow boundary conditions for image-based computational hemodynamics: Impact of idealized versus

- measured velocity profiles in the human aorta', *J. Biomech.*, vol. 46, no. 1, pp. 102–109, 2013, doi: 10.1016/j.jbiomech.2012.10.012.
- [305] M. A. Van Doormaal *et al.*, 'Haemodynamics in the mouse aortic arch computed from MRI-derived velocities at the aortic root', *J. R. Soc. Interface*, vol. 9, no. 76, pp. 2834–2844, 2012, doi: 10.1098/rsif.2012.0295.
- [306] S. Pirola *et al.*, 'On the choice of outlet boundary conditions for patient-specific analysis of aortic flow using computational fluid dynamics', *J. Biomech.*, vol. 60, pp. 15–21, 2017, doi: 10.1016/j.jbiomech.2017.06.005.
- [307] C. Chnafa, O. Brina, V. M. Pereira, and D. A. Steinman, 'Better Than Nothing: A Rational Approach for Minimizing the Impact of Outflow Strategy on Cerebrovascular Simulations', *Am. J. Neuroradiol.*, vol. 39, no. 2, pp. 337–343, 2018, doi: 10.3174/ajnr.A5484.
- [308] C. D. Murray, 'The Physiological Principle of Minimum Work: I. The Vascular System and the Cost of Blood Volume', *Proc. Natl. Acad. Sci.*, vol. 12, no. 3, pp. 207–214, 1926, doi: 10.1073/pnas.12.3.207.
- [309] J. V. Freeman, T. J. Cole, S. Chinn, P. R. M. Jones, E. M. White, and M. A. Preece, 'Cross sectional stature and weight reference curves for the UK, 1990', *Arch. Dis. Child.*, vol. 73, no. 1, pp. 17–24, 1995, doi: 10.1136/adc.73.1.17.
- [310] T. Kaiser, C. J. Kellenberger, M. Albisetti, E. Bergsträsser, and E. R. V. Buechel, 'Normal values for aortic diameters in children and adolescents - Assessment in vivo by contrast-enhanced CMR-angiography', *J. Cardiovasc. Magn. Reson.*, vol. 10, no. 1, 2008, doi: 10.1186/1532-429X-10-56.
- [311] J. E. Ostberg, A. E. Donald, J. P. J. Halcox, C. Storry, C. McCarthy, and G. S. Conway, 'Vasculopathy in Turner syndrome: Arterial dilatation and intimal thickening without endothelial dysfunction', *J. Clin. Endocrinol. Metab.*, vol. 90, no. 9, pp. 5161–5166, 2005, doi: 10.1210/jc.2005-0677.
- [312] M. Sosnowski, J. Krzywanski, and R. Gnatowska, 'Polyhedral meshing as an innovative approach to computational domain discretization of a cyclone in a fluidized bed CLC unit', in *E3S Web of Conferences*, 2017. doi: 10.1051/e3sconf/20171401027.
- [313] 'Procedure for Estimation and Reporting of Uncertainty Due to Discretization in CFD Applications', *J. Fluids Eng.*, vol. 130, no. 7, 2008.
- [314] N. Lewandowska and J. Mosiężny, 'Meshing strategy for bifurcation arteries in the context of blood flow simulation accuracy', in *E3S Web of Conferences*, 2019. doi: 10.1051/e3sconf/201912802003.
- [315] E. Heiberg, J. Sjögren, M. Ugander, M. Carlsson, H. Engblom, and H. Arheden, 'Design and validation of Segment - freely available software for cardiovascular image analysis', *BMC Med. Imaging*, vol. 10, no. 1, p. 1, Dec. 2010, doi: 10.1186/1471-2342-10-1.
- [316] R. Ponzini *et al.*, 'Womersley number-based estimates of blood flow rate in doppler analysis: In vivo validation by means of phase-contrast MRI', *IEEE Trans. Biomed. Eng.*, vol. 57, no. 7, pp. 1807–1815, 2010, doi: 10.1109/TBME.2010.2046484.
- [317] C. Loudon and A. Tordesillas, 'The use of the dimensionless Womersley number to characterize the unsteady nature of internal flow', *J. Theor. Biol.*, vol. 191, no. 1, pp. 63–78, 1998, doi: 10.1006/jtbi.1997.0564.
- [318] C. Cheng *et al.*, 'Large variations in absolute wall shear stress levels within one species and between species', 2007. doi: 10.1016/j.atherosclerosis.2006.11.019.
- [319] R. S. Reneman and A. P. G. Hoeks, 'Wall shear stress as measured in vivo: Consequences for the design of the arterial system', *Med. Biol. Eng. Comput.*, vol. 46, no. 5, pp. 499–507, 2008, doi: 10.1007/s11517-008-0330-2.

- [320] M. Zamir, P. Sinclair, and T. H. Wonnacott, ‘Relation between diameter and flow in major branches of the arch of the aorta’, *J. Biomech.*, vol. 25, no. 11, pp. 1303–1310, 1992, doi: 10.1016/0021-9290(92)90285-9.
- [321] J. Lantz and M. Karlsson, ‘Large eddy simulation of LDL surface concentration in a subject specific human aorta’, *J. Biomech.*, vol. 45, no. 3, pp. 537–542, 2012, doi: 10.1016/j.jbiomech.2011.11.039.
- [322] C. Chnafa, S. Mendez, and F. Nicoud, ‘Image-Based Simulations Show Important Flow Fluctuations in a Normal Left Ventricle: What Could be the Implications?’, *Ann. Biomed. Eng.*, vol. 44, no. 11, pp. 3346–3358, 2016.
- [323] M. O. Khan, K. Valen-Sendstad, and D. A. Steinman, ‘Narrowing the Expertise Gap for Predicting Intracranial Aneurysm Hemodynamics: Impact of Solver Numerics versus Mesh and Time-Step Resolution’, *Am. J. Neuroradiol.*, vol. 36, no. 7, pp. 1310–1316, 2015.
- [324] Z. Chen *et al.*, ‘Vascular Remodelling Relates to an Elevated Oscillatory Shear Index and Relative Residence Time in Spontaneously Hypertensive Rats’, *Sci. Rep.*, vol. 7, no. 1, 2017, doi: 10.1038/s41598-017-01906-x.
- [325] G. J. Riccardello *et al.*, ‘Influence of relative residence time on side-wall aneurysm inception’, *Clin. Neurosurg.*, vol. 83, no. 3, pp. 574–581, 2018, doi: 10.1093/neuros/nyx433.
- [326] V. Peiffer, S. J. Sherwin, and P. D. Weinberg, ‘Computation in the rabbit aorta of a new metric – the transverse wall shear stress – to quantify the multidirectional character of disturbed blood flow’, *J. Biomech.*, vol. 46, pp. 2651–2658, 2013.
- [327] P. J. Kilner, G. Z. Yang, R. H. Mohiaddin, D. N. Firmin, and D. B. Longmore, ‘Helical and retrograde secondary flow patterns in the aortic arch studied by three-directional magnetic resonance velocity mapping’, *Circulation*, vol. 88, no. 5 I, pp. 2235–2247, 1993, doi: 10.1161/01.CIR.88.5.2235.
- [328] S. Laín and A. D. Caballero, ‘Simulación transitoria de la dinámica del flujo sanguíneo en la aorta torácica’, *Ing. E Investig.*, vol. 37, no. 3, pp. 92–101, 2017, doi: 10.15446/ing.investig.v37n3.59761.
- [329] U. Morbiducci *et al.*, ‘Mechanistic insight into the physiological relevance of helical blood flow in the human aorta: An in vivo study’, *Biomech. Model. Mechanobiol.*, vol. 10, no. 3, pp. 339–355, 2011, doi: 10.1007/s10237-010-0238-2.
- [330] G. S. Berenson, S. R. Srinivasan, and T. A. Nicklas, ‘Atherosclerosis: A nutritional disease of childhood’, in *American Journal of Cardiology*, 1998. doi: 10.1016/S0002-9149(98)00719-X.
- [331] K. S. Cunningham and A. I. Gotlieb, ‘The role of shear stress in the pathogenesis of atherosclerosis’, 2005. doi: 10.1038/labinvest.3700215.
- [332] R. Arnold, M. Neu, D. Hirtler, C. Gimpel, M. Markl, and J. Geiger, ‘Magnetic resonance imaging 4-D flow-based analysis of aortic hemodynamics in Turner syndrome’, *Pediatr. Radiol.*, vol. 47, no. 4, pp. 382–390, 2017, doi: 10.1007/s00247-016-3767-8.
- [333] A. Wittek *et al.*, ‘Cyclic three-dimensional wall motion of the human ascending and abdominal aorta characterized by time-resolved three-dimensional ultrasound speckle tracking’, *Biomech. Model. Mechanobiol.*, vol. 15, no. 5, pp. 1375–1388, 2016, doi: 10.1007/s10237-016-0769-2.
- [334] B. Moreau and B. Mauroy, ‘Murray’s law revisited: Quémada’s fluid model and fractal trees’, *J. Rheol.*, vol. 59, no. 6, pp. 1419–1430, 2015, doi: 10.1122/1.4934240.

- [335] H. B. M. Uylings, ‘Optimization of diameters and bifurcation angles in lung and vascular tree structures’, *Bull. Math. Biol.*, vol. 39, no. 5, pp. 509–520, 1977, doi: 10.1007/BF02461198.
- [336] M. Boumpouli, M. H. D. Danton, T. Gourlay, and A. Kazakidi, ‘Blood flow simulations in the pulmonary bifurcation in relation to adult patients with repaired tetralogy of Fallot’, *Med. Eng. Phys.*, vol. 85, pp. 123–138, 2020, doi: 10.1016/j.medengphy.2020.09.014.
- [337] J. Nijs, S. Gelsomino, F. Lucà, O. Parise, J. G. Maessen, and M. La Meir, ‘Unreliability of aortic size index to predict risk of aortic dissection in a patient with Turner syndrome’, *World J. Cardiol.*, vol. 6, no. 5, p. 349, 2014, doi: 10.4330/wjc.v6.i5.349.
- [338] A. Polanczyk, A. Piechota-Polanczyk, C. Domenig, J. Nanobachvili, I. Huk, and C. Neumayer, ‘Computational Fluid Dynamic Accuracy in Mimicking Changes in Blood Hemodynamics in Patients with Acute Type IIIb Aortic Dissection Treated with TEVAR’, *Appl. Sci.*, vol. 8, no. 8, p. 1309, Aug. 2018, doi: 10.3390/app8081309.
- [339] R. M. Romarowski, E. Faggiano, M. Conti, A. Reali, S. Morganti, and F. Auricchio, ‘A novel computational framework to predict patient-specific hemodynamics after TEVAR: Integration of structural and fluid-dynamics analysis by image elaboration’, *Comput. Fluids*, vol. 179, pp. 806–819, Jan. 2019, doi: 10.1016/j.compfluid.2018.06.002.
- [340] R. R. Davies *et al.*, ‘Novel Measurement of Relative Aortic Size Predicts Rupture of Thoracic Aortic Aneurysms’, *Ann. Thorac. Surg.*, vol. 81, no. 1, pp. 169–177, Jan. 2006, doi: 10.1016/j.athoracsur.2005.06.026.
- [341] M. A. Rana, G. S. Oderich, and A. Pochettino, ‘Techniques and Results of Aortic Arch Hybrid Repair’, in *Endovascular Aortic Repair*, G. S. Oderich, Ed., Cham: Springer International Publishing, 2017, pp. 555–566. doi: 10.1007/978-3-319-15192-2\_36.
- [342] G. R. Upchurch *et al.*, ‘Society for Vascular Surgery clinical practice guidelines of thoracic endovascular aortic repair for descending thoracic aortic aneurysms’, *J. Vasc. Surg.*, vol. 73, no. 1, pp. 55S–83S, Jan. 2021, doi: 10.1016/j.jvs.2020.05.076.
- [343] G. H. W. van Bogerijen *et al.*, ‘Aortic Hemodynamics After Thoracic Endovascular Aortic Repair, With Particular Attention to the Bird-Beak Configuration’, *J. Endovasc. Ther.*, vol. 21, no. 6, pp. 791–802, Dec. 2014, doi: 10.1583/14-4778MR.1.
- [344] T. Ueda, D. Fleischmann, M. D. Dake, G. D. Rubin, and D. Y. Sze, ‘Incomplete Endograft Apposition to the Aortic Arch: Bird-Beak Configuration Increases Risk of Endoleak Formation after Thoracic Endovascular Aortic Repair’, *Radiology*, vol. 255, no. 2, pp. 645–652, May 2010, doi: 10.1148/radiol.10091468.
- [345] E. Soudah *et al.*, ‘ESTIMATION OF WALL SHEAR STRESS USING 4D FLOW CARDIOVASCULAR MRI AND COMPUTATIONAL FLUID DYNAMICS’, *J. Mech. Med. Biol.*, vol. 17, no. 03, p. 1750046, May 2017, doi: 10.1142/S0219519417500464.
- [346] F. J. H. Nauta *et al.*, ‘Biomechanical Changes After Thoracic Endovascular Aortic Repair in Type B Dissection: A Systematic Review’, *J. Endovasc. Ther.*, vol. 22, no. 6, pp. 918–933, Dec. 2015, doi: 10.1177/1526602815608848.
- [347] N. Shahbazian, D. A. Romero, T. L. Forbes, and C. H. Amon, ‘Identification of geometric and mechanical factors predictive of bird-beak configuration in thoracic endovascular aortic repair using computational models of stent graft deployment’, *JVS-Vasc. Sci.*, vol. 3, pp. 259–273, 2022, doi: 10.1016/j.jvssci.2022.05.056.
- [348] C. Karmonik, J. Bismuth, M. G. Davies, D. J. Shah, H. K. Younes, and A. B. Lumsden, ‘A Computational Fluid Dynamics Study Pre- and Post-Stent Graft Placement in an Acute Type B Aortic Dissection’, *Vasc. Endovascular Surg.*, vol. 45, no. 2, pp. 157–164, Feb. 2011, doi: 10.1177/1538574410389342.
- [349] M. Midulla *et al.*, ‘Haemodynamic imaging of thoracic stent-grafts by computational fluid dynamics (CFD): presentation of a patient-specific method combining magnetic

- resonance imaging and numerical simulations’, *Eur. Radiol.*, vol. 22, no. 10, pp. 2094–2102, Oct. 2012, doi: 10.1007/s00330-012-2465-7.
- [350] S. Sengupta, X. Yuan, L. Maga, S. Pirola, C. A. Nienaber, and X. Y. Xu, ‘Aortic haemodynamics and wall stress analysis following arch aneurysm repair using a single-branched endograft’, *Front. Cardiovasc. Med.*, vol. 10, p. 1125110, May 2023, doi: 10.3389/fcvm.2023.1125110.
- [351] X. Zhang *et al.*, ‘Evaluation of embedded modular branched stent graft in treating aortic arch aneurysm using imaging-based computational flow analysis’, *Med. Nov. Technol. Devices*, vol. 21, p. 100285, Mar. 2024, doi: 10.1016/j.medntd.2024.100285.
- [352] N. Shahbazian, D. A. Romero, T. L. Forbes, and C. H. Amon, ‘Prediction of bird-beak configuration in TEVAR pre-operatively using patient-specific finite element simulations’, *JVS-Vasc. Sci.*, p. 100108, Apr. 2023, doi: 10.1016/j.jvssci.2023.100108.
- [353] S. Pasta, J.-S. Cho, O. Dur, K. Pekkan, and D. A. Vorp, ‘Computer modeling for the prediction of thoracic aortic stent graft collapse’, *J. Vasc. Surg.*, vol. 57, no. 5, pp. 1353–1361, May 2013, doi: 10.1016/j.jvs.2012.09.063.
- [354] A. Rinaudo, G. M. Raffa, F. Scardulla, M. Pilato, C. Scardulla, and S. Pasta, ‘Biomechanical implications of excessive endograft protrusion into the aortic arch after thoracic endovascular repair’, *Comput. Biol. Med.*, vol. 66, pp. 235–241, Nov. 2015, doi: 10.1016/j.compbiomed.2015.09.011.
- [355] F. P. P. Tan, A. Borghi, R. H. Mohiaddin, N. B. Wood, S. Thom, and X. Y. Xu, ‘Analysis of flow patterns in a patient-specific thoracic aortic aneurysm model’, *Comput. Struct.*, vol. 87, no. 11–12, pp. 680–690, Jun. 2009, doi: 10.1016/j.compstruc.2008.09.007.
- [356] D. Gallo *et al.*, ‘A patient-specific follow up study of the impact of thoracic endovascular repair (TEVAR) on aortic anatomy and on post-operative hemodynamics.’, *Comput. Fluids*, vol. 141, pp. 54–61, Dec. 2016, doi: 10.1016/j.compfluid.2016.04.025.
- [357] Y. Qiao, J. Fan, Y. Ding, T. Zhu, and K. Luo, ‘A Primary Computational Fluid Dynamics Study of Pre- and Post-TEVAR With Intentional Left Subclavian Artery Coverage in a Type B Aortic Dissection’, *J. Biomech. Eng.*, vol. 141, no. 11, p. 111002, Nov. 2019, doi: 10.1115/1.4043881.
- [358] S. Madhavan and E. M. C. Kemmerling, ‘The effect of inlet and outlet boundary conditions in image-based CFD modeling of aortic flow’, *Biomed. Eng. OnLine*, vol. 17, no. 1, p. 66, Dec. 2018, doi: 10.1186/s12938-018-0497-1.
- [359] S. Glagov, C. Zarins, D. P. Giddens, and D. N. Ku, ‘Hemodynamics and atherosclerosis. Insights and perspectives gained from studies of human arteries’, 1988.
- [360] J. Lantz, R. Gårdhagen, and M. Karlsson, ‘Quantifying turbulent wall shear stress in a subject specific human aorta using large eddy simulation’, *Med. Eng. Phys.*, vol. 34, no. 8, pp. 1139–1148, 2012, doi: 10.1016/j.medengphys.2011.12.002.
- [361] M. Nozdrzykowski *et al.*, ‘Outcomes of secondary procedures after primary thoracic endovascular aortic repair’, *Eur. J. Cardiothorac. Surg.*, vol. 49, no. 3, pp. 770–777, Mar. 2016, doi: 10.1093/ejcts/ezv279.
- [362] T. Frauenfelder, M. Lotfey, T. Boehm, and S. Wildermuth, ‘Computational Fluid Dynamics: Hemodynamic Changes in Abdominal Aortic Aneurysm After Stent-Graft Implantation’, *Cardiovasc. Intervent. Radiol.*, vol. 29, no. 4, pp. 613–623, Aug. 2006, doi: 10.1007/s00270-005-0227-5.
- [363] S. M. Black, C. Maclean, P. Hall Barrientos, K. Ritos, A. McQueen, and A. Kazakidi, ‘Calibration of patient-specific boundary conditions for coupled CFD models of the aorta derived from 4D Flow-MRI’, *Front. Bioeng. Biotechnol.*, vol. 11, p. 1178483, May 2023, doi: 10.3389/fbioe.2023.1178483.

[364] M. Boumpouli, 'Blood Flow Dynamics in Surviving Patients with Repaired Tetralogy of Fallot', University of Strathclyde, 2021.

# Appendices

## Appendix 1

A systematic search was conducted on PubMed database for articles published online between 1<sup>st</sup> January 2000 and 31<sup>st</sup> December 2019 whose title and/or abstract contained the keyword “Turner syndrome”. The articles were then evaluated against a set of inclusion and exclusion criteria. To be included, articles must meet the following inclusion criteria:

- the work was an original contribution;
- the original article was written in English;
- the article was an individual case study of a Turner syndrome patient and/or the article was a study of a cohort of Turner syndrome patients;
- the relation between Turner syndrome and cardiovascular risk was discussed;

Excluded from the review were:

- review papers
- letters to the editor;
- rebuttal papers;
- articles focused solely on a vessel other than the aorta;
- articles focused solely on surgical and/or treatment outcomes;
- articles solely describing cardiac imaging techniques in Turner syndrome.

A total of 81 articles meeting all the criteria were selected from an initial set of 2710. Of these articles, 19 were individual patient case studies and 62 were cohort studies. The selected articles presented cover a population of 5126 Turner syndrome individuals. In the individual case studies, the patients age was always reported but patient’s BMI was only reported in 4 papers. In the cohort studies, the mean age of the cohort was reported in 50 papers and the mean BMI in 35 papers. Over half (33 papers) of the cohort studies included a control population, totalling 1765 individuals.

# Appendix 2

Geometric parameters for Turner syndrome and healthy patients across the entire geometry, and within the ascending, aortic arch, and descending regions. Values are colour coded according to magnitude, with blue being low and red high.

FULL GEOMETRY																
PATIENT	volume (mm <sup>3</sup> )	surface area (mm <sup>2</sup> )	shape index	centerline length (mm)	Diameter (mm)			Curvature (1/mm)			Torsion (1/mm)			combined score (1/mm)		
					min	mean	max	min	mean	max	min	mean	max	min	mean	max
TS1	95754	17638	0.39	231.01	12.72	18.61	32.56	0.00	0.03	0.14	-5.55	0.13	12.13	0.00	0.49	12.13
TS2	47040	11585	0.75	189.34	13.32	15.62	17.72	0.00	0.04	0.17	-4.77	-0.04	4.24	0.00	0.50	4.77
TS3	58844	13321	0.57	195.98	12.02	16.50	20.94	0.00	0.03	0.14	-5.71	0.16	17.74	0.00	0.54	17.74
TS4	59122	15870	0.59	193.94	14.56	17.59	24.63	0.00	0.03	0.10	-16.98	-0.03	3.24	0.00	0.44	16.98
TS5	51044	13561	0.67	210.04	12.94	15.03	19.19	0.00	0.03	0.13	-8.77	-0.12	9.40	0.00	0.41	9.40
TS6	64767	15296	0.53	180.36	14.82	17.99	27.89	0.00	0.03	0.11	-4.49	0.06	6.21	0.00	0.39	6.21
TS7	52432	14184	0.58	213.77	12.67	15.51	21.95	0.00	0.03	0.12	-10.29	0.01	6.57	0.00	0.47	10.29
TS8	48797	11348	0.58	165.14	14.02	16.18	24.33	0.00	0.03	0.18	-13.29	-0.02	11.95	0.00	0.54	13.29
H1 0093	39276	12187	0.60	192.20	11.36	13.79	18.89	0.00	0.05	0.48	-27.23	0.14	49.12	0.00	1.39	49.12
H2 0003	58194	16227	0.66	228.26	15.00	17.56	22.62	0.00	0.02	0.11	-30.67	0.13	30.58	-30.67	0.13	30.58
H3 0185	35707	10457	0.65	188.50	12.99	15.50	20.11	0.00	0.03	0.25	-100.79	-0.27	83.13	0.00	3.04	100.79
H4 0121	16649	5958	0.62	132.65	9.19	11.67	14.82	0.00	0.03	0.14	-8.41	0.07	10.16	0.00	0.75	10.16

ASCENDING AORTA															
PATIENT	centerline length (mm)	Diameter (mm)			Curvature (1/mm)			Torsion (1/mm)			combined score (1/mm)				
		min	mean	max	min	mean	max	min	mean	max	min	mean	max		
TS1	49.54	29.80	31.72	32.56	0.00	0.05	0.14	-1.09	0.00	1.48	0.00	0.25	1.48		
TS2	26.63	16.55	17.01	17.48	0.00	0.06	0.16	-2.64	0.00	1.78	0.00	0.45	2.64		
TS3	28.15	17.75	18.91	20.94	0.00	0.04	0.14	-2.43	-0.01	2.33	0.00	0.48	2.43		
TS4	38.00	23.05	24.06	24.63	0.00	0.04	0.16	-1.67	0.05	0.62	0.00	0.21	1.67		
TS5	31.58	18.22	18.73	19.19	0.00	0.03	0.06	-0.93	0.00	0.95	0.00	0.35	0.95		
TS6	29.40	22.82	26.13	27.89	0.00	0.05	0.11	-0.29	0.03	0.42	0.00	0.15	0.42		
TS7	28.90	17.25	20.09	21.95	0.00	0.05	0.12	-1.74	0.09	5.32	0.00	0.43	5.32		
TS8	20.95	21.44	22.99	24.33	0.00	0.04	0.09	-13.29	-0.81	0.01	0.00	0.82	13.29		
H1 0093	41.01	16.52	17.07	17.77	0.00	0.05	0.15	-9.74	0.01	14.36	0.00	0.94	14.36		
H2 0003	29.97	22.10	22.26	22.45	0.00	0.04	0.11	-0.08	0.02	0.19	-0.08	0.02	0.19		
H3 0185	43.65	18.02	19.56	20.11	0.00	0.03	0.18	-9.55	0.18	21.00	0.00	1.46	21.00		
H4 0121	30.11	13.75	14.63	14.82	0.00	0.04	0.13	-2.98	0.06	1.69	0.00	0.34	2.98		

AORTIC ARCH															
PATIENT	centerline length (mm)	Diameter (mm)			Curvature (1/mm)			Torsion (1/mm)			combined score (1/mm)				
		min	mean	max	min	mean	max	min	mean	max	min	mean	max		
TS1	33.41	15.71	20.40	29.76	0.00	0.05	0.13	-5.55	0.03	2.05	0.04	0.51	5.55		
TS2	41.64	14.58	16.06	17.72	0.02	0.06	0.17	-3.67	0.00	2.13	0.04	0.36	3.67		
TS3	30.54	12.25	13.92	17.63	0.02	0.06	0.13	-2.55	-0.08	0.63	0.04	0.34	2.55		
TS4	21.98	17.12	19.59	22.92	0.02	0.05	0.08	-0.12	0.01	0.24	0.03	0.09	0.24		
TS5	37.42	15.18	16.70	19.01	0.01	0.05	0.12	-1.29	0.05	2.38	0.03	0.26	2.38		
TS6	34.42	16.63	18.51	22.62	0.00	0.05	0.10	-0.38	0.16	3.03	0.04	0.29	3.03		
TS7	58.93	15.32	16.05	17.51	0.00	0.04	0.10	-0.58	0.06	2.52	-0.58	0.22	2.52		
TS8	29.85	14.73	17.44	21.32	0.01	0.07	0.18	-1.44	-0.03	2.25	0.05	0.33	2.25		
H1 0093	29.37	12.06	15.83	18.89	0.01	0.09	0.48	-12.00	0.22	18.23	0.02	1.27	18.23		
H2 0003	27.09	20.09	21.74	22.62	0.01	0.05	0.09	-1.82	-0.03	0.93	-1.82	-0.03	0.93		
H3 0185	36.54	16.50	17.05	17.97	0.03	0.05	0.25	-2.80	-0.02	3.86	0.03	0.63	3.86		
H4 0121	21.16	11.73	12.34	13.74	0.03	0.08	0.14	-0.95	0.02	0.90	0.03	0.26	0.95		

DESCENDING AORTA															
PATIENT	centerline length (mm)	Diameter (mm)			Curvature (1/mm)			Torsion (1/mm)			combined score (1/mm)				
		min	mean	max	min	mean	max	min	mean	max	min	mean	max		
TS1	148.06	12.72	14.77	17.54	0.00	0.03	0.07	-1.77	0.19	12.13	0.00	0.54	12.13		
TS2	121.07	13.32	15.11	16.97	0.00	0.02	0.10	-4.77	-0.07	4.24	0.00	0.58	4.77		
TS3	137.29	12.02	16.72	20.32	0.00	0.03	0.10	-5.71	0.26	17.74	0.00	0.61	17.74		
TS4	133.96	14.56	16.07	17.17	0.00	0.03	0.07	-16.98	-0.05	3.24	0.00	0.54	16.98		
TS5	141.04	12.94	13.88	15.34	0.00	0.02	0.13	-8.77	-0.19	9.40	0.00	0.47	9.40		
TS6	116.54	14.82	16.37	17.88	0.00	0.02	0.07	-4.49	0.04	6.21	0.00	0.47	6.21		
TS7	124.94	12.67	14.35	17.20	0.00	0.01	0.05	-10.29	-0.03	6.57	0.00	0.57	10.29		
TS8	114.33	14.02	15.02	16.14	0.00	0.03	0.10	-5.41	0.07	11.95	0.00	0.56	11.95		
H1 0093	121.82	11.36	12.25	12.89	0.00	0.03	0.29	-27.23	0.16	49.12	0.00	1.55	49.12		
H2 0003	171.30	15.00	16.66	20.09	0.00	0.02	0.07	-30.67	0.16	30.58	-30.67	0.16	30.58		
H3 0185	108.31	12.99	14.26	17.25	0.00	0.02	0.14	-100.79	-0.43	83.13	0.00	3.88	100.79		
H4 0121	81.38	9.19	10.66	11.73	0.00	0.02	0.08	-8.41	0.08	10.16	0.00	0.97	10.16		

## Appendix 3

Letter of Access for Research granted by NHS Greater Glasgow and Clyde for the period of 18/03/2019 – 18/07/2020.



Administrator: Mrs Elaine O'Neill  
Telephone Number: 0141 232 1815  
E-Mail: elaine.o'neill2@ggc.scot.nhs.uk  
Website: www.nhsggc.org.uk/r&d

Research & Development  
West Glasgow ACH  
Dalnair Street  
Glasgow G3 8SW

18 March 2019

Miss Lauren Johnston  
University of Strathclyde  
40 George Street  
Glasgow G1 QE

Dear Miss L Johnston,

### Letter of Access for Research

This letter confirms your right of access to conduct research through **NHS Greater Glasgow and Clyde** for the purpose and on the terms and conditions set out below. This right of access commences on **18/03/2019** and ends on **18/07/2020** unless terminated earlier in accordance with the clauses below.

You have a right of access to conduct such research as confirmed in writing in the letter of permission for research from this NHS organisation. Please note that you cannot start the research until the Principal Investigator for the research project has received a letter from us giving permission to conduct the project.

The information supplied about your role in research at **NHS Greater Glasgow and Clyde** has been reviewed and you do not require an honorary research contract with this NHS organisation. We are satisfied that such pre-engagement checks as we consider necessary have been carried out.

You are considered to be a legal visitor to **NHS Greater Glasgow and Clyde** premises. You are not entitled to any form of payment or access to other benefits provided by this NHS organisation to employees and this letter does not give rise to any other relationship between you and this NHS organisation, in particular that of an employee.

While undertaking research through **NHS Greater Glasgow and Clyde**, you will remain accountable to **Dr Avril Mason** in this NHS organisation or those given on her/his behalf in relation to the terms of this right of access.

Where any third party claim is made, whether or not legal proceedings are issued, arising out of or in connection with your right of access, you are required to co-operate fully with any investigation by this NHS organisation in connection with any such claim and to give all such assistance as may reasonably be required regarding the conduct of any legal proceedings.

You must act in accordance with **NHS Greater Glasgow and Clyde** policies and procedures, which are available to you upon request, and the Research Governance Framework.

You are required to co-operate with **NHS Greater Glasgow and Clyde** in discharging its duties under the Health and Safety at Work etc Act 1974 and other health and safety legislation and to take reasonable care for the health and safety of yourself and others while on **NHS Greater Glasgow and Clyde** premises. You must observe the same standards of care and propriety in dealing with patients, staff, visitors, equipment

and premises as is expected of any other contract holder and you must act appropriately, responsibly and professionally at all times.

If you have a physical or mental health condition or disability which may affect your research role and which might require special adjustments to your role, if you have not already done so, you must notify your employer and the health board's HR department prior to commencing your research role at the Health board.

You are required to ensure that all information regarding patients or staff remains secure and *strictly confidential* at all times. You must ensure that you understand and comply with the requirements of the NHS Confidentiality Code of Practice (<http://www.dh.gov.uk/assetRoot/04/06/92/54/04069254.pdf>) and the Data Protection Act 1998. Furthermore you should be aware that under the Act, unauthorised disclosure of information is an offence and such disclosures may lead to prosecution.

You should ensure that, where you are issued with an identity or security card, a bleep number, email or library account, keys or protective clothing, these are returned upon termination of this arrangement. Please also ensure that while on the premises you wear your ID badge at all times, or are able to prove your identity if challenged. Please note that this NHS organisation accepts no responsibility for damage to or loss of personal property.

We may terminate your right to attend at any time either by giving seven days' written notice to you or immediately without any notice if you are in breach of any of the terms or conditions described in this letter or if you commit any act that we reasonably consider to amount to serious misconduct or to be disruptive and/or prejudicial to the interests and/or business of this NHS organisation or if you are convicted of any criminal offence. You must not undertake regulated activity if you are barred from such work. If you are barred from working with adults or children this letter of access is immediately terminated. Your employer will immediately withdraw you from undertaking this or any other regulated activity and you **MUST** stop undertaking any regulated activity immediately.

Your substantive employer is responsible for your conduct during this research project and may in the circumstances described above instigate disciplinary action against you.

**NHS Greater Glasgow and Clyde** will not indemnify you against any liability incurred as a result of any breach of confidentiality or breach of the Data Protection Act 1998. Any breach of the Data Protection Act 1998 may result in legal action against you and/or your substantive employer.

If your current role or involvement in research changes, or any of the information provided in your Research Passport changes, you must inform your employer through their normal procedures. You must also inform your nominated manager in this NHS organisation.

Yours sincerely



Mrs Elaine O'Neill

**Senior Research Administrator**

## Appendix 4

Letter of Access for Research granted by NHS Greater Glasgow and Clyde for the period of 18/03/2019 – 18/07/2021. Reason for extension was due to the COVID-19 pandemic.



Administrator: Mrs Elaine O'Neill  
Telephone Number: 0141 301 4001  
E-Mail: elaine.o'neill2@ggc.scot.nhs.uk  
Website: www.nhsggc.org.uk/r&d

Research & Innovation  
Dykebar Hospital  
Grahamston Road  
Paisley

10 August 2020

Miss Lauren Johnston  
University of Strathclyde  
40 George Street  
Glasgow G1 QE

Dear Miss L Johnston,

### **Letter of Access for Research**

This letter confirms your right of access to conduct research through **NHS Greater Glasgow and Clyde** for the purpose and on the terms and conditions set out below. This right of access commences on **18/03/2019** and ends on **18/07/2021** unless terminated earlier in accordance with the clauses below.

You have a right of access to conduct such research as confirmed in writing in the letter of permission for research from this NHS organisation. Please note that you cannot start the research until the Principal Investigator for the research project has received a letter from us giving permission to conduct the project.

The information supplied about your role in research at **NHS Greater Glasgow and Clyde** has been reviewed and you do not require an honorary research contract with this NHS organisation. We are satisfied that such pre-engagement checks as we consider necessary have been carried out.

You are considered to be a legal visitor to **NHS Greater Glasgow and Clyde** premises. You are not entitled to any form of payment or access to other benefits provided by this NHS organisation to employees and this letter does not give rise to any other relationship between you and this NHS organisation, in particular that of an employee.

While undertaking research through **NHS Greater Glasgow and Clyde**, you will remain accountable to **Dr Avril Mason** in this NHS organisation or those given on her/his behalf in relation to the terms of this right of access.

Where any third party claim is made, whether or not legal proceedings are issued, arising out of or in connection with your right of access, you are required to co-operate fully with any investigation by this NHS organisation in connection with any such claim and to give all such assistance as may reasonably be required regarding the conduct of any legal proceedings.

You must act in accordance with **NHS Greater Glasgow and Clyde** policies and procedures, which are available to you upon request, and the Research Governance Framework.

You are required to co-operate with **NHS Greater Glasgow and Clyde** in discharging its duties under the Health and Safety at Work etc Act 1974 and other health and safety legislation and to take reasonable care for the health and safety of yourself and others while on **NHS Greater Glasgow and Clyde** premises. You must observe the same standards of care and propriety in dealing with patients, staff, visitors, equipment

and premises as is expected of any other contract holder and you must act appropriately, responsibly and professionally at all times.

If you have a physical or mental health condition or disability which may affect your research role and which might require special adjustments to your role, if you have not already done so, you must notify your employer and the health board's HR department prior to commencing your research role at the Health board.

You are required to ensure that all information regarding patients or staff remains secure and *strictly confidential* at all times. You must ensure that you understand and comply with the requirements of the NHS Confidentiality Code of Practice (<http://www.dh.gov.uk/assetRoot/04/06/92/54/04069254.pdf>) and the Data Protection Act 1998. Furthermore you should be aware that under the Act, unauthorised disclosure of information is an offence and such disclosures may lead to prosecution.

You should ensure that, where you are issued with an identity or security card, a bleep number, email or library account, keys or protective clothing, these are returned upon termination of this arrangement. Please also ensure that while on the premises you wear your ID badge at all times, or are able to prove your identity if challenged. Please note that this NHS organisation accepts no responsibility for damage to or loss of personal property.

We may terminate your right to attend at any time either by giving seven days' written notice to you or immediately without any notice if you are in breach of any of the terms or conditions described in this letter or if you commit any act that we reasonably consider to amount to serious misconduct or to be disruptive and/or prejudicial to the interests and/or business of this NHS organisation or if you are convicted of any criminal offence. You must not undertake regulated activity if you are barred from such work. If you are barred from working with adults or children this letter of access is immediately terminated. Your employer will immediately withdraw you from undertaking this or any other regulated activity and you MUST stop undertaking any regulated activity immediately.

Your substantive employer is responsible for your conduct during this research project and may in the circumstances described above instigate disciplinary action against you.

**NHS Greater Glasgow and Clyde** will not indemnify you against any liability incurred as a result of any breach of confidentiality or breach of the Data Protection Act 1998. Any breach of the Data Protection Act 1998 may result in legal action against you and/or your substantive employer.

If your current role or involvement in research changes, or any of the information provided in your Research Passport changes, you must inform your employer through their normal procedures. You must also inform your nominated manager in this NHS organisation.

Yours sincerely



Mrs Elaine O'Neill

**Senior Research Administrator**

## Appendix 5

Permission from Glen Oomen to re-publish Scientific illustrations in this thesis.

**From:** Glen Oomen glenoomen@gmail.com  
**Subject:** Re: Form Submission - New Form - Permission to reprint image in Doctoral Thesis  
**Date:** 18 November 2021 at 17:48  
**To:** lauren.johnston@strath.ac.uk



**CAUTION: This email originated outside the University. Check before clicking links or attachments.**

Hi Lauren,

First, thanks so much for asking! Second, just for asking instead of right-click-save-as-ing, I grant you permission to use them. It's always nice when people offer to pay, but I can completely understand when you're writing your thesis. Those were the bicuspid aortic valves, ejection shear stress and aortic aneurysm pattern images, right? Let me know if the resolution is enough, if it's not I'll see if I can dredge up the original files.

A little bit about those illustrations. I may have mentioned on that behance page (it's been eons since I've checked in there) that those images were meant to be rough drafts. My client, and you may want to credit him also, Dr Subodh Verma (Cardiovascular surgeon at St. Michaels Hospital, University of Toronto - his research is worth reading anyway, not that you need any new citations at this point) was submitting to the New England Journal of Medicine, which we knew has its own staff illustrators so that everything, quality wise, is consistent with them. We thought we were quickly submitting draft illustrations that they would render in their own way, so that's what they got. They copied them exactly - like perfect forgeries! But you don't need to credit NEJM.

Let me know if you need anything else. I've got a small hoard of arterial cross-sections stashed somewhere.

Cheers,

G

On Thu, Nov 18, 2021 at 6:13 AM Squarespace <[form-submission@squarespace.info](mailto:form-submission@squarespace.info)> wrote:

Sent via form submission from [Glen Oomen Illustration](#)

**Name:** Lauren Johnston

**Email Address:** [lauren.johnston@strath.ac.uk](mailto:lauren.johnston@strath.ac.uk)

**Subject:** Permission to reprint image in Doctoral Thesis

**Message:** Hi Glen,

I am a PhD researcher at the University of Strathclyde and currently writing up my Doctoral Thesis. I am interested in blood flow of the Aorta and through my quest to find some nice (and not overly used!) Aorta images to include in my Thesis I came across your work. I would specifically like to include the second image here (<https://www.behance.net/gallery/18098681/Bicuspid-Aortic-Valve-and-aortic-aneurysm>) to display the anatomy of the aorta.

Let me know if you grant permission for me to reprint this image with acknowledgements.

Regards,

Lauren  
[lauren.johnston@strath.ac.uk](mailto:lauren.johnston@strath.ac.uk)

Does this submission look like spam? [Report it here.](#)

## Appendix 6

UKRI – Mitacs Award Letter for research in Canada.



March 21, 2022

Application Ref. : IT17876  
Funding Request Ref. : FR47010  
Mitacs file : ON/ISED

University of Toronto  
100 College Street, Suite 413  
Toronto, ON M5S 3G4  
Attention: Innovations & Partnerships Office (IPO), Contracts Assistant

### NOTICE OF AWARD

#### Mitacs Globalink Research Award - for research in Canada UK Research and Innovation (UKRI)

**Project Title:** Aortic arch haemodynamics in adult women with Turner syndrome: A numerical investigation into obesity-related factors

**Host academic supervisor:** Cristina Amon

**Intern:** Lauren Johnston

**Host Department:** Department of Mechanical and Industrial Engineering

**Host Institution:** University of Toronto

**Home academic supervisor:** Asimina Kazakidi

**Home Institution:** University of Strathclyde

**Accounts:** Please open ONE account in the supervisor's name.

The sum of **\$3,000.00** has been awarded for the above referenced project for the eligible internship listed in **Appendix A**. This award covers expenses, which support the direct costs of research, incurred during the period of **March 14, 2022 – August 14, 2022**. It is recognized that travel costs such as airline flights may be incurred prior to the project dates; as long as the costs are directly related to this project, Mitacs deems these costs as being eligible. Please note that the award excludes costs associated with interruptions due to COVID-19, including but not limited to, costs related to quarantine procedures imposed by governments, flight cancellation, accommodation pursuant to a cancellation, obtaining vaccinations, obtaining negative COVID-19 test results prior to travel, etc. *The end date of the account includes an additional period to spend the materials/research cost portion of the award.* Note: UK Research and Innovation (UKRI) will also be providing the remainder of the funding towards this project.

Please allocate the awarded funds according to the fellowship details, stipend/salary and research allocations outlined in **Appendix A**. The conditions attached to this internship award are outlined in **Appendix B**.

This award is offered in partnership with the UK Research and Innovation (UKRI). Mitacs-Globalink gratefully acknowledges the financial support of the Government of Canada.

● Montréal, QC  
405 avenue Ogilvy  
Bureau 101  
Montréal, QC H3N 1M3

● Ottawa, ON  
56 Sparks Street  
Suite 300  
Ottawa, ON K1P 5A9

● Toronto, ON  
Banting Institute, University of Toronto  
522 – 100 College Street  
Toronto, ON M5G 1L5

● Vancouver, BC  
Suite 301 – 6190 Agronomy Road  
University of British Columbia  
Vancouver, BC V6T 1Z3

1 of 4

## Appendix 7

Signed University of Toronto invitation letter.



Mechanical & Industrial Engineering  
UNIVERSITY OF TORONTO

February 15, 2022

Host Supervisor: Professor Cristina Amon  
Department of Mechanical and Industrial Engineering, University of Toronto  
5 King's College Road, Toronto, ON M5S 3G8

Home Supervisor: Professor Asimina Kazakidi  
Biomedical Engineering, University of Strathclyde  
Wolfson Building  
Scotland, United Kingdom  
G4 0NW

**RE: International Visiting Graduate Student Study Abroad Agreement – Lauren Johnston**

Dear Professor Kazakidi,

This letter confirms the arrangements for the visit of your PhD student, Lauren Johnston for the Study Abroad period of March 14, 2022 to June 14, 2022. I will serve as her supervisor at the University of Toronto, Mechanical and Industrial Engineering while she is a visiting student. An Offer of Admission into the IVGS Study Abroad program will be sent to the student from the University of Toronto, School of Graduate Studies.

Your student will be studying with me in the area of biofluids, cardiovascular biomechanics and cardiovascular engineering. She will be provided a workspace in my lab and I will meet with the student on a weekly/bi-weekly basis to ensure her research is progressing adequately. Lauren Johnston must abide by the University of Toronto's research policies and protocols, including intellectual property and research ethics.

It is our understanding that Lauren Johnston will secure her own funding to cover all the costs associated with her flight, living expenses, and other expenditures during her stay in Canada. We will not cover Lauren Johnston's study stipend nor other costs.

Yours sincerely,

Professor Cristina Amon  
Host Supervisor, University of Toronto

Professor Tobin Filleter  
Associate Chair, Graduate Studies

**We, the undersigned, agree to the terms and provisions set forth in this letter:**

Professor Asimina Kazakidi  
Home Supervisor  
University of Strathclyde

Signature of Student  
Lauren Johnston

Professor Stuart Reid  
Home Department Chair  
University of Strathclyde

## Appendix 8

Both users performed segmentation of the pre-operative data for patient 001 and the differences were analysed in Paraview software. The surface area difference between the two geometries was 3.55% (geometry surface area for user one = 22,251 mm<sup>2</sup> and for user two = 23,070 mm<sup>2</sup>). The *PolyDataDistance* filter was used in Paraview to compute the distance between each segmentation at every point. The result was a colour map distribution of the distance in millimetres. When averaging all the distance values between the two geometries, the average distance was 0.60 mm.

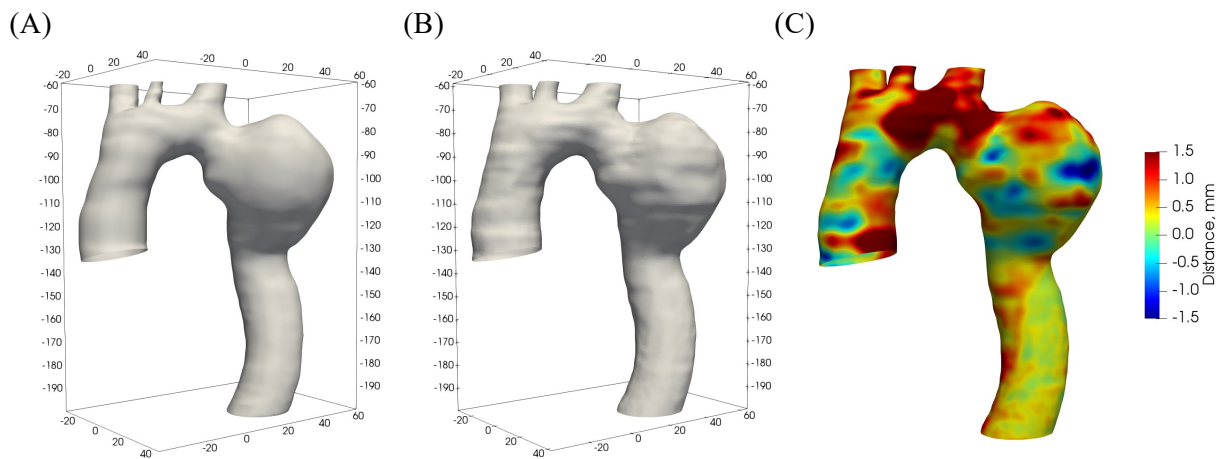


Figure A8. Geometric model of patient 001 pre-operatively segmented by (A) user one and (B) user two, and (C) colour map of the distance (in millimetres) between models (A) and (B) computed using the *PolyDataDistance* filter in Paraview.

## Appendix 9

The geometric centreline was generated from the 3D surface triangulation of each anatomic model to provide the baseline for morphometric analysis. In VMTK, the centreline was automatically extracted (using automatic end point detection) in the form of a set of discrete points in space (computed as the centres of maximal spheres inscribed in the vessel lumen) between the source and target point(s). In the case of the aorta, the centreline was computed from the ascending aorta (the source point) to the descending aorta (target point). The geometric centreline was then smoothed in VMTK which utilises a moving average filter.

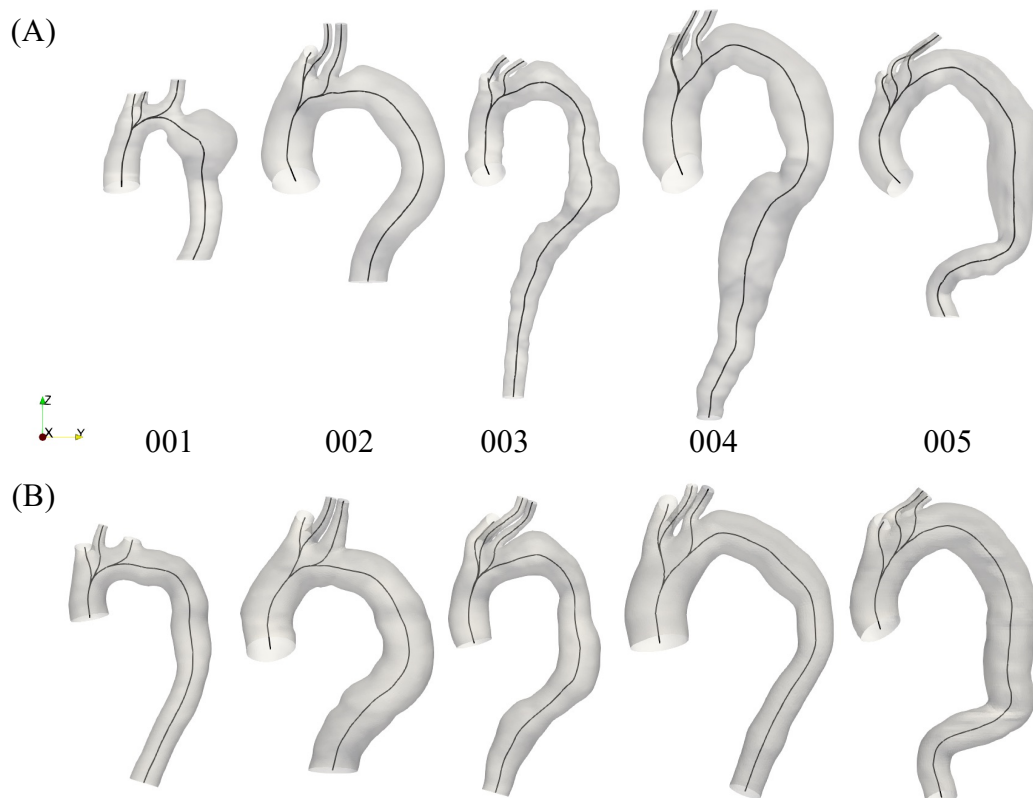


Figure A9. (A) Pre-operative and (B) post-operative geometries of the thoracic aorta for patients 001 – 005 with the geometric centreline included. All geometries are in scale.

## Appendix 10

Table A10. Number of elements used in the mesh generation (ANSYS ICEM CFD) for the pre- and post-operative geometries of patients 001-005.

Case	Number of elements	y value, m	y <sup>+</sup> value
Pre-operative			
001	967, 836	8.20 E-05	0.23
002	1,155,556	8.19 E-05	0.11
003	1,334,478	8.21 E-05	0.23
004	1,325,951	8.65 E-05	0.12
005	1,469,974	8.20 E-05	0.20
Post-operative			
001	724,903	8.19 E-05	0.20
002	1,158,663	8.19 E-05	0.11
003	962,950	8.64 E-05	0.22
004	1,184,220	8.19 E-05	0.09
005	1,290,778	8.37 E-05	0.16